

LOW TEMPERATURE MODELLING
OF VOLATILE ADDITIONS IN
IRONMAKING

by

(C) Ian A. Cameron

A Thesis Submitted to the
Faculty of Graduate Studies and Research
in Partial Fulfilment of the Requirements for the
Degree of Master of Engineering in Metallurgical Engineering

Department of Mining and Metallurgical Engineering
McGill University
Montreal, Canada

March 1982

Ian A. Cameron
Master of Engineering
Dept. of Mining and Metallurgical Engineering

SHORT TITLE OF THESIS:

Modelling of Volatile Additions in Ironmaking

ABSTRACT

To investigate the volatility of magnesium at iron making temperatures, low temperature modelling was carried out using liquid nitrogen as the volatile species. To simulate the release of magnesium vapour as it would occur from "modified" magnesium bullets shot into molten iron, liquid nitrogen was plunged into water and the subsequent evolution of vapour was recorded on video tape.

The addition was observed to release nitrogen vapour in a series of bubble bursts. The nature of the gas flow was investigated with respect to container dimensions or quantity of nitrogen added and the rate of heat transfer. Analysis yielded a three step boiling process; the initial ejection of more than half the addition as the addition begins to boil, the steady state boiling of the remaining nitrogen and finally the displacement of the gaseous addition from its container by the surrounding liquid. The data generated from the low temperature model agreed favourably with previous work done in liquid metals.

RESUME

Une étude de la volatilité du magnésium aux températures de l'acier en fusion a été effectuée en utilisant un modèle à basse température où les matériaux volatiles étaient remplacés par de l'azote liquide. Le dégagement de magnésium gazeux provenant d'un cylindre de magnésium 'modifié' lancé dans du fer en fusion était simulé par de l'azote liquide plongé dans de l'eau et le comportement de la vapeur était enregistré à l'aide d'un magnétoscope.

Il fut observé que la vapeur d'azote s'échappait sous forme de violentes séries de bulles. La nature de l'écoulement du gaz fut étudiée en fonction des dimensions du récipient, de la quantité d'azote utilisée et du transfert de chaleur. L'analyse a montré que l'ébullition se faisait en trois étapes; l'éjection initiale de plus de la moitié de l'azote quand l'ébullition commence, l'ébullition continue et constante de l'azote restant et, finalement, le déplacement du gaz restant dans le récipient par le liquide environnant. Les résultats obtenus à l'aide de ce modèle à basse température se sont avérés en accord avec des travaux précédents faits sur des métaux en fusion.

ACKNOWLEDGEMENTS

The author would like to thank Dr. R.I.L. Guthrie for his encouragement and support.

The author would also like to thank Dr. S. Agryopoulos for his help in preparing and operating the microprocessor. Thanks are also due to Miss. K. Rivett for typing the manuscript and Mrs. M. McIntosh for preparing the diagrams. Discussions with both staff and graduate students in particular Dr. Y. Sahai, Mr. D. Doutre and especially Dr. F. Mucciardi, were helpful in formulating results and ideas.

Finally, the author wishes to thank the Quebec Ministry of Education and the American Iron and Steel Institute for their financial support.

TABLE OF CONTENTS

	<u>Page</u>
ABSTRACT	ii
RESUME	iii
ACKNOWLEDGEMENTS	iv
LIST OF FIGURES	ix
LIST OF TABLES	xv
LIST OF APPENDICES	xvii
CHAPTER 1. INTRODUCTION	
1.1 General	1
1.2 The Present Study	4
1.3 Thermodynamics of Hot Metal Desulphurization	6
1.4 Steel Refining	14
1.5 Pure Magnesium and Calcium Additions	17
1.6 Addition Techniques	25
1.6.1 Pneumatic Techniques	25
1.6.2 Mag - Coke	33
1.6.3 Addition of Pure Magnesium	36
1.7 Summary	44
CHAPTER 2. BULLET SHOOTING TECHNIQUES - PREVIOUS WORK	
2.1 Introduction	45
2.2 Aluminum Bullets	47
2.3 Thermal Aspects of Bullet Shooting	55
2.4 Modified Bullets	65
2.5 Magnesium Bullets	75
2.6 The Physical Model - Present Work	79

Page

CHAPTER 3. GAS - LIQUID INTERACTION PHENOMENA - PREVIOUS WORK

3.1	Introduction	91
3.2	Magnesium Vapour Dissolution	92
3.3	Bubble Formation at a Single Orifice	101
3.3.1	Gas Injection in Aqueous Systems	102
3.3.2	The Motion of Free Bubbles	114
3.3.3	Bubble Formation in Liquid Metals	118
3.4	Two Phase Flow	124
3.5	Gravity Driven Flow	128
3.6	Summary	133

CHAPTER 4. EXPERIMENTAL

4.1	Introduction	134
4.2	Apparatus	134
4.2.1	Water Tank	134
4.2.2	Liquid Nitrogen Containers	137
4.2.3	Documentation	137
4.2.4	Materials	140
4.3	Experimental Variables	144
4.4	Experimental Program	144
4.5	Analysis of the Experimental Data	146

CHAPTER 5. RESULTS

5.1	Introduction	153
5.2	Experimental Data	153
5.3	Results: Qualitative	158

Page

5.3.1	Initial Period: Tube Immersion and Initial Turbulence	158
5.3.2	Mid - Period: Steady State Boiling	159
5.3.3	End Period of Experiment: Displacement of the Boiling Phase	175
5.3.4	The Gallium Tube	182
5.4	Results: Quantitative	
5.4.1	Bath Superheat	186
5.4.2	Shell Thermal Conductivity	190
5.4.3	Shell Geometry: Diameter	194
5.4.4	Shell Geometry: Length	194
5.4.5	Shell Geometry: Orientation	200
5.5	Summary	203

CHAPTER 6. DISCUSSION

6.1	Introduction	204
6.2	Steady State Boiling - Stage Two	204
6.2.1	Steady State Boiling - Heat Transfer	205
6.2.2	Classification of Flow Region	209
6.2.3	Freely Rising Bubbles	217
6.3	Displacement - Stage Three	219
6.3.1	Displacement - Heat Transfer	220
6.3.2	Criteria Limiting Displacement	225
6.3.3	Ethyl Ether and Water System	229

Page

6.4 Initial Ejection - Stage One	232
6.5 Summary	241

CHAPTER 7. INDUSTRIAL IMPLICATIONS AND CONCLUSIONS

7.1 Introduction	244
7.2 Magnesium Bullets - General	244
7.2.1 Bullet Design - Type I	248
7.2.2 Bullet Design - Type II	251
7.2.3 Bullet Design - Type III	253
7.3 Conclusions	255

APPENDICES	258
------------	-----

REFERENCES	268
------------	-----

LIST OF FIGURES

<u>Figure</u>		<u>Page</u>
1.1	Concentration Profiles Describing the Dissolution of Magnesium Vapour into Molten Iron	8
1.2	Chemical Equilibrium between Magnesium and Sulphur in Hot Metal	10
1.3	The Effect of Calcium Sulphide on CaC_2 Particles during Desulphurization	13
1.4	Variation of the Oxygen and Sulphur Contents of Steel during the Injection of Calcium Silicide	16
1.5	Vapour Pressure of Magnesium and Calcium at Elevated Temperatures	20
1.6	A 3.2 mm Magnesium Wire being fed into Molten Iron	21
1.7	Schematic of the Lime-Mag Desulphurization Process	30
1.8	Magnesium Dissolution Efficiency as a Function of the Height of Rise for Various Bubble Compositions	32
1.9	Mag-Coke Plunging Assembly	34
1.10	Plunging Bell Typically used for Mag-Coke Treatments	35
1.11	Schematic of the Vaporizer Equipment used to Desulphurize Hot Metal with Solid Magnesium	37
1.12	Making up a Plunging Charge using Three Coated Magnesium Bars	40
1.13	Schematic Illustration ²³ of the Wire Feeder used by Hieber and Watmough	42
2.1	Water Modelling Apparatus used by Tanoue et al. ⁸ to Evaluate the Hydrodynamics of Bullet Shooting	49
2.2	The Hydrodynamic Stages of Bullet Shooting	49
2.3	Typical Aluminium Bullet used at Sumitomo Metal Industries	50

		x
<u>Figure</u>		<u>Page</u>
2.4	Results of Hydrodynamic Analysis of Bullet Shooting by Tanoue et al. ⁸	53
2.5	Melting Curves for Aluminum Bullets after Tanoue et al. ⁸	54
2.6	Aluminum Bullet Shooter used at Sumitomo Metal Industry's Wakayama and Kashima Works	54
2.7	Results of Mucciardi's ⁹ Hydrodynamic Study of Bullet Shooting	56
2.8	Typical Events when a Cold Addition is Made to Molten Steel	58
2.9	Growth of a Steel Shell on a Rising Aluminum Bullet	58
2.10	Force Sensing Apparatus used by Mucciardi ⁹ to Detect the Release of Aluminum from Aluminum Wires and Bullets	60
2.11	Typical Aluminum Cylinder before Immersion used by Mucciardi ⁹	63
2.12	Experimental Bullet Designs Tested by Mucciardi ⁹	64
2.13	Effect that a Thermal Resistance has on the Iron Shell Formation on Aluminum	66
2.14	Melting Mechanisms of Both Conventional and Modified Bullets	68
2.15	The Release of Aluminum from a Modified Bullet	74
2.16	Artistic Impression of the Release of Magnesium in Hot Metal from a Modified Bullet	78
2.17	Temperature Profiles during Addition Vaporization for both Model and Prototype	83
3.1	The Results of Several Investigations on the Dissolution of Magnesium Vapour in Iron as per Irons ⁶	93
3.2	Magnesium Vaporizer used by Irons ⁶ to Introduce Magnesium Vapour into Molten Iron	95

<u>Figure</u>		<u>Page</u>
3.3	Depth of Iron Required to Completely Dissolve a Magnesium Bubble	99
3.4	Final Magnesium Bubble Size for Incomplete Dissolution	100
3.5	Quantity of Magnesium Vapour Dissolved into Iron for Several Melt Depths	100
3.6	Comparison between Davidson and Schuler's ⁶⁵ Equation and Experimental Data	109
3.7	Transition from Bubbling to Jetting: The Effect on Bubble Diameter	112
3.8	Bubble Classification as per Clift et al. ⁶²	117
3.9	Bubble Formation at a Submerged Orifice for both Wetting (Aqueous) and Non-Wetting (Metallic) Systems	119
3.10	Bubble Volume as a Function of Gas Flow Rate for Metallic Systems	122
3.11	Comparison between Gas Injection in Metallic and Aqueous Systems	123
3.12	Two Phase Cocurrent Flow Patterns in a Vertical Tube Evaporator	125
3.13	Characteristic Pool Boiling Curve for Water Showing the Four Distinct Stages	127
3.14	Characteristic Pool Boiling Curve for Liquid Nitrogen	129
3.15	Growth of an Unstable Perturbation between Water and Air	131
4.1	Apparatus used for Low Temperature Experimentation	135
4.2	The 200 l Pyrex Tank used to Simulate an Iron Bath	136
4.3	Typical Nitrogen Containers used in the Present Study	139
4.4	Typical Frame Generated by the Video System	141

<u>Figure</u>		<u>Page</u>
4.5	Typical Bubble Formation during the Vaporization Process	148
4.6	Oblate and Prolate Ellipsoids	151
5.1	Experimental Results for Test 13c	156
5.2	Experimental Results for Test 7a	157
5.3	Initial Burst of Nitrogen as a Glass Tube is Plunged into Water	160
5.4	Initial Burst of Nitrogen as an Aluminum Tube is Plunged into Water	163
5.5	Initial Turbulence when an Aluminum Tube is Plunged into Water	166
5.6	Comparison of Doublet and Pair Bubbles with High Speed Cinematography Traces after Irons ⁶	168
5.7	The Formation of Double Bubbles at the Opening of an Aluminum Tube	169
5.8	Bubble Development at the Opening of a Glass Tube	172
5.9	Displacement of the Gaseous Phase for a Glass Tube	176
5.10	Gas Flow from a Small Diameter Glass Tube	179
5.11	The Breakup of a Gallium Tube as it is Plunged into Water	183
5.12	Effect of Increasing Bath Superheat on the Bubble Diameter and Frequency for an Aluminum Tube	188
5.13	Effect of Increasing Bath Superheat on the Bubble Diameter and Frequency for a Glass Tube	189
5.14	Nitrogen Gas Flow shown against Container Thermal Conductivity	191
5.15	Residual Ice Shells on a Glass Tube after Plunging into Water	193

<u>Figure</u>		<u>Page</u>
5.16	Effect of Increasing Tube Diameter on the Bubble Diameter and Frequency for a Glass Container	195
5.17	Effect of Increasing Tube Diameter on the Bubble Diameter and Frequency for an Aluminum Container	196
5.18	Effect of Increasing Tube Length on the Bubble Diameter and Frequency for an Aluminum Container	197
5.19	Effect of Increasing Tube Length on the Bubble Diameter and Frequency for a Glass Tube	198
5.20	Effect of Increasing Tube Length on the Bubble Diameter and Frequency for a Small Diameter Aluminum Tube	199
5.21	Effect of Tube Orientation on Bubble Frequency and Gas Flow Rate for an Aluminum Tube	202
6.1	Effect of Increasing Gas Flow Rate on Bubble Volume	206
6.2	Comparison of the Experimental Results to Previous Work on Bubble Formation at Submerged Orifices	212
6.3	Effect of Increasing Gas Temperature on the Results Obtained by Davidson and Harrison ⁶⁷	214
6.4	Details of an Instrumented Nitrogen Containing Tube	221
6.5	Temperature Profiles during Vaporization for an Aluminum Tube	223
6.6	Temperature Profiles during Vaporization for a Glass Tube	223
6.7	Initial Ejection of Nitrogen Gas with Increasing Bath Superheat	235
6.8	Initial Ejection of Nitrogen Gas with Increasing Tube Diameter	236
6.9	Initial Ejection of Nitrogen Gas with Increasing Tube Length	237

FigurePage

6.10	Initial Ejection of Nitrogen Gas as a Function of Tube Orientation	238
7.1	Change in the Interfacial Tension of Iron with Increasing Concentration of Dissolved Magnesium	247
7.2	Proposed Bullet Designs	249
B.1	Temperature Profiles during N ₂ Vaporization from an Aluminum Tube (SH=19K)	266
B.2	Temperature Profiles during N ₂ Vaporization from a Glass Tube (SH=11K)	266
B.3	Temperature Profiles during N ₂ Vaporization from an Aluminum Tube (SH=11K)	267
B.4	Temperature Profiles during N ₂ Vaporization from an Aluminum Tube (SH=11K)	267

LIST OF TABLES

<u>Table</u>		<u>Page</u>
1.1	Popular Pneumatic Techniques	27
1.2	Operating Data for a Submerged Magnesium Vapourizer	38
1.3	Operating Results for the Injection of Steel Clad Magnesium Wire	43
2.1	Melting Times for Conventional Bullets	61
2.2	Melting Times for Modified Bullets	73
2.3	Physical Properties of the Light Metals	76
2.4	Properties of Some Cryogenic Gases	80
3.1	Values for K_1 Describing the Solubility of Magnesium in Cast Iron ¹	94
3.2	Constants Obtained for Equation (3.16)	108
3.3	Factors Influencing Bubble Size	113
3.4	Influence of Liquid Properties on Bubble Volume as Reported by Various Investigators	115
4.1	Dimensions of the Nitrogen Containers Used in the Present Study	138
4.2	Thermal and Physical Properties of Liquid Nitrogen and Water	142
4.3	Thermal and Physical Properties of the Construction Materials Used for Nitrogen Tubes	143
4.4	Experimental Parameters	144
5.1	Data from Experiment 12c	154
6.1	Orifice Reynolds Number as a Function of Bath Superheat	216
6.2	Flow Characterization for Several Nozzle Diameters	226

<u>Table</u>		<u>Page</u>
6.3	Comparison of the Displacement of Ethyl Ether to the Vaporization for Several Tubes	231
6.4	Initial Gas Ejection for the Shell Material Tested	239
A1	Bath Superheat Experiment: Aluminum Tubes	259
A2	Bath Superheat Experiment: Glass Tubes	260
A3	Shell Thermal Conductivity Experiment	261
A4	Shell Geometry Experiment: Diameter	262
A5	Shell Geometry Experiment: Length	263
A6	Shell Geometry Experiment: Angle	264

LIST OF APPENDICES

<u>Appendix</u>		<u>Page</u>
A	Experimental Results	258
B	Temperature Profiles during Nitrogen Gas Evolution	265

CHAPTER 1

INTRODUCTION

1.1 GENERAL

Many additives commonly used in the iron and steelmaking industries for desulphurization and/or inclusion modification contain either calcium or magnesium. Although these elements are added in a variety of forms, they are unique due to their volatile nature at temperatures associated with iron and steelmaking. Thus in the production of raw steel, calcium and magnesium may enter the flowsheet at two places; the first between the blast furnace and steel production facility, while the second would follow the production of raw steel.

The iron product of a blast furnace known as 'hot metal' is essentially liquid iron saturated with carbon ($>4\%$ C). A number of other impurities are also present in blast furnace iron. Typical impurities and their concentrations are shown below¹.

<u>Impurity</u>	<u>Weight %</u>
C	4.3
Mn	0.9
Si	0.7
S	0.03

Sulphur is one of the most notorious impurities in steel. The detrimental effects of high sulphur levels include increased amounts of surface cracks during processing and an

increased inclusion content which in turn adversely affects the physical and mechanical properties of steel. For the most common steel grades sulphur levels must be maintained below 0.05% S with 0.02% S usually considered as acceptable². As J.P. Orton³ noted, 'All steel mill operators and metallurgists spend a considerable portion of their working lives trying to deal with the sulphur problem, trying to balance its undesirable effects with the cost of eliminating it.'

The main source of sulphur found in hot metal derives from the metallurgical coke used in blast furnace ironmaking. Until recently all sulphur control was done through the selection of low sulphur coal and the maintenance of a favourable sulphur partition coefficient between the hot metal and blast furnace slag. To obtain low hot metal sulphur levels, larger slag volumes are needed to achieve effective sulphur loading. This is detrimental to a blast furnace's fuel efficiency as the coke rate must increase to melt the additional flux.

Since the late 1960's and early 1970's the practice of removing sulphur from the hot metal outside the blast furnace has received considerable attention from both steelmaking researchers and operators. Known as external desulphurization, this step allows the blast furnace operators to increase the hot metal sulphur level up to 0.08-0.10% S. The subsequent processing step lowers the hot metal sulphur content to the desired level of 0.02% S.

The advantage to the blast furnace operations are significant. During a two week trial at Dofasco⁴ when the hot metal sulphur content was increased from 0.02% to 0.045%, there was a 13% increase in hot metal production. This was due to a 4.3% increase in the wind rate and an 8.8% decrease in the coke rate. Other advantages which were cited include, increasing the alkali removal rate from 60% to 80% and an increased burden permeability. The high sulphur practice and better alkali removal allowed Dofasco to consider less expensive raw materials which previously had unacceptable impurity concentrations. The net savings, when comparing the cost of desulphurization to the blast furnace saving for the trial, was quoted as 69%. In view of this trial Dofasco went to a complete external desulphurization practice and blast furnace hot metal levels of 0.06-0.08% S. Based on experiences typical of Dofasco's, many steel producers have added external desulphurization of hot metal to improve their existing facilities.

In steelmaking, the majority of impurities originally present in the hot metal are reduced to specified levels. These impurities would include carbon, silicon and manganese. Sulphur is one of the elements which is difficult to remove during conventional steelmaking. For the majority of the grades which receive sufficient hot metal desulphurization, sulphur is not a problem; however, an increased demand for

low sulphur pipeline grades has necessitated a further desulphurization step following steelmaking. Pipeline steel requires a thorough desulphurization as the sulphur specification for this grade calls for a maximum of 0.005% S.

Pipeline grades also require secondary refining for inclusion modification and removal. This involves agglomeration of the oxide inclusion particles in the steel, so that they will more readily float to the slag covering the refined steel, thereby improving the cleanliness and mechanical properties of the steel.

1.2 THE PRESENT STUDY

The addition of calcium and magnesium is the basis of most external desulphurization processes. The pure substances are rarely added for several reasons. Magnesium which boils at 1363 K^5 under normal conditions, exerts high vapour pressures when it is plunged into hot metal, typically at 1533 K . Calcium which is even more reactive than magnesium, is rarely used in the elemental form as it readily oxidizes in the atmosphere. The large potential for calcium oxide formation requires more stable calcium compounds to be used in commercial practice. Another volatile system involves the use of a calcium reagent during secondary refining of steel. Here again, the same difficulty as was cited above for the magnesium arises. Calcium normally boils at 1757 K^5 and is therefore very readily

vapourized at steelmaking temperatures of 1900 K.

Although both magnesium and calcium are thermodynamically excellent desulphurization agents the processes for adding them have yet to be perfected. The industrial solution to the high vapour pressures associated with these elements is to use a variety of diluents to reduce the overall vapour pressure of the addition. Recently, pneumatic techniques whereby nitrogen or argon is used both as a carrier gas and diluent have gained popularity. Surprisingly little fundamental work has been carried out on the vapourization process associated with either the desulphurizing reagents or pure calcium and magnesium. The present study has been oriented toward magnesium desulphurization of hot metal since the problems of metal volatility in this system outweigh those for calcium refining of steel.

Only a few studies have dealt with magnesium vapour and its dissolution kinetics.^{6,7} To the author's knowledge, no work has been carried out in the area of the heat transfer and hydrodynamic phenomena associated with the boiling of a volatile addition. The present study was therefore initiated to investigate the phenomena of volatile additives. Due to the fear of explosions and other problems associated with introducing magnesium to iron, a low temperature analogue of the system was first developed.

In modelling an addition technique, a patented modification of Sumitomo Metal Industry's bullet shooting technique

for adding buoyant additions was selected.⁸ This technique is known to have good potential for quickly exposing large quantities of the volatile buoyant addition to the melt. The bullet shooting technique will also permit the fast and simple introduction of pure magnesium. Before expanding into the modelling of bullet shooting technology, a review of hot metal desulphurization and steel refining is first presented.

1.3 THERMODYNAMICS OF HOT METAL DESULPHURIZATION

The desulphurization of hot metal is based on the use of one of three reagents - magnesium, calcium carbide (CaC_2) or lime (CaO). All three are thermodynamically excellent desulphurizing agents, but they all have associated kinetic problems which has limited the perfection of any one desulphurizing process. The chemical thermodynamics of these reagents will be summarized using the excellent review of desulphurization processes by Mucciardi.⁹ Upon inspection of the thermodynamics it should be clear that the solution to the kinetic problems of the desulphurization reactions could result in an extremely efficient process for sulphur removal.

Magnesium has a very strong affinity for sulphur, forming magnesium sulphide according to the reaction:



Here, the underlined elements refer to those dissolved in liquid iron with their concentrations at the one weight

percent standard state. Recently, there has been some debate as to the precise mechanism of magnesium desulphurization. Preliminary research indicated that desulphurization occurred at the magnesium bubble-melt interface and that the rate controlling step was the diffusion of sulphur to this interface.¹⁰ Work by Irons and Guthrie^{11,12} has shown that magnesium readily dissolves in iron and that it is the reaction of dissolved magnesium with dissolved sulphur that predominates during desulphurization operations. The concentration profiles for desulphurization proposed by Irons and Guthrie¹² are shown in Figure 1.1. The solid phase referred to in Figure 1.1 includes small inclusion ($\approx 2 \mu\text{m}$ diameter) and solid interfaces in the bath which could support magnesium sulphide formation and precipitation.

Through this mode of reaction very low sulphur levels are possible from both kinetic as well as thermodynamic considerations. The equilibrium constant for equation 1.1 (at 1533 K) is given by Irons⁶ as:

$$\log K = \log\{(f_{\text{Mg}} \cdot \% \text{Mg}) \cdot (f_{\text{S}} \cdot \% \text{S})\} = -5.05 \quad (1.2)$$

Assuming the activity of MgS solid to be one, the activity coefficients for dissolved sulphur and dissolved magnesium (at 1533 K) are given by the following equations:^{6,13,14}

$$\log f_{\text{S}} = -0.028(\% \text{S}) - 1.82(\% \text{Mg}) + 0.11(\% \text{C}) \quad (1.3)$$

$$\text{and} \quad \log f_{\text{Mg}} = -1.41(\% \text{Mg}) - 1.38(\% \text{S}) - 0.14(\% \text{C}) \quad (1.4)$$

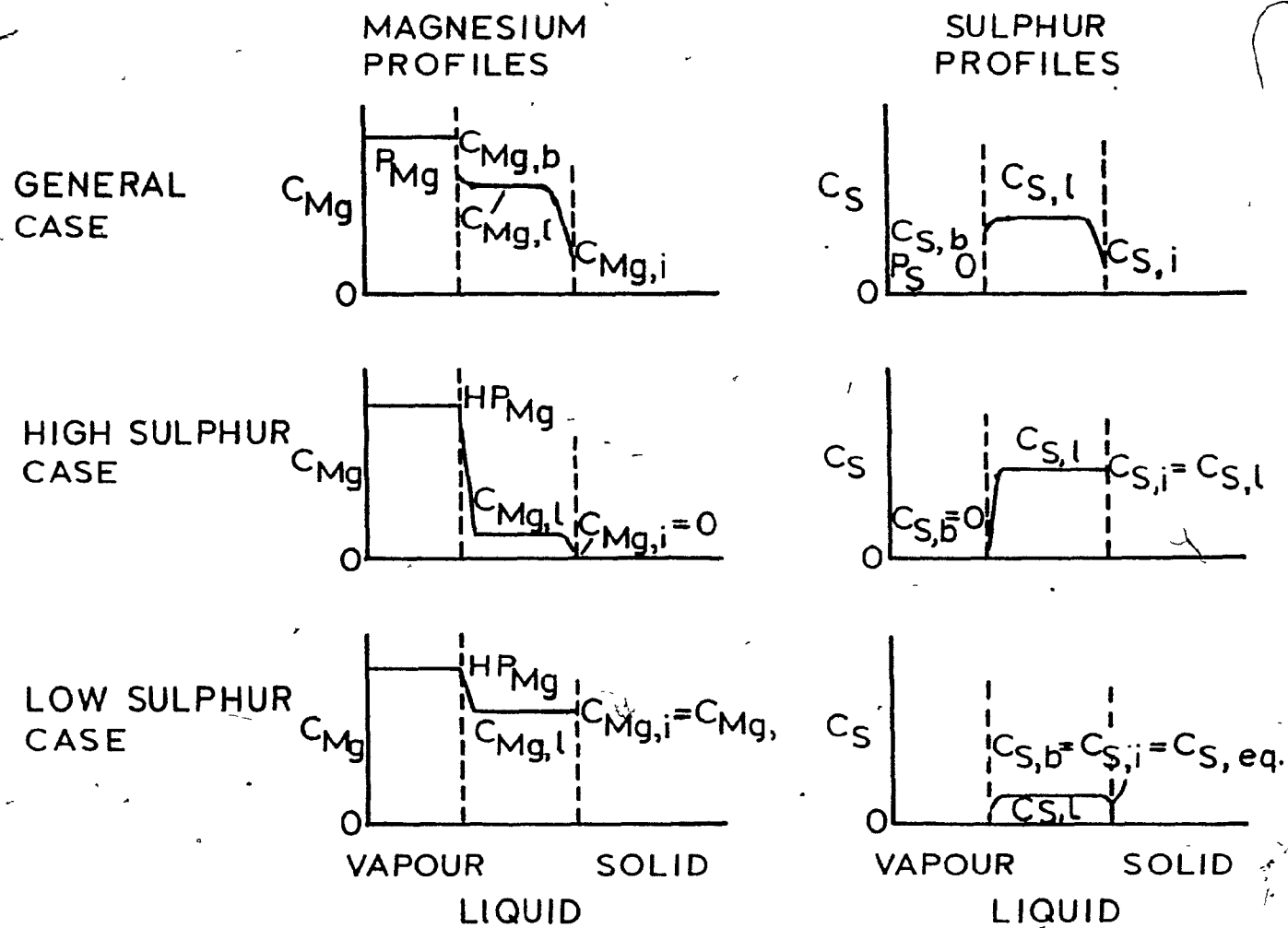


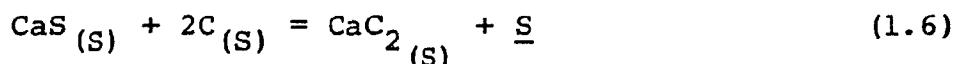
Figure 1.1 Concentration Profiles Describing the Dissolution of Magnesium from Magnesium Vapour into Molten Iron. Profiles are Shown for the Magnesium Vapour, Liquid Iron and Solid MgS Phases.

Solving equations 1.2 - 1.4 yields the following result at 1533 K:

$$\begin{aligned} -1.408(\%S) - 3.23(\%Mg) - 0.03(\%C) + \log(\%Mg) \\ + \log(\%S) = -5.05 \end{aligned} \quad (1.5)$$

The equilibrium curve for a typical hot metal averaging 4.5% C is shown in Figure 1.2. Clearly magnesium can effectively eliminate dissolved sulphur if equilibrium is approached.

Another excellent desulphurizer from a thermodynamic viewpoint is calcium carbide. The removal of sulphur via CaC_2 is described at 1533 K by the following equation:



The equilibrium constant for the above equation is:¹⁴

$$\log K = \log f_S(\%S) = 5.712 - \frac{18750}{T(K)} \quad (1.7)$$

where

$$\log f_S = -0.028(\%S) + 0.11(\%C) \quad (1.8)$$

Therefore, at a hot metal content of 4.5%C and temperature of 1533 K, equations 1.7 and 1.8 reduce to:

$$-0.028(\%S) + \log(\%S) = -7.014 \quad (1.9)$$

Solving Eq. 1.9 yields a sulphur concentration of $9.7 \times 10^{-8} \%S$ in equilibrium with the calcium carbide at 1533 K:

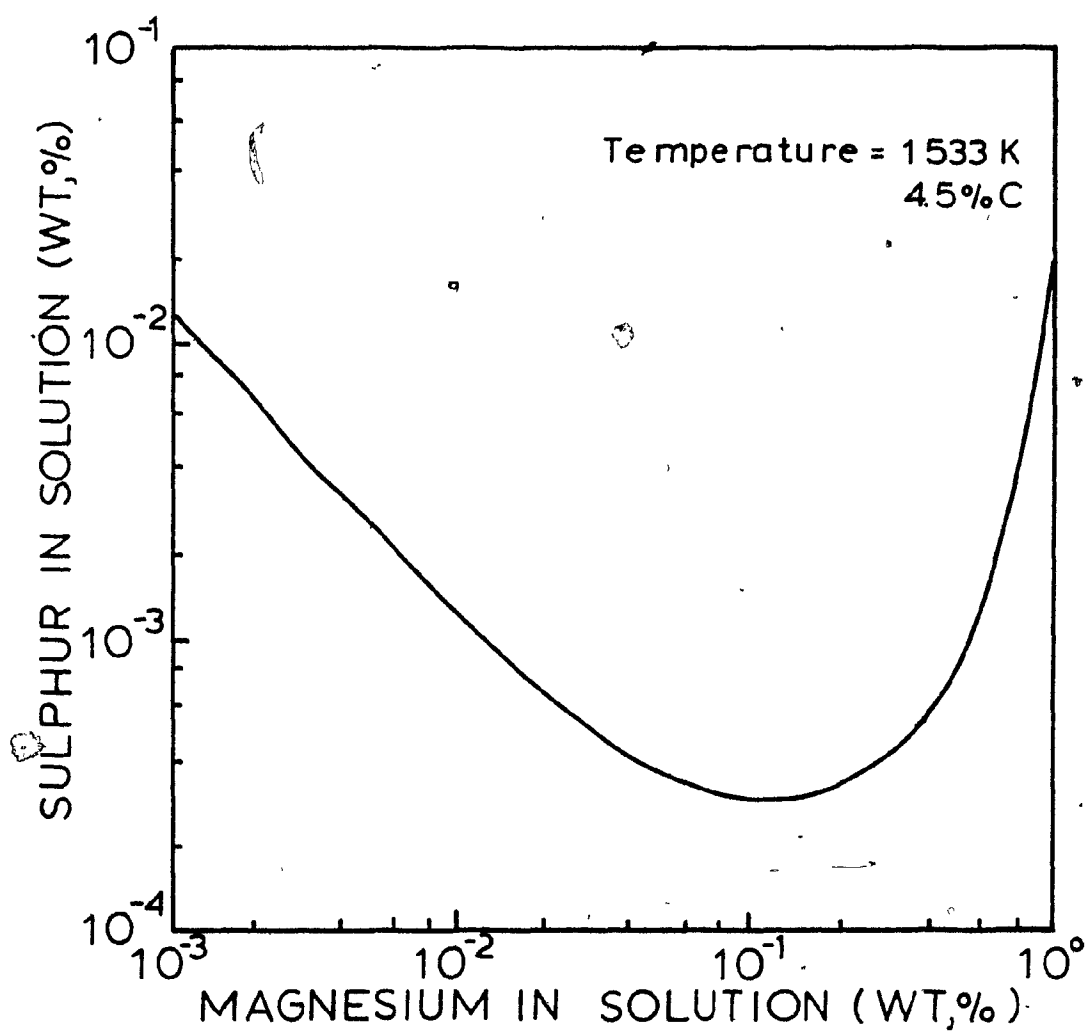


Figure 1.2 Chemical Equilibrium between Magnesium and Sulphur in Hot Metal.⁹

This is far lower than the 0.005% sulphur required for most low sulphur grades.

The last reagent, lime, is also thermodynamically an excellent desulphurizer. Sulphur elimination is achieved by lime according to the following reaction:



The equilibrium constant and associated activity data at 1533 K are given below:¹⁴

$$\log K = \log \frac{f_S(\%S)}{f_O(\%O)} = \frac{5693}{T(K)} - 1.528 \quad (1.11)$$

where

$$\log f_O = -0.20(\%O) - 0.45(\%C) - 0.09(\%S) \quad (1.12)$$

$$\text{and } \log f_S = -0.028(\%S) + 0.11(\%C) - 0.18(\%O) \quad (1.13)$$

Solving Eqs. 1.11-1.13 yields the following result:

$$\begin{aligned} 0.062(\%S) + 0.56(\%C) + 0.02(\%O) + \log(\%S) \\ - \log(\%O) = 2.186 \end{aligned} \quad (1.14)$$

Assuming that the melt contains 4.5% C and that only a small amount of oxygen (i.e. $5 \times 10^{-4} \%$) is soluble in hot metal, a solution to equation 1.14 for %S yields a sulphur level of $2.3 \times 10^{-4} \%$ S at 1533 K. This value is much closer to the lowest sulphur levels that steelmakers demand but if equilibrium was achieved it would be an excellent grade by any standard.

As shown above all three desulphurizing agents, magnesium, calcium carbide and lime, should provide excellent results. Industrial and laboratory studies have shown far less than perfect results for desulphurization using these reagents. A chemical efficiency of 50% would be considered good practice by most steel mill operators. Chemical efficiency is defined as the weight of reagent X which participated in the desulphurization reaction to the weight of X added to the iron treated. This treatment ignores the amount of reagent X dissolved into the iron, and for most situations this is quite accurate since calcium has an overall limited solubility in iron while magnesium solubility is low for high sulphur levels ($>0.01\%S$).

The problem with calcium carbide and lime is the fact that the chemical reaction occurs at a solid-liquid interface. For both CaC_2 and CaO particles the initial CaS reaction product tends to coat the remaining reagent available for desulphurization.^{15,16,17} Subsequent desulphurization is limited by the diffusion of the sulphur through the CaS boundary layer. This concept is shown schematically in Figure 1.3. Other variables which limit desulphurization are diffusion of sulphur to the solid-liquid interface and the sulphur level in the melt.

As a particle is consumed, its rate of consumption decreases as the reaction product layer thickens. To solve this, finer reagent particles should be selected so as to increase the net surface area available for reaction. This

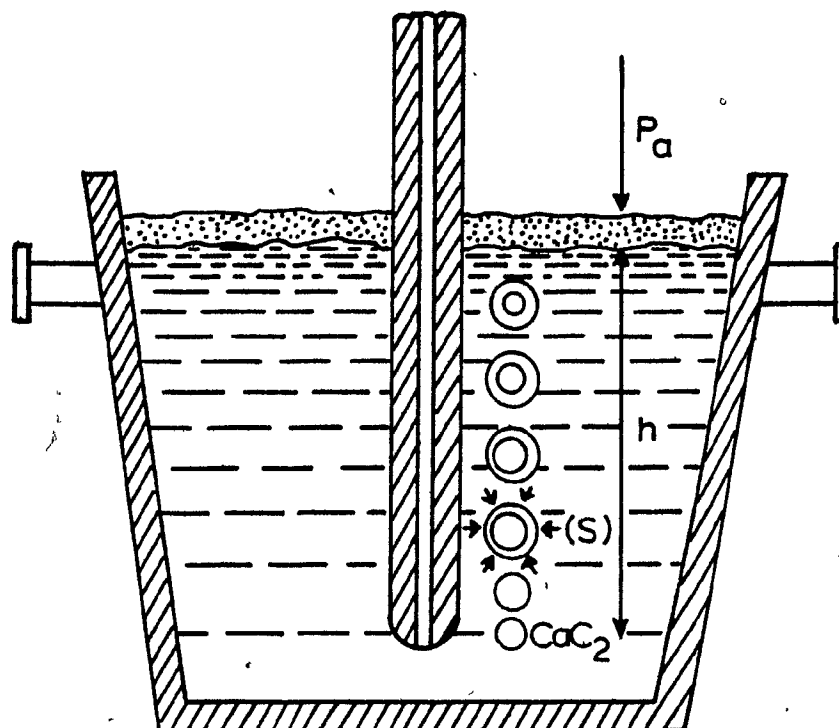


Figure 1.3 The Effect of Calcium Sulphide on CaC_2 Particles During Desulphurization.

has a secondary beneficial effect in terms of the time it takes for the lighter lime particles to rise through the hot metal. From Stoke's law, rising times are inversely proportional to particle diameter. Thus, smaller particles will take longer to rise through the iron bath. For both calcium carbide and lime, the efficiency of the process is related to the particle distribution and hence may be optimized through control of this parameter.

The problems associated with magnesium desulphurization are related to its extremely high vapour pressure. This problem will be more completely examined in section 1.5.

1.4 STEEL REFINING

A major portion of secondary steel refining is performed using calcium based reagents. Calcium is both an excellent desulphurizer and deoxidizer. Another valuable aspect of calcium additions is the modification and removal of oxide and sulphide inclusions. Calcium is usually alloyed with silicon so as to moderate the vapour pressure of calcium. Unlike magnesium, calcium exhibits a very low solubility in steel with values of 0.032 weight % dissolved calcium in pure iron being reported at 1873 K.¹⁸ Since calcium does not exhibit excessive vapour pressures at steelmaking temperatures (see section 1.5) its vapourization can be suppressed through the addition of a calcium silicon alloy. Another important reason for alloying calcium is the fact that the pure species

rapidly oxidizes in the atmosphere. Handling of such a material would require sophisticated transport equipment using inert gas shielding. The alloy which is commonly used is known as calcium silicide and is generally composed of 30% Ca, 63% Si and 7% Fe.⁹ Other possible alloys comprise of Ca and Si mixed with manganese, barium, aluminum and iron.¹⁹

Since calcium is very reactive, special procedures must be taken so as to insure that the calcium performs the desired refining. The procedures should guarantee that the oxygen content of the steel, particularly the dissolved oxygen, is as low as possible. For this reason, the steel must be fully aluminum killed and the use of dolomitic lime for ladle refractories is recommended.²⁰ The reaction products, particularly CaS, readily revert to dissolved sulphur and CaO in the presence of free oxygen. To eliminate back reactions with the atmosphere, a CaO-CaF₂ synthetic slag is used to cover the steel during treatment.²¹ Once added to the melt, calcium first eliminates all of the dissolved oxygen forming CaO. As the dissolved oxygen approaches lower levels (20-30 ppm) the calcium then eliminates the dissolved sulphur and modifies the remaining oxide particles. This process has been summarized by Pircher and Klapdar²⁰ and is presented in Figure 1.4.

There are two types of inclusions which precipitate during the solidification of steel, spherical or globular inclusions and intergranular films.²² The globular inclusions which have a high oxide content are not too detrimental to the steel as

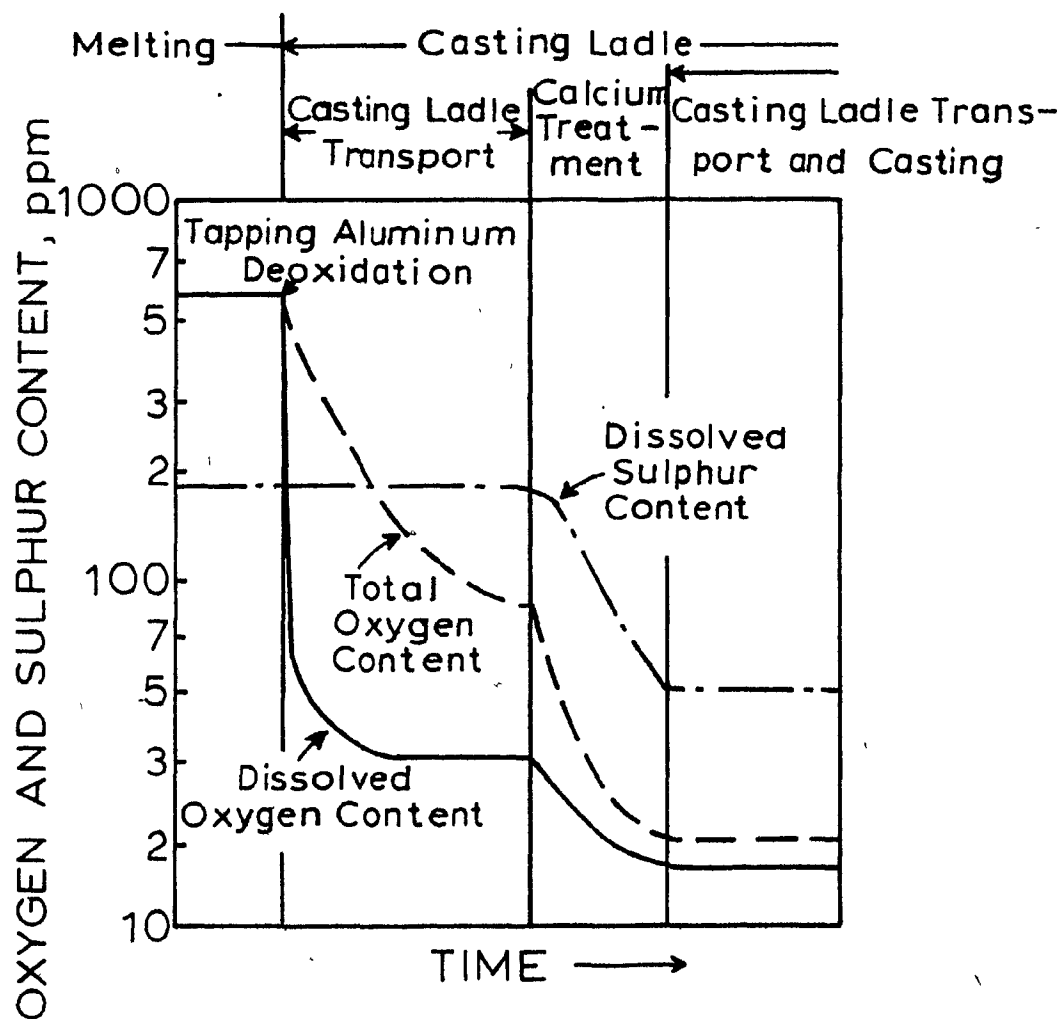


Figure 1.4 Variation of the Oxygen and Sulphur Contents of Steel during the Injection of Calcium Silicide.²⁰

they retain their shape during hot rolling. Conversely, inclusions which are intergranular in nature tend to promote hot shortness in hot rolling. These inclusions which are generally MnS also tend to decrease the mechanical properties transverse to the rolling direction.⁴ The calcium treatment tends to eliminate all of the MnS type inclusions through the presence of extremely low sulphur levels in the melt.

The inclusion found in calcium modified melts are generally round multiphase structures. Picher and Klapdar²¹ have found that the inclusions tend to be spinels of the $\text{CaO-Al}_2\text{O}_3$ type containing dissolved sulphur. Since these round inclusions are relatively harmless, the calcium treated steel is nearly isotropic with excellent through-thickness direction ductility.⁴

1.5 PURE MAGNESIUM AND CALCIUM ADDITIONS

To date, the author was only able to find a few industrial addition systems where pure magnesium or calcium is used without the aid of a carrier gas.^{23,24} The reasons why the pure elements are rarely used are due to the high vapour pressures they exhibit at operating temperatures. As previously mentioned in hot metal desulphurization, which typically takes place at 1600 K, elemental magnesium is 237 K over its normal atmospheric boiling point (1363 K). For calcium the problem is not as large, but calcium which normally boils at 1757 K is 116 to 160 K over its boiling point in most steel refining operations.

Being so unstable, the additives tend to have large vapour pressures at the melt temperature. These pressures can be thermodynamically evaluated at high temperatures via the Clausius-Clapeyron equation:²⁵

$$\ln \frac{P_2}{P_1} = \frac{\Delta \bar{H}_V}{R} \left(\frac{1}{T_1} - \frac{1}{T_2} \right) \quad (1.15)$$

where P_1, T_1 - refer to the vapour pressure and temperature (K) at any point;

P_2, T_2 - refer to the vapour pressure and temperature at any point other than point 1;

R = ideal gas constant

$\Delta \bar{H}_V$ = enthalpy of vapourization per unit mass of material.

If point one is taken as the normal boiling point of the specimen considered then the vapour pressure at a higher temperature can be evaluated. The reader is reminded that the Clausius-Clapeyron equation describes the vapour pressure of species A over pure species A. For pure magnesium and calcium additions this should hold true since the gaseous phase rapidly evolves from the pure species in the melt. Applying the Clausius-Clapeyron equation to magnesium in hot metal:⁵

$$P_1 = 101.3 \text{ kPa}$$

$$T_2 = 1600 \text{ K}$$

$$T_1 = 1363 \text{ K}$$

$$R = 8313.6 \text{ J/kg mole K}$$

$$\Delta \bar{H}_V = 1.46 \times 10^8 \text{ J/kg mole}$$

$$P_2 = 101.3 \text{ kPa} \exp\left\{\frac{1.46 \times 10^8 \text{ J/kg mole}}{8313.6 \text{ J/kg mole K}} \left(\frac{1}{1363\text{K}} - \frac{1}{1600\text{K}}\right)\right\}$$

$$= 683.1 \text{ kPa}$$

Magnesium would therefore exhibit a vapour pressure of over six times atmospheric pressure at a hot metal temperature of 1600 K. It is this high vapour pressure which causes the magnesium to boil in a violent fashion.²⁶ Any containment of the magnesium vapour can lead to explosions within the melt as the high pressure gas is released.

Another well documented problem is the flashing that occurs when the magnesium vapour reaches the melt surface.^{6,15,23,26} Upon contact, magnesium vapour instantly reacts with any oxygen in the surrounding atmosphere, leading to the copious generation of oxide smoke. The vapour pressure curves for both magnesium and calcium have been given by de Barbadillo²⁶ and are presented in Figure 1.5.

Some work presently being carried out at McGill University gives an excellent indication of the explosive potential of magnesium. Briefly, the investigation is into the possibilities of wire feeding pure magnesium into the hot metal. In the preliminary experiments bare magnesium wires were fed into the hot metal and the results proved to be most spectacular. Figure 1.6 shows the sequence of events that occur as a 3.2 mm magnesium wire is fed into the melt. As is evident from the photographs, the magnesium tends to readily vapourize and react

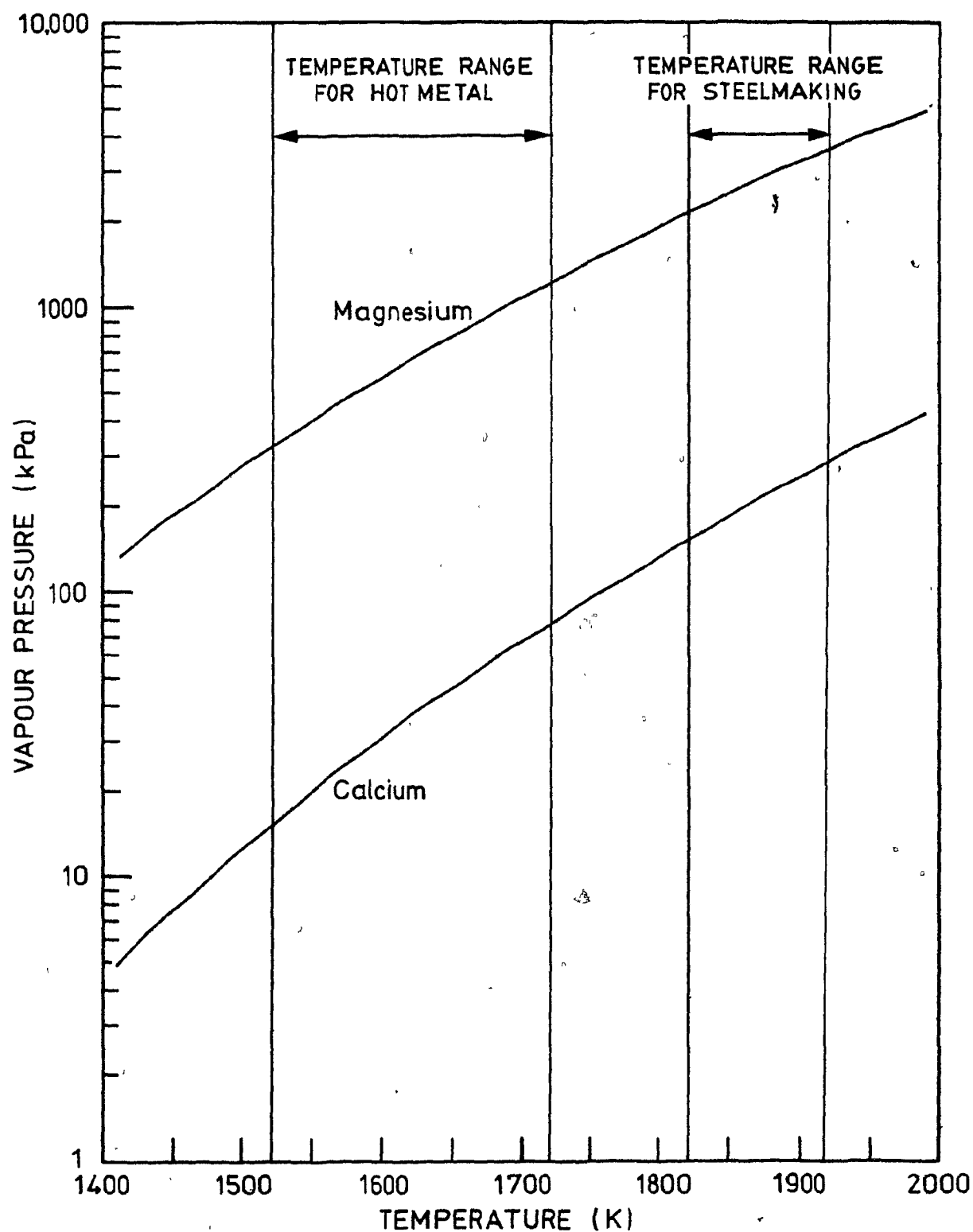
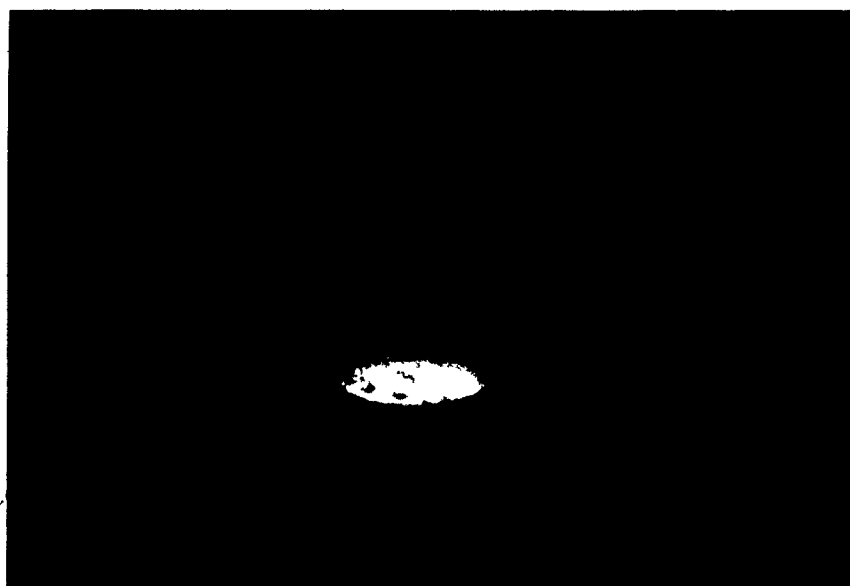
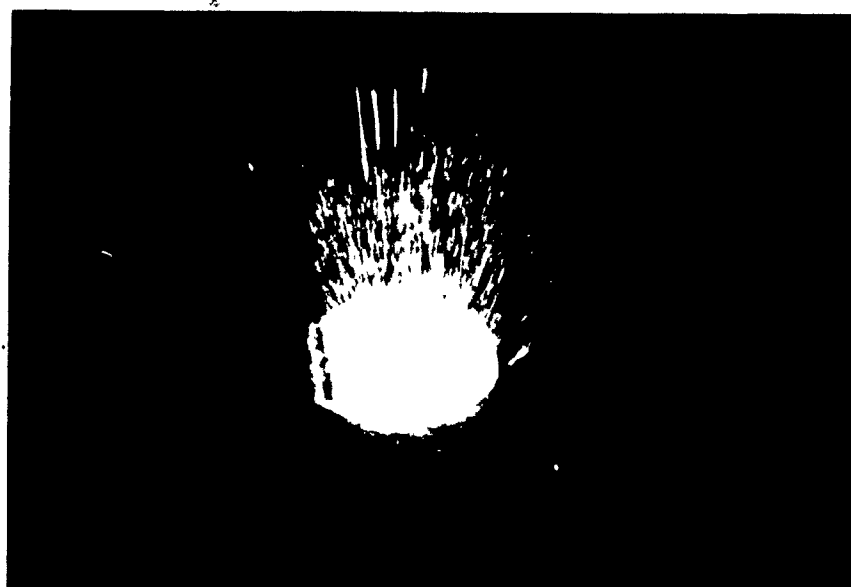


Fig. 1.5 Vapour Pressure of Magnesium and Calcium at Elevated Temperatures²⁶



(a) $t = 0$

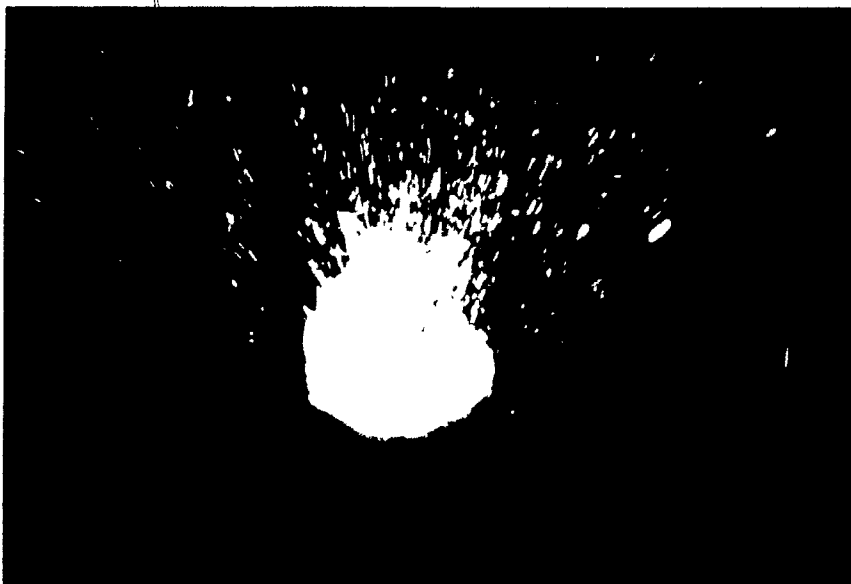


(b) $t = 10.0$ ms

Figure 1.6 A 3.2 mm Diameter Magnesium Wire being fed into Molten Iron at 20 mm/s.

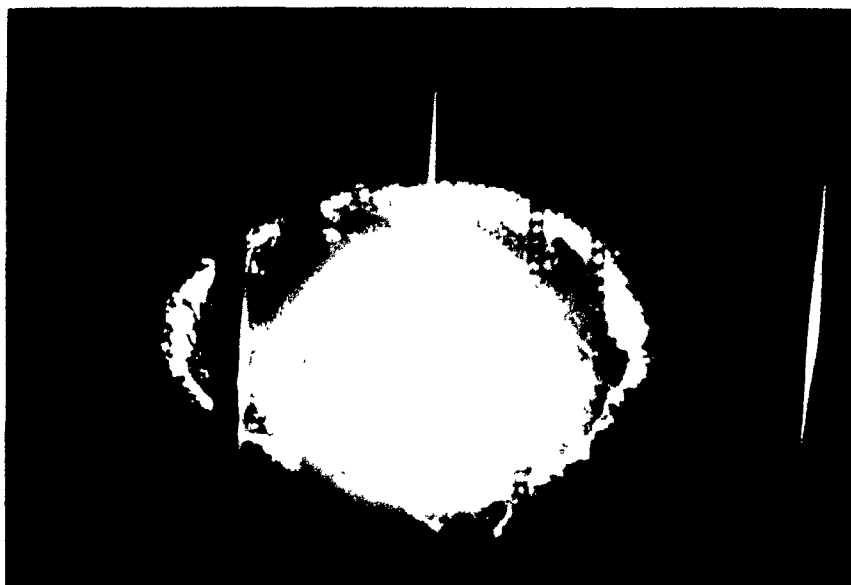


(c) $t = 20.0$ ms

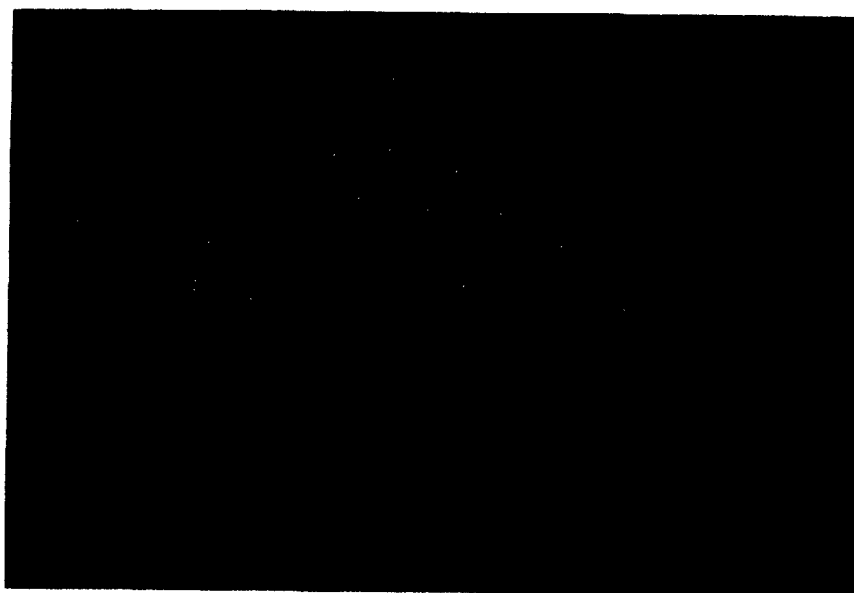


(d) $t = 30.0$ ms

Figure 1.6 (cont.)



(e) $t = 40.0$ ms

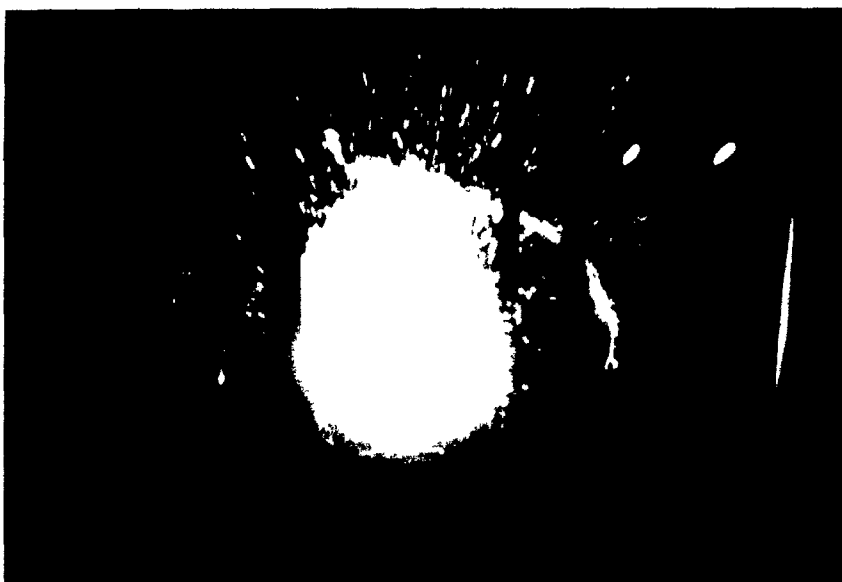


(f) $t = 50.0$ ms

Figure 1.6 (cont.)



(g) $t = 110$ ms



(h) $t = 200$ ms

Figure 1.6 (cont.)

with the surrounding atmosphere. The brilliant flashes characteristic of magnesium vapour are well documented as noted above.

1.6 ADDITION TECHNIQUES

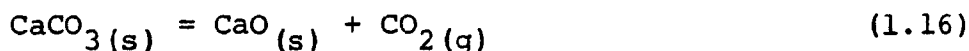
To overcome the problems of reactivity and vapour evolution associated with the common desulphurization agents, a number of sophisticated systems have been developed. Each system has both its merits and areas which could use improvements. Since the present study is more oriented towards addition techniques than to thermodynamics and chemical kinetics, the addition techniques will be reviewed from a mechanistic viewpoint. All of the major techniques will be reviewed irrespective of whether their usage is more toward hot metal or steel applications.

1.6.1 Pneumatic Techniques

Pneumatic injection techniques are presently the most popular method of introducing a large variety of desulphurization agents. The technique basically consists of the injection of the reagent through a submerged refractory coated lance with the aid of a carrier gas. In several cases, additional solid reagents are added to aid the reaction mechanisms associated with the primary desulphurization reagent. The technique is used to inject calcium carbide, lime, magnesium

powders, magnesium granules and salt coated magnesium granules into hot metals. Pneumatic injection is also used to add calcium silicide to steel. All of these techniques are summarized in Table 1.1 and will be briefly reviewed below.

Calcium carbide injection was developed simultaneously by Nippon Steel Corporation and August Thyssen Huette during the late sixties.⁹ The system has undergone constant evolution since its conception. One of the most significant improvements was found when calcium carbonate was mixed with the calcium carbide in a 1:3 ratio. The calcium carbonate reacts as follows:



The carbon dioxide produced from the CaCO_3 decomposition has been reported to hinder nozzle blockage and aid in the dispersion of the calcium carbide particles.²⁷ As a dispersant, the calcium carbonate is claimed to double the chemical efficiency of the calcium carbide.²⁸ Virtually all calcium carbide based injection systems use CaCO_3 to improve the performance of the operations.

One of the main problems with calcium carbide injection involves the handling of CaC_2 . When exposed to moisture CaC_2 readily decomposes into acetelyne and lime. Acetelyne (C_2H_2) is extremely flammable and potentially explosive if a large volume of the gas is ignited. To minimize this danger, sophisticated safety devices and procedures must be utilized.

TABLE 1.1
Popular Pneumatic Techniques

Process	Injectants	Carrier Gas	Melt	Typical* Chemical Efficiency	Reference
Calcium Carbide Injection	CaC_2 with CaCO_3	Nitrogen	Hot Metal	20% 40%	27, 28
Lime Injection	CaO	Nitrogen	Hot Metal	7%	30
Lime-Mag Process	Mg powder plus lime	Nitrogen	Hot Metal	75% based on Mg desulphurization 11% when CaO is considered	35, 36
Magnesium Granules	Salt coated Mg granules $d = 0.5-2 \text{ mm}$	Air/Nitrogen	Hot Metal	48%	33
Magnesium Granules	Mg granules $d = 1-2 \text{ mm}$ plus lime	Nitrogen	Hot Metal	55% based on Mg desulphurization 10% when CaO is also considered	31
Salt-coated Magnesium Granules	Mg granules coated by MgCl_2 and NaCl based salt compound	Nitrogen	Hot Metal	51%	34
TN/CAB Process	Calcium silicide 30% Ca, 63% Si 7% Fe	Argon	Steel	15%	16, 21

* The typical chemical efficiency for hot metal desulphurization pertains to the reduction of the sulphur level from 0.04% S to 0.02% S. For steel desulphurization the typical chemical efficiency is related to achieving a sulphur level of less than 0.010% S.

The calcium carbide must be stored, fluidized and transported using nitrogen. Air tight storage and handling facilities are also required.

The acetelyne problem is further compounded when the wet deslagging of the hot metal torpedo car is performed. Normally, after desulphurization the high sulphur slag remaining in the torpedo car is discarded into pools of water. In calcium carbide based systems, this has led to explosions due to the acetelyne produced by the reaction of the unreacted CaC_2 left in the slag with the water.²⁹

One of the first pneumatic systems developed was the injection of lime into hot metal. The industrial injection of lime at the Sidmar Steelworks has been described by Beyne.³⁰ This system combines lime with natural gas as the carrier gas. The natural gas was chosen to supply a strong reducing atmosphere at the lance opening thereby assuming that any CaS which had been formed would not reoxidize back to CaO . The chemical efficiency, quoted by Beyne to be 7%, has since been substantiated by other similar systems.^{31, 32}

A variety of systems have been based on the injection of magnesium powder or granules. The first magnesium injection systems were developed in the U.S.S.R. during the late sixties. Soviet researchers were considerably ahead of Western experts when Voranova et al.³³ reported on the state of the art of external desulphurizing systems in 1974. After examining several systems (Mg/lime, Mg/dolomite) the Soviet researchers had decided that

the injection of salt coated magnesium granules offered the best results. By 1974 this was the preferred technique for the Soviet steel industry. The purpose of the salt was to passivate the magnesium vapourization and hence, help eliminate nozzle blockage. It was to be nearly six years before this system was introduced in the Western steel industry.³⁴ Other advantages of this system, is the safety aspect of using the larger magnesium granules. The granules are reported to be much more stable and do not have the explosive potential that magnesium powders have. Granules are also reported to have much better flow properties than the corresponding powder.^{31,34}

In 1976, Koros was awarded a patent for an injection process combining magnesium and lime powders.^{35,36} Known as the 'Lime-Mag Process' the details of the injection equipment is schematically shown in Figure 1.7. In this process, large quantities of lime are injected with magnesium powder. Koros has stated that the lime acts as a magnesium dispersant, nucleating small magnesium bubbles.³⁶ The efficiencies based only on magnesium desulphurization are excellent as seen in Table 1.1. The main disadvantages of the Lime-Mag process are the generation of large slag volumes due to the unreacted lime and the danger of handling magnesium powder.

In 1980 Engh et al.³¹ presented the results of an injection system using magnesium granules and lime. This system was said to eliminate the transport and safety problems associated with the magnesium powder while maintaining a good chemical efficiency.

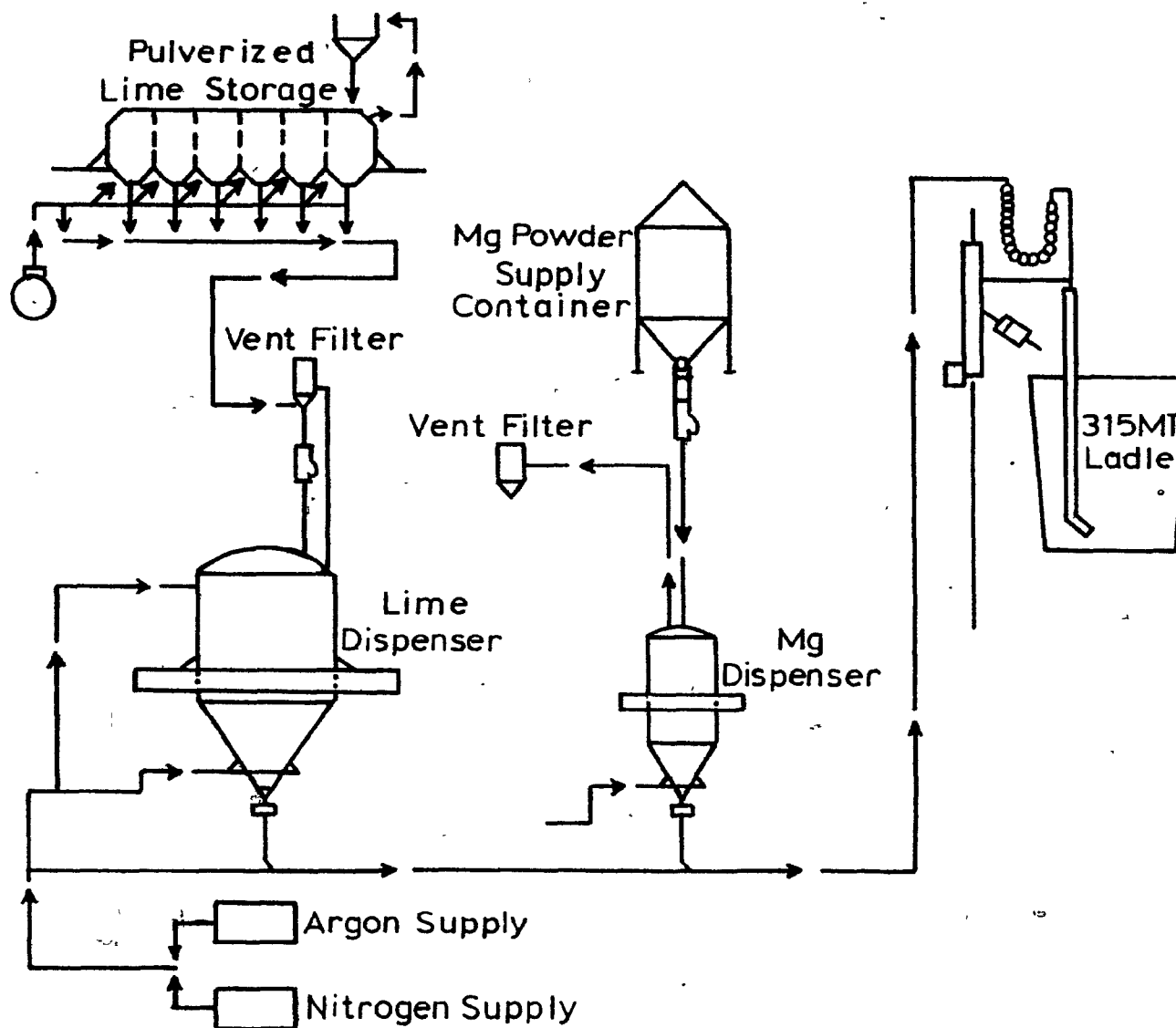


Figure 1.7 Schematic of the Lime-Mag Desulphurization Process.

Based on 54 injection experiments Engh achieved good results but not near the excellent chemical efficiency that Koros obtained.³⁶

There has been little fundamental work done on any of the injection processes. Work done by Irons and Guthrie³⁷ on the dissolution kinetics of magnesium vapour in pig iron yields some insight as to why chemical efficiencies for most injection systems are approximately less than or equal to 50%. They found that as the magnesium vapour is diluted by the inert carrier gas, the dissolution efficiency of the magnesium is dramatically reduced. Since this is the first stage of the desulphurizing reaction there should also be a corresponding drop in the chemical efficiency. The results of the calculations by Irons and Guthrie are shown in Figure 1.8. It is this reduction in dissolution efficiency due to dilution which makes improvements in the injection processes difficult.

The last pneumatic process cited is the TN/CAB process developed by Thyssen Niederrhein A.G. in the mid sixties.²¹ Used for the more chemically sensitive steel system, the process involves injection of calcium silicide with argon. Careful precautions must be taken to ensure that no oxidizing slag is carried over to the treatment vessel. Moreover, an inert lime-calcium fluoride slag cover must be added to the melt. The low efficiencies which are observed are normally attributed to the powerful oxidizing capacity associated

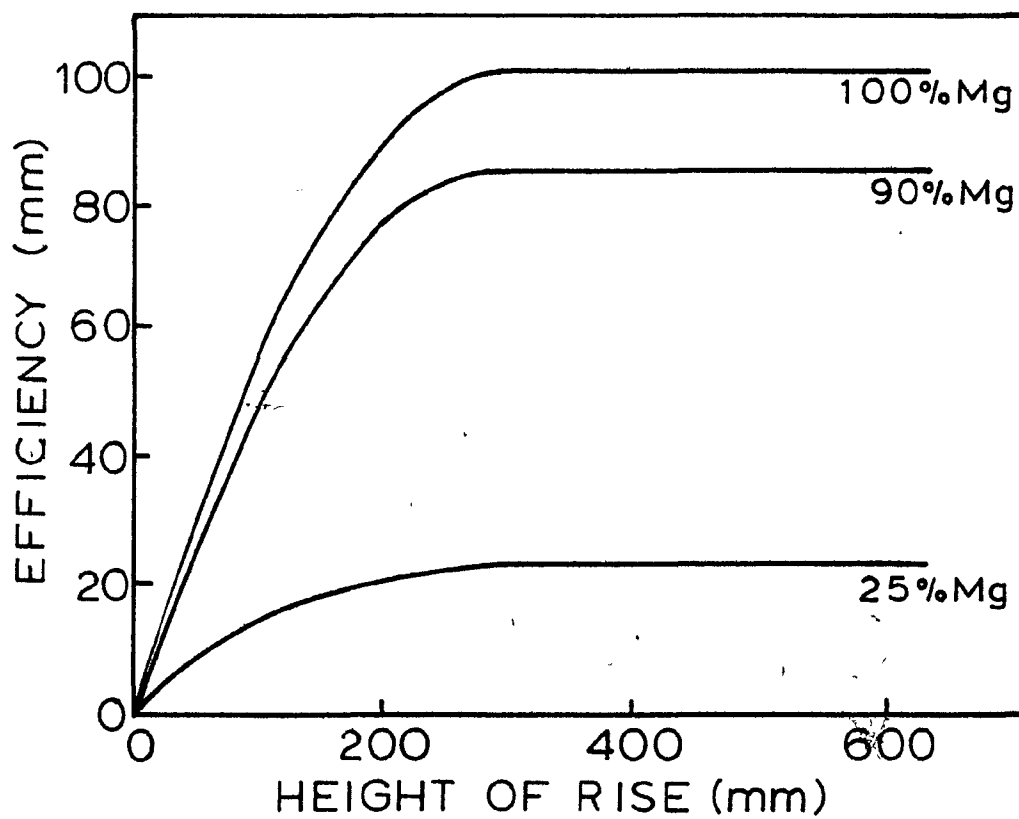


Figure 1.8 Magnesium Dissolution Efficiency as a Function of the Height of Rise for Various Bubble Compositions.³⁷

with calcium coupled with calcium's limited solubility in steel.¹⁸

1.6.2 Mag-Coke

The plunging of magnesium impregnated coke was one of the first large scale treatment systems for the desulphurization of hot metal. This compound, more commonly referred to as 'Mag-Coke', was used to moderate the vapourization of the magnesium. Mag-Coke is typically 46% Mg.⁴ Generally a steel canister containing the Mag-Coke is plunged into the hot metal using a graphite or a refractory coated T-shaped bell. A schematic of the plunging assembly is shown in Figure 1.9 while Figure 1.10 shows a photograph of a plunging bell. When the Mag-Coke is plunged into the hot metal, the magnesium vapourizes and escapes through holes in the bell.

There have been numerous investigations into the Mag-Coke process. Chemical efficiencies are typically 44% for hot metal sulphur changes from 0.05 - 0.02% S.^{4,30,35,38,39} The main drawback to Mag-Coke usage is the time associated with each treatment.^{9,36} Since only one drum can be added at a time, and a typical torpedo car requires at least two drums, the net process is time consuming. Other complaints with Mag-Coke include the cost of the reagent, the amount of fume generated by the plunging procedure and the lack of control over the rate at which the magnesium gas is released.³⁶ As

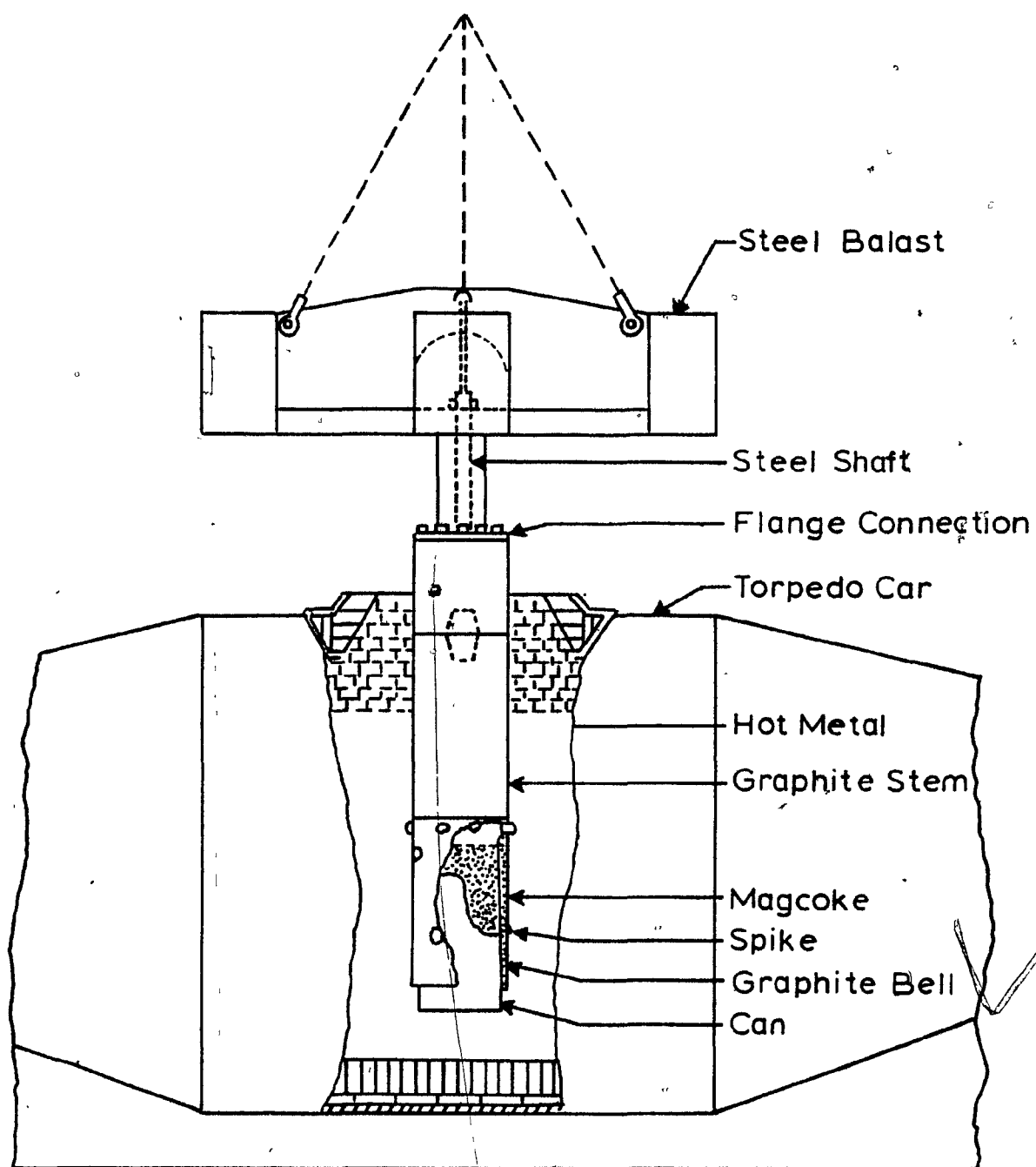


Figure 1.9 Mag-Coke Plunging Assembly.

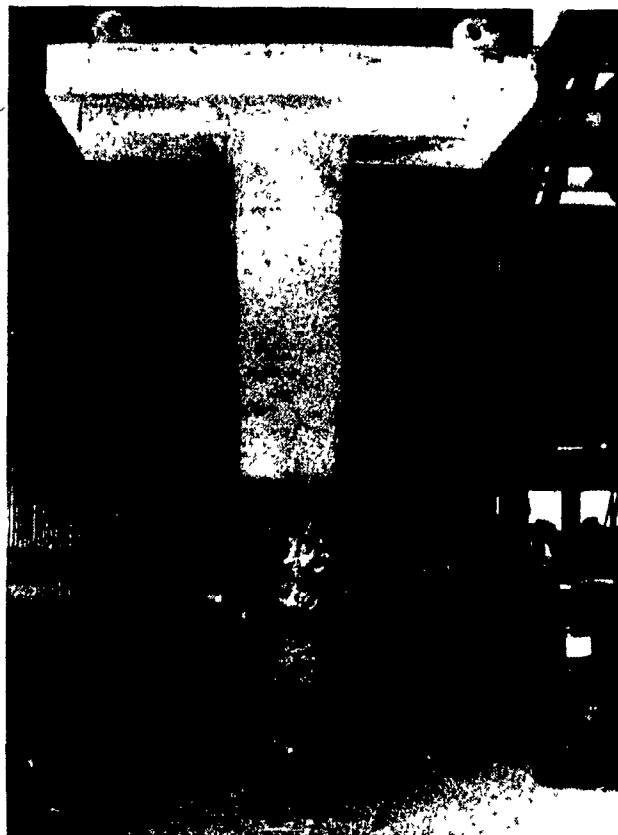


Figure 1.10 Plunging Bell Typically used for Mag-Coke Treatments.

a result Mag-Coke has been slowly phased out in favour of the pneumatic techniques previously mentioned.

1.6.3 Addition of Pure Magnesium

Due to the vapourization problem mentioned in section 1.5 the addition of pure magnesium has not yet been mastered. There have been some interesting procedures proposed and these will be briefly discussed.

Soviet researchers were the first to try and immerse magnesium into iron in a controlled fashion. Using a complex vapourizer shown in Figure 1.11 Polovchenko et al.²⁴ tried adding magnesium ingots as early as 1963. The original test work involved plunging pure magnesium lumps or bars. The violent reaction and subsequent ejection of iron led to innovations in the procedure. To delay the magnesium vapourization the magnesium was coated with a thin layer of refractory clay. This moderated the vapourization enough to limit the sudden release of a large amount of magnesium gas. Later work on the process refined the coating thickness and material. In one case magnesium lumps were coated with 20-40 mm of a waterglass material.^{*40} The alternative procedure involved immersing magnesium bars which were coated with the same material but only to a thickness of 3-5 mm.⁴¹ The performance of these two systems is shown in Table 1.2. The U.S.S.R. steel industry abandoned this process for reasons unknown for the pneumatic

* Waterglass - a substance composed of salts or silicates of potassium or any of the alkali group metals.

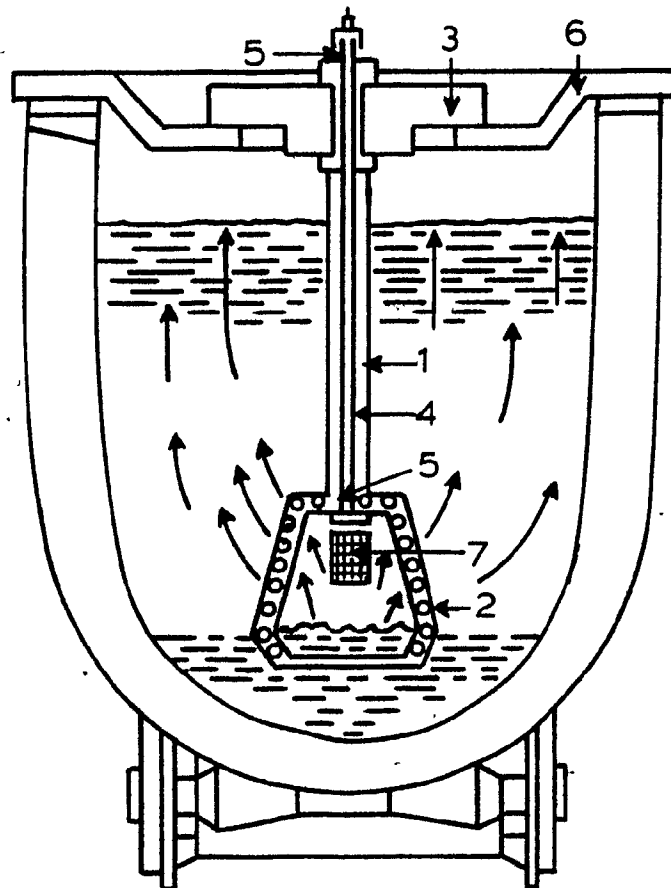


Figure 1.11 Schematic of the Vaporizer Equipment Used to Desulphurize Hot Metal with Solid Magnesium where 1) Refractory Coating, 2) Bell, 3) Counterweight, 4) Rod, 5) Coupling Rod, 6) Lid, and 7) Charged Magnesium.²⁴

TABLE 1.2
Operating Data For a Submerged Magnesium Vaporizer

Sulphur Content %		Consumption of Magnesium (kg/t of hot metal)	Chemical Efficiency
Before	After		
----- M a g n e s i u m L u m p s -----			
0.022	0.010	0.44	20.8
0.021	0.009	0.37	24.7
0.030	0.012	0.48	28.6
0.030	0.010	0.37	41.2
0.037	0.013	0.46	39.6
0.037	0.012	0.54	35.2
0.043	0.013	0.57	40.0
0.060	0.010	0.60	63.3
0.070	0.012	0.65	68.0
0.078	0.011	0.86	59.4
0.125	0.008	1.10	81.0
Average			45.6
----- M a g n e s i u m B a r s -----			
0.035	0.010	0.34	38.5
0.037	0.009	0.37	40.9
0.043	0.010	0.42	42.7
0.048	0.005	0.54	45.4
0.057	0.005	0.52	58.1
0.064	0.009	0.47	66.4
0.064	0.007	0.51	64.6
0.068	0.003	0.65	60.3
0.070	0.010	0.48	70.0
0.076	0.009	0.56	67.9
0.079	0.007	0.60	68.7
0.080	0.008	0.61	68.4
0.080	0.010	0.54	75.4
0.085	0.007	0.62	72.6
0.087	0.003	0.75	67.3
0.102	0.010	0.68	79.5
0.107	0.005	0.83	72.5
0.113	0.010	0.72	82.0
0.119	0.007	0.81	80.8
0.120	0.008	0.78	83.5
Average			65.3

injection of salt coated magnesium granules. The author suspects that failure of the plunging bell and a lack of control of the rate of magnesium vapourization were among the reasons for the switch.

A process similar to the Soviet process was developed by the French in the mid 1970's.⁴² Known as the MAP Process, it consisted of a plunging procedure using coated magnesium bars. The coating which was refractory and highly insulating was applied at a thickness of 2-5 mm to three sides of a magnesium ingot. The fourth side was covered with the same material but only to a thickness of 0.1 - 0.2 mm. The idea was that only one side of the ingot would break down and thus release the magnesium vapour in a controlled fashion. A small charge of the magnesium bars is shown in Figure 1.12. Although Jarysta⁴² claimed that the process was viable for both the large scale desulphurization of hot metal and the inoculation of small amounts of cast iron, no results on the chemical efficiency of the process were presented.

The possibility of adding pure magnesium wire has been investigated by Ashton et al.^{43,44} The idea was to inject a fine magnesium wire of a 3.2 mm diameter from the bottom of a treatment ladle. A nitrogen shrouding gas was also injected with the wire. Pilot plant tests based on a treatment of 250 kg of iron showed the technique to have problems resulting in chemical efficiencies averaging 22% in going from sulphur levels of 0.05 - 0.015% S. The authors found that the nitrogen



Figure 1.12 Making up a Plunging Charge using Three Coated Magnesium Bars.

shrouding gas injected with the wire had detrimental effects on the dissolution of the magnesium vapour. The three problems they highlighted were the dilution of the magnesium vapour by the nitrogen, the removal of magnesium which had been previously dissolved in the melt by the rising nitrogen bubbles and increased oxidation of the magnesium at the melt surface due to the vigorous stirring from the nitrogen gas. Lowering the gas flow rate was found to improve the chemical efficiency but also increased the probability of nozzle blockage. The authors claimed that in light of the small melt size treated that the results were comparable to similar pilot plant scale work for Mag-Coke and magnesium injection processes. The safety, simplicity and low cost were claimed to be the chief advantages of the wire feeding technique.

Following Ashton's ideas Hieber and Watmough²³ recently developed a magnesium wire system of their own. The system involved the injection of steel clad 3.2 mm magnesium wire into a small treatment ladle (1000 kg). The process is shown schematically in Figure 1.13. Although the authors achieved good magnesium recoveries, the chemical efficiency for desulphurization is quite poor, the highest value being 9%. The results of the tests are shown in Table 1.3. The low efficiencies may be attributed to the flashing and large amount of MgO fumes which were reported.

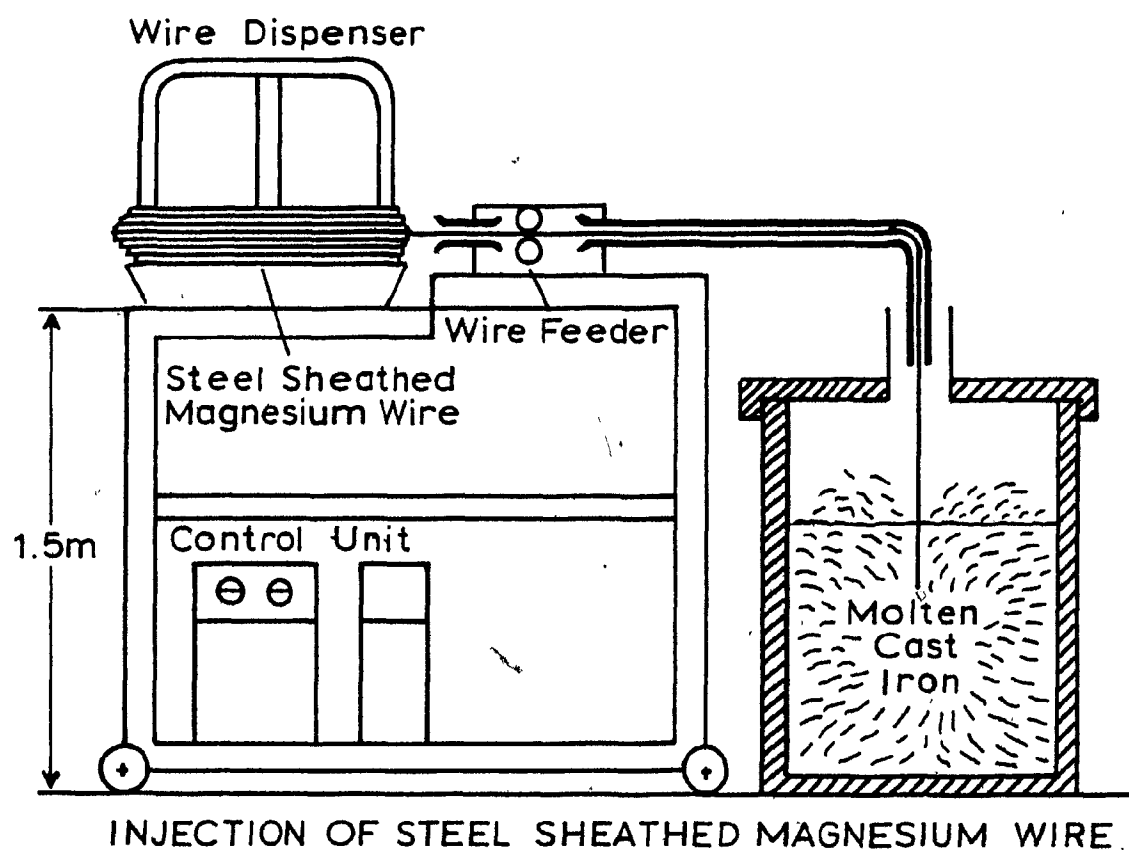


Figure 1.13 Schematic Illustration of the Wire Feeder Used by Hieber and Watmough.²³

TABLE 1.3
Operational Results for the Injection of
Steel Clad Magnesium Wire

Sulphur Content %		Magnesium Consumption (kg/t iron)	Chemical Efficiency %
Before	After		
0.025	0.011	1.67	6.3
0.025	0.007	1.67	8.1
0.025	0.007	1.68	8.0
0.025	0.006	1.67	8.6
0.025	0.004	1.76	9.0
0.025	0.004	1.93	8.2
0.025	0.006	1.93	7.4
0.025	0.010	1.93	5.8
0.025	0.004	2.03	7.8
0.025	0.006	1.93	7.4
0.024	0.005	2.00	7.1
0.024	0.004	1.85	8.1
0.024	0.008	1.85	6.5
0.024	0.011	1.93	5.1
0.024	0.008	1.83	6.6
0.024	0.009	1.93	5.8
0.024	0.006	2.02	6.7
0.024	0.014	1.85	4.1
0.024	0.010	2.02	5.2
0.024	0.006	2.00	6.8
0.024	0.012	1.63	5.5
0.024	0.004	2.00	7.5
0.024	0.005	2.01	7.1
0.024	0.011	1.75	5.6
0.024	0.006	2.01	6.7
0.024	0.006	1.86	7.3
0.024	0.006	1.85	7.3
0.024	0.014	1.18	6.4
Average			6.9

1.7 SUMMARY

A survey of the past and present techniques for desulphurizing both steel and hot metal has been presented. It has been shown that although magnesium and calcium based desulphurization are thermodynamically superior, extensive kinetic or contacting problems associated with each of the processes has prevented their full potential to be realized. The author has also distinguished between the volatile and non volatile addition systems, detailing those problems associated with the volatile systems. Dilution of magnesium or calcium vapour was noted as a particular problem towards attaining high efficiencies. This thesis will be concerned with techniques aimed at adding pure materials without the aid of a carrier gas or moderating compounds.

CHAPTER 2

BULLET SHOOTING TECHNIQUES - PREVIOUS WORK

2.1 INTRODUCTION

The present chapter is devoted to reviewing the state of the art in bullet shooting technology. A thorough understanding of this area was essential for the development of the low temperature model. This model is detailed at the end of this chapter.

The addition of buoyant additives to steel has been a general problem which has recently received considerable attention. To reach the final melt specifications, a wide variety of refining agents which include calcium and magnesium must often be added to steel. Typical non-gas evolving additions invariably used in steelmaking include aluminum, ferro-silicon and ferromanganese.

A considerable amount of work has been done on understanding and improving methods of adding aluminum to steel. The problem with aluminum is associated with its buoyancy. To obtain good, reliable recoveries of aluminum it is best that the addition melts below the steel surface. This improves mixing between the steel and aluminum limiting the amount of aluminum oxidation by the surrounding atmosphere and overlying slag. Since aluminum and magnesium have similar thermal and physical properties, it is possible that some of the techniques developed for adding buoyant aluminum additions can be adapted for magnesium additions.

Recently developed techniques for adding aluminum to steel include wire feeding, bullet shooting and the plunging of aluminum rods or rings. The technique gaining the most popularity for aluminum is wire feeding. It will be appreciated from sections 1.3 and 1.6.3 that wire feeding of bare magnesium wire would be difficult, in fact, while attempts have been made the process has not really been mastered. The problem with magnesium wire is the relatively high surface area to volume ratio. This yields high heat fluxes to the wire resulting in rapid boiling of the magnesium. The bubbles which are subsequently formed, are released at a shallow depth and do not have sufficient time to react with the iron. This was clearly shown by the wire feeding experiments shown in Figure 1.5. To circumvent these problems, Hieber and Watmough²³ tried injecting a steel clad magnesium wire into molten iron. From their results, shown in Table 1.3, they met with limited success.

An alternative method of adding buoyant additives has been the shooting of a projectile of the material deep into the bath. Although the bullet shooting technique was conceived by Hardy and Scott⁴⁵ in the 1930's, it would be 1966 before Sumitomo Metal Industries⁸ initiated a developmental program for shooting aluminum into liquid steel for deoxidation purposes. The idea was that if a suitably sized aluminum projectile were to be fired deep into the steel bath, it would allow the aluminum ample time to melt and mix with the steel before being lost to slag or air oxidation.

For the present work this addition technique was selected for investigation for several reasons. Bullets have the advantage that they can be quickly immersed deep in the melt without any continuous contact with the melt surface by either the injection equipment (submerged lance) or the addition itself (wire feeding). A bullet shooter is unique since it can be fairly remotely located with the bullet being transported to the melt by a long barrel. The compact bullet shooting equipment can be easily fitted into most melt shops. The author also felt that a large number of gas evolving bullets, randomly scattered in the hot metal, could yield high chemical efficiencies.

However, before outlining the present investigation into the possible usage of magnesium bullets for hot metal desulphurization, previous work on aluminum bullets is now reviewed.

2.2 ALUMINUM BULLETS

Tanoue et al.⁸ first published the developmental work of Sumitomo Metal Industries in 1973. In this report they detailed their research on the hydrodynamics of bullet shooting. Since it was impossible to follow the motion of the bullets in opaque steel, a water model was constructed to study the process. Wooden bullets were used so the density ratio of steel (7070 kg/m³) and aluminum (2700 kg/m³) could be modelled. As is well known, water can be an excellent medium for modelling hydrodynamic phenomena in liquid steel since the kinematic viscosities of the two are quite similar. On this basis,

Tanoue et al.⁸ performed extensive water model tests to evaluate the behaviour of a bullet shot into a liquid steel bath. The experimental apparatus which was used for this study is detailed in Figure 2.1.

The hydrodynamic stages of a bullet shot into steel has been summarized by Aoki.⁴⁶ The process was split into four stages, the surface collision followed by the bullet moving down to its maximum depth, the buoying up of the addition and finally the melting and dispersion of the aluminum. These stages are shown schematically in Figure 2.2.

Based on their experiments and hydrodynamic analysis, Tanoue et al.⁸ were able to identify the main parameters describing subsurface motion of the bullets. They experimentally found that each bullet decelerated to approximately half its initial velocity upon impacting the bath surface. When evaluating the maximum depth which a bullet would reach when fired into the melt Tanoue et al.⁸ found that a critical aspect ratio existed. Bullets whose length to diameter ratio (L/D) was greater than 11.5 were found to be affected less by the drag forces resulting in a deeper penetration of the melt. With longer projectiles the bullet's momentum increases while the drag forces remain relatively constant for a given initial velocity. Based on this analysis, Sumitomo Metal Industries selected a bullet measuring 25 mm in diameter by 400 mm in length and weighing approximately 0.44 kg.⁴⁶ A photograph of a typical aluminum bullet is shown in Figure 2.3. A larger

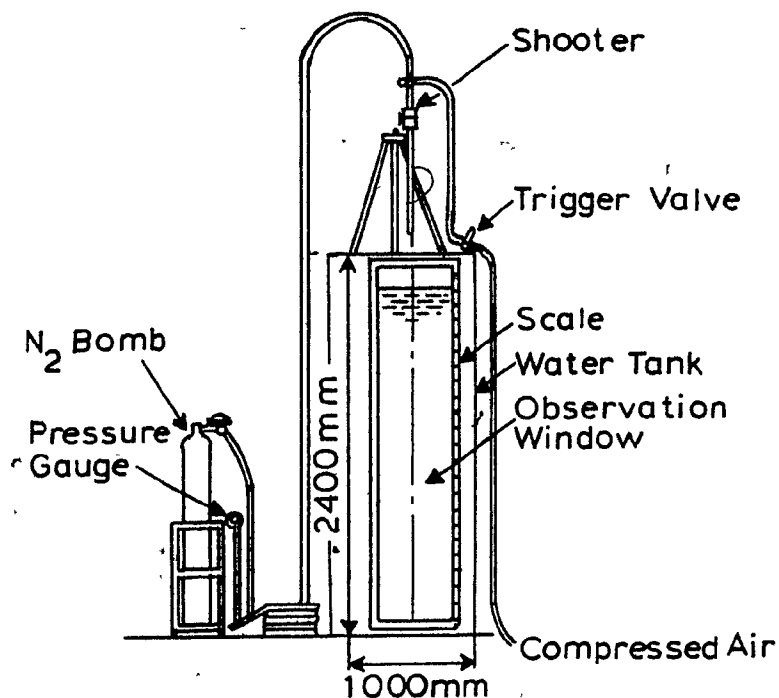


Figure 2.1 Water Modelling Apparatus used by Tanoue et al. to Evaluate the Hydrodynamics of Bullet Shooting.⁸

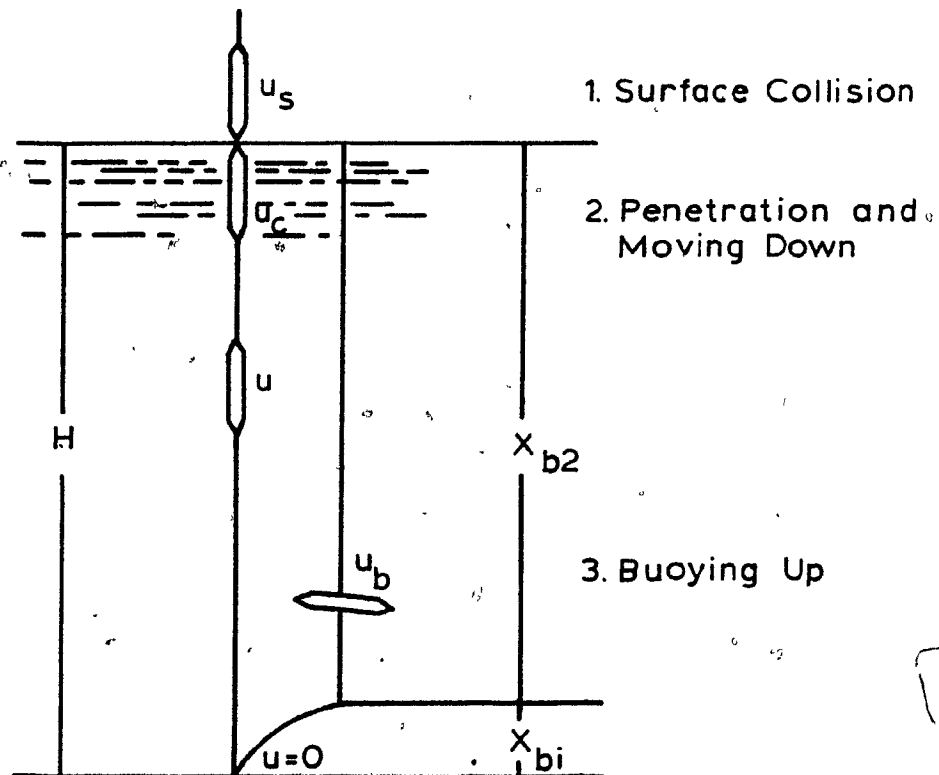


Figure 2.2 The Hydrodynamic Stages of Bullet Shooting.⁸

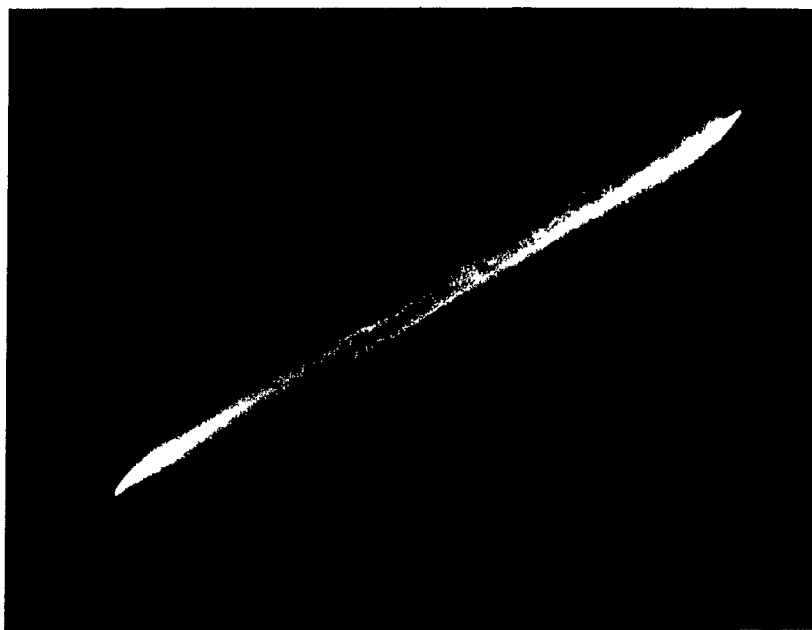


Figure 2.3 Typical Aluminum Bullet used at Sumitomo Metal Industries.⁹

bullet of 0.71 kg measuring 30 mm in diameter by 450 mm in length was also used.⁴⁶

Aoki⁴⁶ indicated 90% of the time that the projectile is submerged corresponds to the buoying up stage of the process. Since the bullets are comparatively light they rapidly reach their terminal velocities. This velocity can be described by balancing the bullet's buoyancy and drag forces:⁴⁷

$$(\rho_f - \rho_s) V_B g = \frac{1}{2} \rho_f U^2 A_B C_D \quad (2.1)$$

where ρ_f = density of the molten steel

ρ_s = density of the addition,

V_B = volume of the bullet

U = terminal velocity of the rising bullet

A_B = cross sectional area of the bullet perpendicular to the flow

C_D = drag coefficient

g = acceleration due to gravity

rearranging,

$$U = \left[\frac{2(\rho_f - \rho_s)}{\rho_f} \frac{V_B g}{A_B C_D} \right]^{\frac{1}{2}} \quad (2.2)$$

To simplify the above equation, Tanoue et al.⁸ introduced two terms:

$$b = \frac{(\rho_f - \rho_s) g}{\rho_s} \quad (2.3)$$

and

$$\eta = \frac{\rho_f C_D A_B}{2 \rho_s V_B} \quad (2.4)$$

rearranging equation 2.2:

$$U = \left(\frac{(\rho_f - \rho_s)g}{\rho_s} \cdot \frac{2 \rho_f V_B}{A_B C_D \rho_f} \right)^{\frac{1}{2}} \quad (2.5)$$

$$= \left(\frac{b}{\eta} \right)^{\frac{1}{2}} \quad (2.6)$$

Using the water model Tanoue et al.⁸ evaluated η as a function of the bullet aspect ratio (L/D) for various bullet diameters. Their results are shown in Figure 2.4. For the bullets which Sumitomo chose, $\eta = 100 \text{ m}^{-1}$ and $b = 15.25 \text{ m/s}^2$ yielding a terminal velocity of 0.39 m/s. If the bullets were shot to the bottom of the ladle they would then have its entire depth of approximately 3 m through which to rise. Since the buoying up of the bullet accounts for 90% of its time in the melt, a bullet should remain immersed for about 8.5 s.

Tanoue et al.⁸ evaluated the melting time for the aluminum bullets by immersing aluminum rods of corresponding diameters into a 1 ton high frequency induction furnace. During these experiments the formation of a large encapsulating steel shell on the aluminum bar was observed. However, the full ramifications of the shell were not evaluated and the melting times were determined experimentally. The results of these tests are shown in Figure 2.5.

Based on this developmental program, Sumitomo Metal Industries installed a full scale bullet shooter in two of their melt shops, at the Wakayama and Kashima Steelworks. A schematic of a bullet shooter is given in Figure 2.6. The

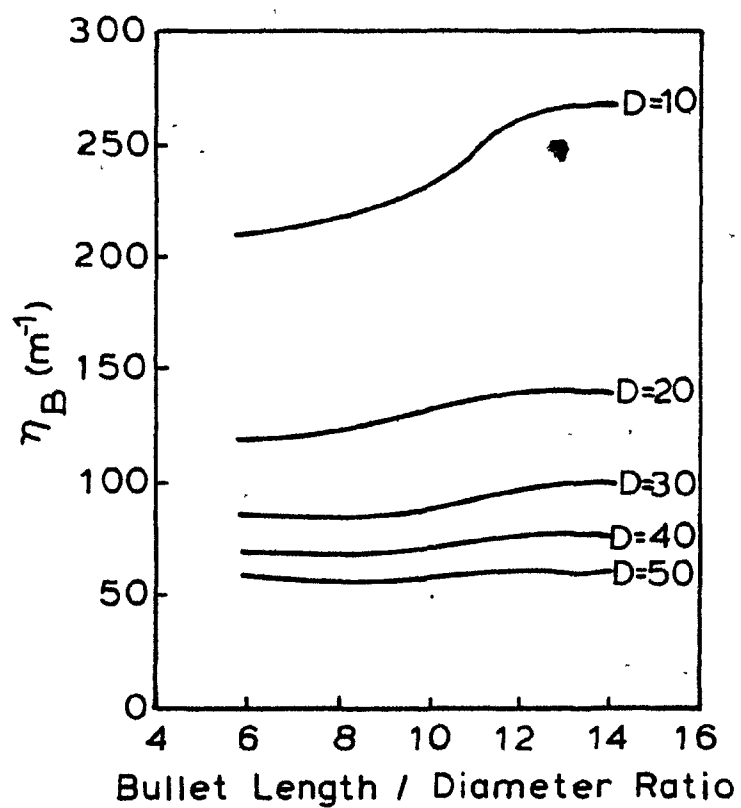


Figure 2.4 Results of Hydrodynamic Analysis of Bullet Shooting by Tanoue et al.

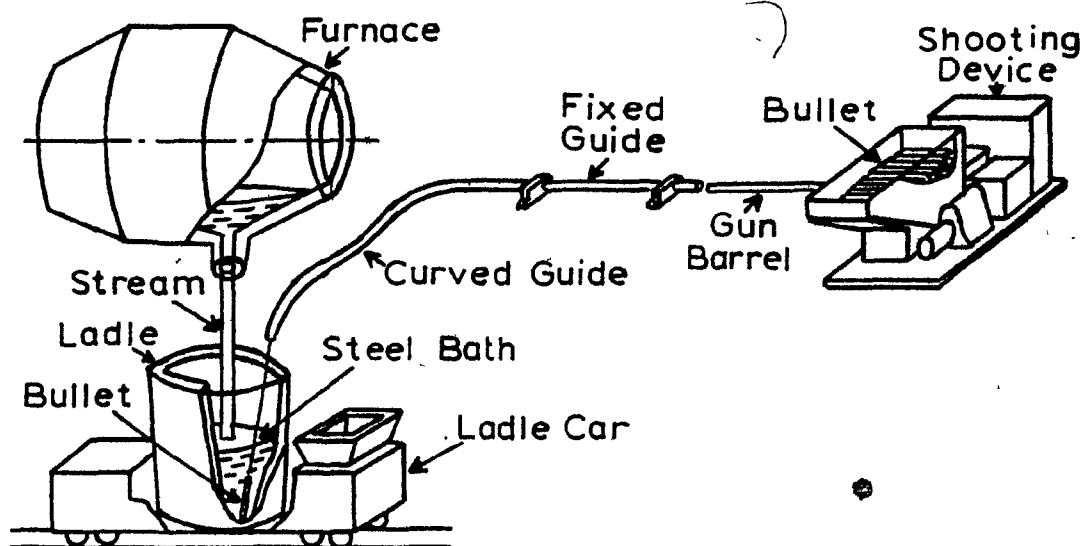


Figure 2.6 Aluminum Bullet Shooter used at Sumitomo Metal Industry's Wakayama and Kashima Works.⁹

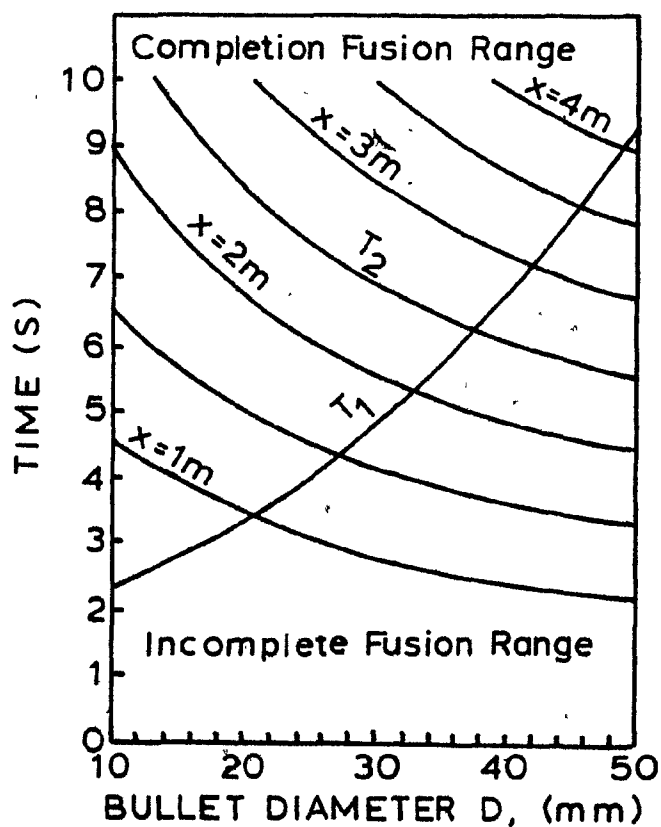


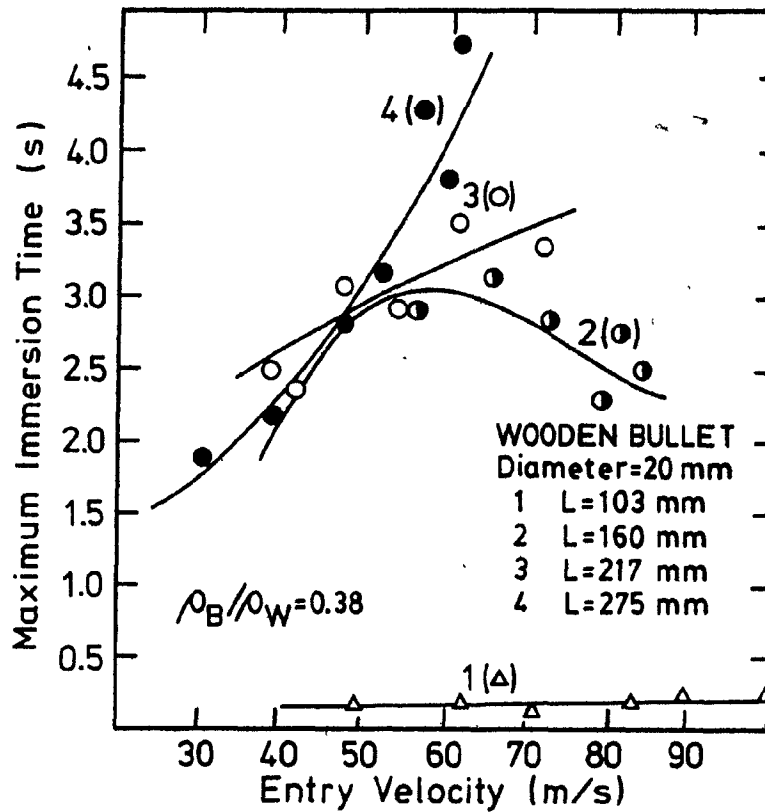
Figure 2.5 Melting Curves for Aluminum Bullets after Tanoue et al.⁸ where T_1 is the Melting Time, T_2 is the Time of Submergence beneath the Bath Surface and x is the Maximum Penetration Depth.

results presented by both Aoki⁴⁶ and Tanoue et al.⁸ showed that the amount of aluminum required to meet an average grade was reduced by 20%. More importantly, the scatter in the soluble aluminum was reduced to one third of that obtained by adding aluminum shot or ingots.

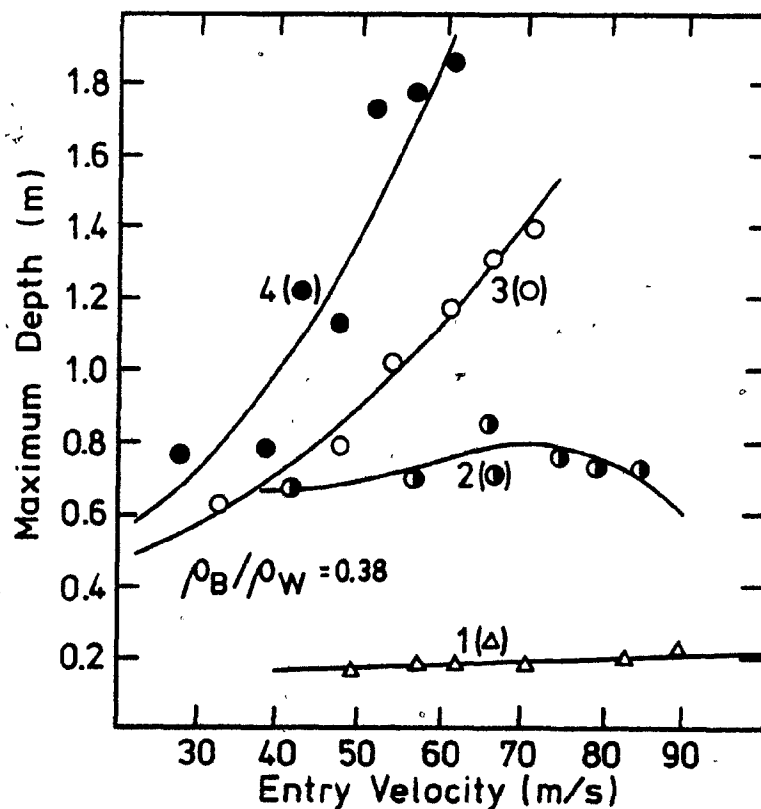
During the early seventies a considerable amount of research was also carried out at McGill University, on the thermal and hydrodynamic aspects of addition techniques.^{9,48,52} To evaluate the preliminary work done at Sumitomo, a similar series of bullet shooting experiments were conducted at McGill.^{50,51} Using similar equipment, the results from the water model⁹ agreed with three hydrodynamic stages of bullet shooting and that a critical aspect ratio (L/D) in the order of 10 must be exceeded to acquire bullet penetration. However, the maximum depth of bullet penetration was found to be 30% lower for the McGill test work. This discrepancy was attributed to Tanoue et al.'s⁸ underestimation of the drag forces acting on the bullet. The results of the McGill study are shown in Figure 2.7.

2.3 THERMAL ASPECTS OF BULLET SHOOTING

A major area of contention between the two groups involved the thermal aspects of bullet shooting. Based on previous studies^{48,49,50} the McGill researchers were aware that the extent of steel shell formation was critical in predicting actual release times for an addition. The melting mechanisms proposed



(a) Maximum Immersion Time of a Wooden Bullet as a Function of Entry Velocity and Size



(b) Maximum Depth of Penetration of a Wooden Bullet

Fig. 2.7 Results of Mucciardi's Hydrodynamic Study of Bullet Shooting.⁹

by Guthrie et al.,⁵⁰ and in fact observed by Tanoue et al.⁸ are given in Figure 2.8. As a cold aluminum addition enters the bath a large steel shell freezes around it encapsulating the addition. The heat of fusion released from the freezing steel plus the convective heat transfer in the melt quickly melts the aluminum. However, the surrounding shell often takes much longer to melt resulting in aluminum release times which are much longer than the corresponding melting times. In evaluating the release time for aluminum rods, Tanoue et al.⁸ evidently did not appreciate the consequences of steel shell formation on the dispersion of the aluminum. More detailed work on shell formation by Guthrie et al.⁵⁰ predicted that the results obtained by Tanoue et al.⁸ were too short. Based on these results, Mucciardi^{9,52} then performed a full experimental evaluation of the thermal aspects of the bullet shooting method.

To fully describe the shell formation process, Mucciardi⁹ developed a mathematical model describing events which occur as a bullet is immersed in a steel bath. His results showed the extent to which the shell could limit the addition's dispersion. The results for Mucciardi's model are shown in Figure 2.9 for a low value of melt superheat.⁵¹ It is clear that the aluminum has melted and the bullet has resurfaced before the steel shell has even reached its maximum thickness. Under these conditions aluminum would surely react with the surrounding atmosphere rather than with the steel it was intended to

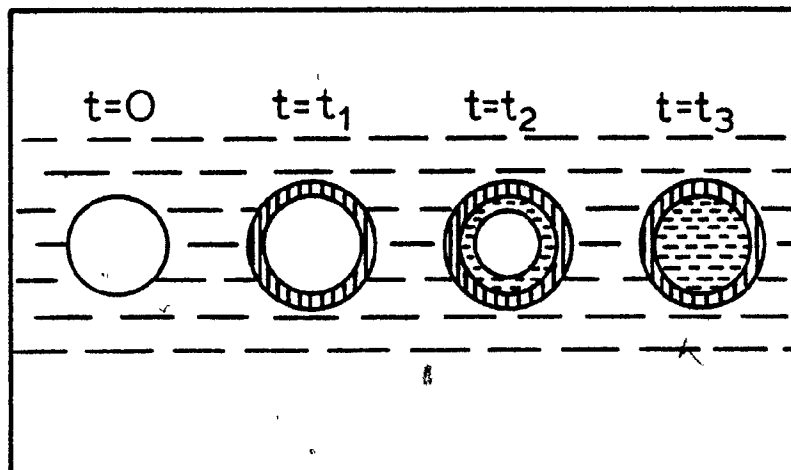


Figure 2.8 Typical Events when a Cold Addition is Made to Molten Steel (a) $t = 0$: Instant of Immersion; (b) $t = t_1$: Solid Steel Shell; (c) $t = t_2$: Addition Core Melts; (d) $t = t_3$: Molten Core, Steel Shell Melts Back.

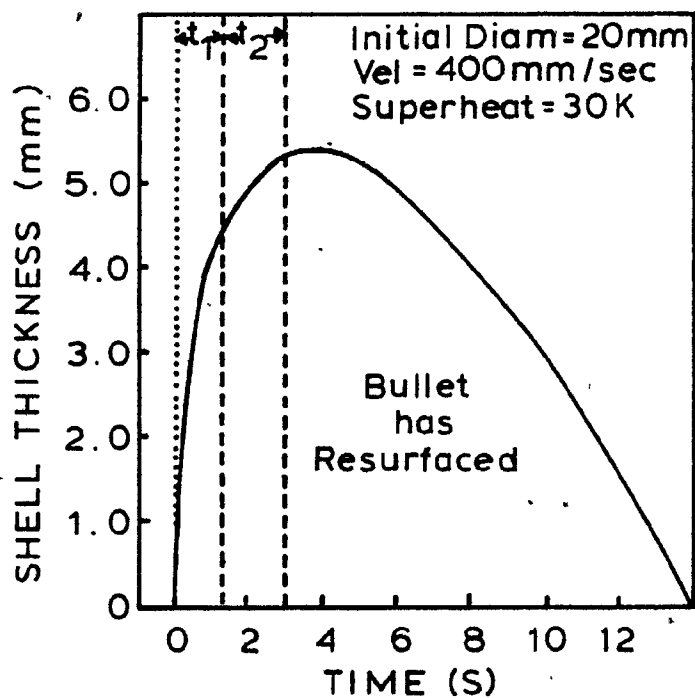


Figure 2.9 Growth of a Steel Shell on a Rising Aluminum Bullet where Time, t_1 Represents the Time for the Aluminum to Melt while $t_1 + t_2$ is the Total Time the Bullet is Submerged.

deoxidize. The reader is reminded that the time for the shell to melt back, shown in Figure 2.9 as 14 s, is due to the low superheat of 30 K. This superheat is not typical of most steel plant operations. As the superheat is increased, the kinetics for the shell to melt back are correspondingly boosted.

To confirm the predictions of the model, Mucciardi set up an experimental program to establish the release times for aluminum bullets.⁹ The heart of the experimental apparatus was a force sensing device which measured the net force the aluminum addition exerted against a precise load cell. The entire apparatus is depicted in Figure 2.10. The experimental procedure consisted of immersing the aluminum cylinders and monitoring the force exerted against the load cell as a function of time. As the buoyant aluminum was released the net upward force quickly decreased. This decrease in force was registered by the load cell and stored using a G.E 4020 process control computer. The release time or effective melting time was correlated by Mucciardi and is presented in Table 2.1. These times correspond to the initial release of the aluminum from the steel shell. Using the force monitoring equipment, Mucciardi was also able to evaluate the length of time it took for the aluminum to be released into the bath. This value is also presented in Table 2.1.

Mucciardi tested two types of aluminum cylinders. Most of the samples were aluminum cylinders measuring 20 mm in diameter by 152 mm in length. A typical test sample is shown

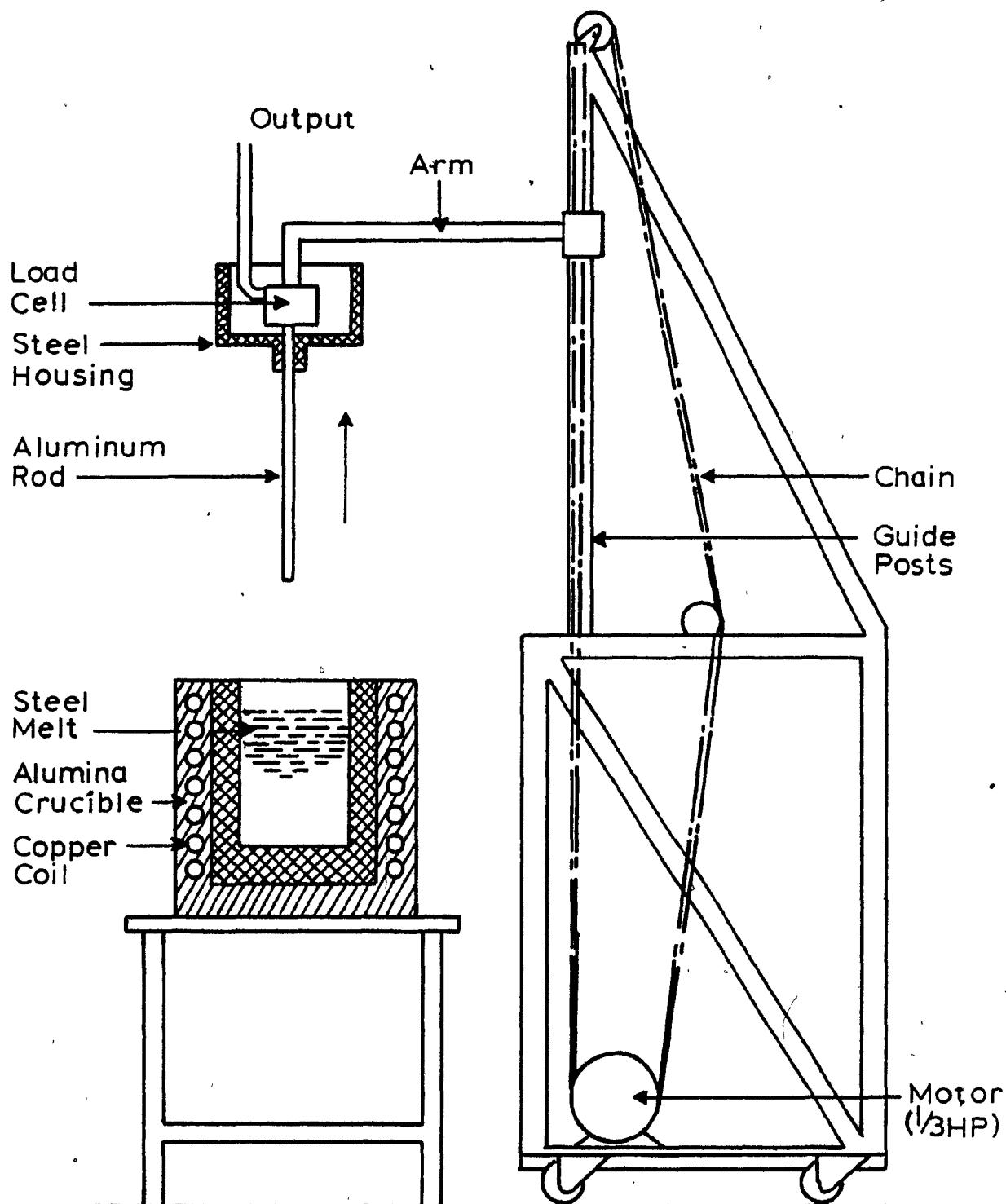


Figure 2.10 Force Sensing Apparatus used by Mucciardi⁹ to Detect the Release of Aluminum from Aluminum Wires and Bullets.

Table 2.1

Melting Times for Conventional Bullets⁹

Expt. No.	Bath Superheat (K)	Time Until the Initial Al Release(s)	Total Melting Time(s)
1/21	48	4.8	6.6
6/30 ^a	48	4.4	5.2
1/20 ^a	50	4.4	5.6
2/19 ^b	52	4.1	5.9
5/19	52	4.6	6.4
1/18	74	3.8	4.6
5/18	76	3.5	4.6
7/30 ^c	103	3.2	4.9

a - Bullet shaped cylinder was used

b - Cylinders were only barely immersed below the bath surface

c - Sample was 25.4 mm in diameter vs 20.0 mm for all other specimens

in Figure 2.11. To better simulate the aluminum bullets, some tests were done using samples which were pointed at both ends. The overall dimensions of these samples were the same as with cylindrical samples. A schematic of both types of bullets is shown in Figure 2.12.

The results shown in Table 2.1 indicate that the melting or release time for the aluminum is in the order of 4-5 s. When comparing this to Mucciardi's total immersion time of approximately 6.5 s (see Figure 2.7) it is obvious that the bullets are melting close to the surface of the steel bath. Using a single shot air powered gun Mucciardi, Barnhurst and Guthrie⁹ tested this hypothesis at Dofasco. The results of the tests indicated that the bullets in fact resurfaced after about 4 s and that the aluminum was released on the steel surface where it rapidly oxidized. From this it would seem that it would be difficult to obtain the 20% improvement in aluminum yield that Tanoue et al.⁸ and Aoki⁴⁶ reported.

Alternate reasons for these improvements were given by both Mucciardi⁹ and Guthrie et al.⁵⁰ The important points to note about Sumitomo's procedure was that high superheats were used (100 K) and that the bullets were not in fact shot into a full stagnant ladle.⁵⁴ The steel was kept relatively hot (1888 K), since it was destined for continuous casting (i.e. long holding times, and small (150 tonne) ladles). The bullets are normally shot into the 'eye' of the tapping stream as the ladle is filled. This gives regular bullets a better chance

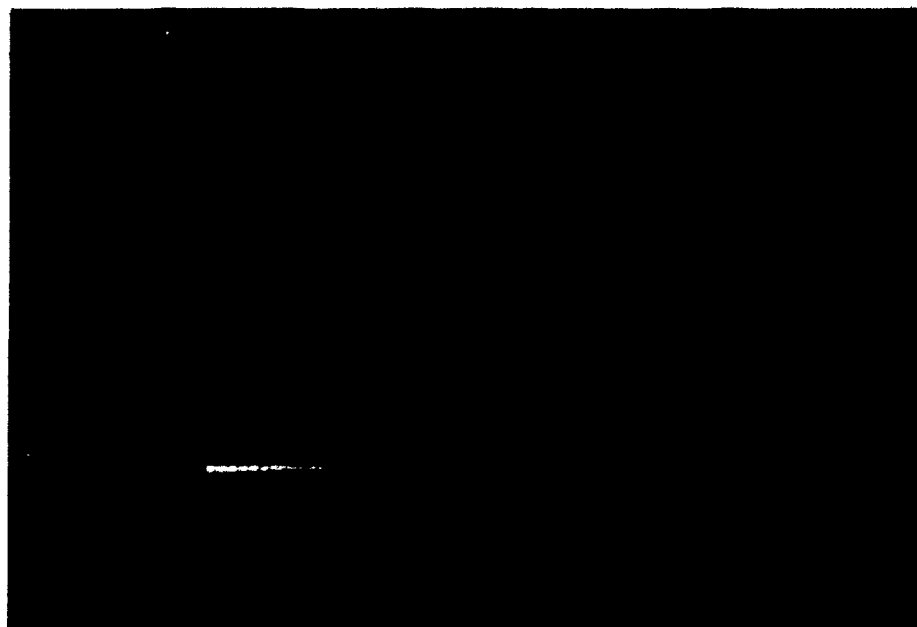


Figure 2.11 Typical Aluminum Cylinder before Immersion Used
by Mucciardi.⁹

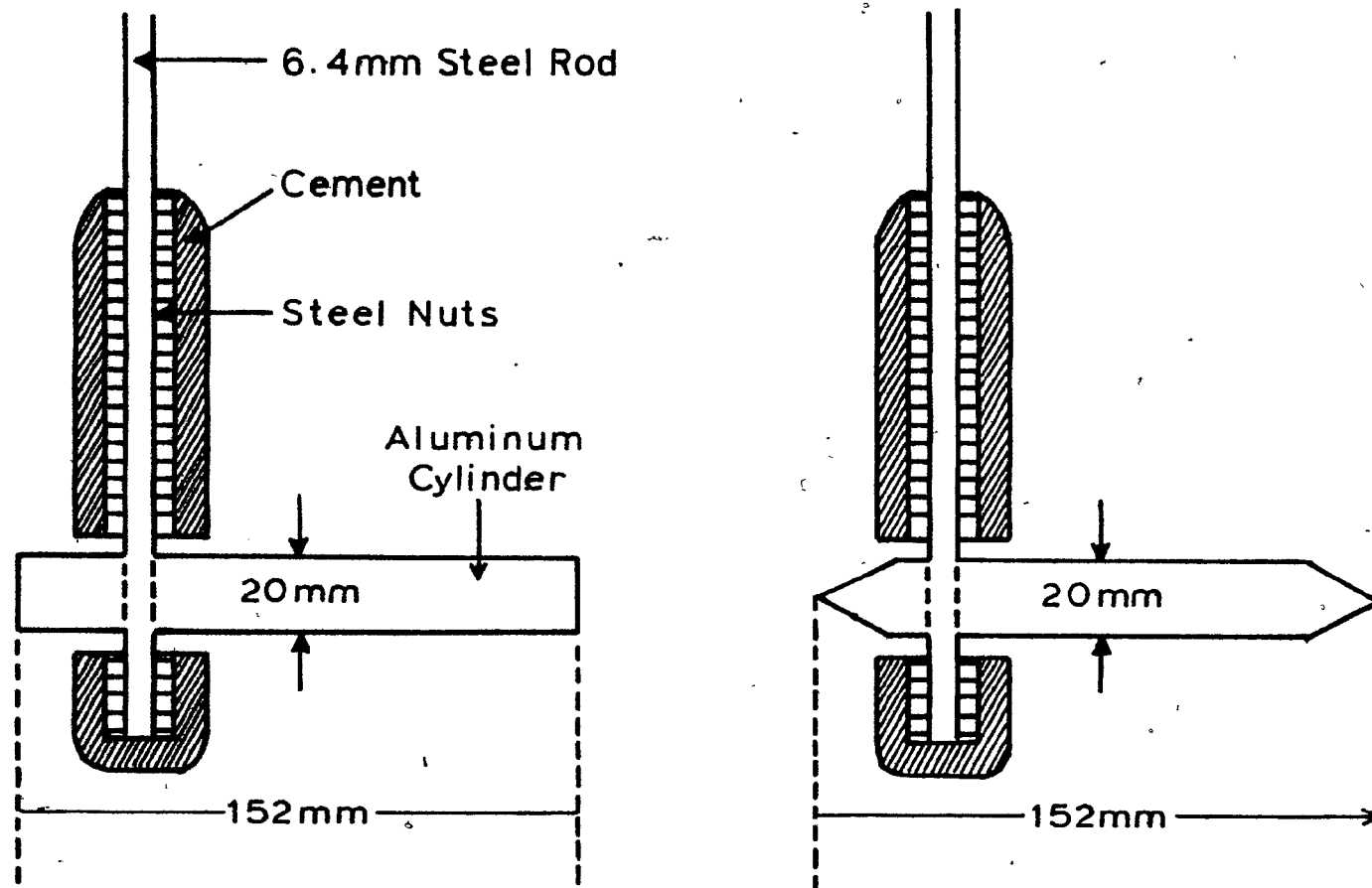


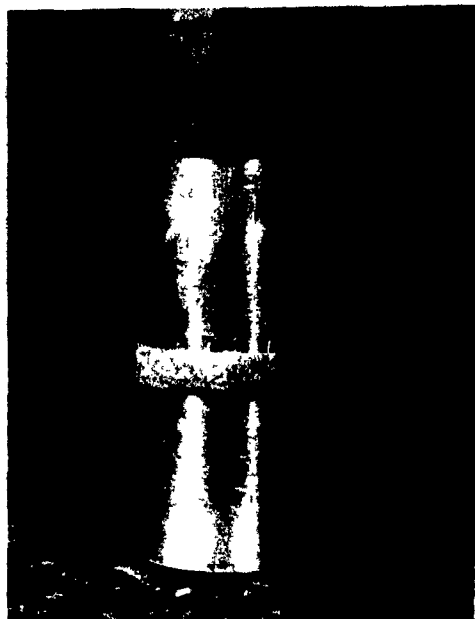
Figure 2.12 Experimental Bullet Designs Tested by Mucciardi.⁹

to penetrate the steel and become caught up in the recirculating flow of steel in the ladle before they resurface.

2.4 MODIFIED BULLETS

As a result of their work, Mucciardi and Guthrie developed a new proprietary bullet design.⁵³ The new design eliminates the formation of the steel shell at selected locations on the bullet's periphery. Since the aluminum melts quickly but is trapped by the steel shell, the new design provides select locations on the bullet's surface where steel will not be able to freeze. Once the aluminum has melted at this location it can be immediately dispersed into the liquid steel.

To eliminate local formation of the steel shell, a highly insulating material is added to the circumference of the bullet before it is injected into the melt. The result of adding an insulating layer to the surface of an aluminum cylinder is shown in Figure 2.13. The lack of a steel shell at the area protected, in this case by a layer of refractory cement, enabled the aluminum to be dispersed in the melt before the steel shell had melted back. Another successful thermal resistance was obtained when gas evolving materials were placed on the exterior of the aluminum cylinder. The evolution of gas from, for instance, paper tape provides an excellent insulating layer on the exterior surface of the bullet. This enables the dispersion of the aluminum once the aluminum has melted at the exposed area.



(a) Aluminum Cylinder Containing a Ring of Refractory Cement.



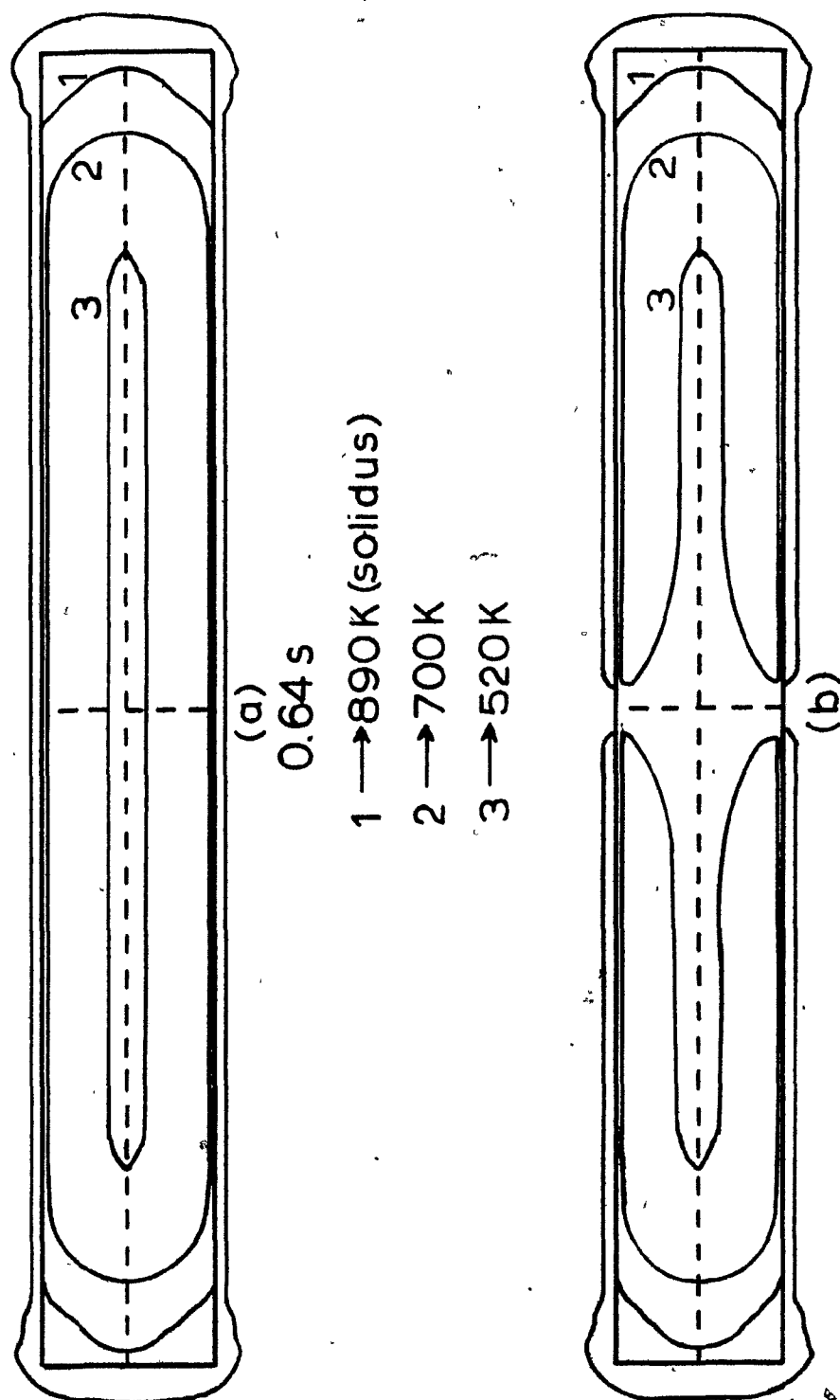
(b) The Cylinder Shown in (a) after being Immersed in Pig Iron for 7's.

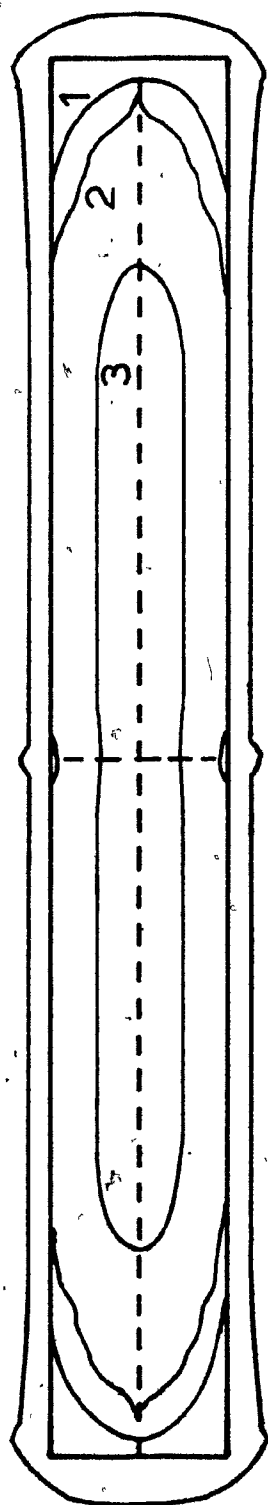
Figure 2.13 Effect that a Thermal Resistance (Refractory Cement) has on the Iron Shell Formation on Aluminum.

To gain more insight into the melting mechanisms the process was modelled mathematically by Mucciardi.⁹ In Figure 2.14 the shell formation and subsequent melting of the aluminum is developed for both conventional and modified bullets. Since the modified bullet is only sensitive to the melting rate of addition and not to that of the steel shell, the addition can be dispersed into the liquid steel at a rate which is effectively independent of the melt superheat. The behaviour of the modified bullets would be more predictable due to their dependency on the addition melting rate.

To evaluate the melting rates of the modified bullets they were tested using the force sensing device previously mentioned. The results, listed in Table 2.2, showed that modified bullets had a faster release rate, particularly those bullets which used the gas evolving paper tape insulation. The release mechanism is depicted in Figure 2.15. This particular sample was hand dipped for 2-3 s then removed from the melt. It was then possible to observe the bullet just as it broke open, spilling its contents on the laboratory floor. The aluminum central core was recovered and is shown in Figure 2.15b. The detail of the machined groove on the core showed the remarkable insulating qualities of the gas phase. The cone like shape of the solid core confirmed the predictions of the mathematical model shown in Figure 2.14.

Figure 2.14 Melting Mechanisms of Both Conventional and Modified Bullets. Conventional Bullets are Shown in Diagrams (a), (c), (e) and (g), while Modified Bullets are Seen in (b), (d), (f) and (h).





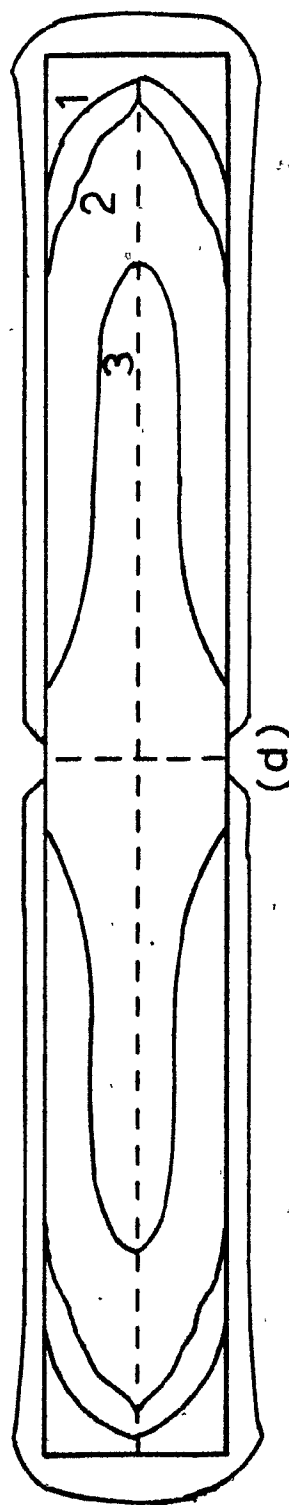
(c)

1.12s

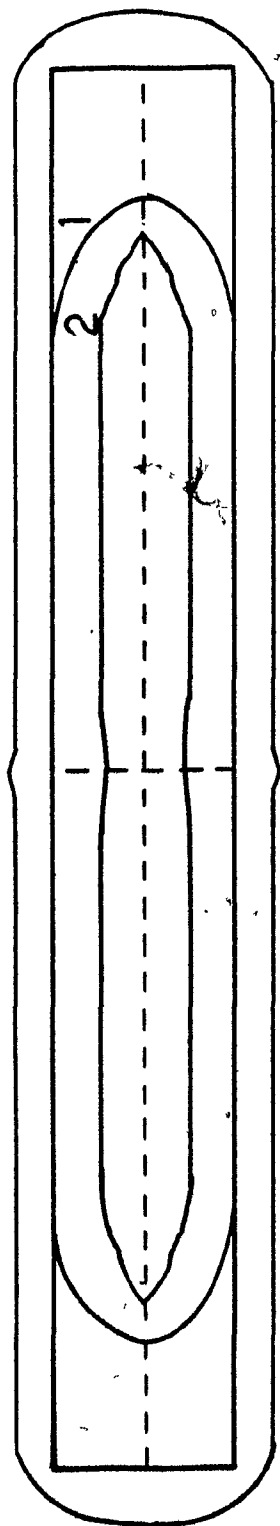
1 → 1170K

2 → 890K (solidus)

3 → 800K



(d)

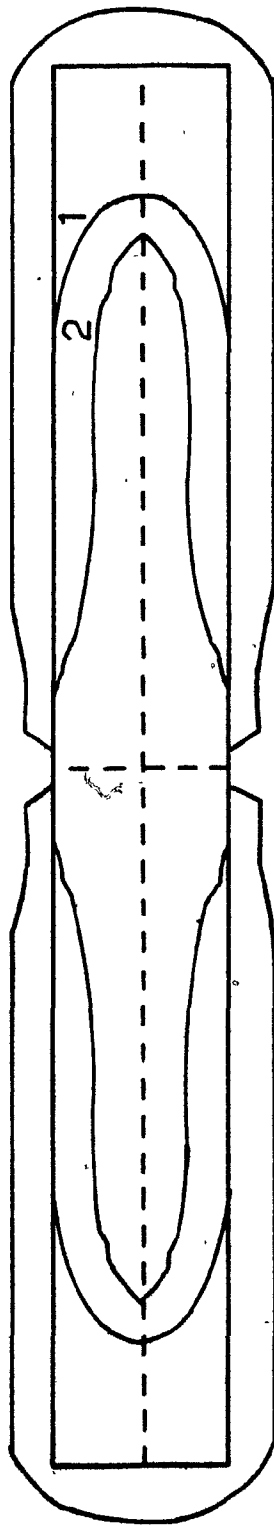


(e)

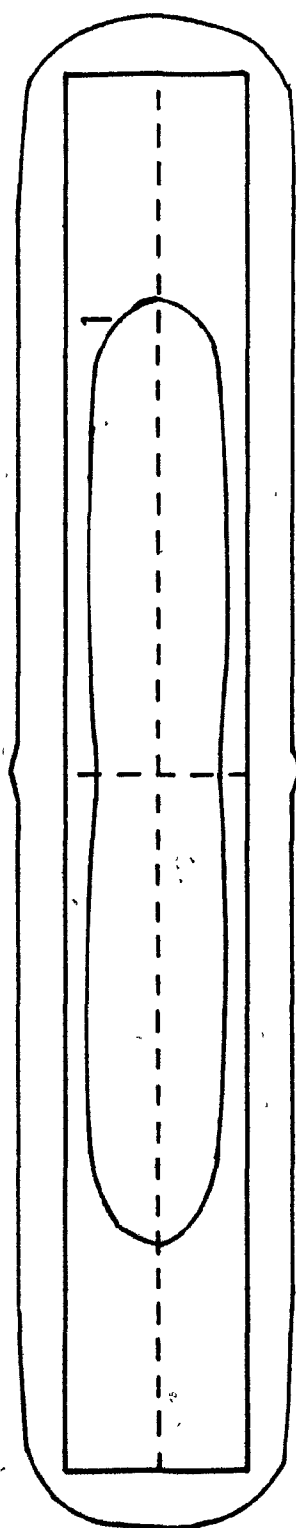
2.08s

1 → 1170 K

2 → 890 K (solidus)



(f)

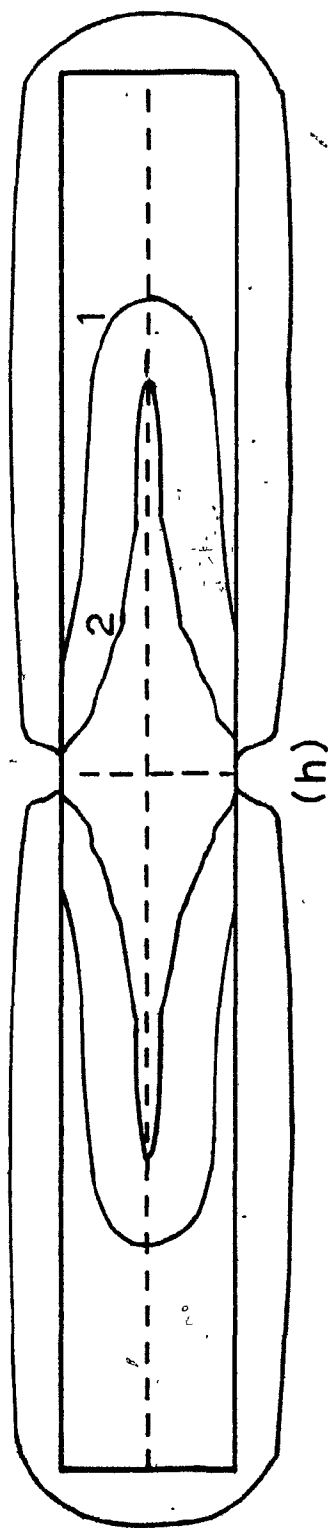


(g)

2.72 s

1 → 1170 K

2 → 890 K (solidus)



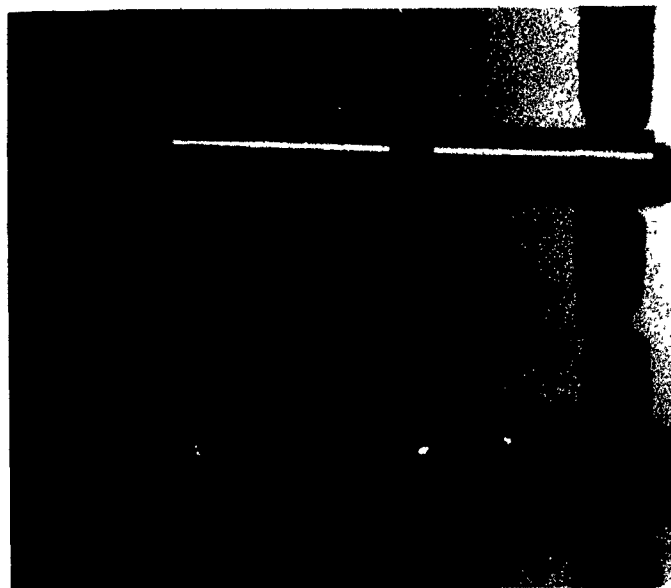
(h)

TABLE 2.2

Melting Times for Modified Bullets⁹

Expt. No.	Type of Thermal Resistance	Groove Size Width x Depth (mm)	Bath Superheat (K)	Time Until Initial Al Release (s)	Total Melting Time (s)
7/19	cement	12.7 x 3.2	49	5.1	7.9
5/20*	cement	12.7 x 3.2	50	3.9	4.6
8/19	cement	12.7 x 3.2	51	3.8	5.2
4/18	cement	12.7 x 3.2	72	2.4	3.6
2/18	cement	12.7 x 3.2	74	3.8	4.7
3/21	tape	12.7 x 3.2	46	3.3	4.8
2/20*	tape	12.7 x 3.2	48	3.1	4.6
4/20*	cement	6.4 x 3.2	47	4.4	5.1
4/19	cement	6.4 x 3.2	51	2.7	4.3
6/18	cement	6.4 x 3.2	78	3.2	3.8
7/20*	cement	6.4 x 1.6	50	4.0	4.7
3/14	cement	6.4 x 1.6	52	3.4	4.7
7/18	cement	6.4 x 1.6	78	3.5	4.4
3/20*	tape	6.4 x 1.6	44	2.3	3.7
2/21	tape	6.4 x 1.6	50	2.2	3.6

* Bullet shaped cylinder was used.



(a) The Effect of a Thermal Resistance (paper tape) on the Mechanism of Aluminum Release.



(b) Three Distinct Sections of an Aluminum Cylinder after Thermal Splitting

Figure 2.15 The Release of Aluminum from a Modified Bullet

In 1980 full scale industrial tests were performed by Sumitomo Metal Industries at their Wakayama Steelworks⁹ using modified bullets. The results showed a relative improvement of approximately 10% over the regular bullets. This small increase in aluminum recovery was attributed to the relatively high superheats (100 K) used at Wakayama Steelworks. Under such conditions the rate at which the steel shell melts back approaches the aluminum melting rate. However, it is important to note that bullets fired into filled ladles of steel at lower superheats (50-70 K) would only melt subsurface through the 'thermal break' of a modified bullet.

2.5 MAGNESIUM BULLETS

The primary objective of the present research project was to investigate the potential of adding magnesium bullets to hot metal. Using bullets of the modified design, it was speculated that the magnesium should be released in the molten iron as soon as the bullet splits open. The time for this to occur should be similar to the aluminum case since the two materials are thermally similar. The thermal and physical properties of aluminum and magnesium are compared in Table 2.3.

Since the release time for a modified bullet is 'shell independent' and only 'addition dependent' it was speculated that the possibility of explosions from magnesium gas trapped within an iron shell would be minimal. Thus the bullet would break open once solid magnesium adjacent to the thermal resistance melts. On doing so, two 'half shells' full of

Table 2.3
Physical Properties of the Light Metals^{5,55,52}

Property	Aluminum	Magnesium	Calcium
Specific Gravity (kg/m ³)	2707	1746	1540
Thermal Conductivity (W/mK) at 293 K	204	171	201
Specific Heat (J/kg K) at 293 K	896	1013	651
Heat of Fusion (kJ/kg)	400	370	212
Heat of Vapourization (kJ/kg)	12,046	6006	4441
Melting Point (K)	933	922	1112
Boiling Point (K)	2740	1363	1757

liquid magnesium would result. Due to the high heat input and magnesium's low boiling point (1363 K), it was expected that the magnesium would quickly boil, producing large quantities of vapour. An artistic impression of the boiling process is shown in Figure 2.16.

The potential advantages of such a system could be numerous. By having a large number of gas evolving bullets randomly scattered in an iron melt, the kinetics of dissolution and desulphurization might be improved. Since the magnesium vapour released is undiluted it would therefore have the highest possible rate of magnesium vapour dissolution. Through control of the bullet length and diameter it was felt that an optimum bubble size and bubbling time could be obtained for magnesium vapour dissolution.

At Sumitomo Metal Industries experiments with magnesium bullets have been carried out. Guthrie⁵⁴ reported that magnesium bullets fired into foundry ladles at Sumitomo's Osaka Ironworks, violently shook the ladles as the magnesium vapour was released. The only other experience in injecting gas evolving bullets at Sumitomo is through the addition of calcium containing bullets into steel.⁴⁶ Known as the SCAT process (Sumitomo Calcium Treatment), calcium silicide powder is packed tightly into an aluminum capsule before being fired into the melt. Aoki⁴⁶ reported that since the bullets melted deep in the steel, the calcium did not volatilize due to a high hydrostatic head. Aoki also stated that dissolved calcium levels of 0.004% or greater could be obtained using the SCAT process.

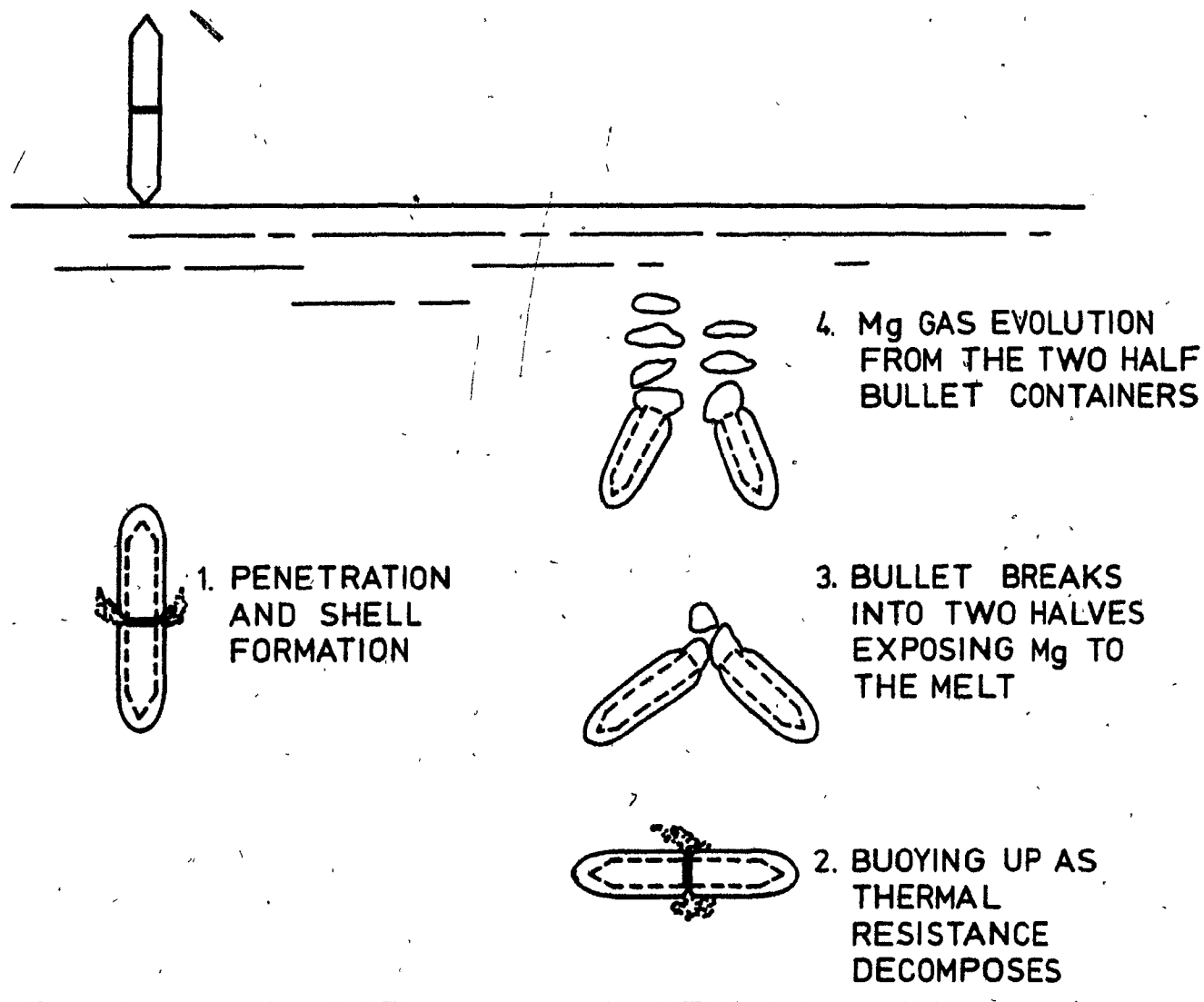


Figure 2.16 Artistic Impression of the Release of Magnesium in Hot Metal From a Modified Bullet.

2.6 THE PHYSICAL MODEL - PRESENT WORK

Based on the previous research work the next logical step would be to investigate the phenomena involved when volatile additions contained within iron or steel shells are suddenly exposed to molten metal. Thus, the physical model developed for the present thesis is intended to simulate the events of a magnesium bullet just after it has broken into two halves. Each half shell would then be full of liquid magnesium. It was known that the unstable magnesium would rapidly reach its boiling point of 1363 K. Since it was thought unwise to stage these events in the small iron melts available at McGill University without a preliminary study, a low temperature analogue of the system was built. The advantages of the low temperature system were that more variables could be controlled and detailed visual observations were possible. The objectives with the low temperature tests were to try and gain more insight into the mechanisms of the violent boiling associated with unstable magnesium liquid in the hot metal environment.

Simulation of magnesium at room temperatures required the selection of an appropriate cryogenic material. The potential liquids, summarized in Table 2.4, were limited by the constraints of the model and the availability of the materials. From that viewpoint, the only feasible cryogenic materials were natural gas (CH_4), ammonia (NH_3) and liquid nitrogen. The first two liquids were eliminated due to safety

Table 2.4

Properties of Some Cryogenic Gases 54

Property	GAS:	He	Ne	Ar	CH ₄	NH ₃	N ₂	O ₂
Boiling Point (K)		4.07	26.6	87.3	109.0	239.7	77.2	90.0
Melting Point (K)		0.80*	24.3	83.8	90.5	195.3	63.1	54.6
Liquid Density at Boiling Point (kg/m ³)		125	1200	1390	424	682.1	804.0	1142.0
Heat of Vapourization (kJ/kg)		23.9	87.0	162.8	577.4	1368	199.2	212.9
Heat of Fusion (kJ/kg)		4.18	16.7	28.0	60.7	352	25.5	13.7

*at a pressure of 2634 kPa

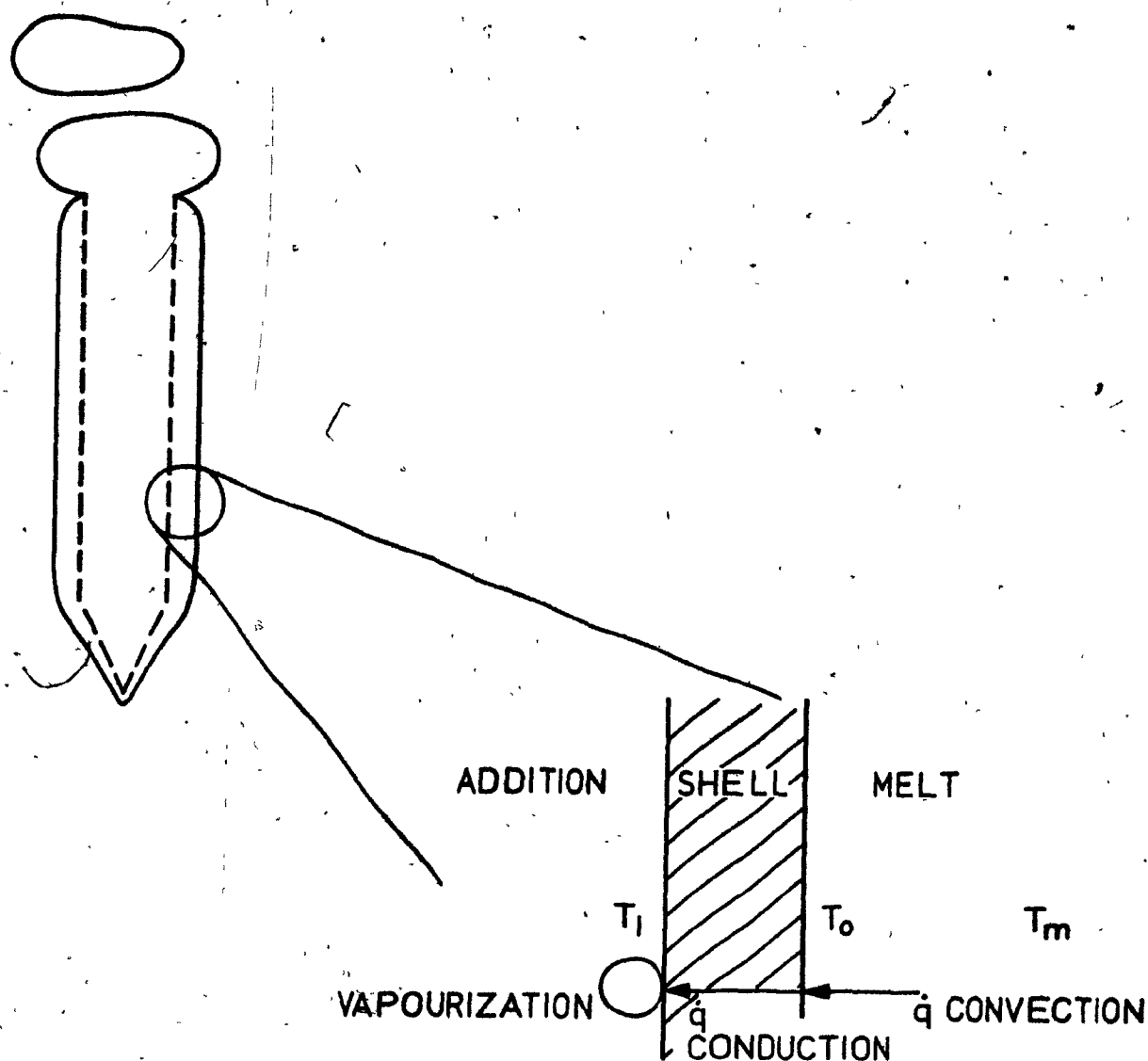
problems associated with their usage. Liquid nitrogen was selected due to its availability and inert characteristics. At the same time the liquid nitrogen satisfied many of the thermal requirements of the model. One aspect which was completely ignored was chemical reactivity. Since nitrogen is inert, the present study only focuses on the hydrodynamic and physical aspects of a boiling addition. It was felt that sufficient work had already been performed on the dissolution and reaction kinetics of magnesium vapour, so that attempts to model this aspect would only lead to further complications.

Several materials both inert and decomposable were used as containing shells in the study. Gallium (M.P. = 303 K) which easily melts in warm water was chosen to simulate the freely melting iron shell. Inert materials such as glass, aluminum and graphite were used to investigate the effect that shell thermal conductivity might have on the addition's boiling rate. Although it is recognized that the thermal conductivity of the iron shell in the prototype would be fixed, this approach was used to evaluate the importance of thermal conduction. By varying the shell material in the model, the heat input due to conduction could be effectively evaluated.

As previously, mentioned, water is often chosen when modelling liquid iron or steel systems due to the similarity in the kinematic viscosities of the two fluids. In this study the use of water also had the advantage that the water superheat

could easily be varied between 0-100 K. When the concept of superheat is considered in conjunction with the boiling point of nitrogen, the overall driving force of the model can be compared with the prototype. Thus, when the water superheat is varied between 0-100 K the overall driving force lies between 200-300 K. Since magnesium rapidly reaches its boiling point (1363 K) the overall driving force is taken as the difference between the melt temperature and the additive's boiling point. For hot metal systems, between iron temperatures of 1473 K and 1663 K, the temperature driving force is 110-300 K. Consequently, the model applies mainly to higher hot metal temperatures. These concepts are shown schematically in Figure 2.17.

Simulation of the boiling magnesium was achieved by plunging half shell containers full of liquid nitrogen into water and observing the gas produced by the boiling nitrogen. Although different sized bullets were investigated, they were all based on the bullets presently used at Sumitomo Metal Industries. There were several discrepancies between the experimental procedures and the behaviour of the prototype. In the present study, the half shell containers were plunged into the water and held stationary while the boiling phenomena was observed. This is in contrast to the hot metal system where the bullets are rising upwards at their terminal velocity when the magnesium gas is initially released. Consequently, less heat is supplied to the liquid nitrogen



Temperature	Model	Prototype
T_m - Melt Temperature (K)	273-373	1473-1663
T_o - Shell Melting Point (K)	273	1448 (4.3% C)
T_l - Addition Boiling Point (K)	77.2	1363
$T_s = T_o - T_l$ = Shell Temp. Drop (K)	195.8	85
$T_T = T_o - T_l$ = Total Temp. Drop (K)	195.8-295.8	110-300

Figure 2.17 Temperature Profiles during Addition Vaporization for both the Model and Prototype.

due to the lack of forced convection. The magnitude of this drop is estimated later. The other less serious discrepancy is with the half shell's orientation. The bulk of the low temperature simulation work was done by holding the half shell container vertically with the opening facing up. Conversely, the prototype bullet is initially nearly horizontal at the onset of magnesium vapourization. To evaluate the magnitude of this difference the effects of the container's orientation were investigated using the present model.

The last and perhaps most important comparison to be made is between the respective rates of heat transfer in the two systems. To appreciate the convective components of the heat transferred, the natural and forced convective heat transfer coefficients must first be evaluated.

For liquid metals which are characterized by low values of the Prandtl number and correspondingly high rates of heat transfer, forced convection over a flat plate is described by Holm⁵⁵ as:

$$\bar{Nu}_L = 1.02 (Pr \cdot Re_L)^{1/4} \quad (2.7)$$

where

\bar{Nu}_L = the average Nusselt number over the entire length of the plate

$$= h_L L / k$$

Pr = the Prandtl number of the liquid metal

$$= C_p \mu / k$$

Re = the Reynolds number describing the fluid flow over the plate

$$= \frac{\rho Lu}{\mu}$$

\bar{h}_L = average forced convective heat transfer coefficient

k = the thermal conductivity of the fluid

L = characteristic dimension of the plate

C_p, μ = specific heat and dynamic viscosity of the fluid, respectively

ρ = fluid density

u = velocity of the fluid over the plate

The correlation for forced convective heat transfer from a flat plate was used to gain a first approximation of the convective component for a cylindrical bullet. In a more rigorous analysis, correlations for flow over cylindrical bodies should be used. For the horizontally rising bullet, the characteristic length will be the diameter of the bullet (0.025 m). The rising velocity will equal the terminal rising velocity for the bullet. Hence for the iron system:

$$\rho = 7070 \text{ kg/m}^3$$

$$u = 0.4 \text{ m/s}$$

$$L = 0.025 \text{ m}$$

$$\mu = 0.011 \text{ N-s/m}^2$$

$$k = 20.9 \text{ W/mK}$$

$$Pr = 0.10$$

$$Re = 10,280$$

Therefore $\frac{\bar{h}_L L}{k} = \bar{Nu} = 32.7$

$$\bar{h}_L = 27,340 \text{ W/m}^2\text{K}$$

For fluids like water which are characterized by moderate Prandtl numbers, a different expression describing convective heat transfer must be used. The following correlation must be used for water flowing over a flat plate:

$$\bar{Nu}_L = 0.664 Re_L^{1/2} Pr^{1/3} \quad (2.8)$$

Describing the heat transfer for the same situation depicted above, the water system is expressed by the following:

$$\rho = 1000 \text{ kg/m}^3$$

$$u = 0.4 \text{ m/s}$$

$$L = 0.04 \text{ m}$$

$$\mu = 9.8 \times 10^{-4} \text{ N}\cdot\text{s/m}^2$$

$$k = 0.604 \text{ W/mK}$$

$$Pr = 6.78$$

$$Re = 16,330$$

Therefore

$$\bar{Nu}_L = \frac{\bar{h}_L L}{k} = 160.6$$

$$\bar{h}_L = 2,425 \text{ W/m}^2\text{K}$$

Comparing the two values of the heat transfer coefficient, it is found that heat is transferred approximately 11 times faster in iron for forced turbulent convection. By applying the

the same type of analysis the natural convection heat transfer rates of the two systems can be determined. The low temperature system will be the basis of this analysis since it is the only time that natural convective heat transfer predominates. The calculation will be simultaneously made for the iron system so the two rates of heat extraction can be compared. The estimation of the Nusselt number for natural convection from vertical plates or cylinders is based on the following expression⁵⁵:

$$\bar{Nu}_L = C(Pr \cdot Gr_L)^m \quad (2.9)$$

where

Gr_L = The Grashof number corresponding to the free or natural convective heat transfer

$$= \frac{g \rho^2 L^3 \beta \Delta T}{\mu^2}$$

β = volumetric coefficient of expansion

T = the temperature driving force for natural convection

L = characteristic dimension of the plate or cylinder

C, m = constants which are determined from the $Gr \cdot Pr$ product

Since the product of the Grashof and Prandtl numbers are needed to evaluate the constants C and m they will be evaluated first for both systems. The characteristic dimension for the

half shell containers used in the low temperature model equals the length of the half shell. For the majority of the containers tested, the standard length was 0.20 m. In evaluating the driving force for natural convection in the low temperature model, it was necessary to assume that a thin shell of ice forms on the liquid nitrogen container. This would be expected due to the extreme temperature difference between the outer wall of the container (77.2K) and the water temperature (273-353K). Since the bulk of the experimental work was done at a water temperature of 353 K the driving force would be 80 K. Considering this with the other properties of water at 293 K, the Grashof number can be evaluated⁵⁵:

$$\rho = 1,000 \text{ kg/m}^3$$

$$L = 0.2 \text{ m}$$

$$g = 9.81 \text{ m/s}^2$$

$$\Delta T = 80 \text{ K}$$

$$\mu = 9.8 \times 10^{-4} \text{ N-S/m}^2$$

$$\beta = 2.108 \times 10^{-4} \text{ 1/K}$$

Hence $Gr_L = 1.38 \times 10^9$

and since $Pr = 6.78$

$$Gr \cdot Pr = 9.3 \times 10^9 = 10^{10}$$

Since the product of Grashof and Prandtl numbers is closer to 1×10^{10} than 1×10^9 , the analysis for values greater than 10^9 will be used. From Holman⁵⁵ for $10^9 < Gr \cdot Pr < 10^{13}$, $C = 0.021$ and $m = 2/5$, in equation 2.8.

Consequently:

$$\bar{Nu} = \frac{\bar{h}_L L}{k} = 204.4$$

and

$$\bar{h}_L = 617.2 \text{ W/m}^2 \text{ K}$$

The driving force in the iron system varies widely.

The melt superheat and subsequently the driving force for free convection is a function of the carbon content of the iron resulting in driving forces lying between 50-200 K. For comparison's sake the same driving force used for the water system will be used here. Hence for iron at 1433⁵²

$$\rho = 7070 \text{ kg/m}^3$$

$$L = 0.2 \text{ m}$$

$$g = 9.81 \text{ m/s}^2$$

$$\Delta T = 80 \text{ K}$$

$$\mu = 0.011 \text{ N-s/m}^2$$

$$\beta = 1.137 \times 10^{-4} \text{ 1/K}$$

Therefore $Gr_L = 2.95 \times 10^8$

and since $Pr = 0.10$

$$Gr \cdot Pr = 2.95 \times 10^7$$

For $10^4 < Gr \cdot Pr < 10^9$, $C = 0.59$ and $m = 0.25$ for equation 2.8.

$$\bar{Nu} = \frac{\bar{h}_L L}{k} = 43.5$$

and

$$\bar{h}_L = 4,544 \text{ W/m}^2 \text{ K}$$

Comparison of the two heat transfer coefficients indicate that heat will transfer approximately 7 times faster in iron due to natural convection. At first glance it might therefore seem that the low temperature analogue cannot simulate heat transfer at elevated temperatures. However, the amount of energy required to vapourize the nitrogen is significantly less than that for magnesium. From Tables 2.3 and 2.4:

$$\frac{\Delta H_v \text{ Mg}}{\Delta H_v \text{ N}_2} = \frac{6,006 \text{ kJ/kg}}{200 \text{ kJ/kg}} = 30 \quad (2.10)$$

Consequently, the heat demands of the prototype are 30 times that of the model. With heat being transferred only 7 times faster at the higher temperatures, the heat transfer rate for the low temperature analogue is therefore about 4 times faster than that for the iron-magnesium system.

CHAPTER 3

GAS-LIQUID INTERACTION PHENOMENA - PREVIOUS WORK

3.1 INTRODUCTION

The objective of this chapter is to present to the reader the topics in hydrodynamics which are important for the understanding of the present work. The main subject areas which will be covered are the dissolution of magnesium bubbles rising through molten iron, the hydrodynamics of bubble formation at a single orifice in both aqueous and metallic systems and a review of two phase flow with the main emphasis on gas-liquid flows.

The nature of magnesium addition in molten iron is to produce large quantities of vapour. Within the constraints of the present study, this gas flow will issue from only one opening. The flow through this orifice will determine the number and quantity of bubbles injected into the melt. This information is essential to evaluate the potential for dissolving all of the magnesium vapour in the iron. Since only a limited amount of gas is injected from each bullet, two phase flow between the surrounding fluid and the gaseous addition becomes important in characterizing the type of flow which will issue from each half bullet. However, before discussing the hydrodynamics of bubble formation, the kinetics of magnesium vapour dissolution into molten iron will be presented.

3.2 MAGNESIUM VAPOUR DISSOLUTION

During the 1960's and the early seventies several investigations have concentrated on the kinetics of magnesium vapour dissolution into hot metal. The results of these studies indicated that magnesium dissolves into cast iron as a function of its vapour pressure.^{7,57-59} These results have been summarized by Irons⁶ and are presented in Figure 3.1. This dissolution behaviour is described by Henry's Law:

$$Mg_{(v)} = \underline{Mg} \quad K_1 = \frac{\%Mg}{P_{mg}} \quad (3.1)$$

The value of K_1 in equation (3.1) is enhanced by an increase in the carbon content of the iron and depressed by increasing silicon content and temperature. Some typical values of K_1 are presented in Table 3.1.

Most of the researchers evaluated the magnesium solubility using a two temperature zone tube furnace so that the vapour pressure of magnesium could be arbitrarily controlled. It would appear that Irons⁶, in his study of the kinetics of magnesium dissolution and desulphurization was the only researcher to have introduced magnesium vapour directly into an iron melt. He used a vapourizer of novel design to pump magnesium gas into pilot scale iron melts (70 kg). The vapourizer is shown schematically in Figure 3.2. From the injection experiments into low sulphur melts, Irons⁶ determined that the mass transfer coefficient for magnesium dissolution from a rising bubble was approximately 4×10^{-5} m/s.

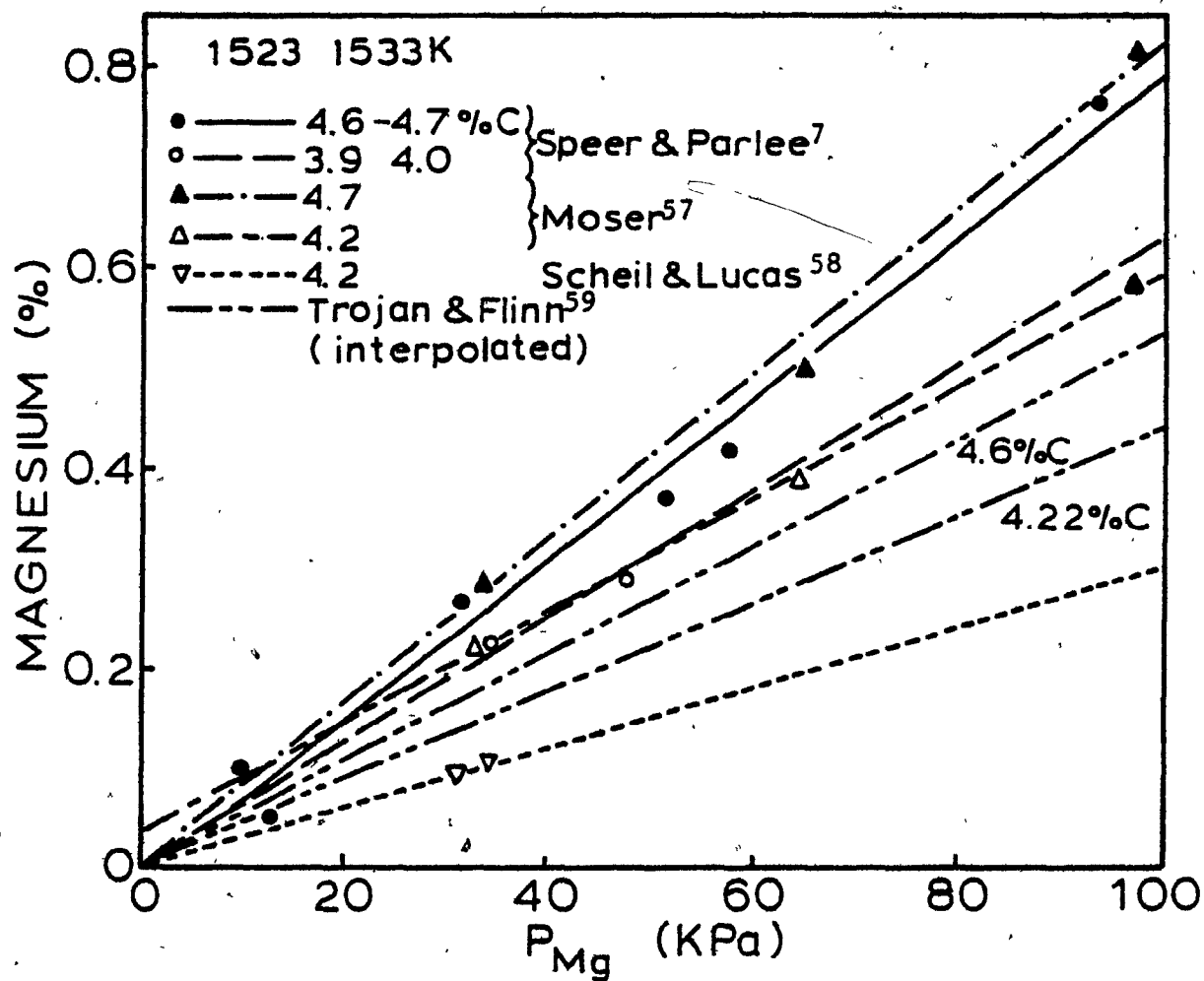


Figure 3.1 The Results of Several Investigations on the Dissolution of Magnesium Vapour in Iron as per Irons.⁶

Table 3.1
Values for K_1 Describing the Solubility of
Magnesium in Cast Iron⁶

Temperature (K)	% C	% Si	K_1 (%Mg kPa ⁻¹)
1523	4.4	0.1	0.0069
1523	4.7	0.1	0.0079
1523	4.4	1.1	0.0059
1573	4.4	0.1	0.0049

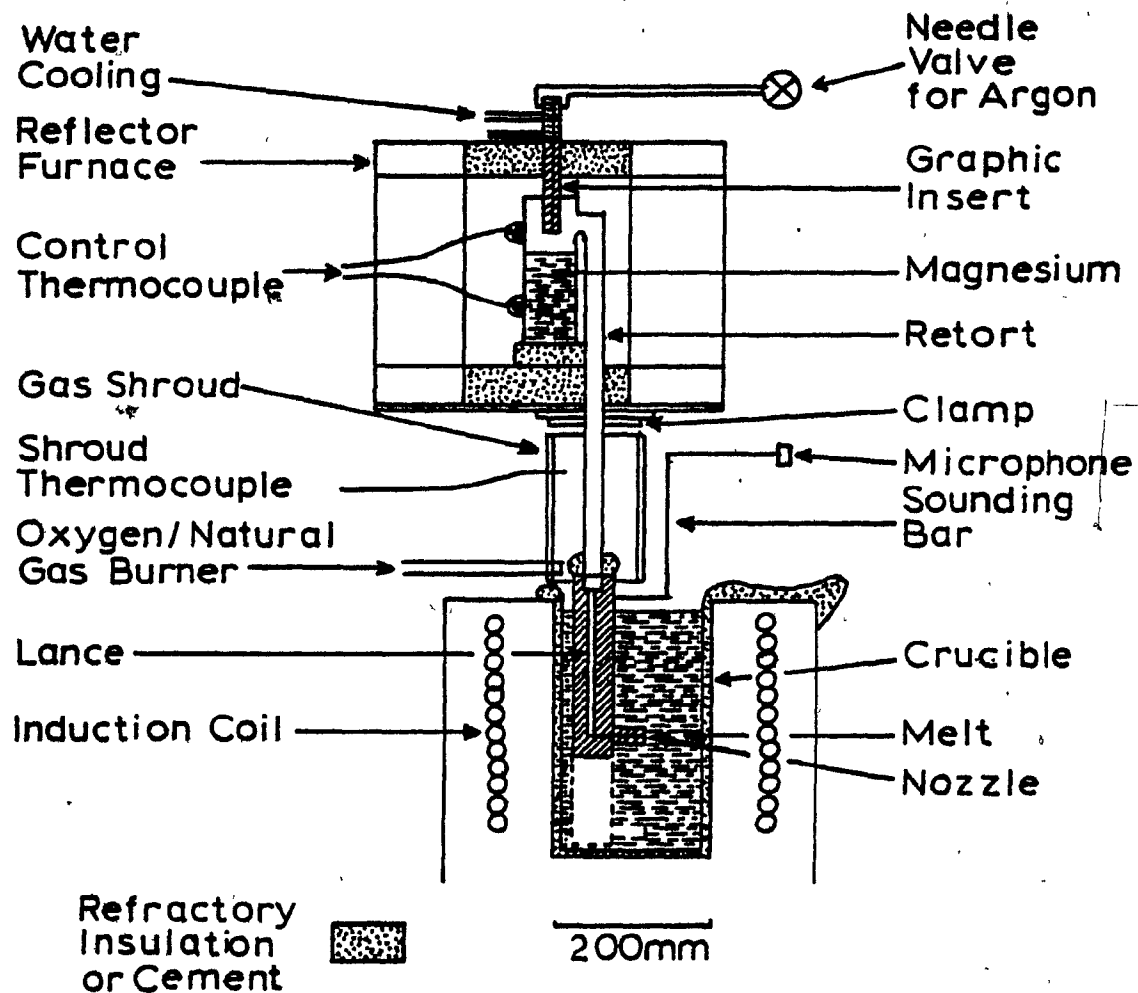


Figure 3.2 Magnesium Vaporizer Used by Irons⁶ to Introduce Magnesium Vapour into Molten Iron.

By measuring the sulphur content of the melt, it became possible to deduce the kinetic mechanisms that take place during magnesium desulphurization reactions. The results showed that most of the desulphurization occurred in the liquid phase through a heterogeneous reaction between dissolved sulphur and dissolved magnesium. The process involves co-diffusion and subsequent precipitation of magnesium sulphide on nucleation 'seeds' of magnesium sulphide. The 'seeds' are stripped from the front surface of rising spherical cap bubbles of magnesium.

Based on the kinetic study of Irons and Guthrie¹², Mucciardi⁹ developed an analytical relationship between the initial volume of a vapour bubble of magnesium and the minimum depth of release for it to dissolve before breaking through the melt surface.⁹ As a magnesium bubble rises through iron two factors are in play. First, the bubble tends to expand due to the decreasing head of liquid above it and second, it tends to contract because of the dissolution process. By performing a mass balance on a single bubble, the relationship between depth and bubble radius can be evaluated. To simplify the problem, the following assumptions are made:

- 1) the bubbles can be treated as equivalent spheres,
- 2) the rate controlling step is the dissolution of magnesium from the bubble into the melt, and
- 3) the liquid phase mass transfer coefficient is constant.

Balancing the changes of the mass in the bubble to the amount of magnesium leaving the bubble through dissolution, the following is obtained:

$$-K(4\pi r^2)\Delta C = \frac{d}{dt}(VC) \quad (3.2)$$

where K = liquid phase mass transfer coefficient of Mg
 r = equivalent radius of the bubble at time, t
 ΔC = concentration gradient in the liquid phase
 V = volume of the bubble
 C = concentration of the gas in the bubble.

Solving equation (3.2):

$$H = \frac{P_o}{\rho g} \left[\frac{-K\Delta C}{-K\Delta C + \frac{1.02 \rho g^{1.5} r_o^{1.5} M}{3RT}} \right]^2 - \frac{P_o}{\rho g} \quad (3.3)$$

where P_o = the ambient pressure
 T, ρ = the temperature and density of the melt, respectively
 r_o = initial bubble diameter
 M = molecular weight corresponding to the gas phase
 R = universal gas constant
 g = acceleration due to gravity.

Using the above equation, the depth at which a magnesium bubble of initial radius, r_o takes to completely dissolve can

be estimated. Mucciardi evaluated equation (3.3) for the magnesium-iron system using the following values:

$$P_0 = 1.013 \times 10^5 \text{ Pa}$$

$$\rho = 7000 \text{ kg/m}^3$$

$$g = 9.81 \text{ m/s}^2$$

$$K = 4 \times 10^{-5} \text{ m/s}$$

$$\Delta C = 49 \text{ kg/m}^3$$

$$R = 8314.1 \text{ Pa-m}^3/\text{kg mole K}$$

$$M = 24.3 \text{ kg/kg mole}$$

$$T = 1650 \text{ K}$$

The results of this analysis are shown in Figures 3.3-3.5. In Figure 3.3, the initial bubble radius is shown as a function of the depth required for that bubble's complete dissolution. In the latter two diagrams, the initial bubble radius and the melt depth are correlated first with the final bubble radius signifying incomplete dissolution and secondly, with the maximum amount of magnesium vapour which dissolves into the iron. For Figure 3.3, an asymptotic solution was obtained at an initial bubble radius equal to 61 mm. Magnesium vapour bubbles greater than this volume (951 ml) would never completely dissolve irrespective of the height of iron to the surface. For bubbles having an initial equivalent radius of 30 mm ($V_B = 113 \text{ ml}$) approximately 2 m of iron is required for their complete dissolution. Knowledge

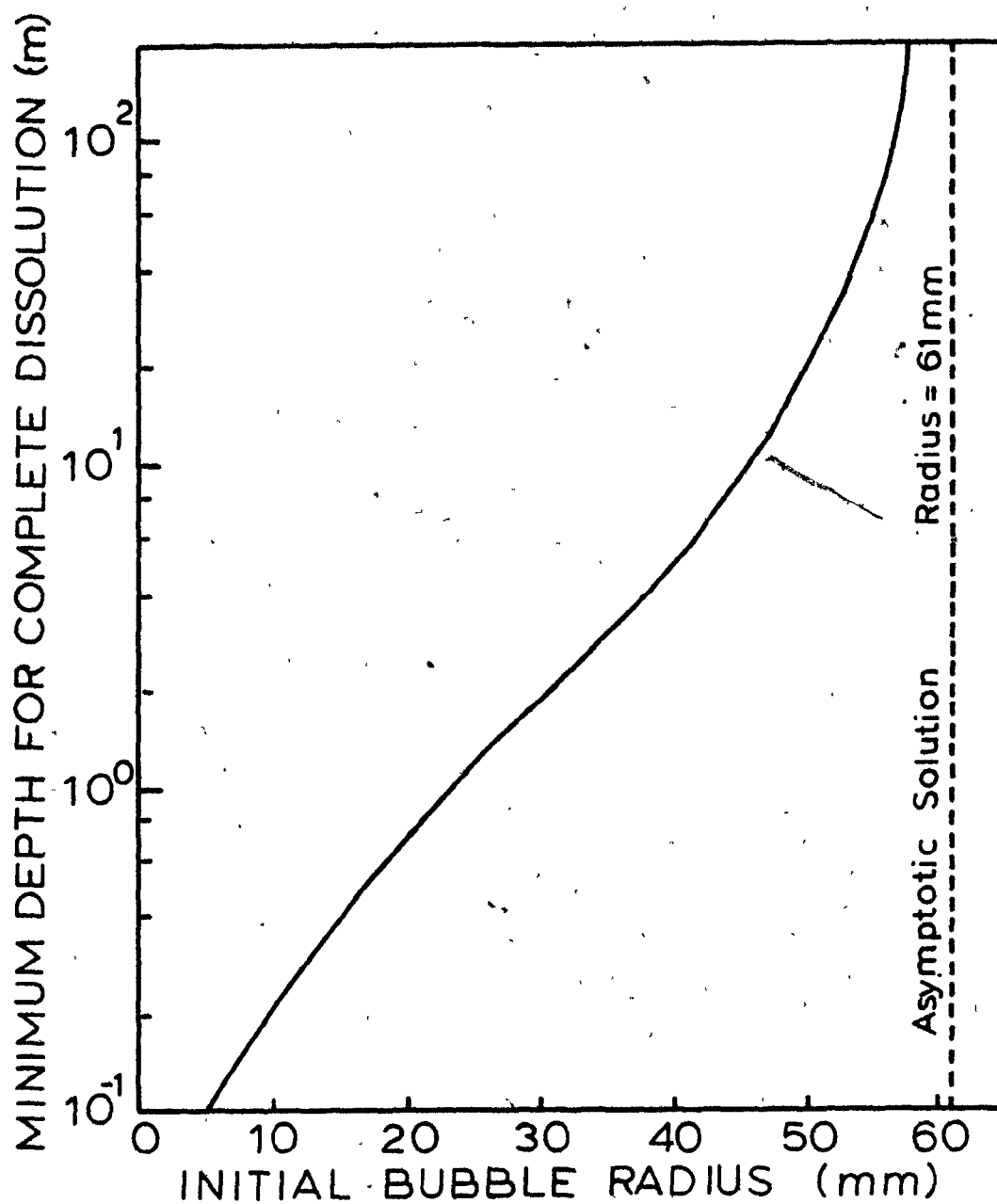


Figure 3.3 Depth of Iron Required to Completely Dissolve a Magnesium Bubble.

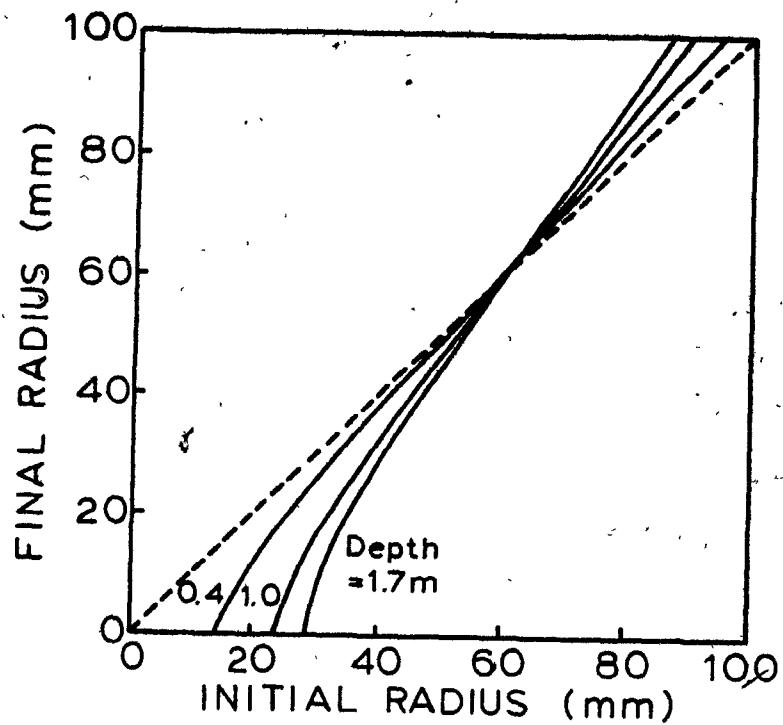


Figure 3.4 Final Magnesium Bubble Size for Incomplete Dissolution.

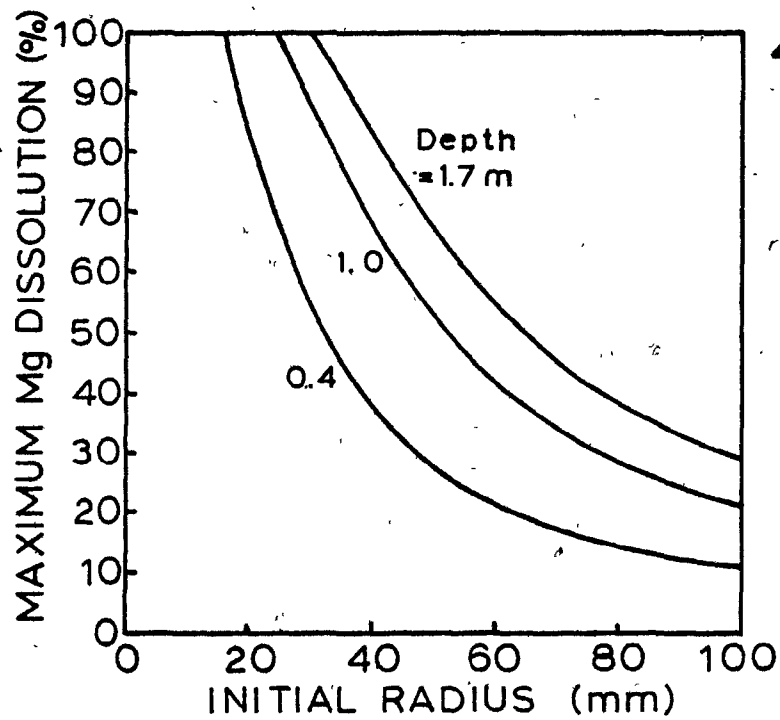


Figure 3.5 Quantity of Magnesium Vapour Dissolved into Iron for Several Melt Depths.

of how the magnesium vapourizes and the size and frequency of the bubbles which are initially formed are important in understanding magnesium based desulphurization operations. To aid in the understanding of bubble hydrodynamics, previous work performed on gas injection from submerged orifices is summarized in the next section.

3.3 BUBBLE FORMATION AT A SINGLE ORIFICE

Since the mid 1950's there has been considerable research in the area of gas injection from a single orifice. This type of flow can be broken into two general categories, bubble and jet formation. At high orifice Reynolds numbers, the flow issuing from an orifice can be termed as a jet. The transition from bubbling to jetting is not a sharp one and the value of the Reynolds number for the change is subject to debate. Szekely⁴⁷ suggests that an orifice Reynolds number (Re_o) of 5000 should denote the onset of a turbulent jet. It is generally agreed that in aqueous systems for $Re_o > 2,100$ there is considerable turbulence associated with the formation and break up of gas bubbles.

For lower values of the orifice Reynolds number, discrete bubbles form in a regular fashion. There has been a large effort to understand and characterize the formation of bubbles at single orifices due to their importance in both the chemical and metal processing industries. Several excellent reviews have been written on bubble formation, notably the work of Kumar and Kuloor⁶⁰, Valentin⁶¹ and Clift et al.⁶²,

among others.^{47,63,64} Although most of the research has been done for aqueous systems, there have been recent studies where bubble formation in metals has been investigated. To gain a comprehensive view of bubbles in both water and liquid metals this section will be divided into three subsections. The first part will concern aqueous gas injection, while the latter two parts will discuss the motion of free bubbles and the injection of gas into liquid metals.

3.3.1 Gas Injection in Aqueous Systems

The injection of an inert gas into water or an organic solution can be separated into four distinct stages, each of which has been closely examined in the laboratory. Although there have been several attempts, a successful model describing all four stages has not yet been developed due to the complexity of bubble formation. Valentin⁶¹ cited eighteen factors as being significant and it has been the inability thus far, of correlating all the important factors which has limited complete understanding of this phenomenon. Clift et al.⁶² cited some of the shortcomings of the models as follows:

- 1) the assumption that bubbles are spherical is not generally applicable;
- 2) assumptions regarding lift off and detachment events are often arbitrary;
- 3) when surface tension forces are involved, contact angles are usually determined under static conditions

- even though bubble formation is dynamic;
- 4) expressions for drag and added mass are at best approximations. No allowance for history effects is made;
 - 5) the terms describing the updraught due to the wake of the preceding bubble are generally ignored, but may be important.

Consequently, the description of bubbling is left at a four stage basis, each stage being unique and all four encompassing bubbling phenomena up to the jetting stage.

The first stage is known as the constant volume region and covers flowrates from zero flow to $Re_0 = 200$. In this stage, the buoyancy force is balanced with the surface tension forces as the bubble slowly forms. Assuming the bubble is spherical and of diameter d_b at the moment of lift off, the buoyancy force is given by:

$$F_b = (\pi/6) d_b \Delta \rho g \quad (3.4)$$

where $\Delta \rho$ = density difference between the liquid and gas
 g = acceleration due to gravity

The surface tension force is given by:

$$F_s = \pi d_o \sigma (\cos \theta) f(d_o/a) \quad (3.5)$$

where d_o = inside orifice diameter

σ = surface tension of the liquid

θ = contact angle at the triple interface

$f(d_o/a)$ = shape factor

For a sphere $f(d_o/a) = 1$ and perfect wetting of the tube by the liquid yields $\theta = 0$. Balancing the two forces,

$$(\pi/6) d_o^3 \Delta \rho g = \pi d_o \sigma \quad (3.6)$$

and rearranging

$$V_B = \frac{\pi d_o^3 \sigma}{\Delta \rho g} \quad (3.7)$$

For increasing values of Re_o the slowly increasing volume region is established. The zone for Re_o up to 1,000 is particularly well covered by the experiments of Davidson and Schuler^{65,66}. Equation (3.7) must be rewritten to account for the increasing effects of the inertial forces on the gas flowrate. Davidson and Schuler suggested the following equation:

$$V_B = \text{const} \left(\frac{d_o \sigma}{\Delta \rho} \right)^{1/2} (v \mu_L)^{1/2} \quad (3.8)$$

where v = linear velocity of the gas in the orifice

μ_L = dynamic viscosity of the liquid

As the orifice Reynolds number is increased to between 1,000 and 3,000 the well known constant frequency regime is entered. This regime is one of the most common in chemical processing and as its name indicates, the bubble frequency is constant, any changes in flowrate being absorbed by changes in the bubble size. One of the first and most popular equations for evaluating the bubble volume in this regime was given by Davidson and Harrison⁶⁷ in 1963. In this approach the buoyancy

force of the bubble is balanced against the change in upward momentum of the liquid surrounding the bubble. The momentum of the air leaving the orifice and the inertia of the air in the bubble are assumed negligible at low flowrates. Therefore, at any instant of time, the upward equation of motion is:

$$\rho_L V_B g = \frac{d}{dt} \left(\frac{1}{2} \rho_L V_B \frac{ds}{dt} \right) \quad (3.9)$$

where $\rho_L V_B g$ = the upward buoyancy force of the bubble

$\frac{1}{2} \rho_L V_B$ = mass of fluid accelerated upwards with the rising bubble, termed the added mass.

$\frac{1}{2} \rho_L V_B ds/dt$ = upward momentum of the surrounding liquid at any point in time

ρ_L = density of the liquid

V_B = bubble volume

but for the formation of a single bubble,

$$V_B = Qt \quad (3.10)$$

where Q = volumetric gas flowrate

t = time to form on bubble

$$\rho_L Qt g = \frac{d}{dt} \left(\frac{1}{2} \rho_L Qt \frac{ds}{dt} \right) \quad (3.11)$$

expanding the R.H.S. and simplifying,

$$2g = \frac{d^2s}{dt^2} + \frac{1}{t} \frac{ds}{dt}$$

or in short hand notation,

$$2g = S'' + \frac{1}{t} S' \quad (3.12)$$

Solving by the method of undetermined coefficients:

$$S = At^2 + Bt + C$$

$$S' = 2At + B$$

$$S'' = 2A$$

Substituting into Equation (3.12) and solving for A, B and C

$$A = g/2$$

$$B = 0$$

$$C = 0$$

$$S = \frac{1}{2} gt^2 \quad (3.13)$$

This indicates that the bubble has an upward acceleration equal to that of gravity owing to the added mass effect. When the bubble lifts off, $S = r$ where r is the radius of the bubble. The time to form one bubble can be evaluated by combining equations (3.10) and (3.13)...

Assuming the bubble is spherical at lift off:

$$\frac{4\pi}{3} \left(\frac{1}{2} gt^2 \right)^3 = Qt \quad (3.14)$$

rearranging,

$$t = (6/\pi)^{1/5} Q^{1/5} / g^{3/5} \quad (3.15)$$

Substituting into Equation (3.10):

$$v_B = \left(\frac{6}{\pi}\right)^{1/5} \frac{Q^{6/5}}{g^{3/5}} \approx 1.138 \frac{Q^{6/5}}{g^{3/5}} \quad (3.16)$$

Equations of this form have appeared frequently in the literature and there is some discussion as to the proper added mass coefficient for equation (3.9). Davidson and Schuler⁶⁶ used a coefficient of 11/16 to simulate a bubble in tangential contact with an accelerating plate or disc to obtain:

$$v_B = 1.378 Q^{6/5} g^{-3/5} \quad (3.17)$$

Other workers have arrived at a similar equation through both experimental results and complex two stage bubble growth models. The constants which have arisen for this equation are summarized in Table 3.2. Although bubble development can be described by more rigorous mathematics, an equation in the form:

$$v_B = k Q^{6/5} g^{-3/5} \quad (3.18)$$

should provide a reasonably good fit to the experimental points. Kumar and Kuloor⁶⁰ claim this type of equation fits sophisticated theory to within 10-20%.⁶⁰ As a first approximation it is an excellent way to evaluate whether the gas flow is in the constant frequency region. A comparison of predictions of equations (3.18) where $K = 1.138$ and experimental data is given in Figure 3.6.

Upon exceeding a Reynolds orifice value of 2,100, bubble coalescence and break up tend to invalidate results predicted

Table 3.2

Constants Obtained for Equation (3.16)

$$V_B = K Q^{6/5} g^{-3/5}$$

K	Method by Which it was Obtained	Reference
1.138	Added mass coefficient of $\frac{1}{2}$ for a spherical bubble distant from any surface	67
1.378	Added mass coefficient of $\frac{11}{16}$ for a spherical bubble in tangential contact with a plate	66
0.976	Two stage bubble growth mechanism	60
1.090	Two stage bubble growth mechanism	68
1.54	Two stage bubble growth with stem coalescence	68
1.722	Experimental	69

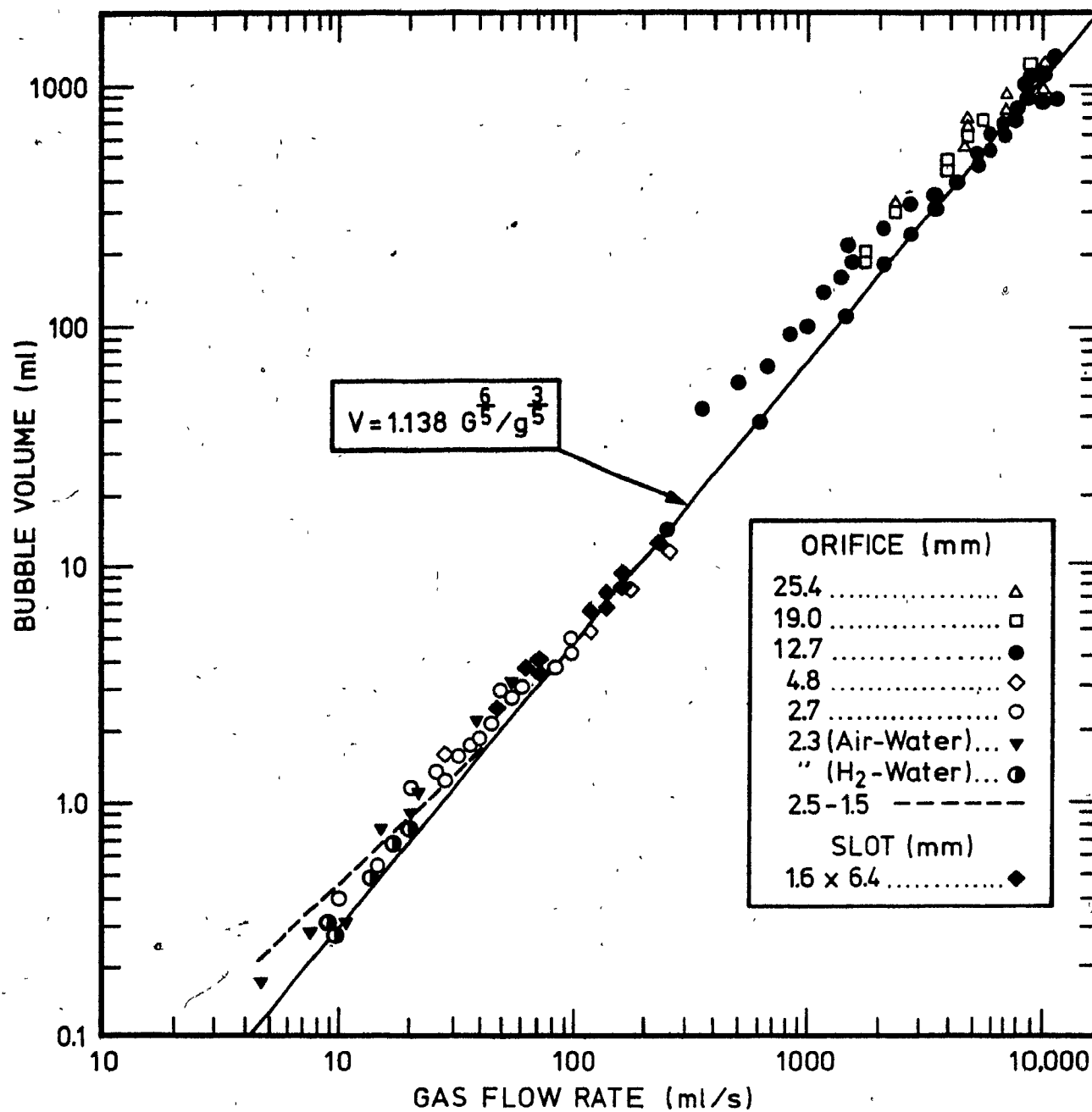


Figure 3.6 Comparison between Davidson and Schuler's⁶⁶ Equation and Experimental Data.

by equation (3.18). The change is not sharp and equation (3.18) can yield satisfactory results quite far into the turbulent region. At the higher flow rates the number of unstable toroidal bubbles increases creating more turbulence and bubble break up in the immediate area of the orifice.

Rene and Evans⁷⁰ found that even at orifice Reynolds numbers of 40,000 there still is bubble formation followed by break up into toroidal or irregular bubbles. These authors also noted that bubbles tend to form at the orifice in pairs or triplets, with the turbulence in the wake of one bubble "sucking in" the next one. During this process the second bubble is largely deformed, forming a neck between the primary bubble and the orifice. As the neck detaches from the orifice its momentum may push it through the center of the primary bubble, thus breaking up the bubble. This process can be slow, with a spherical cap bubble forming first and subsequently being broken up into smaller bubbles when the rear surface catches up with the front surface.

The turbulence caused by the bubbles breaking up also tends to promote the formation of many very small bubbles (5-50 μm in diameter).⁶¹ These bubbles can cause considerable disturbance particularly on the surfaces of the larger primary bubbles. This can enhance mass transfer and chemical reactions in any active chemical system.

Liebson et al.⁷¹ found that as the orifice Reynolds number exceeds 2,000, the dependency of bubble size on the orifice size

drops off dramatically. The results from Liebson's experiments are summarized in Figure 3.7. The mathematical representation of this region is still open to debate. For the less turbulent part of this regime the results from the constant frequency region often supply satisfactory solutions. As jet formation is approached there is no generally accepted technique for representing the events that occur. However, the models developed by Wraith^{68,72} and Kumar and Kuloor⁶⁰ are the most notable in interpreting this phenomena.

The reader is reminded that there is no precise transition from region to region. The ranges given in the text are values which have been determined largely by experiment. It is possible that the behaviour of one region may carry over quite far into the subsequent region. This arises due to the difficulty in correlating all the variables which are important in the formation of a bubble. Unfortunately any given parameter can have dramatic effects in one region and be insignificant in another. The major factors affecting bubble size can be broken down into three categories: equipment, system and operating variables. The important items in each group are summarized in Table 3.3.

The more significant factors when comparing metallic and non-metallic systems are the wetting effects of the orifice and the gas-liquid density differences. These will be more thoroughly developed in later sections.

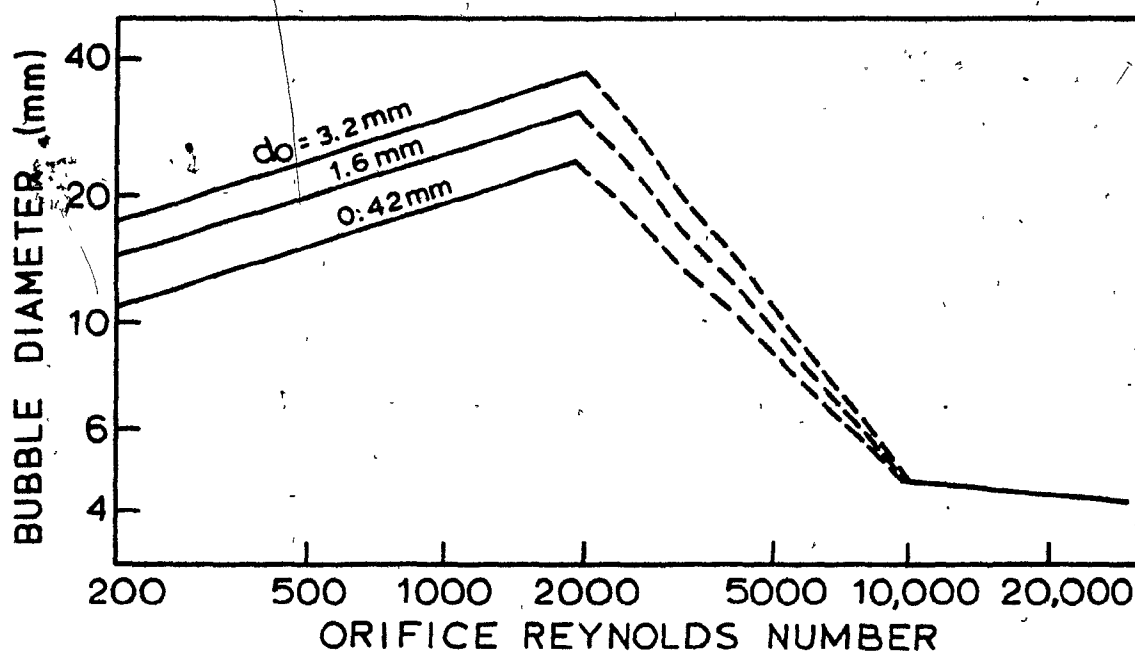


Figure 3.7 Transition from Bubbling to Jetting: The Effect on Bubble Diameter in Aqueous Systems⁷¹ (d_o - Orifice Diameter).

Table 3.3

Factors Influencing Bubble Size

Variable	Important Factors
Equipment	Diameter, geometry, orientation, nature and material of construction of the nozzle Chamber volume
System	Surface tension Density and viscosity of the liquid Density and viscosity of the gas Contact angle Velocity of sound in the gas
Operating	Volumetric flow rate of the gas Velocity in the continuous phase Head of liquid in the column (submergence) Pressure drop across the nozzle Temperature of the system

In summarizing the understanding of bubble formation and its theoretical description in aqueous systems, Kumar and Kuloor⁶⁰ state that there is a considerable amount of discrepancy in the literature regarding the various effects of the factors mentioned in Table 3.3. They attributed these discrepancies to the lack of appreciation by most investigators of the effects of chamber volume and the interaction of several variables such as viscosity, surface tension and flowrate. In virtually all studies the properties of the gas such as momentum and density have been ignored. To emphasize their point, Kumar and Kuloor presented some of the discrepancies found in the literature. These results are reproduced in Table 3.4.

3.3.2 The Motion of Free Bubbles

The motion of freely rising bubbles has been well documented with the theoretical work closely agreeing with the experimental results. The motion of a bubble rising in an infinite medium can be described by the following dimensionless numbers;

$$\text{Eötvös Number} \quad E_o = \frac{g \Delta \rho d_e^2}{\sigma} \quad (3.19)$$

$$\text{Morton Number} \quad M_o = \frac{g \mu^4 \Delta \rho}{\rho_L^2 \sigma^3} \quad (3.20)$$

$$\text{Reynolds Number} \quad Re = \frac{\rho_L d_e U}{\mu} \quad (3.21)$$

Table 3.4

The Influence of Liquid Properties on Bubble Volume as
Reported by Various Investigators⁶⁰

Investigator	Viscosity	Reported Effect of Surface Tension [*]	Density
1) Datta et al. ⁷³	Negative (small)	Positive	-
2) Quigley et al. ⁷⁴	Positive (small)	None	None
3) Coppock and Meiklejota ⁷⁵	None	Positive	Negative
4) Davidson and Schuler ^{65,66}	Positive (large)	None - constant flow	Negative
		Positive - constant pressure	
5) Benzing and Myers ⁷⁶	None	Positive	Negative
6) Siemes and Kaufmann ⁷⁷	Positive (large)	None	None

*'Positive' means the bubble volume increases with the increasing value of the property while 'negative' corresponds to a decrease in bubble volume.

where d_e = the diameter of a sphere of equivalent volume to the measured bubble

σ = surface tension between the gas and liquid phases

ρ_L = density of the liquid phase

$\Delta\rho$ = difference in density between the liquid and gas phase

g = acceleration due to gravity

μ = dynamic viscosity

U = rising velocity of the bubble

The resulting graph of these values and the bubble regimes they represent has been prepared by Clift⁶² and is presented in Figure 3.8. There are three general types of bubbles which can form. Spherical bubbles which are closely approximated by spheres if the interfacial and/or viscous forces are much greater than the inertial forces. Bubbles which are oblate with a convex surface enclosing the gas envelope are termed ellipsoidal. Large bubbles which tend to have flat or indented bases and lack any top to bottom symmetry are known as spherical or ellipsoidal cap bubbles. In trying to understand the motion of a particular bubble it is first important to establish the bubble type using Figure 3.8. Once this is done, theoretical and empirical expressions are available to predict the rising velocity of the particular type of bubble.

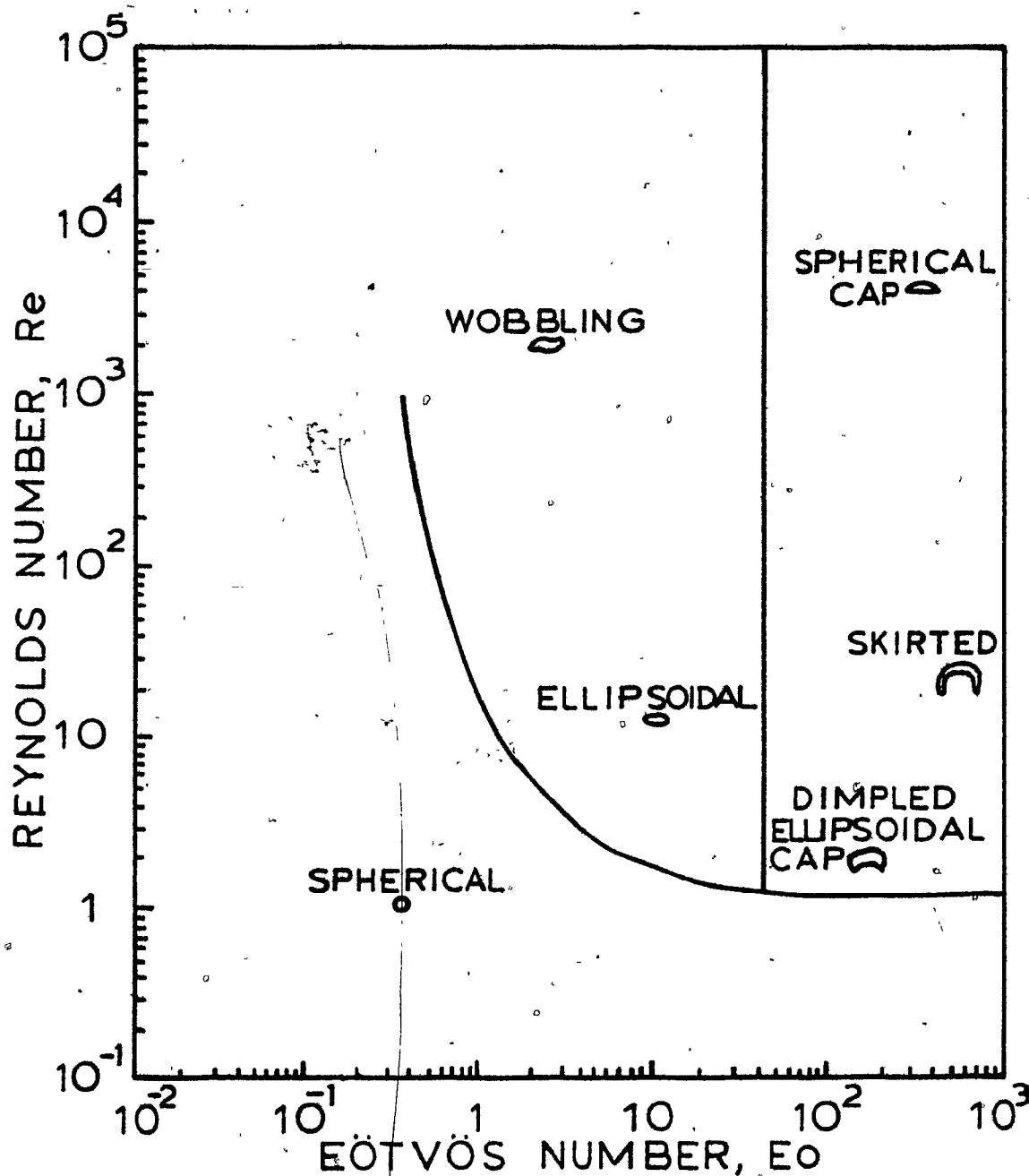


Figure 3.8 Bubble Classification as per Clift⁶²

3.3.3 Bubble Formation in Liquid Metals

The formation of bubbles in liquid metals differs from that of aqueous systems because of the effects of the chamber volume, the wetting properties of the nozzle and density effects. Liquid metals tend to be non-wetting to most materials which are used to construct the nozzle. Consequently bubbles tend to form at the outer circumference of the nozzle producing larger than predicted bubbles. The difference between the two systems is shown schematically in Figure 3.9. For the low flow rates associated with the constant volume region, Irons showed that for liquid metals the bubble volume is described as:

$$V_B = \frac{\pi d_{n,o} \sigma}{\rho g} \quad (3.22)$$

where $d_{n,o}$ = outer diameter of the nozzle.

This is similar to equation (3.7) used for the aqueous system except that the value for the orifice diameter is changed from the inner to the outer diameter. In the constant frequency region, these wetting effects become small and as a result, nozzle diameter is not then needed in the mathematical description of bubble formation.

The chamber volume is defined as the volume between the last large pressure drop and the actual nozzle. As a bubble forms there is a gradual build-up of pressure in this antechamber. When the bubble is released, the final volume is

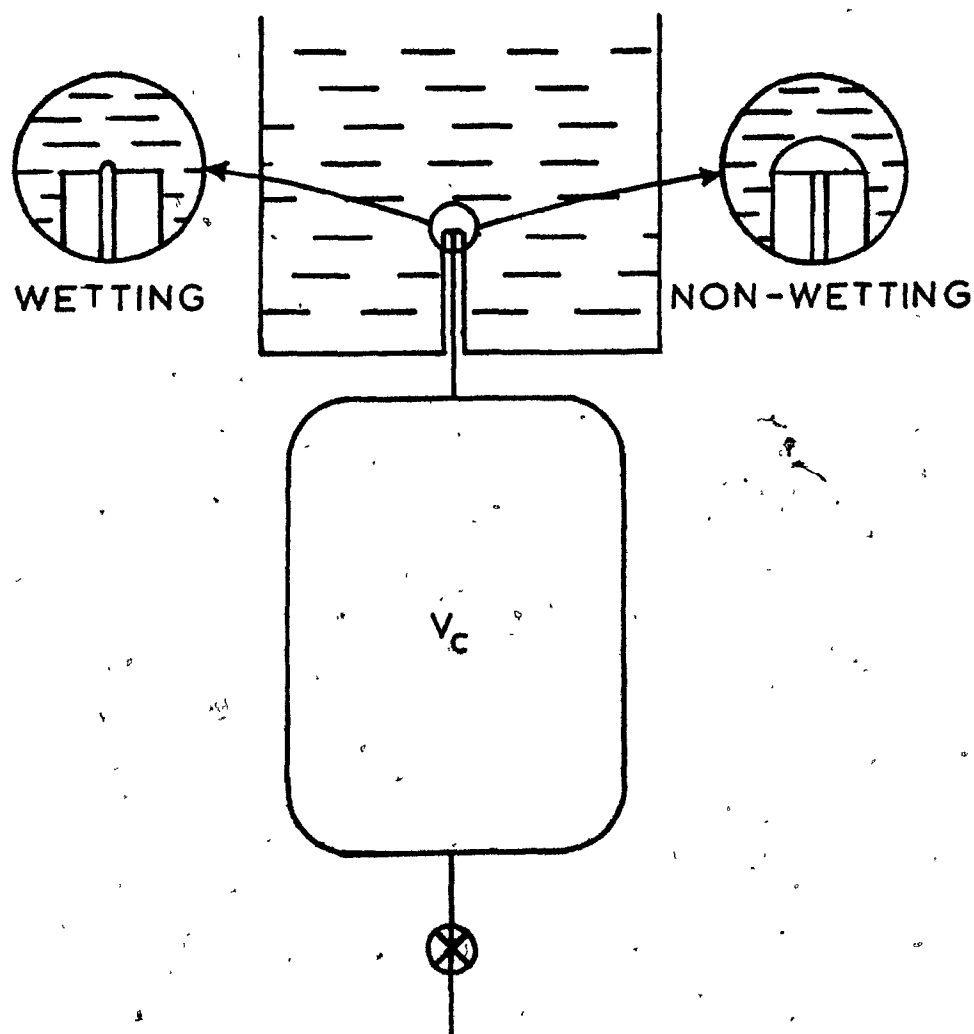


Figure 3.9 Bubble Formation at a Submerged Orifice for both Wetting (Aqueous) and Non-Wetting (Metallic) Systems.

larger than that calculated by static balance techniques. For non-wetting systems, the effect of chamber volume can be described by the dimensionless capacitance group given by the following:

$$N'_C = \frac{4 \rho_L g V_C}{\pi d_o d_{n,o} P_s} \quad (3.23)$$

where ρ_L = density of the liquid

V_C = chamber volume

$d_o, d_{n,o}$ = inner and outer nozzle diameters respectively

P_s = pressure at the nozzle

The effects of capacitance on the effective bubble diameter are summarized by the following equations:¹²

$$(d_B)_{\text{eff}} = d_B \quad \text{for } N'_C < 1$$

$$(d_B)_{\text{eff}} = (N'_C)^{1/3} d_B \quad \text{for } 1 < N'_C < 9$$

$$(d_B)_{\text{eff}} = 2.08 d_B \quad \text{for } N'_C > 9$$

A more sophisticated equation to describe bubble formation for a wide range of flow rates as proposed by Sano and Mori⁷⁸ is:

$$U_B = \frac{\pi \sigma d_{n,o}}{2 \rho g} N'_C + \frac{\pi}{6} \left(\frac{9 \sigma^2 d_{n,o}^2}{\rho^2 g^2} N'_C + \frac{10 Q^2 d_{n,o}}{g} \right)^{1/2} \quad (3.24)$$

It is important to remember that the above equation is semi empirical and that the centimeter, gram and second (cgs) system of units must be used.

A comparison between the results of equation (3.24) and several experimenters has been presented by Irons and Guthrie⁷⁹ and is shown in Figure 3.10.

Another interesting aspect of metallic systems is presented in Figure 3.11. The bubble sizes obtained by Sano and Mori⁷⁸ have been plotted against the results obtained by Leibson et al.⁷¹ (see Figure 3.7). It is interesting to note that the drop in bubble diameter at $Re_0 = 2,000$ has not been observed by investigators working on liquid metals. This should extend the results obtained for the constant frequency region up to very high values of Re_0 . According to the results in Figure 3.11 the behaviour is unchanged up to $Re_0 = 20,000$. Sahai and Guthrie⁸⁰ have recently presented more theoretical work detailing the importance of liquid density and gas properties on the nature of the bubble formed in liquid metals.

In summary, it has been shown that bubbling in metallic liquids is substantially different to that in water. At the low flow rates corresponding to the constant volume region, the outer nozzle diameter is important in the prediction of bubble volumes. The importance of the chamber volume and capacitance on bubble volume was shown using the semi empirical equation of Sano and Mori.⁷⁸ The experimental results of Irons and Guthrie⁷⁹ showed the transition from the constant volume to the constant frequency flow region. Further tests by Sano and Mori have established that the results from the constant frequency region hold for much higher flowrates in metals than in water.⁴⁷

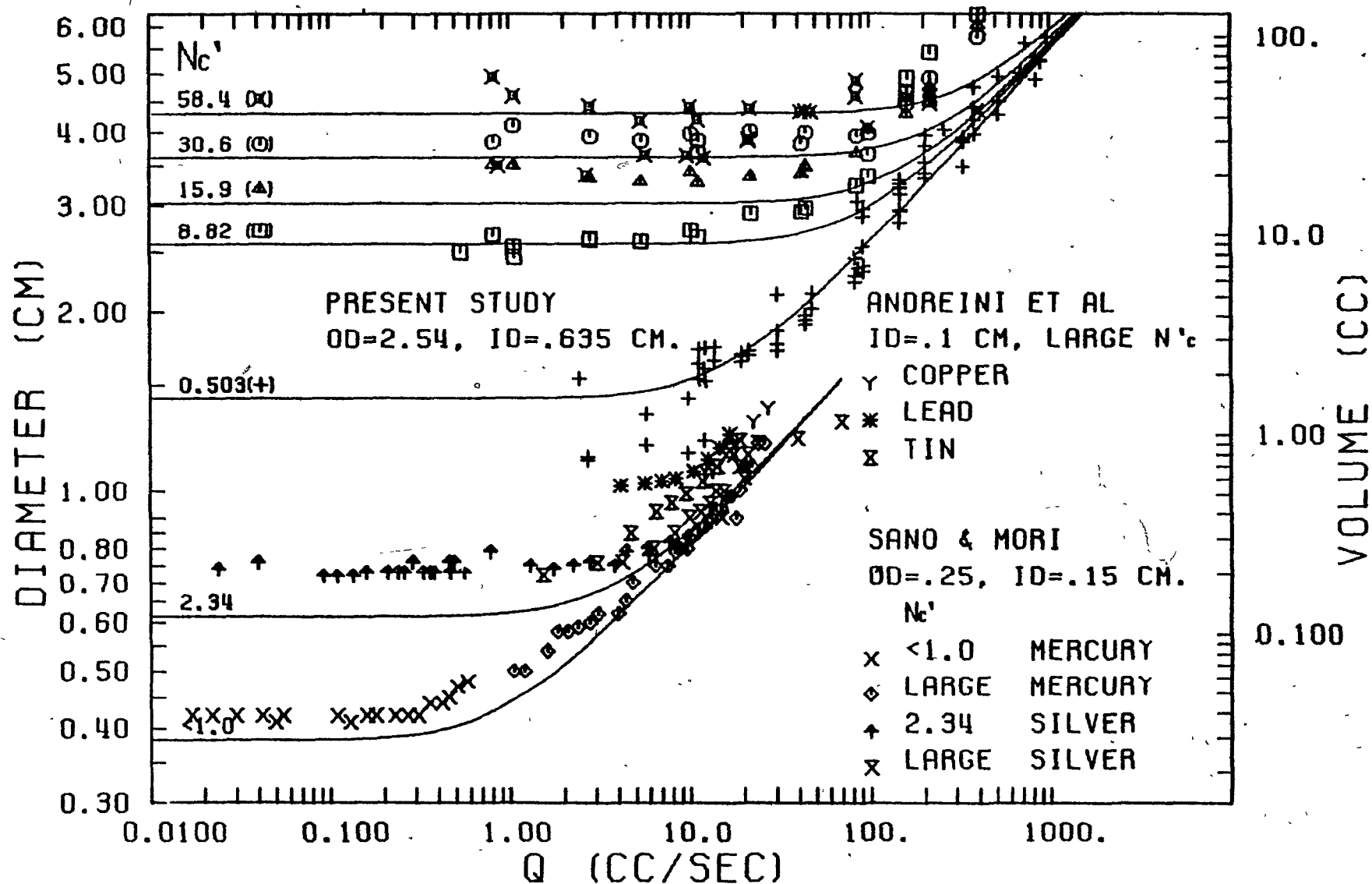


Figure 3.10 Bubble Volume as a Function of Gas Flow Rate for Metallic Systems after Irons.⁶ Solid lines refer to Equation (3.24).

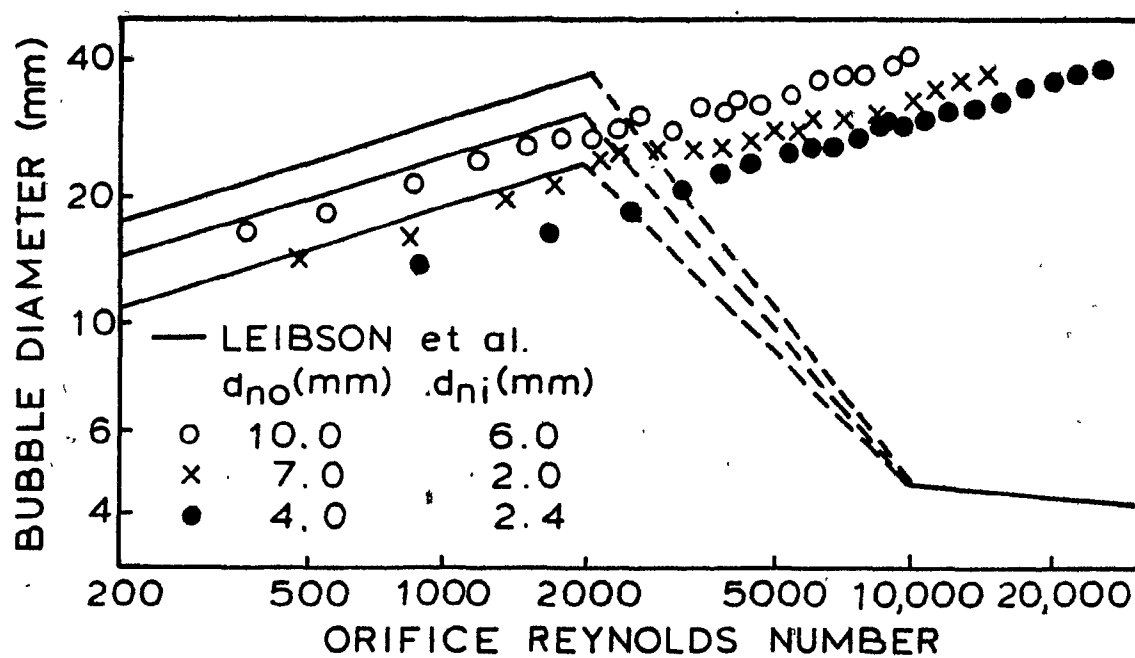


Figure 3.11 Comparison between Gas Injection in Metallic Systems (Sano and Mori⁷⁸) and Aqueous Systems (Leibson et al.⁷¹).

3.4 TWO PHASE FLOW

When gas is introduced into the liquid phase, counter-current flow between the two phases is established except when very high gas velocities are used. This has been substantiated in metallurgical systems by Engh et al.⁸¹ In this study, Engh et al. investigated the clogging problems in tuyeres and lances. For a wide range of gas velocities, the authors found that particles of the surrounding fluid always infiltrated the injection nozzles. Even at velocities approaching one quarter the sonic velocity of the nozzle, infiltration was observed. Based on these results it is possible that if the magnesium vapour bubbles rather than jets out of the containing iron shell, infiltration of hot metal may be an integral part of the vapourization process. Unfortunately, the analytical solution of gravity driven two phase countercurrent flow is difficult and often impossible to obtain. When a flow regime is established there can be several types of flow including slug and bubble flow. These regimes are summarized in Figure 3.12 for the cocurrent flow patterns established in a vertical tube evaporator.⁸²

When two phase flow is set up between unstable fluids, an understanding of the boiling characteristics of the volatile fluid is important. Little or no work has been done on characterising the vaporization of magnesium or calcium.

However, for low temperature systems such as nitrogen and particularly water, the boiling characteristics are well

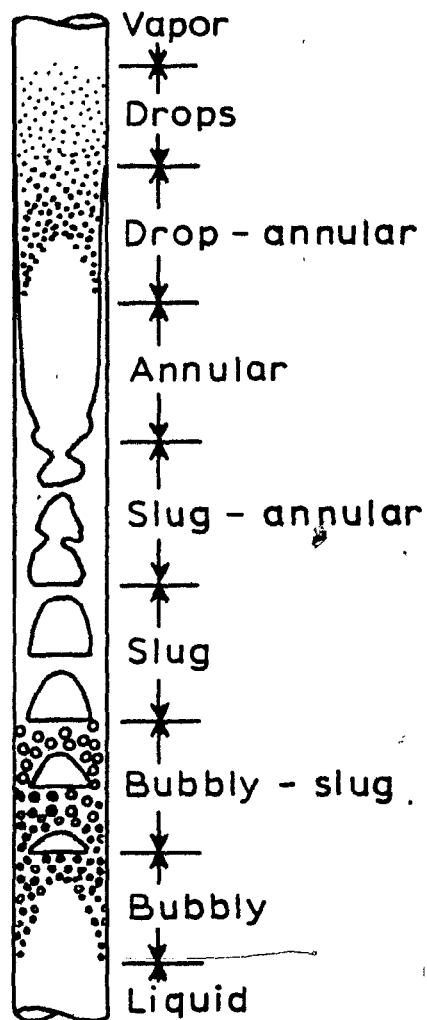


Figure 3.12 Two Phase Cocurrent Flow Patterns in a Vertical Tube, Evaporator.

known. For the pool boiling of a liquid there are four distinct regions describing the heat transfer rate from the heating source to the liquid. These stages include free convection, nucleate boiling, transitional boiling and stable film boiling. As the driving force heating the liquid increases heat is first transported through natural convection. The first stage of boiling is known as nucleate boiling. In this stage heat can be transferred very rapidly due to the high exchange rates between the vapour and the liquid at the heating surface. From the boiling curve for water, shown in Figure 3.13 the nucleate boiling regime reaches a point of maximum heat transfer. This represents the optimum transfer of heat by both the liquid and vapour phases. As the driving force is increased the proportion of vapour generated increases. This causes a large drop in the heat flux due to the insulating qualities of the vapour.

The transitional zone between nucleate and stable film boiling is complex in nature. In general there is an inverse relationship between the relative amount of vapour and the ability to transfer heat. The minimum heat flux is reached when a stable film of insulating vapour is produced. Transfer of heat in the stable film region is difficult since heat is mainly transferred via radiation through the gas film. The peak heat flux established in nucleate boiling is only exceeded when the heat transferred via radiation through the gas phase becomes very large.

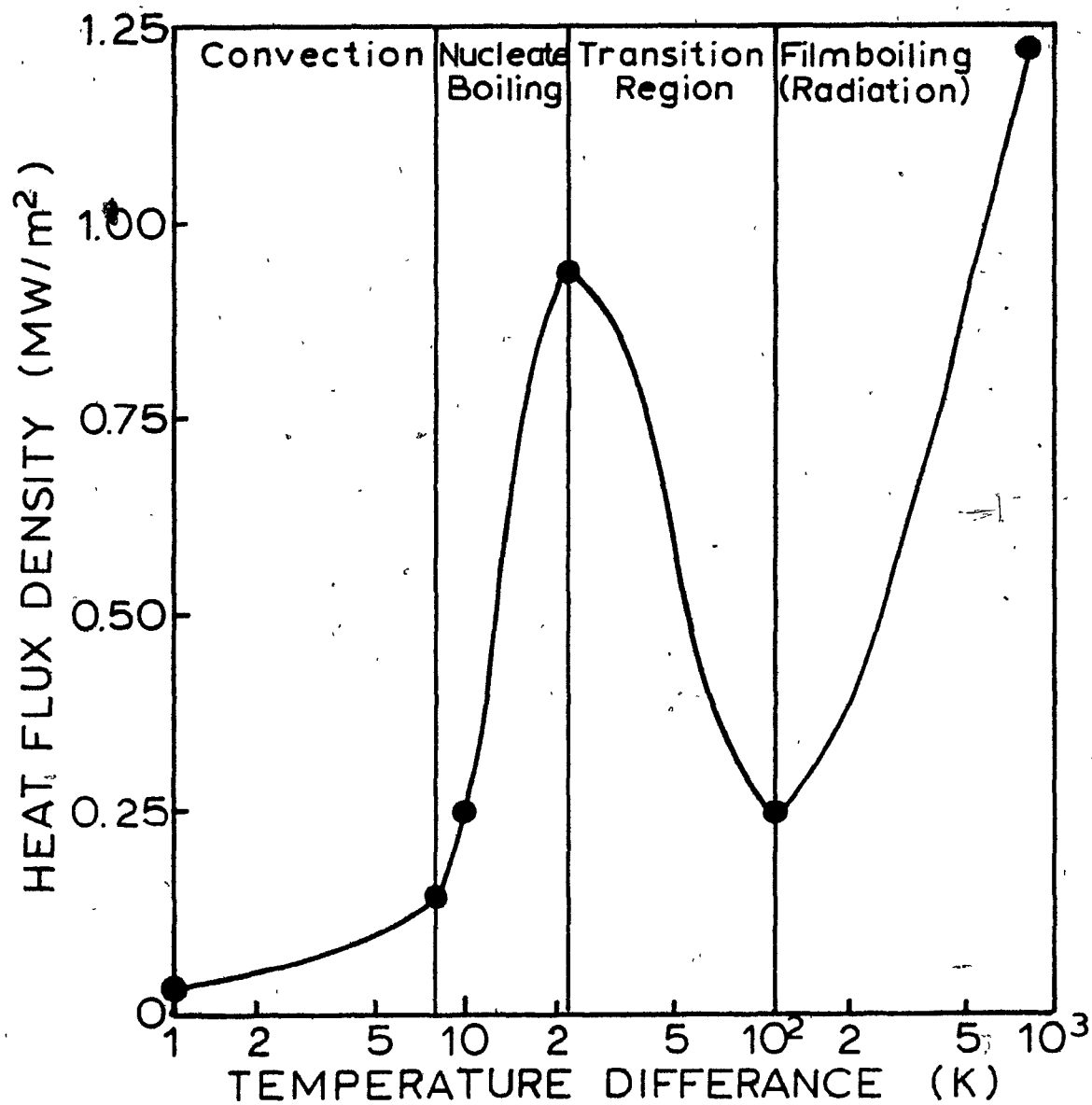


Figure 3.13 Characteristic Pool Boiling Curve for Water Showing the Four Distinct Stages.

The pool boiling curve characteristic of liquid nitrogen is shown in Figure 3.14. Comparing the two boiling curves it is easily seen that liquid nitrogen goes through the four boiling stages faster than water does. Speculation as to the type of boiling which magnesium incurs is scarce. It is the author's opinion that the high rate of heat transfer by convection through the metallic liquid would tend to 'stretch out' the curve for magnesium when compared to the water curve. Consequently each stage would exist for a greater range of temperature driving force. Even so, for a temperature difference of 200 K it is still difficult to estimate whether the magnesium would have exceeded the peak flux associated with nucleate boiling.

3.5 GRAVITY DRIVEN FLOW

Gravity driven counter current flow between two unstable fluids has been described by Taylor⁸³ in terms of a classical instability analysis. Examples of this type of flow system are bubbles issuing from a submerged orifice and the formation of water drops below a flat plate. At very low flow rates bubbles forming at an orifice are largely controlled by the surface tension and buoyancy forces in effect at the nozzle. If an instability exists the bubble lifts off due to its relatively high buoyancy force. However, if the surface tension forces are strong enough the bubble will remain attached to the nozzle and flow will be discontinued. For

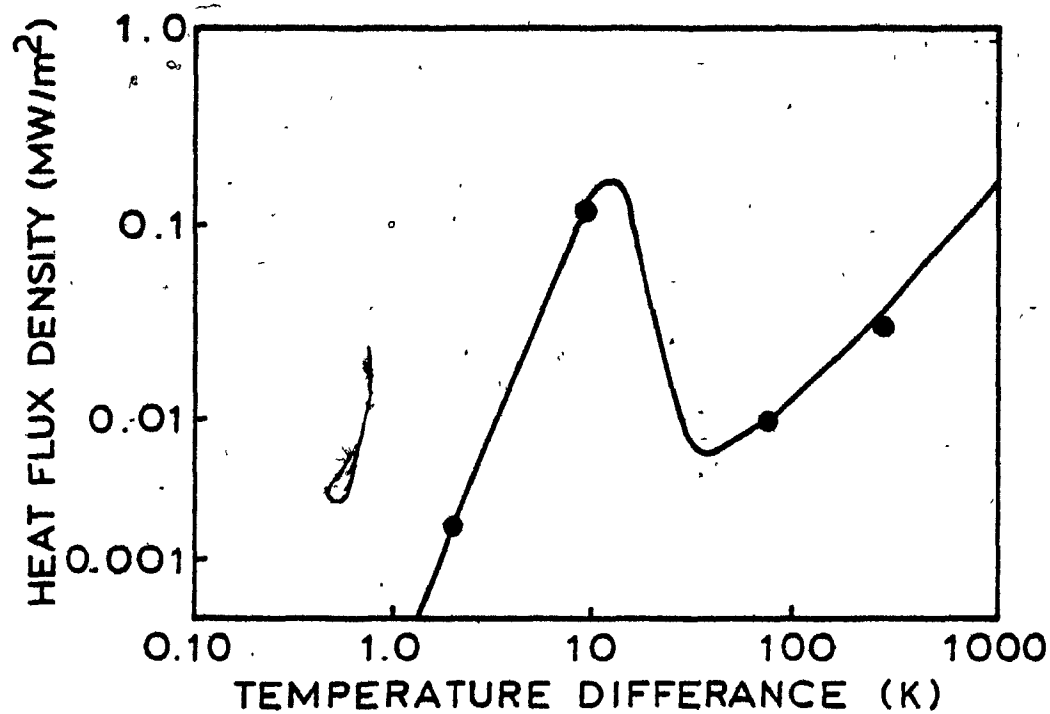


Figure 3.14 Characteristic Pool Boiling Curve for Liquid Nitrogen.

magnesium vapour issuing from an iron tube, large surface tension forces may limit the flow of the vapour. The results of Taylor's theory then become useful in understanding the gas flow when surface tension forces predominate (low flow rates, small orifices).

For the second example, stability is reached when water forms a hanging drop on the bottom of the flat plate. At this moment the surface tension force between the water and air films have exceeded the gravitational forces causing the droplet to hang. As the gravitational forces increase the stability is destroyed and water drops fall from the plate.

Taylor instability predicts the growth rate of perturbations placed on the interface between the two fluids. Given a surface disturbance, Taylor's theory will predict if the perturbation will grow and if so, how fast. Perturbations which grow are termed unstable. Figure 3.15 shows an artistic impression describing the growth of an unstable perturbation between water and air films.

Since this type of flow is surface tension dependent, there exists a critical wavelength which establishes whether a perturbation will grow or not. Ignoring the effects of viscosity, this critical wavelength is predicted by Taylor instability as:

$$\lambda_C = 2\pi \left(\frac{\sigma}{\Delta \rho g} \right)^{1/2} \quad (3.25)$$

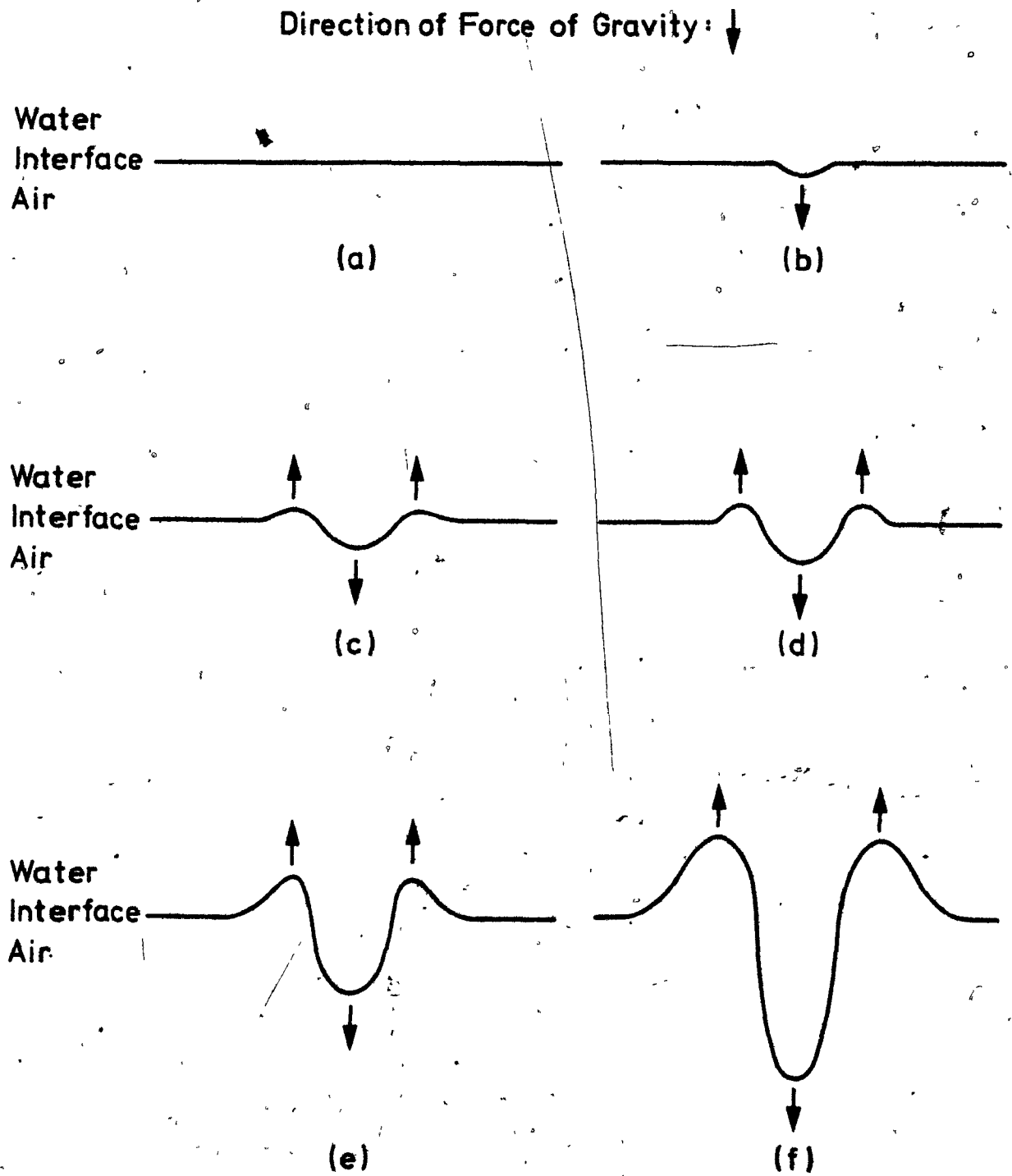


Figure 3.15 Growth of an Unstable Perturbation between Water and Air.

where λ_C = critical wavelength for the perturbation to grow
 σ , $\Delta\rho$ = surface tension and density difference between
 the two fluids, respectively
 g = acceleration due to gravity

Thus when the perturbation size exceeds λ_C , the perturbation should grow. For water and air $\lambda_C = 17.3$ mm. Consequently, any drops hanging from a flat plate should not exceed this diameter. The actual critical diameter would be different due to circular symmetry and fluctuations in the system (i.e. fluid flow in either the water or air films).

A more important result of the Taylor instability analysis is not the wavelength but half that value. When gravity driven flow is physically restricted by a constriction which is less than $\lambda_C/2$ the flow should be totally inhibited due to surface tension forces. Evidence for this phenomenon has been cited by Zuber.⁸⁴ In one case "...water was retained by atmospheric pressure in an inverted tumbler whose mouth was closed by a gauze of sufficiently fine mesh. The mesh size did not exceed $\lambda_C/2$."⁸⁴ Unstable stagnant fluids will not exhibit countercurrent flow when they are faced with a restriction corresponding to the critical length or diameter ($\lambda_C/2$) characteristic of two phase flow. This fact becomes important in evaluating the magnesium gas flow issuing from the half bullets as they rise through the iron.

3.5 . SUMMARY

The author has attempted to provide a background survey of aspects of gas-liquid interactions which are important and relevant to the present work. This has included summarizing how magnesium bubbles dissolve in hot metal, the various flow regions which occur when gas is injected through a single orifice and the mechanisms of boiling and two phase flow. These concepts will later be used to characterize the vaporization process inside the containing shell and the type of gas stream produced during the boiling process. This combined with the knowledge of how fast magnesium bubbles dissolve in hot metal will lead to a thorough evaluation of the potential for magnesium bullets.

CHAPTER 4

EXPERIMENTAL

4.1 INTRODUCTION

The materials and procedures used for the low temperature study will be further outlined in this chapter. As mentioned earlier the essence of the low temperature tests was the plunging of half bullet shaped containers into a water bath. The first part of this chapter will describe the equipment used for these tests while the end of the chapter summarizes the experimental program and the subsequent analysis of the data.

4.2 APPARATUS

Figure 4.1 shows the basic apparatus used to perform the immersion tests. In the following sections the water tank, the liquid nitrogen containers and the filming equipment are described briefly.

4.2.1 Water Tank

A 0.20 m³ pyrex tank was used to simulate an iron bath. Shown in Figure 4.2, the tank consisted of a pyrex tube 0.46 m in diameter and 1.22 m in length which rested on a steel base-plate. The tank was equipped with two individually controlled 3000 W Chromalux immersion heating elements. This flexibility enabled the bath temperature to be maintained at any level between room temperature (293 K) and 373 K. By adding ice to

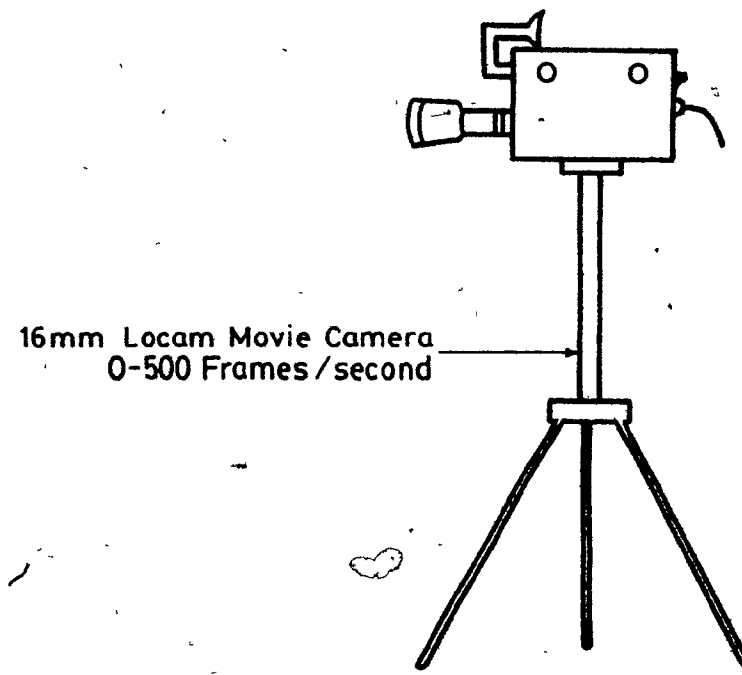
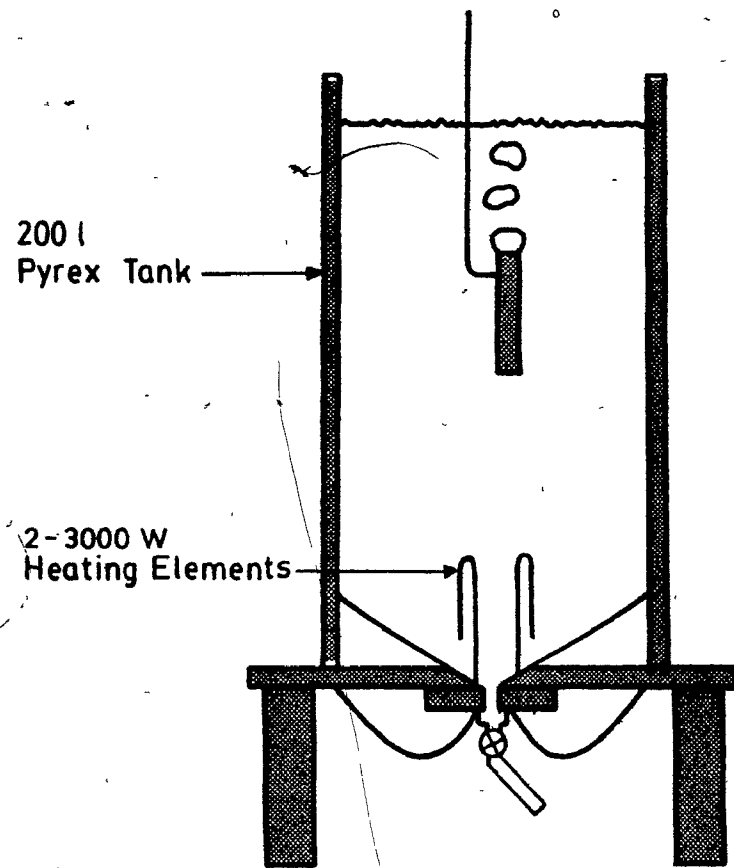


Figure 4.1 Apparatus used for Low Temperature Experimentation.

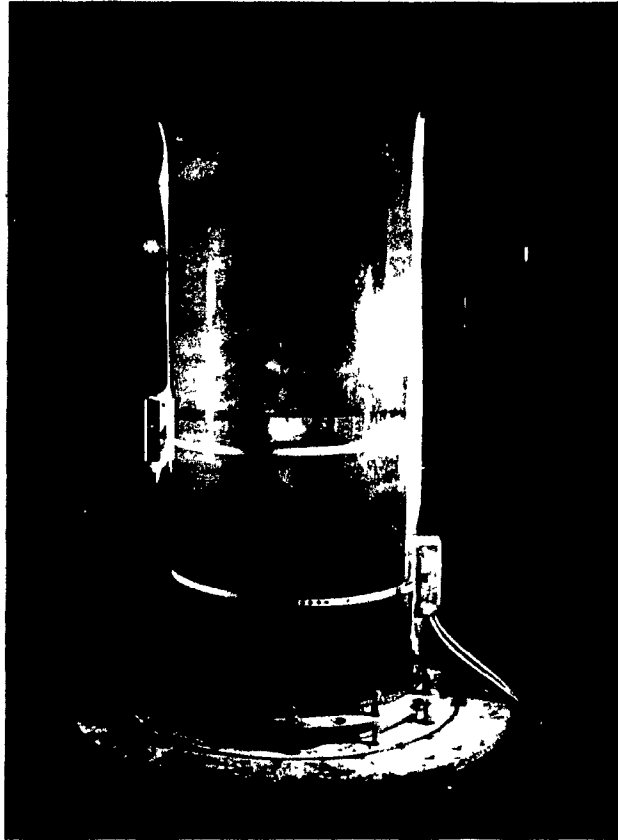


Figure 4.2 The 200 l Pyrex Tank used to Simulate an Iron Bath.

the bath, temperatures down to 273 K were investigated.

4.2.2 Liquid Nitrogen Containers

The tubes used to immerse the liquid nitrogen were cylindrical containers closed at one end with a long side arm attached to facilitate the plunging procedure. Tubes of different materials were used to investigate the importance of shell thermal conductivity. Different shaped tubes were also used. Table 4.1 summarizes the different types of tubes used in the experimental program. By using arms bent to different angles the effect of tube orientation could also be observed. Figure 4.3 shows three tubes of different materials and geometries.

4.2.3 Documentation

Since the boiling reaction occurs very rapidly, it was essential to record each test on either film or video tape for reviewing at a later time. This type of documentation enabled the author to make detailed observations of the boiling reaction through a frame by frame analysis of each experiment. Although a number of film and video systems were used, the bulk of the documentation was done on video tape. The most successful results were obtained when a master tape was recorded on 19.1 mm (3/4 inch) video tape using a U-matic video system. The system used in this study included a Panasonic video player-recorder (NU-2125) and a Sony 3400 black and white video camera.

TABLE 4.1
Dimensions of the Nitrogen Containers
Used in the Present Study

Container Material	Length (mm)	Outer Diameter (mm)	Inner Diameter (mm)	Volume (ml)
Aluminum	200	6.35	4.62	3.4
	200	13.34	10.00	16.0
	200	22.30	20.00	61.6
	200	31.75	29.29	137.5
	300	12.70	10.16	25.2
	100	12.70	10.16	8.2
	50	12.70	10.16	4.2
Glass Pyrex Type - Borosilicate glass	200	6.78	4.59	3.3
	200	11.99	9.68	15.3
	200	22.05	18.92	55.2
	190	24.11	22.50	75.9
	200	32.00	28.58	128.0
Glass	250	11.99	9.68	19.0
	150	11.99	9.68	11.6
	100	11.99	9.68	7.7
	50	11.99	9.68	3.9
Graphite	200	24.18	17.58	47.3
Gallium	190	25.50	20.16	54.3

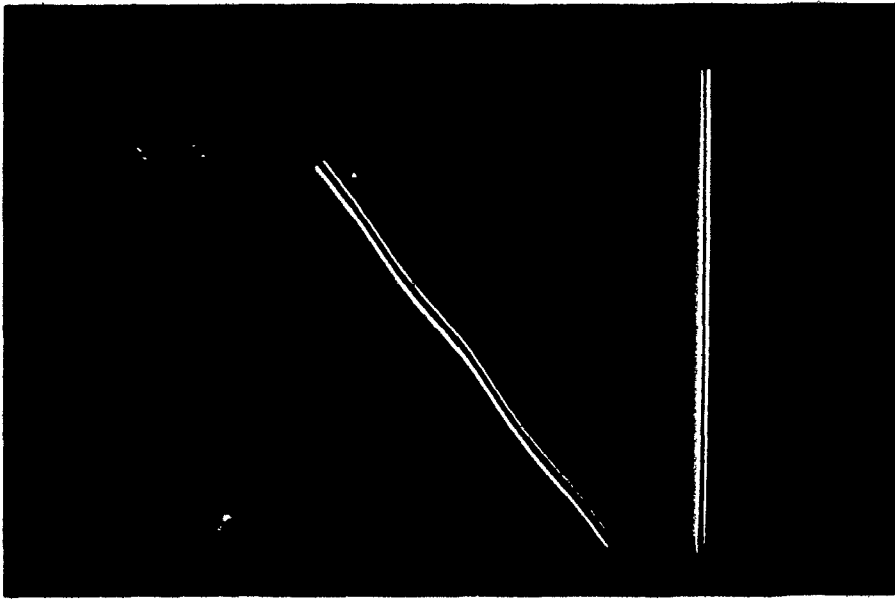


Figure 4.3 Typical Nitrogen Containers used in the Present Study.

For the subsequent analysis the master tape was copied onto a 12.7 mm (1/2 inch) video tape. In this format the results were viewed using a Sony 3650 video player with special stop and slow motion functions. To further aid the analysis a digital clock was dubbed onto each videotape allowing time to be measured to an accuracy of 0.01 s. Figure 4.4 shows a typical frame taken with the video system. The position of the equipment and tank wall as well as the nitrogen container and boiling nitrogen bubbles are shown.

As per Figure 4.1 a portion of the documentation was done using a 16 mm variable speed cine camera (Locam, model 51-002). The advantage of film is that it facilitates the presentation of the results. The majority of photographs presented in this thesis derive from films rather than video tape.

4.2.4 Materials

The materials used fall into two categories. The first group comprises the fluids used in the study; liquid nitrogen and water. The liquid nitrogen was supplied and manufactured at McGill University. The thermal and physical properties of these fluids are summarized in Table 4.2.

The other group of materials are those used to fabricate the liquid nitrogen containers. The chemical compositions, thermal and physical properties, of these materials are shown in Table 4.3.

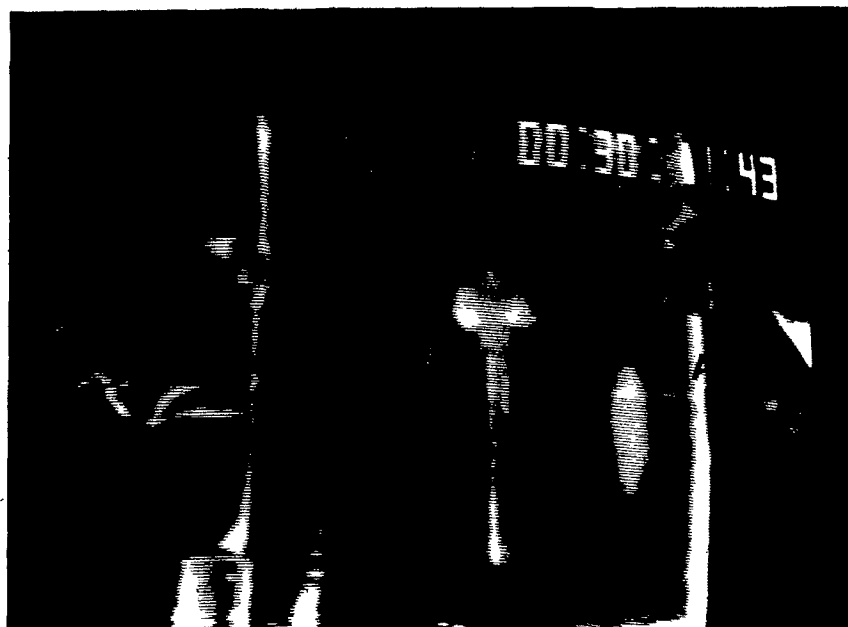


Figure 4.4 Typical Frame Generated by the Video System.
A - Tank Walls, B - Nitrogen Containing Tube,
C - Arm used to Hold the Tube (Test Using
20.0 mm Pyrex Tube at a Superheat of 80 K).

TABLE 4.2

Thermal and Physical Properties of
Liquid Nitrogen and Water⁸⁵

Property	Liquid Nitrogen	Water
Density kg/m ³	808.1 (77.2 K)	1000
Thermal Conductivity (W/m K)	0.141 ⁵⁴	0.574
Specific Heat (J/kg K)	1987 (64-76 K)	4182 (293 K)
Boiling Point (K)	77.2	373
Heat of Vapourization (J/kg)	199,200	2,261,000
Heat of Fusion (J/kg)	25,500	333,800

TABLE 4.3

Thermal and Physical Properties of the Construction Materials Used for the Nitrogen Tubes⁸⁵

Properties	Al-2024	Glass	Graphite	Gallium
Composition	4.4% Cu, 0.6% Mn 1.5% Mg	81% SiO ₂ , 13% B ₂ O ₃ 2.2% Al ₂ O ₃ , 3.6% Na ₂ O	Mainly C	99.9999%
Density (kg/m ³)	2770	2230	1.68	5950
Thermal Conductivity (W/m K)	192.5	1.088	157.5	48.3
Specific Heat (J/kg K)	883	778.	771	377

4.3 EXPERIMENTAL VARIABLES

The independent variables and their respective ranges are summarized in the following table:

TABLE 4.4

Experimental Parameters

Variable	Range	Tube Material Investigated
Bath Superheat	0-80 K	Glass, Aluminum
Shell Thermal Conductivity	1-200 w/mk	Glass, Aluminum, Graphite and Gallium
Tube Diameter	5-30 mm	Glass, Aluminum
Tube Length	25 mm - 300 mm	Glass, Aluminum
Tube Orientation	Horizontal-Vertical ie 0-90°	Aluminum

4.4 EXPERIMENTAL PROGRAM

The purpose of the present low temperature study was to investigate as wide a range of variables as possible affecting volatile additions, to gain a more comprehensive understanding of how magnesium boils in hot metal. To this end the variables of bath superheat, and the aspect ratio of the nitrogen containers were investigated for both the aluminum and glass containers. The aspect ratio is defined for axisymmetric shapes by Clift et al.⁶² as 'the ratio of the length projected on the axis of symmetry to the maximum diameter normal to the axis'. For a cylindrical shape, the axis of symmetry is the axis associated

with the length of the cylinders. The maximum 'diameter' normal to this axis corresponds to the cylinder's diameter, hence the aspect ratio for the nitrogen containers is l/d . In studying various aspect ratios, either length or diameter was kept constant while the other was varied.

For tests independent of the aspect ratio, several combinations of containers were used. For the experimental investigation of the effects of bath superheat, container geometry and container thermal conductivity; the various containers used are summarized below:

<u>VARIABLE</u>	<u>Aluminum</u>	<u>Glass</u>	<u>Graphite</u>	<u>Gallium</u>
Superheat	200 x 20mm*	190 x 23mm	-	-
Thermal Conductivity	200 x 20 mm	200 x 19mm	200 x 18mm	190 x 20mm
Tube Orientation	200 x 10mm	-	-	-
Tube Length	200 x 10mm	-	-	-

* $l \times d$

The majority of these tests used containers approximately 200 x 20mm. This size was chosen as it is identical to the aluminum bullets presently used by Sumitomo Metal Industries.^{9,46} The smaller size was selected for the orientation and length tests as the reaction was calmer and facilitated experimental observations. The glass tubes had an extra advantage in that they permitted the inside of the tube to be viewed during vapourization.

4.5 ANALYSIS OF THE EXPERIMENTAL DATA

In the study of bubbling reactions, three critical parameters can be identified: gas flow rate, bubble volume and bubble frequency. At least two of these variables must be measured if the third is to be deduced. As outlined by Kumor and Kuloor⁶⁰ there are two techniques for evaluating bubble volume: the direct and indirect methods.

Direct methods involve photography in one form or another. For aqueous systems cinephotography is commonly used while x-ray cinephotography is used in systems with opaque fluids. The main advantage of this technique is that it allows direct observation of each and every bubble and the option of following the growth and development of a particular bubble. The fact that the bubble volume is not measured directly and that the technique is very labourious are among its main disadvantages.

Indirect techniques are the simplest, and hence the most extensively used methods for evaluating bubble volumes at single orifices. These techniques involve measuring the gas flow rate and bubble frequency. The two big drawbacks of the indirect method are that only an average bubble volume is obtained and that no information concerning the bubble shape and hence its surface area are found.

Since the present study concerns itself with the boiling of an unstable volatile liquid, indirect methods of analysis could not yield the precise values of flow rate needed. This was the main motivating force behind using a direct technique.

The photographic method enabled the bubble volumes and the gas flow rates to be deduced from direct measurements of bubble diameter and frequency. The bubble diameter was measured just as the fully developed bubble lifted off the tube. This corresponded to a distance above the top of the tube opening equal to about half an average bubble diameter. Some typical bubbles are shown in Figure 4.5 for a glass tube.

In many tests the boiling of the nitrogen gas was very turbulent, causing bubbles forming at the nozzle tip to occur in cycles of two and three bubbles. The cycle usually involved one large bubble followed by smaller more turbulent bubbles. In many experiments these secondary effects were ignored due to the difficulty of evaluating precise bubble sizes and hence volumes.

The scaling factor for each experiment was based on a comparison of each tube's outer diameter, as measured on the video screen, to its actual value. By measuring the tube diameter at the tube opening an accurate reference for calculating the bubble diameters was established. This was thought to be the best approach since both reference and subject incurred similar visual distortions due to their close proximity.

The eccentricity of the bubbles was estimated for each experiment by taking a trace of approximately five bubbles and evaluating the eccentricity of this sample. The bubbles were assumed to be circular in the x-y plane and elliptical in the x-z plane, i.e. an ellipse in the x-z plane and rotated about



(a) $t = 0$



(b) $t = 48 \text{ ms}$



(c) $t = 216 \text{ ms}$

Figure 4.5 Typical Bubble Formation During the Vaporization Process.



(d) $t = 352$ ms



(e) $t = 464$ ms



(f) $t = 560$ ms

Figure 4.5 (cont.)

the z-axis. Such an analysis yields a bubble which is an oblate ellipsoid. Both oblate and prolate ellipsoids are shown in Figure 4.6.

For the purposes of comparison with other work, the equivalent bubble diameter must be calculated. This value corresponds to the diameter of a sphere of equivalent volume as the measured bubble. The equivalent diameter can be obtained from the bubble diameter and eccentricity as follows:

Considering the general equation of an ellipsoid:

$$\frac{x^2}{a^2} + \frac{y^2}{b^2} + \frac{z^2}{c^2} = 1 \quad (4.1)$$

For an ellipsoid which is circular in the x-y plane $a = b = 1$, hence, for the ellipse in the x-z plane the equation simplifies to:

$$x^2 + \frac{z^2}{c^2} = 1 \quad (4.2)$$

The aspect ratio of an ellipse rotated around the z axis as previously defined is:

$$E = c/a$$

$$\text{but } a = 1$$

$$\text{hence } E = c$$

Considering the volume of an ellipsoid:

$$V = \pi/6 (abc) d^3 \quad (4.4)$$

$$\text{but } a = b = 1 \text{ and } E = c$$

$$\text{hence } V = \pi/6 E d^3 \quad (4.5)$$

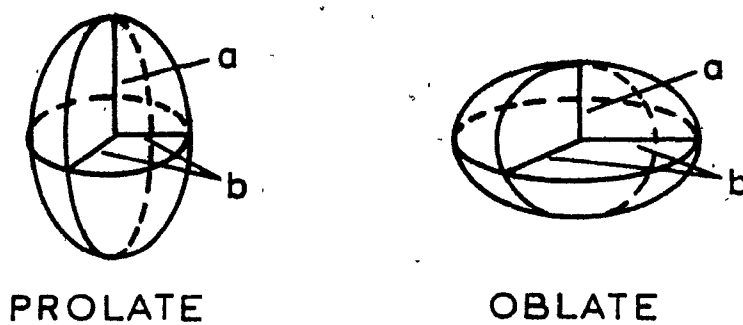


Figure 4.6 Oblate and Prolate Ellipsoids.

Comparing this to a sphere of equal volume:

$$\pi/6 d_e^3 = \pi/6 E d_b^3 \quad (4.6)$$

$$d_e = E^{1/3} d_b \quad (4.7)$$

Once the average value of the aspect ratio was calculated from the sample bubble traces, the equivalent bubble diameter was evaluated using equation 4.7.

CHAPTER 5

RESULTS

5.1 INTRODUCTION

In presenting the results of this study, Chapter 5 has been divided into three main sections. The first part of the chapter will deal with the experimental data while in the later parts, the results will be presented in both qualitative and quantitative fashions. The more obvious points will be discussed in this chapter to prepare for more detailed discussions in Chapter 6.

5.2 EXPERIMENTAL DATA

To familiarize the reader with the type of experimental data recorded, that from a typical experiment is presented in Table 5.1. Since the final results of this study yield some 100 similar data sets (based on 47 experiments) it was impractical to publish all the raw data in this thesis. The experimental data and original video tapes remain available in the research files of the Department of Mining and Metallurgical Engineering of McGill University (c/o Professor R.I.L. Guthrie). Figures 5.1 and 5.2 show other typical results obtained for different test conditions.

TABLE 5.1

Data from Experiment 12c - An aluminum tube of an inner diameter = 10.0 mm immersed with water at a superheat of 81 K

Starting Time of the Video Tape - 13:30:59 (min:s:s/100)

Time of Bubble Release	Bubble Diameter (mm)	Time of Bubble Release	Bubble Diameter (mm)
13:30:89	48	13:34:70	34
13:31:04	29	83	36
13	31	98	39
21	26	13:35:11	30
29	30	24	35
36	20	40	32
63	29	55	29
81	28	70	35
93	25	83	32
13:32:03	31	98	29
13	29	13:36:15	36
21	22	28	28
31	31	43	31
43	25	60	24
54	25	73	26
70	36	90	23
83	24	98	22
13:33:03	38	13:37:07	23
18	28	13	18
31	37	25	27
48	30	47	22
63	29	68	23
80	28	78	23
95	39	87	24
13:34:03	33	13:38:07	25
18	37	22	28
38	35	39	30
53	37	59	27
13:38:77	35	13:44:43	20
92	31	53	20
13:39:05	21	64	22
25	24	88	14
35	22	13:45:03	14
52	19	23	13
69	21	39	23
87	22	59	25

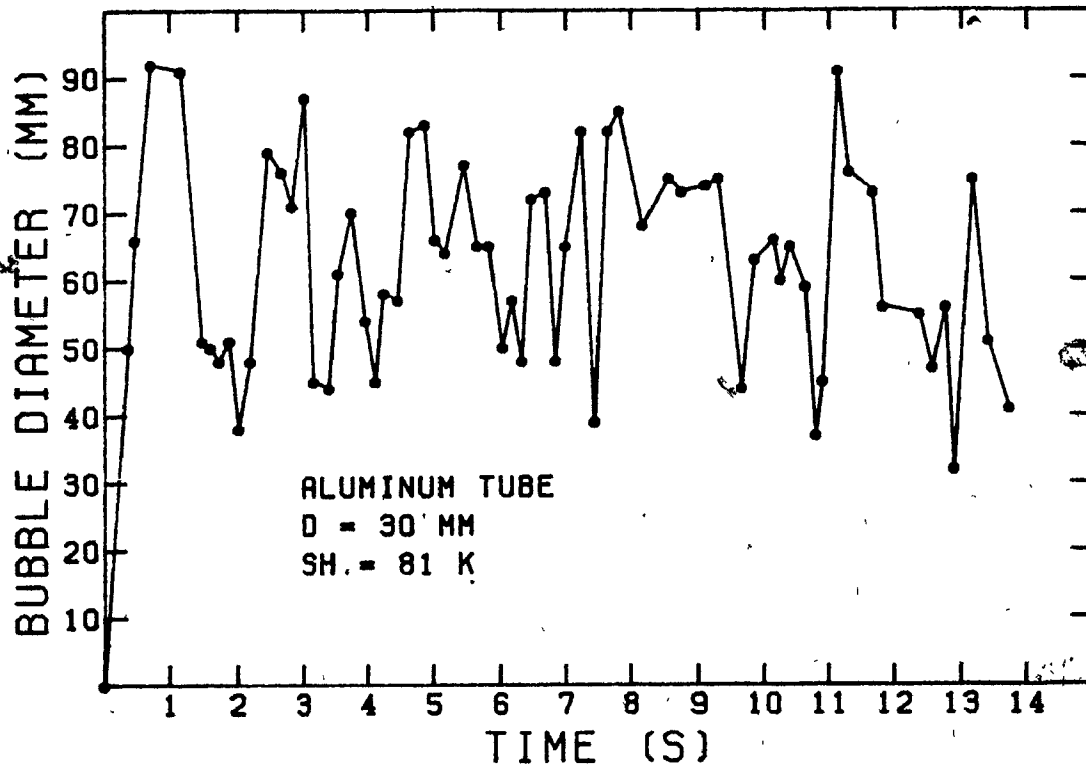
continued...

TABLE 5.1 continued

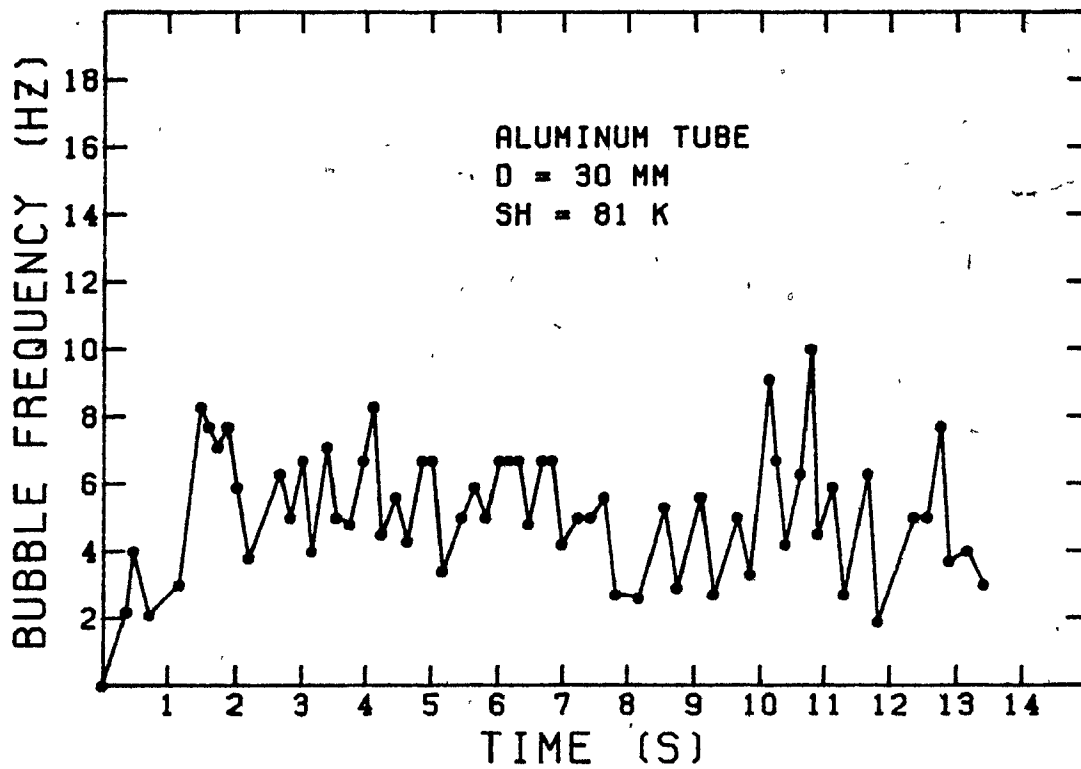
Time of Bubble Release	Bubble Diameter (mm)	Time of Bubble Release	Bubble Diameter (mm)
13:40:00	20	79	23
17	22	94	20
30	20	13:46:03	18
40	23	11	20
55	22	21	20
75	24	24	19
94	29	39	19
13:41:17	18	49	20
22	20	56	19
36	22	66	22
51	22	74	14
72	27	84	25
94	32	13:46:16	21
13:42:09	30		
27	26		
46	25		
64	25		
82	25		
13:48:01	21		
26	19		
37	18		
47	24		
56	25		
76	16		
83	18		
93	15		
13:44:01	12		
09	22		
18	19		
26	19		
34	18		

$$\bar{f} = 7.09 \text{ Hz}$$

$$\bar{d} = 28.3 \text{ mm}$$

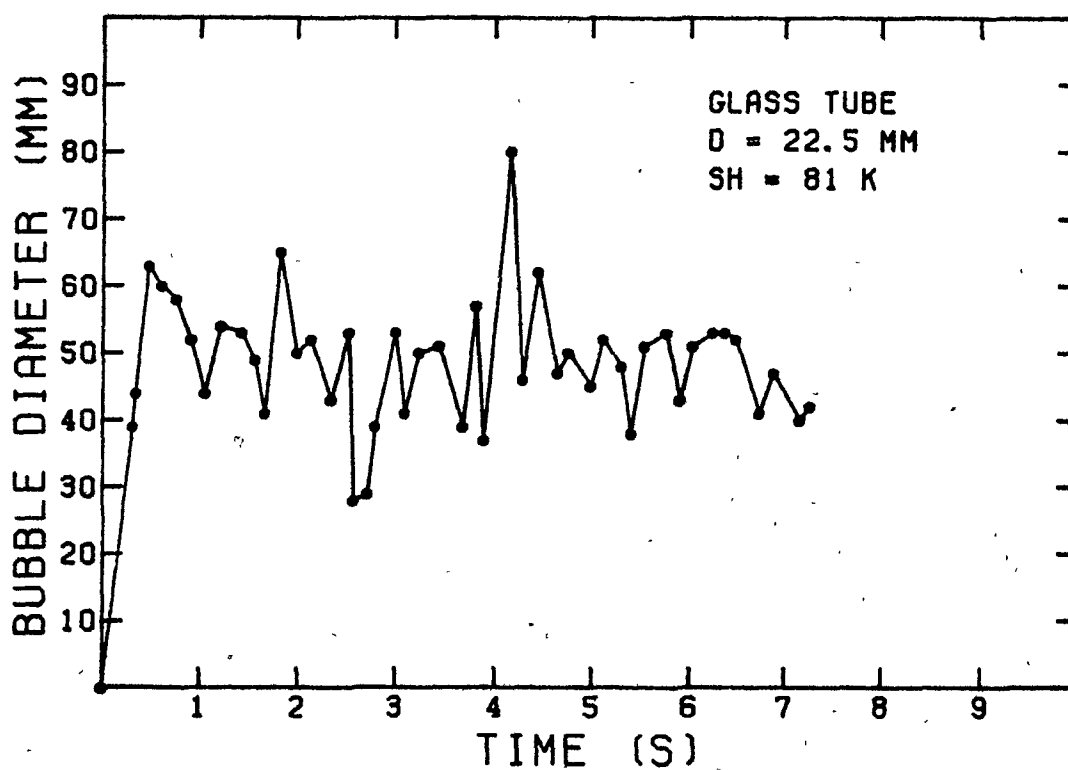


(a) Bubble Diameter Plot.

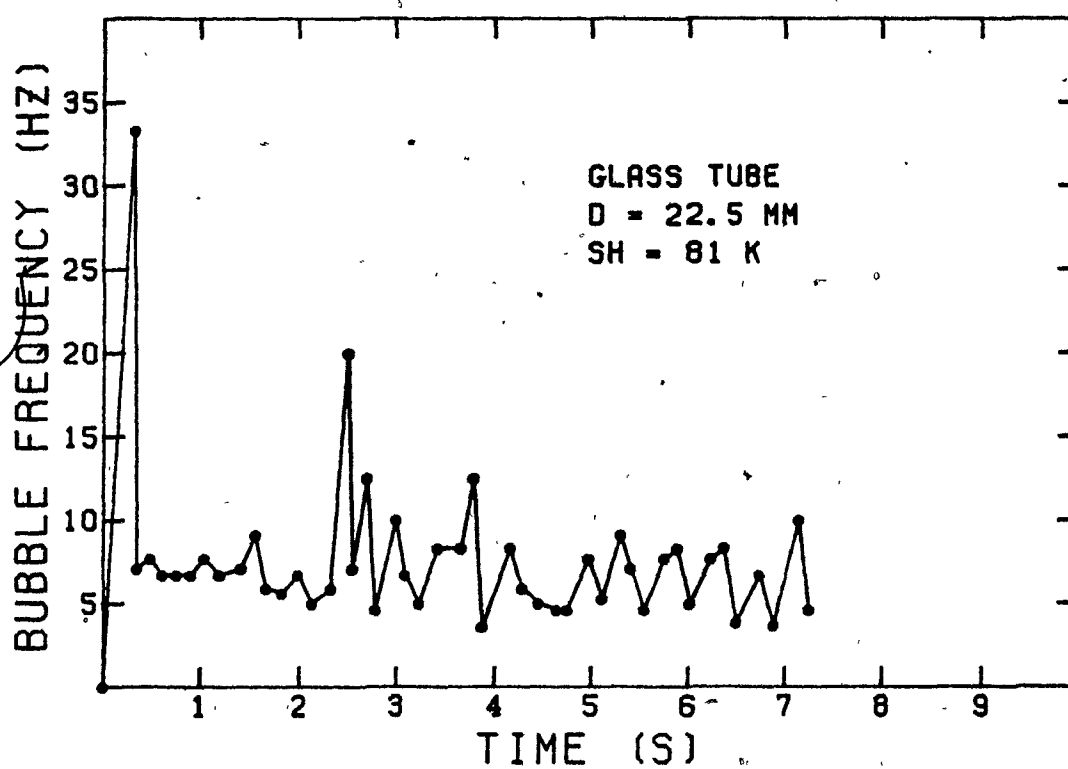


(b) Instantaneous Bubble Frequency Plot.

Figure 5.1 Experimental Results for Test 13c.



(a) Bubble Diameter Plot.



(b) Instantaneous Bubble Frequency Plot.

Figure 5.2 Experimental Results for Test 7a.

5.3 RESULTS: QUALITATIVE

In presenting a qualitative description of the results the boiling phenomena will be highlighted from a mechanistic viewpoint. A boiling mechanism will be introduced here and further supported later in the thesis. Individual experiments will show that the mechanism holds true in each case and that it is the magnitude and duration of each stage that changes the overall results from experiment to experiment. The majority of the qualitative results will be presented for the glass tubes as they enabled the boiling reaction inside the tube to be seen. The same points highlighted for the glass tubes also hold true for the aluminum and graphite tubes. The differences between these tubes will be presented in greater detail in a qualitative analysis of the results. The results of the test using the gallium tube were both surprising and spectacular and as such they will be presented separately at the end of this section.

5.3.1 Initial Period: Tube Immersion and Initial Turbulence

As each tube is immersed in the water there is a rapid burst of nitrogen gas due to the large initial heat flux to the liquid nitrogen. During this stage, gaseous nitrogen leaves the tube in a jet like fashion. The gas flow quickly becomes less turbulent and discrete bubbles begin to form. Although this initial turbulence only lasts for a very short length of time (<1 s), a large quantity of gas can be expelled. It is

difficult to estimate how much of the total gas produced in each experiment is ejected during the period of initial turbulence. Experiments presented in the next chapter indicated that between 30% and 70% of the total gas evolved can be produced during this initial period.

A typical sequence of photographs for a glass tube ($d = 22.5$ mm) characterising this rapid ejection is shown in Figure 5.3. Figures 5.4 and 5.5 give the same sequence for two of the aluminum tubes.

5.3.2 Mid-Period: Steady State Boiling

Once the initial turbulence has subsided, discrete bubbles are regularly formed. The bubbles form in a cyclic fashion producing double bubbles more commonly known as doublets. Bubble traces for the common double bubbles, pairs and doublets as summarized by Irons and Guthrie⁷⁹ are shown in Figure 5.6. The photographic sequence shown in Figure 5.7 for an aluminum tube ($d = 20.0$ mm) shows the nature of the double bubbles formed in the liquid nitrogen/water system. The experiments done for the study are under the same conditions that Irons and Guthrie⁷⁹ propose for doublets to form. The chamber volume for the boiling liquid nitrogen is effectively zero and the measured flow rates are moderate to high (100 - 1000 ml/s). Figure 5.8 shows the bubble development for a glass tube ($d = 22.5$ mm). In all cases the steady state bubbling, once established, continued until all of the liquid nitrogen vaporized.

(a) $t = 0$ (b) $t = 52 \text{ ms}$

Figure 5.3 Initial Burst of Nitrogen as a Glass Tube ($d_t = 22.5 \text{ mm}$) is Plunged into Water ($SH = 80 \text{ K}$).



(c) $t = 88 \text{ ms}$

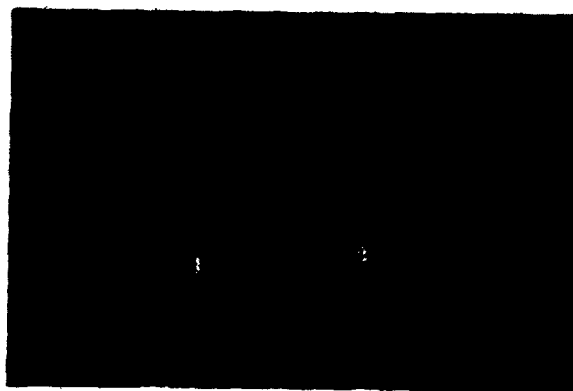


(d) $t = 196 \text{ ms}$



(e) $t = 298 \text{ ms}$

Figure 5.3 (cont.)



(f) $t = 376 \text{ ms}$



(g) $t = 444 \text{ ms}$



(h) $t = 584 \text{ ms}$

Figure 5.3 (cont.)



(a) $t = 0$



(b) $t = 188 \text{ ms}$

Figure 5.4 Initial Burst of Nitrogen as an Aluminum Tube ($d_t = 20.0 \text{ mm}$) is Plunged into Water ($SH = 40 \text{ K}$).



(c) $t = 248$ ms



(d) $t = 308$ ms



(e) $t = 416$ ms

Figure 5.4 (cont.)



(f) $t = 512 \text{ ms}$



(g) $t = 624 \text{ ms}$



(h) $t = 760 \text{ ms}$

Figure 5.4 (cont.)

(a) $t = 0$ (b) $t = 70 \text{ ms}$ (c) $t = 130 \text{ ms}$

Figure 5.5 Initial Turbulence when an Aluminum Tube ($d_t = 10.0 \text{ mm}$) is Plunged into Water ($SH = 80 \text{ K}$).



(d) $t = 200 \text{ ms}$



(e) $t = 230 \text{ ms}$



(f) $t = 270 \text{ ms}$

Figure 5.5 (cont.)



	Doublets	Pairs
Traces of High Speed Cinematography		
During Formation	First Bubble is Flattened or Toroidal, while Second is Elongated.	The Second Bubble becomes a Connecting Tube or "Tail" from the Orifice to the First One.
Cause	Reduced Pressure in the Wake of the First Bubble.	Residual Pressure in the Gas Chamber Upstream.
Characteristics	Each Bubble is 2-15% Larger than a Single Bubble. 2 Bubbles of the Same Volume which Coalesce during Rise. Frequently Revert to Single Bubbles.	The Pair has the Same Volume as a Single Bubble. The "Tail" Increases in Volume with Flowrate, and may become Detached. Under Some Conditions Can Revert to Single Bubbles.
Conditions	Small V_c . At Least Moderate Flow rates	Large V_c ($N_c > 10$). At all Flow rates.

Figure 5.6 Comparison of Doublet and Pair Bubbles with High Speed Cinematography Traces after Irons.⁶



(a) $t = 0$



(b) $t = 60 \text{ ms}$

Figure 5.7 The Formation of Double Bubbles at the Opening of an Aluminum Tube ($d_t = 20.0 \text{ mm}$, $SH = 40 \text{ K}$).



(c) $t = 84$ ms



(d) $t = 96$ ms



(e) $t = 108$ ms

Figure 5.7 (cont.)



(f) $t = 120$ ms



(g) $t = 148$ ms



(h) $t = 260$ ms

Figure 5.7 (cont.)



(a) $t = 0$



(b) $t = 44 \text{ ms}$

Figure 5.8 Bubble Development at the Opening of Glass Tube ($d_t = 22.5 \text{ mm}$,
SH = 80 K).



(c) $t = 72 \text{ ms}$

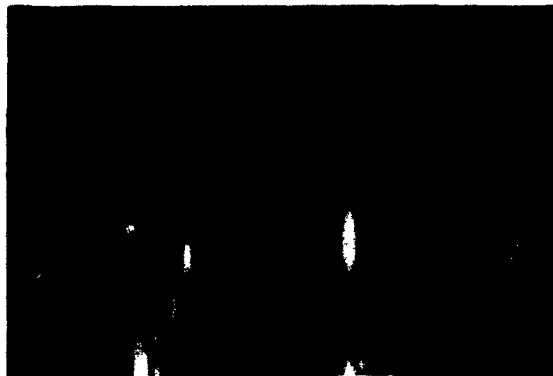


(d) $t = 88 \text{ ms}$



(e) $t = 112 \text{ ms}$

Figure 5.8 (cont.)



(f) $t = 116$ ms



(g) $t = 120$ ms



(h) $t = 136$ ms

Figure 5.8 (cont.)

5.3.3 End Period of Experiment - Displacement of the Boiling Phase

In experiments using the glass tube, events occurring inside the tube could be observed. One of the more important points which was noted is the countercurrent flow of water and nitrogen. As the boiling proceeds, a pool of water forms at the bottom of the tube. This pool grows, filling the tube and eventually displaces all of the boiling nitrogen in the tube. Figure 5.9 shows this sequence for a glass tube ($d = 22.5$ mm). The infiltration of water does not seem to effect the boiling nitrogen; once the nitrogen reaches the steady state boiling regime the boiling continues until all of the nitrogen is displaced. No noticeable change in the boiling could be observed at the onset of the countercurrent flow of water.

One key point which was experimentally observed was the existence of a critical diameter for the countercurrent flow of water. When the diameter of the glass tube was decreased to 10.0 mm there was no change in the mechanism, the displacement of the contents occurred in the same fashion as shown in Figure 5.9. However, when the diameter was reduced further to 5.0 mm, the mechanism of gas evolution changed. The results of this test are shown in Figure 5.10. The first two stages of the boiling mechanism still occurred, but infiltration of water was completely suppressed. The same result was observed in the experiments using the aluminum tubes. The existence of such a critical diameter is discussed in the next chapter.

(a) $t = 0$ (b) $t = 316 \text{ ms}$

Figure 5.9 Displacement of the Gaseous Phase for a Glass Tube ($d_t = 22.5 \text{ mm}$, $SH = 40 \text{ K}$).



(c) $t = 1552 \text{ ms}$



(d) $t = 1956 \text{ ms}$



(e) $t = 2792 \text{ ms}$

Figure 5.9 (cont.)



(f) $t = 3848$ ms



(g) $t = 5660$ ms



(h) $t = 6672$ ms

Figure 5.9 (cont.)

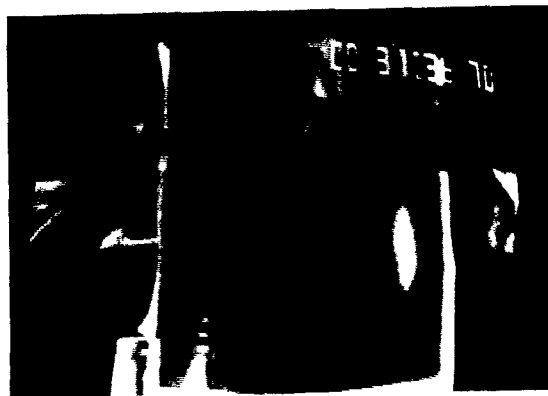
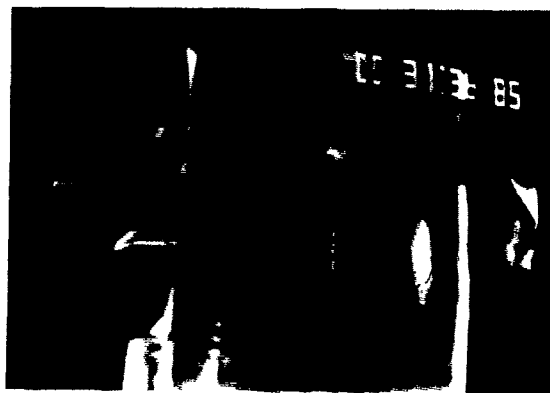
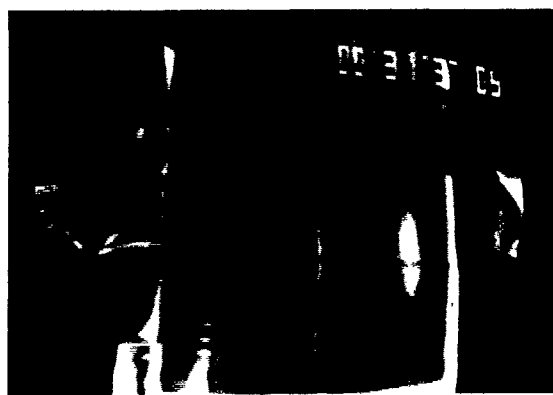
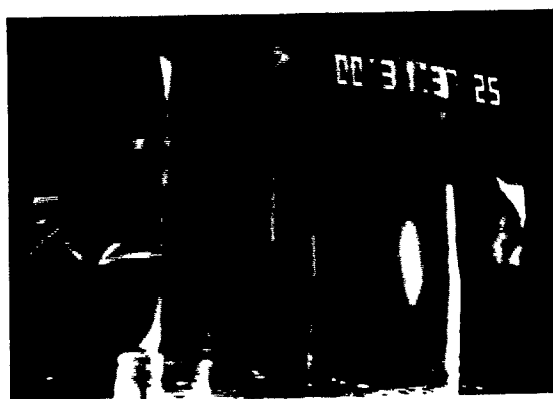
(a) $t = 0$ (b) $t = 0.15$

Figure 5.10 Gas Flow from a Small Diameter Glass Tube ($d_t = 4.6$ mm, SH = 80 K).



(c) $t = 0.35$

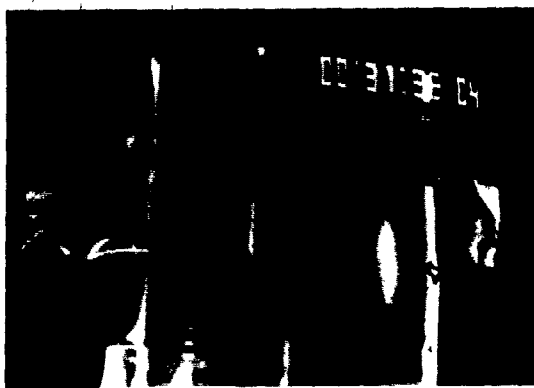


(d) $t = 0.55$

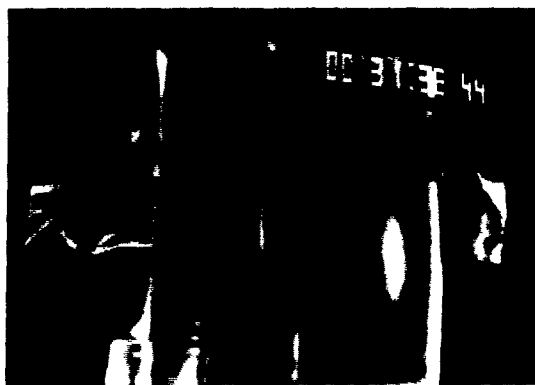


(e) $t = 0.99$

Figure 5.10 (cont.)



(f) $t = 1.34$



(g) $t = 1.74$



(h) $t = 3.36$

Figure 5.10 (cont.)

5.3.4 The Gallium Tube

The experiments with gallium shells were originally designed to simulate the performance of an encasing iron shell as it remelted. The gallium (m.p. 303 K) was cast into a half bullet shell using a lucite mold. The gallium tubes were filled with liquid nitrogen and then dropped into hot water (superheat 80 K). Unfortunately the gallium was not able to withstand the thermal shock of the rapid 280 K temperature change associated with the experiment and some leakage occurred. Shortly after contact with water, the tubes broke open prematurely at weak spots of the shell. A large amount of liquid nitrogen contacted water creating a huge gas column. This was caused by the rapid heating of the nitrogen through convective heat transfer from water. The events described are shown sequentially in Figure 5.11. This type of result shows the danger and potential inefficiency that may be incurred through a rapid release of the volatile addition, while in the liquid state. A more controlled release as shown in the previous section, is evidently more desirable for the safe efficient introduction of the volatile addition.

5.4 RESULTS: QUANTITATIVE

Through a quantitative analysis of the experimental data, the independent variables such as superheat and geometry could be more fully appreciated. Each experiment was used to provide a mean bubble diameter, mean bubble frequency and total reaction time characterizing that particular set of independent variables.



(a) $t = 0$



(b) $t = 96 \text{ ms}$



(c) $t = 158 \text{ ms}$

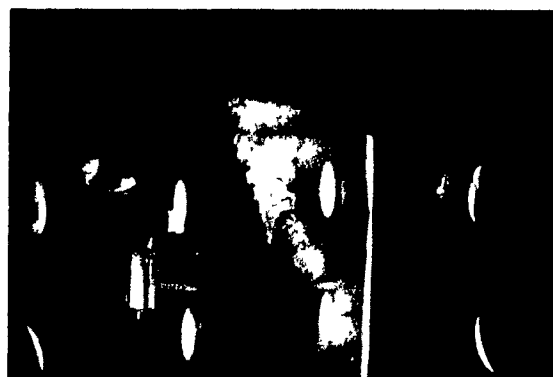
Figure 5.11 The Breakup of a Gallium Tube as it is Plunged into Water
(SH = 80 K).



(d) $t = 196 \text{ ms}$



(e) $t = 218 \text{ ms}$



(f) $t = 242 \text{ ms}$

Figure 5.11 (cont.)



(g) $t = 288$ ms



(h) $t = 320$ ms



(i) $t = 472$ ms

Figure 5.11 (cont.)

Adopting this approach allowed any large changes between the various experiments to be observed.

Before the equivalent bubble diameter or bubble volume could be calculated, the eccentricity of bubbles characteristic of the specified experiment had to be calculated as shown in Chapter 4, Section 4.5. For example, taking experiment 12c (see Table 5.1), the average bubble eccentricity was $\bar{E} = 0.68$, while the mean base diameter was $\bar{d}_b = 28.3$ mm. Using the relationship:

$$d_e = \bar{E}^{1/3} d_b \quad (5.1)$$

d_e for experiment 12c is,

$$\bar{d}_e = 24.9 \text{ mm}$$

and

$$\begin{aligned} \bar{V}_b &= \pi/6 \bar{d}_e^3 \\ &= 8.08 \text{ ml} \end{aligned} \quad (5.2)$$

This quantitative analysis was done in the same fashion for all experiments. The data sets and calculated result are correlated with the independent variables in Appendix A for all of the present experimental work. The results will be presented in order of the independent variables in the next five sub-sections.

5.4.1 Bath Superheat

Bath superheat was investigated over an 80 K range starting from zero superheat conditions. Results for the aluminum and

glass tubes are shown in Figures 5.12 and 5.13, respectively. As seen, equivalent bubble diameter varied with superheat in a linear manner, while bubble frequency remained roughly constant at 8 to 9 per second. Although there is some scatter for the frequency data points, regression analysis supports a slight frequency drop with increasing superheat. The correlation coefficients for Figures 5.12 and 5.13 are 0.22 and 0.16, respectively. This frequency drop gives the first clues as to the type of flow regime which describes the vaporization phenomena. If a 'constant frequency flow regime' as described by Davidson and Schuler⁶⁶ (see Chapter 3) is assumed, then the flow would be described by an equation of the form:

$$V_b = k Q^{1.2} \quad (5.3)$$

For bubbles forming at a submerged orifice:

$$Q = V_b f \quad (5.4)$$

but

$$V_b = k Q^{1.2}$$

hence

$$Q = k Q^{1.2} f$$

$$f = k' Q^{-0.2}$$

This implies that the frequency in the 'constant frequency regime' is in fact not constant but drops slightly with increasing flow rate. Interpreting increasing superheat as increasing the gas flow rate, then the observed frequency drop

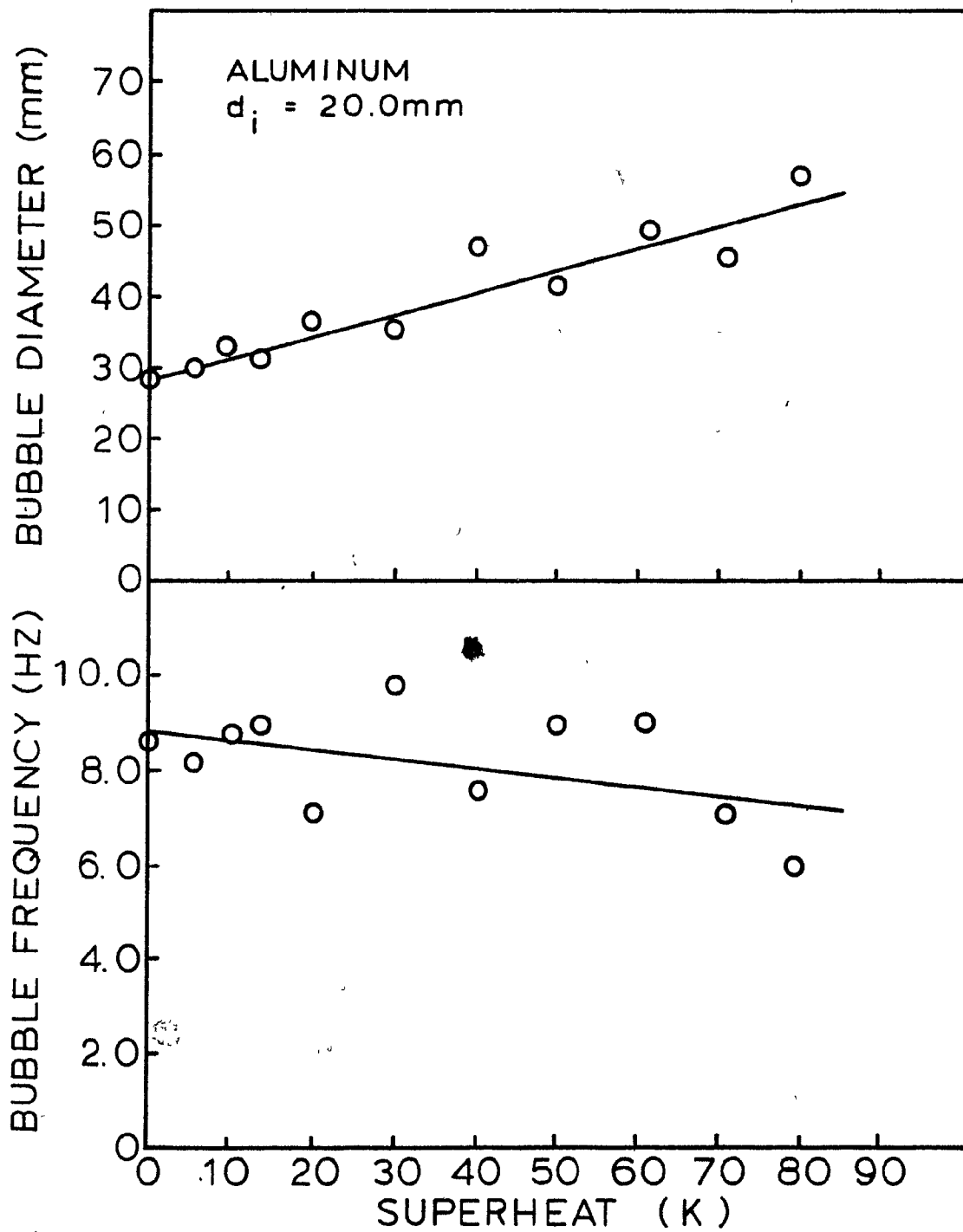


Figure 5.12 Effect of Increasing Bath Superheat on the Bubble Diameter and Frequency for an Aluminum Tube ($d_i = 20.0\text{ mm}$).

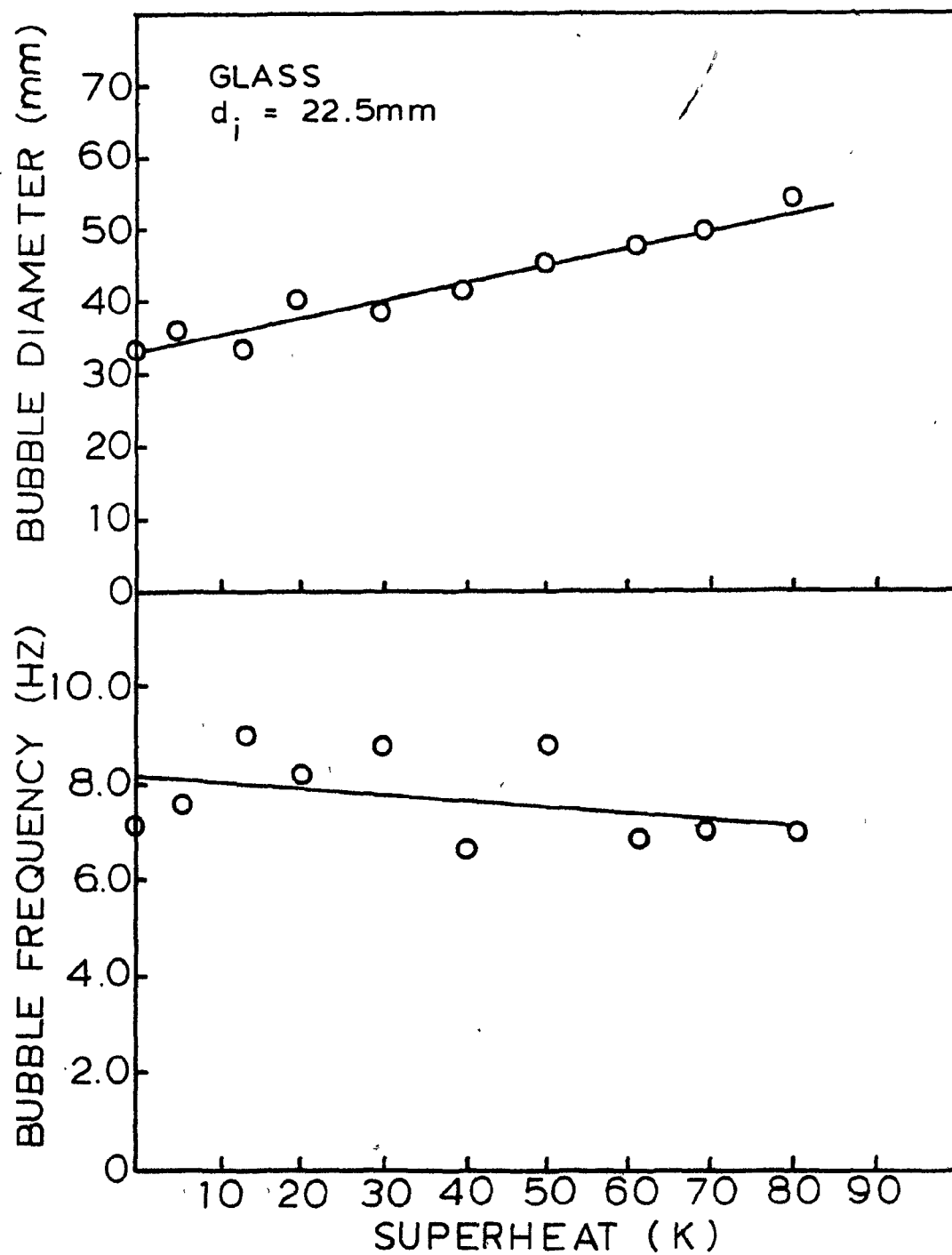


Figure 5.13 Effect of Increasing Bath Superheat on the Bubble Diameter and Frequency for a Glass Tube ($d_t = 22.5\text{ mm}$).

implies that flow is in the constant frequency regime. Further evidence for this is presented in Chapter 6.

5.4.2 Shell Thermal Conductivity

The high degree of similarity in the results between the glass and aluminum tubes noted in the previous section reflected the negligible effects of the shell thermal conductivity. If thermal conduction played a major role in the boiling phenomena, the aluminum tube should have yielded a much higher gas flow rate than glass since the heat conduction through aluminum is approximately 200 times better than that for glass. The similarity of Figures 5.12 and 5.13 indicate that on a qualitative basis, the gas flow from and hence the heat transfer to each tube are virtually identical. Visual observations were surprising in that liquid nitrogen contained within the aluminum tubes took longer to boil away, and appeared less violent, than for the same reaction using a glass tube.

Gas flow rates for the glass, aluminum and graphite tubes are compared based on their thermal conductivity in Figure 5.14. For this wide range of conductivity the gas flow rate is relatively constant at approximately 460 ml/s. The variation between the points can be attributed to their slightly different inner diameters. As described in Section 5.3.4, a bubble's diameter is generally influenced strongly by the diameter of the nozzle. From the data in Table 4.1, the progression in size for the tubes used in the present experiments is graphite (17.58 mm), glass (18.92 mm) and aluminum (20.00 mm). Since small changes

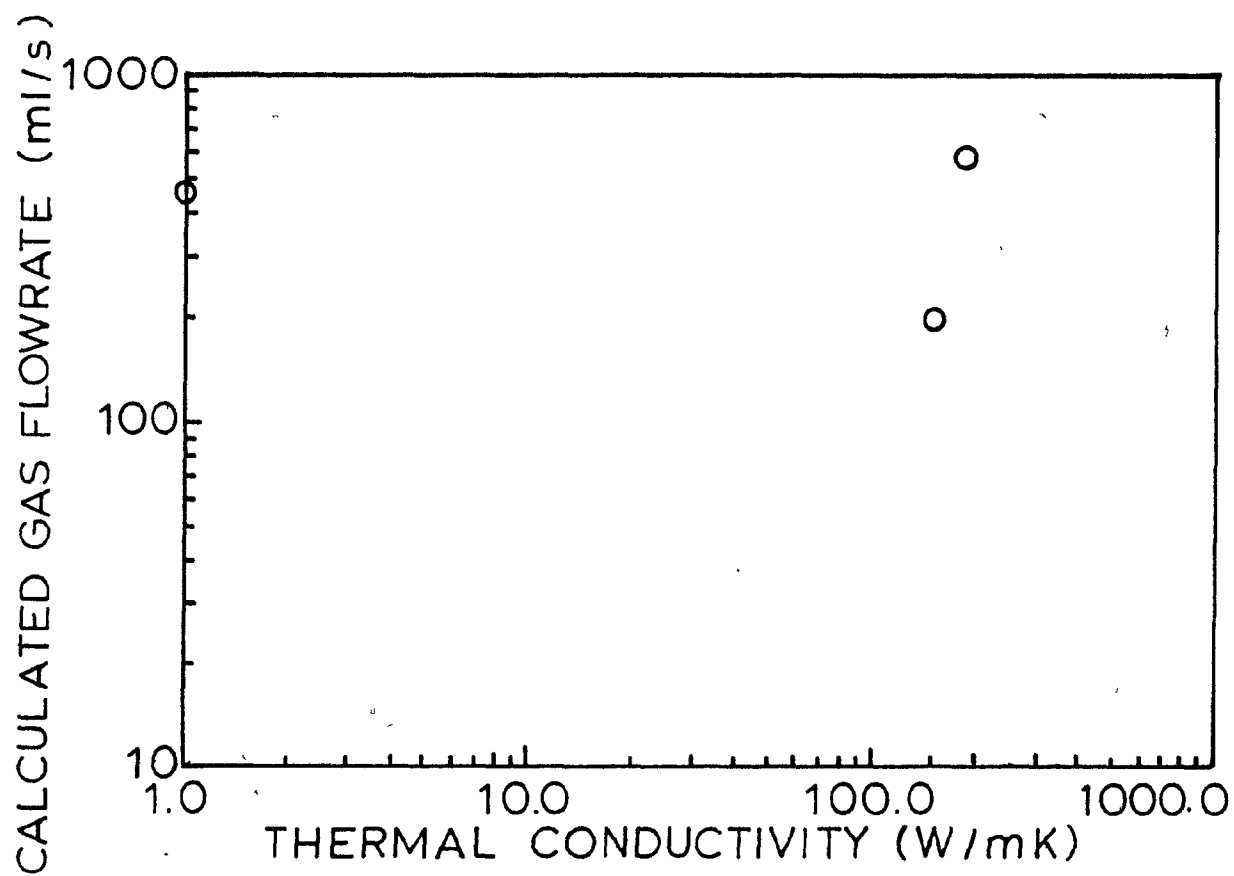


Figure 5.14 Nitrogen Gas Flow shown against Container Thermal Conductivity.

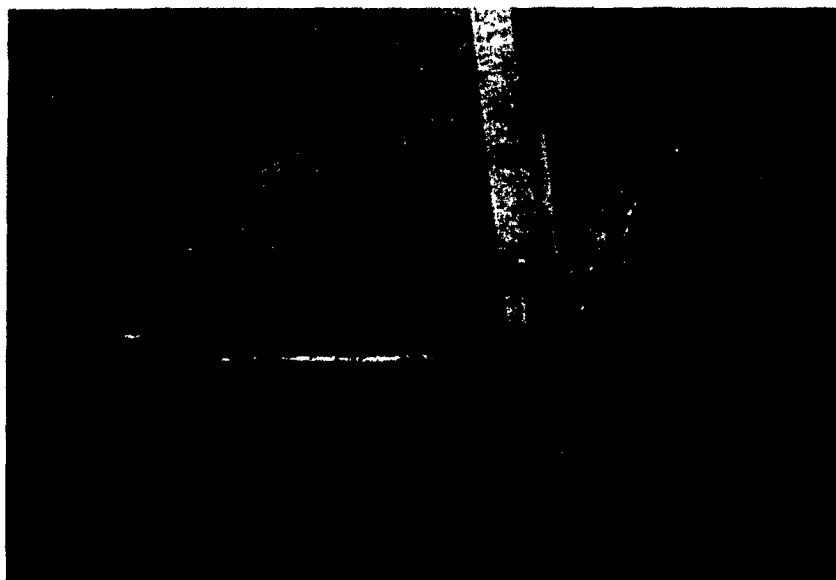
in the bubble diameter mean large changes in flow rate it is easier to appreciate the difference between the graphite ($Q = 350$ ml/s) and aluminum ($Q = 570$ ml/s) tubes. If the average bubble diameter for the graphite were increased from the measured value of 43.5 mm (Appendix A) to 47 mm the flow rate would increase to 440 ml/s. The average bubble diameters for the glass and aluminum tube are 48.2 mm and 57.0 mm, respectively. Based on these considerations the effect of thermal conduction through the shell walls can be neglected, the rate controlling step being some other mode of heat transfer.

The results from the gallium tube have not been included because of the results presented earlier. The gallium tube's early release of the nitrogen due to the lack of its integrity resulted in a very different type of bubbling system. For this reason the quantitative results for this test will not be included in this section.

In all tests below a superheat of approximately 60 K, an ice shell was formed over the exterior surface of the tube. Some typical ice shells and the corresponding conditions are shown in Figure 5.15. The formation of the low thermal conductivity ice shells ($k_{ice} = 2.25$ W/mK) did not cause any large discontinuities for the glass and aluminum boiling curves as per Figures 5.12 and 5.13. This is more evidence that the heat input to the boiling nitrogen via conduction through the tube walls is not rate limiting on the boiling process. It is felt that the freezing of the ice shell and the convective heat



(a) Superheat = 10 K



(b) Superheat = 40 K

Figure 5.15 Residual Ice Shells on a Glass Tube ($d_t = 22.5$ mm) after Plunging into Water.

transfer in the melt phase combine to satisfy the heat demand of the liquid nitrogen.

5.4.3 Shell Geometry: Diameter

In the first stage of studying shell geometry, the effect of tube diameter for both glass and aluminum tubes was investigated.

The results are summarized in Figures 5.16 and 5.17. In both cases there was a strong linear correlation between the equivalent bubble diameter and the tube or nozzle diameter. This is indicated by the values of the correlation coefficients shown for each curve. A surprising observation which remains unresolved is the drop in bubble frequency observed for the glass tubes. The implications of flow dependence on preferred bubble diameters are treated in the next chapter.

5.4.4 Shell Geometry: Length

As would be expected, the length of the tube or shell does not dramatically affect the bubbling characteristics. This was substantiated with the test results shown in Figures 5.18 and 5.19. The values of bubble diameter and frequency are essentially constant for this set of tests.

Due to the surprising behaviour of the small 5 mm diameter tubes, the length test was repeated using a set of these smaller tubes.

The most important point to note from these results shown in Figure 5.20 is the strong frequency drop associated with

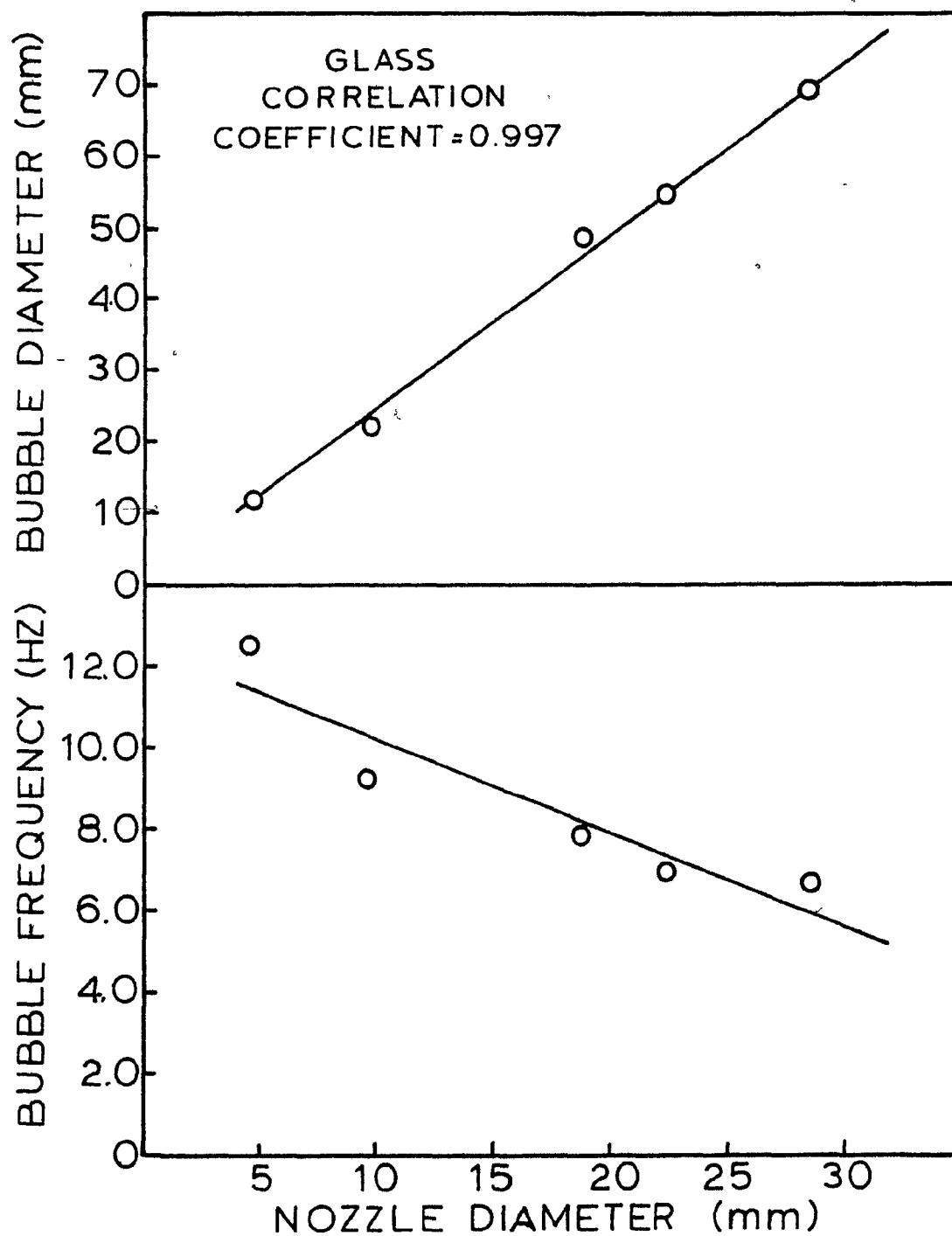


Figure 5.16 Effect of Increasing Tube Diameter on the Bubble Diameter and Frequency for a Glass Container (SH = 80 K).

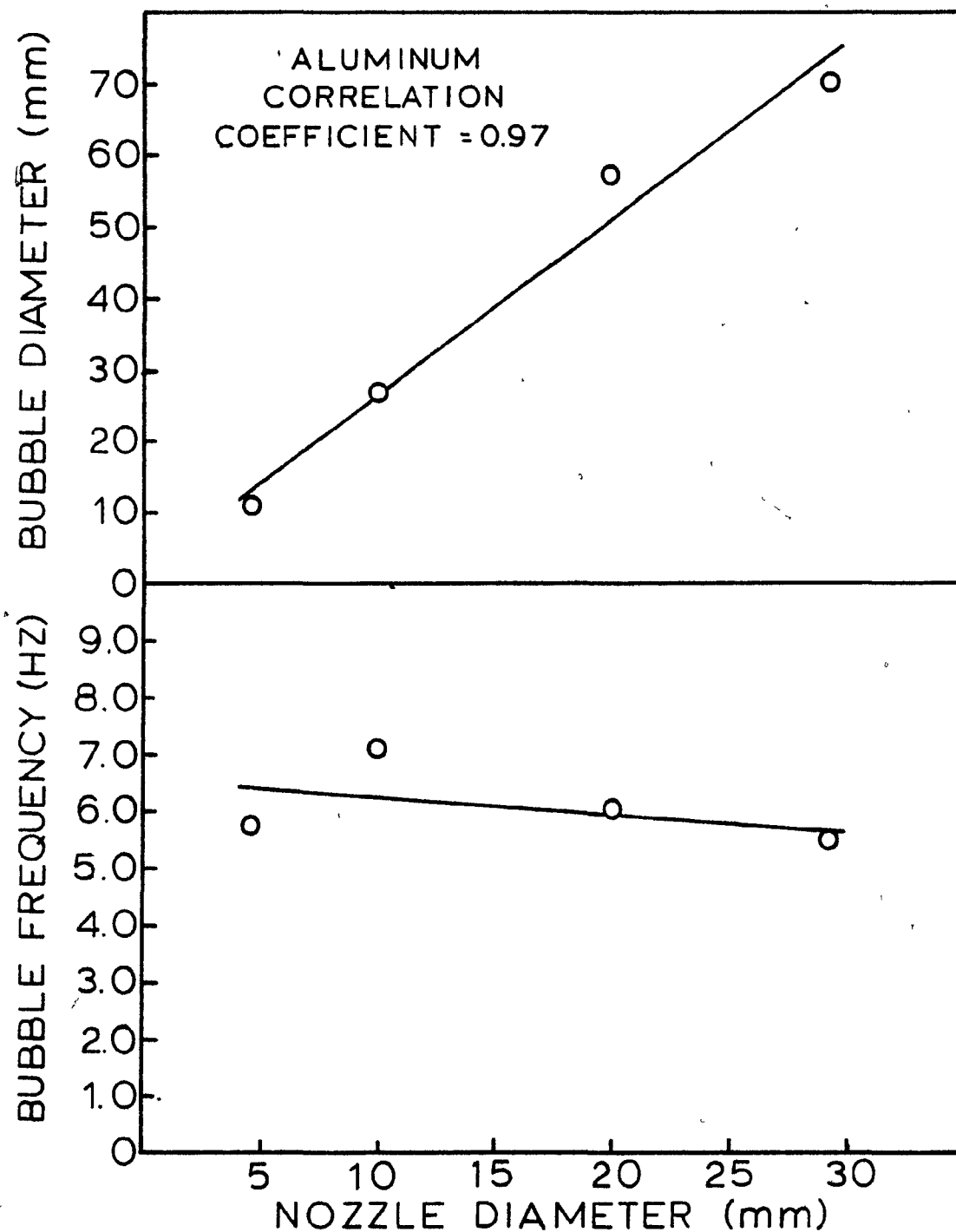


Figure 5.17 Effect of Increasing Tube Diameter on the Bubble Diameter and Frequency for an Aluminum Container (SH = 80 K).

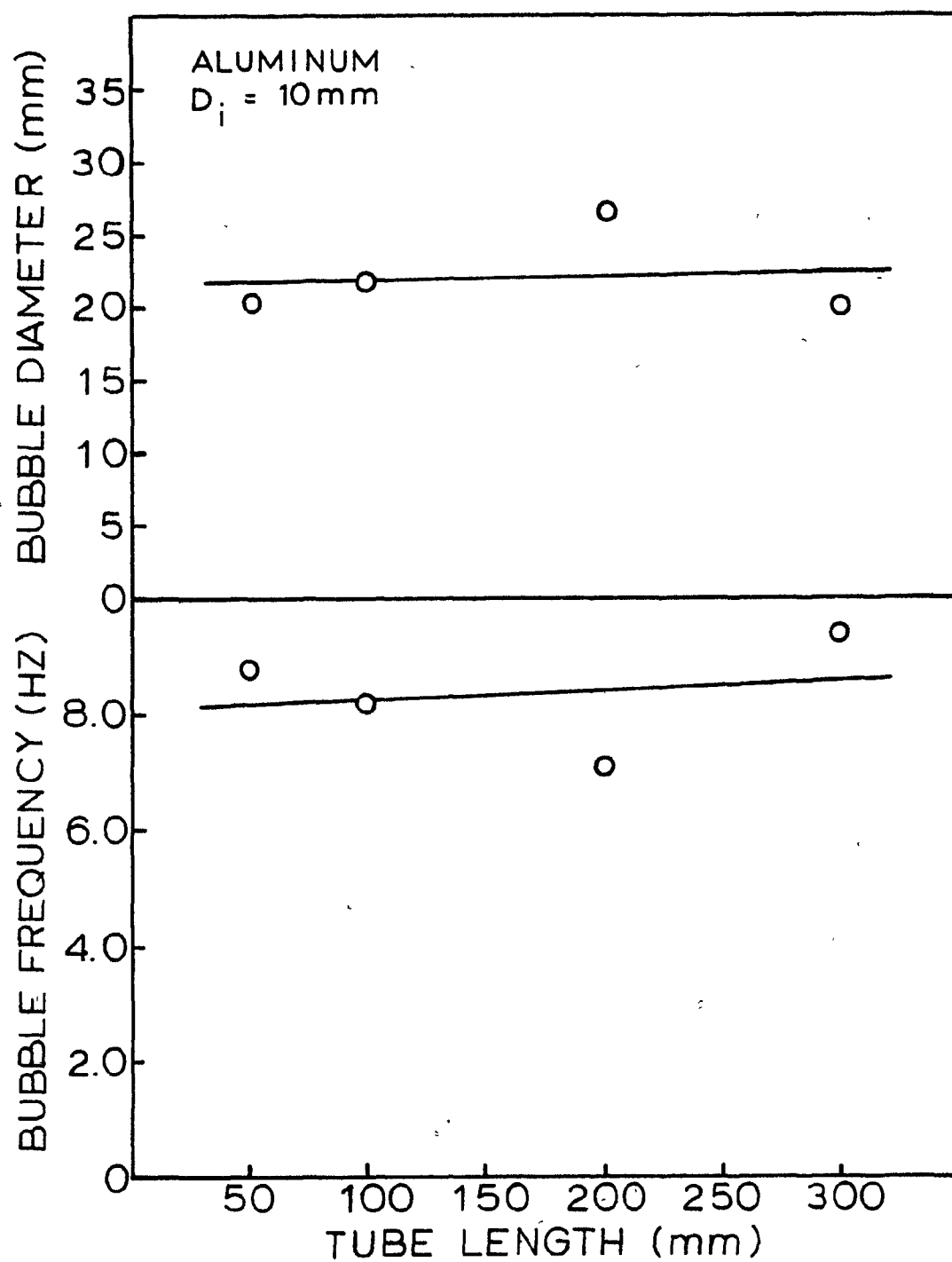


Figure 5.18 Effect of Increasing Tube Length on the Bubble Diameter and Frequency for an Aluminum Container ($d_t = 10 \text{ mm}$, $SH = 80 \text{ K}$).

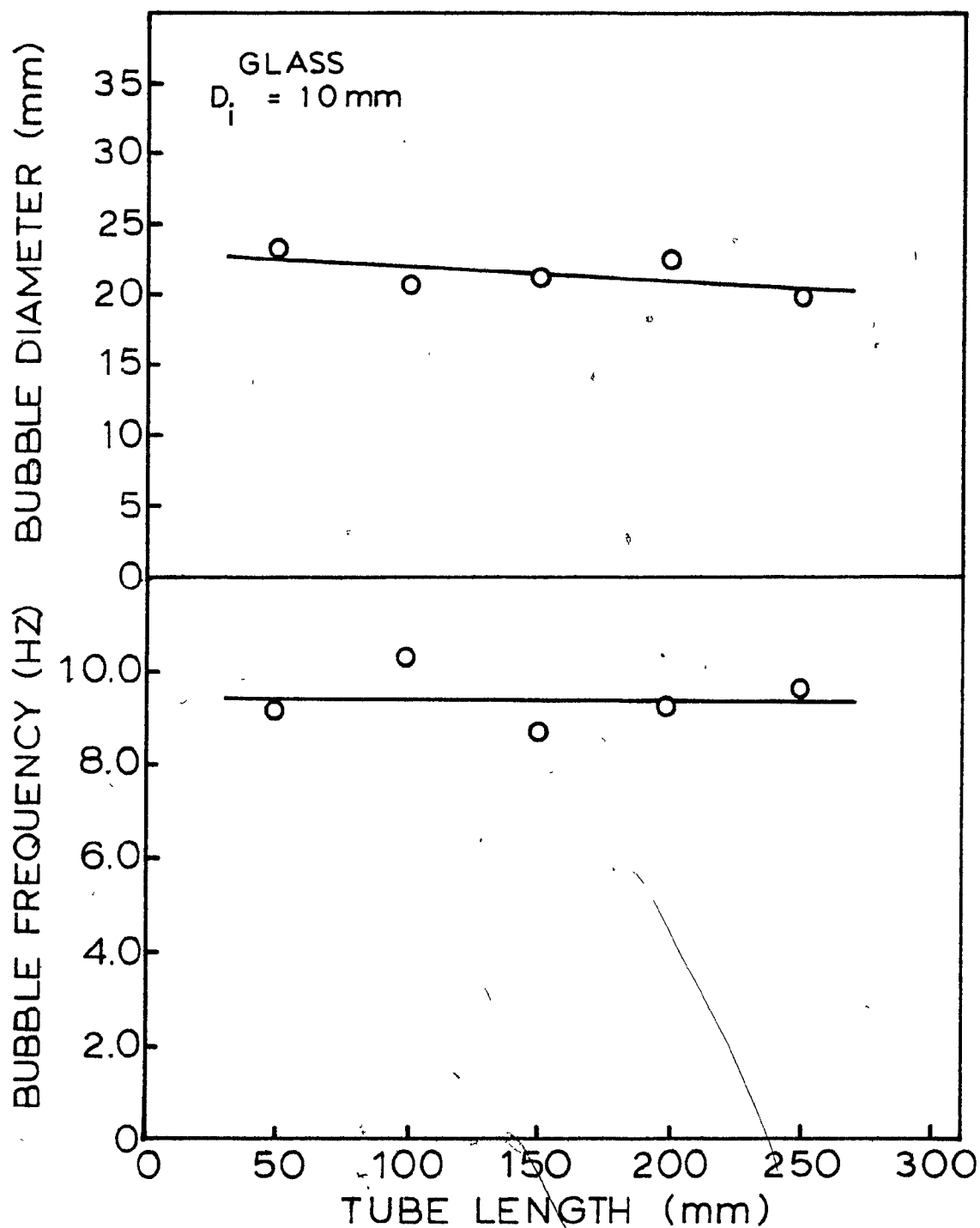


Figure 5.19 Effect of Increasing Tube Length on the Bubble Diameter and Frequency for a Glass Tube ($d_t = 10 \text{ mm}$, $SH = 80 \text{ K}$).

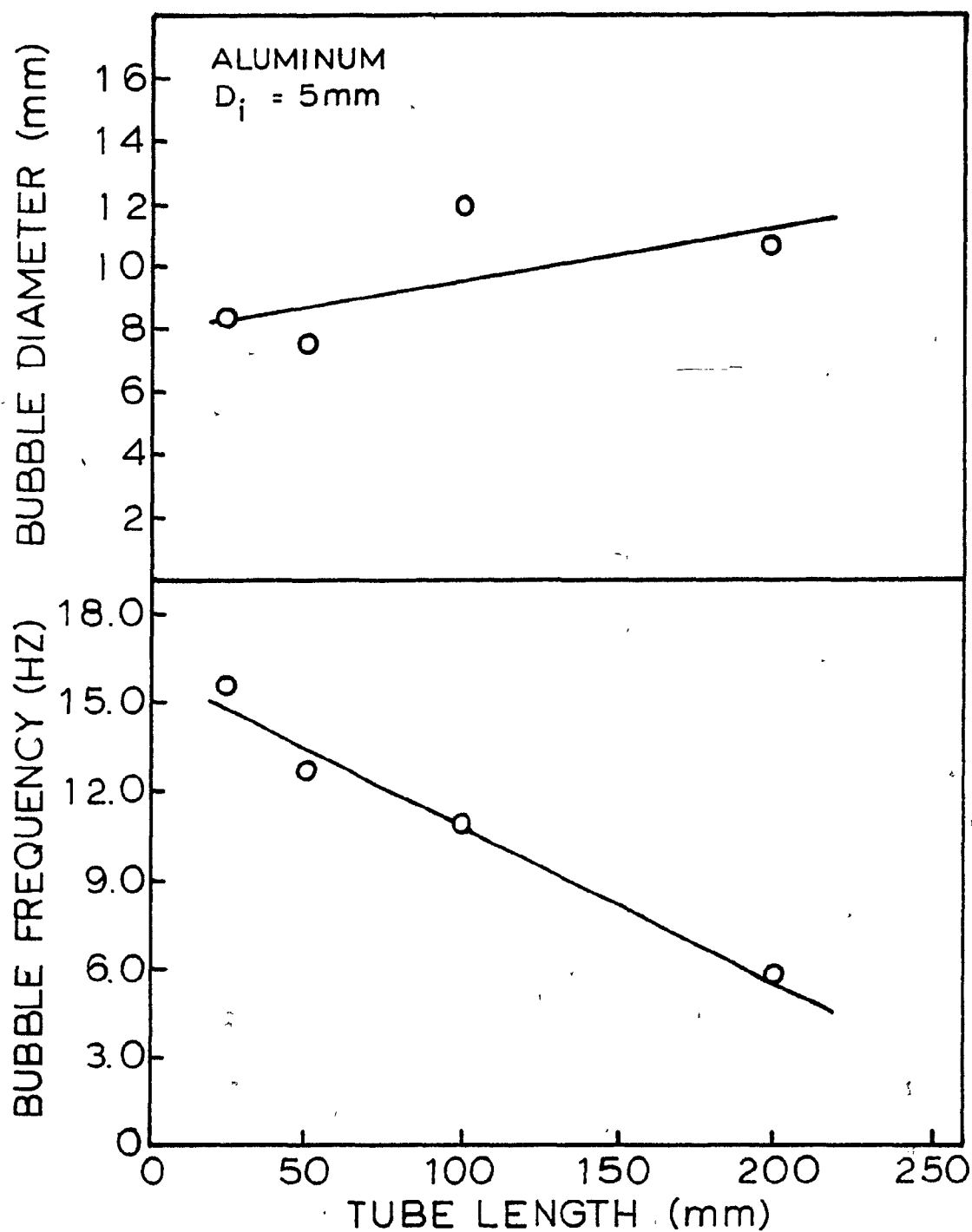


Figure 5.20 Effect of Increasing Tube Length on the Bubble Diameter and Frequency for a Small Diameter Aluminum Tube ($d_t = 5\text{ mm}$, $SH = 80\text{ K}$).

longer tubes. This drop can be correlated with the bubbling mechanism previously proposed in the qualitative section. As mentioned in that section, the last stage of the bubbling mechanism did not apply for the 5 mm diameter tubes, the frequency drop further supports this observation.

For very short tubes the entire gas evolution is primarily associated with the first stage of the mechanism, the rapid expansion and ejection of the gas. Since in this stage the boiling is similar to a low velocity jet, the measured bubble frequency is relatively high. As the tube length is gradually increased there is a greater amount of liquid nitrogen left in the tube after the initial period of turbulence has passed. This raises the total time for the steady state boiling step and consequently increases this step's contribution to the calculated average frequency. The result is as observed in Figure 5.20, a decreasing average frequency with increasing tube length.

The slight increase in bubble volume can also be explained in the same fashion. In steady state boiling, the bubbles are able to become fully developed and are consequently larger. As in the frequency case, the longer the steady state boiling step, the higher the average bubble volume.

5.4.5 Shell Geometry: Orientation

The last variable examined was the shell orientation. The nozzle angle was varied from the nozzle pointing vertically

upwards (90°) to the nozzle facing horizontally (0°). The results are summarized in Figure 5.21. These results again yield a constant frequency type behaviour but the gas flow rate shows definite maximum and minimum values. The interesting point to note is that the minimum flow rate occurs at $\theta = 0^\circ$ while the maximum is at $\theta = 15^\circ$. The slightest angle of inclination greatly enhances the infiltration of water into the tube. This speeds up the displacement aspect of the three stage bubbling mechanism. When the tube is in the horizontal position, the infiltration aspect is virtually eliminated and gas is expelled from the tube based solely on its own expansion characteristics. As the angle increases beyond $\theta = 15^\circ$, the bubbles leaving the tube can more effectively block the incoming water, reducing the speed of displacement. This blocking effect becomes constant at $\theta = 60^\circ$ as reflected by the constant bubble volumes seen in Figure 5.21. The net effect of the infiltrating water is very significant with an increase of 150% from the minimum to maximum values of gas flow rate. The maximum value at $\theta = 15^\circ$ is 100% higher than the corresponding value for the vertical case ($\theta > 60^\circ$). Clearly the near horizontal orientation will lead to the quickest release time for the boiling addition.

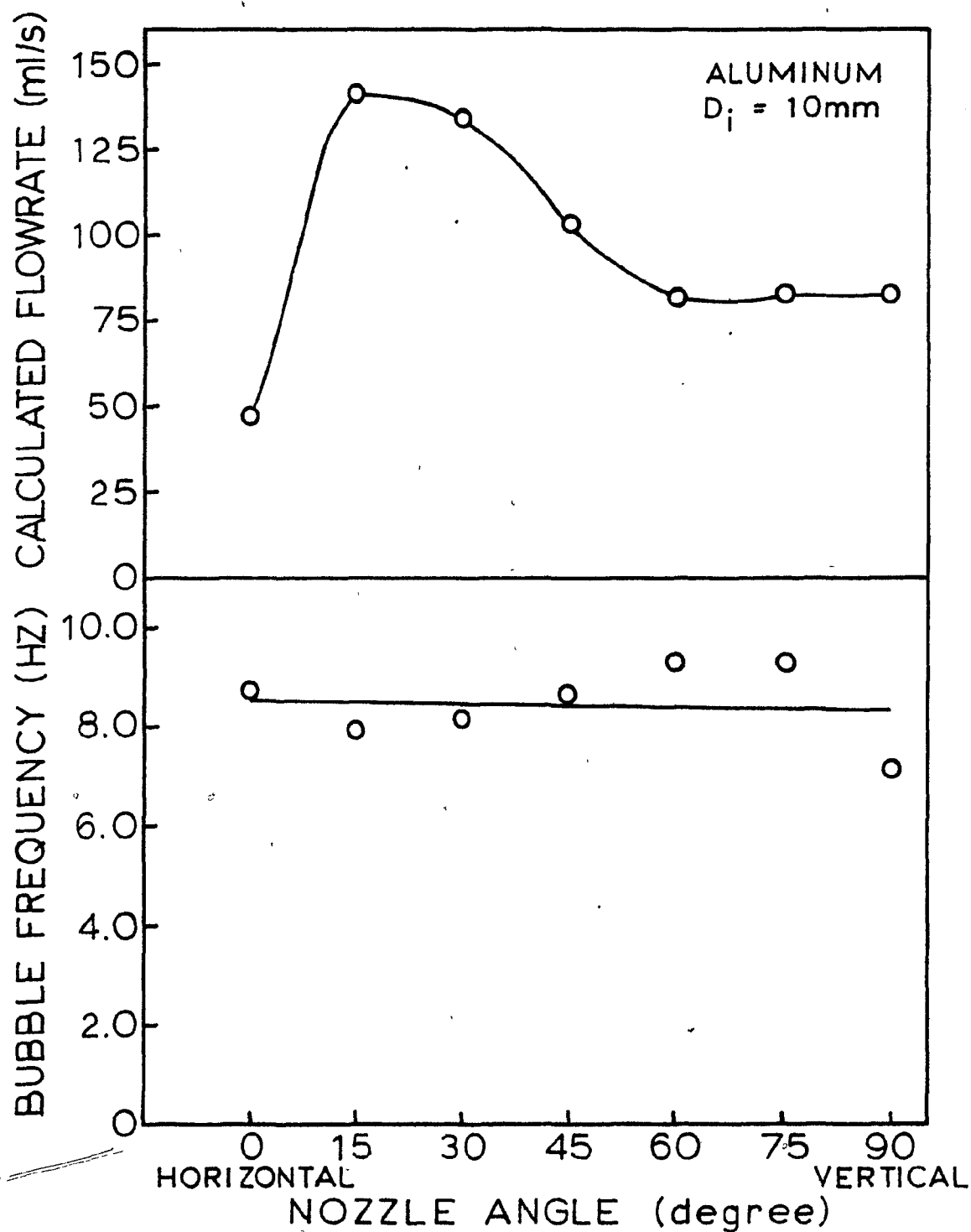


Figure 5.21 Effect of Tube Orientation on Bubble Frequency and Gas Flow Rate for an Aluminum Tube ($d_t = 10\text{ mm}$, $SH = 80\text{ K}$).

5.5 SUMMARY

The results of the study on the physical model have been presented. The qualitative description indicated that three unique steps were involved in the boiling process. A full discussion of these steps or stages is presented in Chapter 6. In the qualitative analysis, the effects of bath superheat, shell thermal conductivity and shell geometry were investigated. One of the highlights of these analyses was that the bubbling behaviour was independent of the thermal conduction properties of the shell material. Shell orientation and diameter had a strong effect on nitrogen gas flow rate. In the tube orientation experiment, a minimum flow rate was observed when the tube was horizontally held, while the maximum occurred with only slight positive inclination of the tube. Increasing nozzle or tube diameter showed a strong linear correlation with increasing bubble size.

As the bath superheat was increased, the gas flow rate showed a corresponding increase. This trend was similar for both the aluminum and glass tubes. This point was also reflected in the nozzle diameter test. The measured bubble frequency was constant for most of the tests with an average frequency in the order of 8 Hz.

CHAPTER 6

DISCUSSION

6.1 INTRODUCTION

As indicated in the last chapter, the following three step vaporization mechanism was postulated for the physical model:

1) As the addition begins to boil there is a rapid initial ejection of liquid and/or gas into the melt.

2) The boiling process then quickly reaches a less turbulent steady state which continues until the addition has completely vaporized.

3) Toward the end of the steady state boiling step the gaseous addition is displaced by the surrounding fluid.

The three stage mechanism was established through the visual observations presented in Chapter 5. In this chapter, discussion and qualification of the three stages is attempted. The resulting design implications of these findings on the magnesium/hot metal system is dealt with in the final chapter. To help understand the mechanisms involved, stages two and three are now described before concluding with an explanation for stage one.

6.2 STEADY STATE BOILING - STAGE TWO

The continuous formation of discrete bubbles at the tube opening was first confirmed by visual observations. Upon initiation, this stage of the boiling reaction continues at

a stable pace until all of the gaseous species has boiled off. Neither the formation of an ice shell nor the displacement of the gaseous phase by the surrounding water seemed to affect the size or rate at which the bubbles were generated. In fact, the frequency of bubble generation was very stable over the whole range of experiments. The average bubble frequency for all the experiments was 7.8 Hz with the majority of values falling between 7 Hz and 9 Hz. The indication that the flow describing steady state boiling falls in the constant frequency region was further substantiated by the bath superheat experiment.

6.2.1 Steady State Boiling: Heat Transfer

The similarity of boiling rates previously noted between the glass and aluminum tubes was confirmed when the gas flow rate from each tube was evaluated. Since there was no direct control of gas flow rate this variable could only be investigated indirectly. Controlling the bath superheat yielded the desirable range of gas flow rates which were required to properly evaluate the flow regime. The gas flowrate corresponding to each temperature was calculated from the bubble volume and frequency. These values were in turn plotted against the bubble volume to yield the curves shown in Figure 6.1. The similarity between these two curves further substantiates the observations cited in Sections 5.3.1 and 5.3.2.

Based on this and other observations, the effect thermal conduction has on controlling the rate of gas evolution can be regarded as negligible. The steadily increasing flow rate do

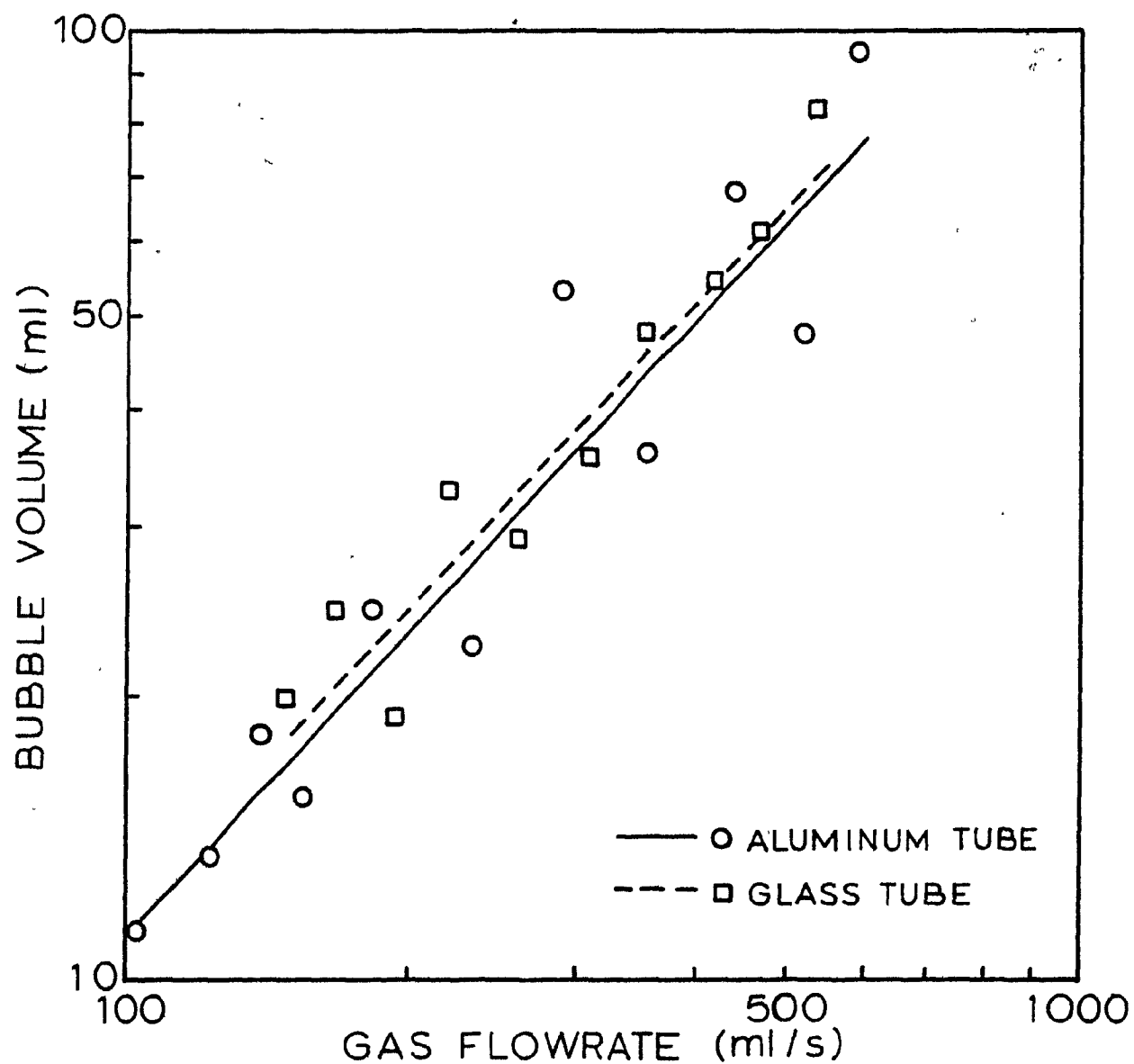


Figure 6.1 Effect of Increasing Gas Flow Rate on Bubble Volume (Glass Tube; $d_t = 22.5$ mm, Aluminum Tube; $d_t = 20.0$ mm).

however, confirm the influence of convective heat transfer on the overall process. As the superheat is varied over the 80K range the steady state flow rate increases from slightly greater than 100 ml/s to approximately 600 ml/s. Since the outside of the shell is assumed to be at 273K due to the formation of an ice shell, the driving force for convection is varied from approximately 0 K through to 80 K. At the lower temperatures, the heat demands of the nitrogen are partially satisfied from the heat of fusion released as an ice shell forms around the artificial shell. In the limiting case of no convective heat transfer (SH = zero), all heat is supplied from the freezing of ice. Consequently the two modes balance each other. With decreasing temperatures there is an increasing contribution from the heat of fusion of ice as the amount of heat transferred via convection is decreased.

Balancing the heat demands of the liquid nitrogen with the energy generated by ice formation, the maximum thickness of the ice shell that would form in the absence of any convective heat input from the bath can be evaluated. Therefore:

$$\rho_1 V_1 \Delta H_v = \rho_2 V_2 \Delta H_f \quad (6.1)$$

where ρ_1 = density of the liquid nitrogen

V_1 = volume of liquid nitrogen contained in tube

ΔH_v = heat of vaporization of liquid nitrogen

ρ_2 = density of ice

V_2 = volume of ice

ΔH_f = heat of fusion of ice

Since the ice thickness is much less than the diameter of the tube the total volume of ice can be estimated by:

$$V_2 = A_T \Delta r \quad (6.2)$$

where $A_T = 2\pi r_T l + \pi r_T^2$
 = area of cylinder plus bottom disc
 Δr = thickness of the ice layer

For the aluminum tube (20.0 mm inner diameter) near zero superheat the following values are substituted into equation (6.1).

$$\begin{aligned} \rho_1 &= 808.1 \text{ kg/m}^3 \\ V_1 &= 61.63 \text{ ml} \\ \Delta H_V &= 199.6 \text{ kJ/kg} \\ \rho_2 &= 900 \text{ kg/m}^3 \\ \Delta H_f &= 333.8 \text{ kJ/kg} \\ l &= 200 \text{ mm} \\ r_T &= 11.2 \text{ mm} \end{aligned}$$

Solving for V_2 ,

$$V_2 = \frac{\rho_1 V_1 \Delta H_V}{\rho_2 \Delta H_f} = 33.09 \text{ ml}$$

Solving equation (6.2) for the ice thickness yields $\Delta r = 2.3 \text{ mm}$.

Although the thickness of the ice layer was not measured precisely, visual estimations (see Figure 5.15) indicated shell thicknesses in the order of 2 mm. Hence, the freezing of the ice shell at low values of bath superheat can provide

most of the liquid nitrogen's heat requirements. The balance of the heat is supplied by natural convection. While an experimental condition of 0 K superheat was not attained, the lowest reached was 1-2 K superheat. This superheat, while small, provided the convective heat transfer component responsible for the balance of the heat requirements.

The continuity observed for the curves in Figure 6.1 illustrates that the heat requirements of the liquid nitrogen are continuously met. If the heat requirements cannot be supplied by convection, an ice shell will freeze on either the glass or aluminum shell to an appropriate thickness to satisfy the heat balance. As the bath superheat is increased the ice layer gets progressively thinner until approximately 60 K superheat when this shell no longer forms.

6.2.2 Classification of Flow Region

The linear curves of bubble volume versus gas flow rate shown in Figure 6.1 indicates that the steady state boiling phenomena takes place under conditions equivalent to the constant frequency region. The lines shown on the graph were generated by performing linear regressions on the experimental data. The correlation was excellent in both cases with the correlation coefficients equalling 0.91 and 0.92 for the aluminum and glass tubes, respectively. Due to the linear relationship between bubble volume and gas flow rate expressed in Figure 6.1, the results can be expressed by the following equation:

$$V_b = k Q^m \quad (6.3)$$

where V_b = equivalent bubble diameter

Q = gas flow rate

m = slope of the line

$k = 10^c$ where c = the y intercept.

For the glass and aluminum tubes, k and m were equal to 0.0814, 1.08 and 0.0691, 1.10, respectively. For comparison to the popular Davidson and Schuler⁶⁶ equation given in section 3.3.1 the constant term must be expressed as $k = k'/g^{3/5}$. Applying this for the results obtained for the two experimental tubes yields the following expressions for the bubbles formed at each orifice:

for the glass tube:

$$V_b = 5.08 Q^{1.08} g^{-3/5} \quad (6.4)$$

and for its aluminum counterpart:

$$V_b = 4.31 Q^{1.10} g^{-3/5} \quad (6.5)$$

When the general form of the equation describing the constant frequency region is considered:

$$V_b = k Q^{1.2} g^{-3/5} \quad (6.6)$$

it is apparent that the gas flow falls in this region. This agreement is quite strong due to the similarity in the exponents of the gas flow rate terms in the above equations. Since the

two experimental lines are close, these results will be expressed using an average of the two constants shown above. Therefore, for this study the experimental data will be represented by:

$$V_b = 4.70 Q^{1.1} g^{-3/5} \quad (6.7)$$

This equation is compared with the Davidson and Harrison⁶⁷ equation for bubbles forming at a protruding orifice in Figure 6.2 ($k = 1.138$). The results obtained by Irons and Guthrie⁸⁶ for constant frequency bubble formation in liquid metals have also been included. The equation which these researchers used differs from the general equation for this flow region. Based on their experimental results Irons and Guthrie⁸⁶ developed the following empirical equation:

$$V_b = 0.08 Q^{0.87} d_{n,o}^{0.44} \quad (6.8)$$

where Q = gas flow rate in ml/s.

$d_{n,o}$ = outside nozzle diameter in cm and

V_b = equivalent bubble volume in ml

The dependence of the outer nozzle diameter was applicable for $d_{n,o} < 35$ mm. Above this diameter no further dependence on outer nozzle diameter applies since the nozzle then behaves like an orifice. In the present system, inside and outside diameters were very similar so this factor was eliminated.

Irons and Guthrie's⁸⁷ results compare well to the Davidson and Harrison⁶⁷ equation for the aqueous system. The results

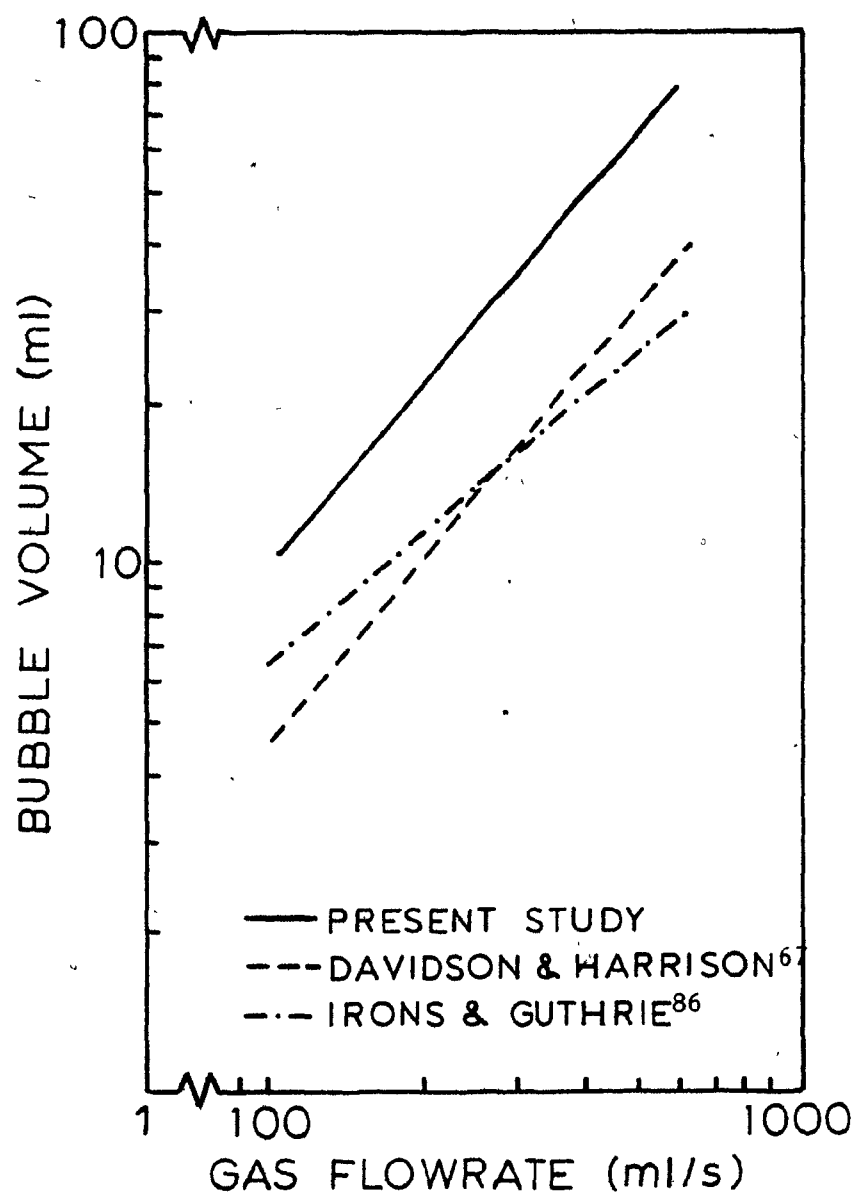


Figure 6.2 Comparison of the Experimental Results to Previous Work on Bubble Formation at Submerged Orifices.

obtained by the present author indicate the same trend as Davidson and Harrison⁶⁷ but the predicted bubble volumes are larger. This is readily explained when the equations describing these two curves are compared. The value for the constant term in equation (6.6) is significantly higher for the experimental values (4.70 vs 1.138). To explain these discrepancies, the aspects which differ between the two systems must be evaluated.

The bubbling experiments on which the theory is based were performed under practically isothermal conditions. Consequently, the bubbles formed at the orifice did not undergo any thermal expansion. For the boiling of liquid nitrogen this is far from reality. Since the gas phase leaves the tube at a temperature equal to the boiling point of liquid nitrogen (77.2 K) the bubbles rapidly expand upon contacting the warmer water. To investigate how strongly this would affect the predictions of Davidson and Harrison,⁶⁷ this gas expansion had to be considered. Assuming that the gas leaves the tube at 77.2 K, arbitrary increments of 50 K to the bubble temperature yields a series of equations describing bubble size. The results are plotted as a function of the gas temperature and gas flow rate in Figure 6.3. The experimental results are included for comparison. From this graph a gas temperature of 100 K between the moment of bubble formation and time of bubble diameter measurement allows bubbling theory to be matched with

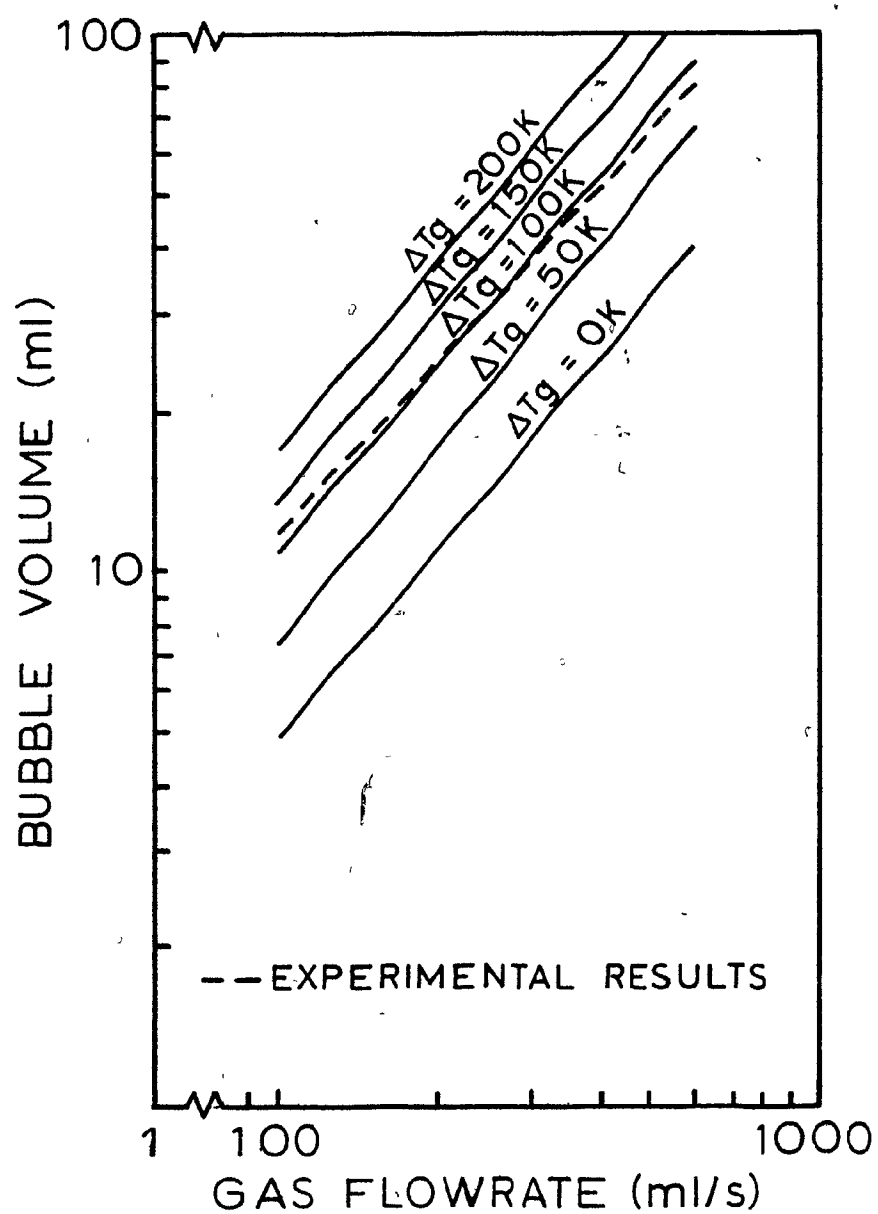


Figure 6.3 Effect of Increasing Gas Temperature on the Results Obtained by Davidson and Harrison.⁶⁷

experimental results. An attempt was made to measure the temperature of the gas bubbles as they lifted off from the tube. Unfortunately the residence time of each bubble at the temperature probe was too short to register any temperature changes. Observations indicated that the bubbles incur most of their expansion close to the nozzle opening. After approximately 50 mm of rise, bubbles have reached thermal equilibrium and stop expanding. Since the bubble size is measured 10-20 mm above the nozzle opening it is the author's opinion that the bubble temperature could easily rise by 100 K.

Examining the orifice Reynolds number (Re_0) for these two tests also yield some insight into the precise bubbling region. In Table 6.1 Re_0 is listed against the bath superheat. These tests encompass the range of Reynolds numbers between 2,500 to 13,000. According to the classification given by Valentin⁶¹ (see Chapter 3) gas flow would not fall in the constant frequency region but rather the turbulent region. The transition point which was given by Valentin⁶¹ is approximately at $Re_0 = 2100$, so the results presented in Table 6.1 are at the low end of the turbulent region. Consequently it is quite plausible and has been previously shown that the constant frequency region solutions still apply.

The visual interpretation which several investigators^{61,70,71} reported for this region was substantiated in the present work. The formation of double and triple bubbles was frequently observed and some evidence of their existence was presented

TABLE 6.1
The Orifice Reynolds Number As A
Function Of The Bath Superheat

Superheat (K)	<u>Reynolds Number</u>	
	Glass	Aluminum
0	2894	2271
5.5	3241	2689
10	--	3067
14	3784	3379
20	4265	4009
30	5070	5111
40	5960	6370
50	6931	7791
60	8099	9543
70	9012	11,306
80	10,353	12,830

in Chapter 5. The phenomenon which Valentin⁶¹ noted about one bubble "sucking in" the next one was particularly prevalent in the present experiments.

Combining the above ideas with those presented in Figures 6.1 - 6.3, the flow issuing from the tubes can be described as turbulent but in the lower end of the turbulent region where the solutions of the constant frequency region still apply. One point of contention between this classification and the present experimental results is the effect of the nozzle diameter. Several researchers, particularly Liebson et al.⁷¹, found that the dependency of the bubble size on the nozzle size drops off dramatically for $Re_0 > 2,000$. The strong linear relationship between the nozzle and bubble diameter which was observed in this study contradicts these findings. A factor which may explain this difference is the absolute size of the experimental nozzles. The bulk of the work published for submerged orifices was based on very small nozzles, typically 1 to 5 mm. In this study, much larger nozzles were used ranging between 5 and 30 mm.

6.2.3 Freely Rising Bubbles

From the video analysis, the size and rising velocity of the stable bubbles generated from the boiling nitrogen were evaluated. Although these values are not directly related to the magnesium bubbles formed in hot metal because of the inert nature of nitrogen, they were measured to provide a better

understanding of the model. Summarizing the results, terminal rising velocity between 318-462 mm/s were measured while the corresponding stable bubble size fell between diameters of 10.6 to 69.9 mm. Taking the average terminal velocity, the bubble Reynolds and Eötvös numbers can be evaluated. Therefore:

$$Re_B = \frac{\rho_L d_e U}{\mu} \quad (6.9)$$

and

$$E_O = \frac{g \Delta \rho d_e^2}{\sigma} \quad (6.10)$$

where ρ_L , μ , σ = density viscosity and surface tension of the fluid medium, respectively

d_e = equivalent bubble diameter

U = terminal rising velocity

g = acceleration due to gravity

$\Delta \rho$ = density difference between the gas and liquid phase

For the data presented above on nitrogen bubbles rising through water:

$$1230 < Re_B < 11,780$$

and

$$14.7 < E_O < 616$$

Comparing these values to the "bubble map" presented in Figure 3.9 indicates the existence of two possible types of

bubbles, spherical cap or wobbling bubbles. However, when the critical value of $E_0 = 40$ bordering between the two bubbles types is considered in equation (6.10) the corresponding critical bubble diameter equals 17.8 mm. This implies that bubbles with a diameter greater than 17.8 mm will be spherical cap and those bubbles which are smaller will be wobbling or ellipsoidal depending on the bubble's Reynolds number. Such small bubbles can only be generated by the 5.0 mm diameter tubes (see Appendix A). Consequently, the bubbles issuing from all of the other tubes are spherical cap in nature while the bubbles from the smaller tubes are usually wobbling.

It is difficult to extrapolate these results to the magnesium system. A magnesium bubble rising through liquid iron is continually changing in size due to dissolution reactions with the iron and a constantly lessening pressure head. The results which have just been presented would only apply very close to the nozzle. However, the indications are that for larger nozzles, spherical cap bubbles will predominate.

6.3 DISPLACEMENT - STAGE THREE

After the steady state boiling stage has been well established, displacement of the gas phase by the surrounding liquid begins. Displacement continues until the nitrogen gas in the tube is completely displaced and vaporization is complete. During this stage the heavier water penetrates the gas phase and accumulates in the bottom of the tube. As time passes the amount of water collected in the tube increases as it steadily

(displaces any remaining liquid nitrogen and cold nitrogen gas. As was noted in the previous section, displacement does not seem to affect the rate of steady state boiling. Whether a tube is nearly full of water, half full or empty the flow issuing from the nozzle remains constant. To understand the events occurring inside each tube, a brief series of experiments were performed to evaluate temperature changes at a selected point inside the tube. These results will be presented before outlining the criteria limiting the inflow of water.

6.3.1 Displacement: Heat Transfer

(Once visual observations confirmed infiltration of water into the tubes, it was essential to evaluate the temperature of the tubes' contents as a function of time. These measurements would help determine if heat is transferred to the boiling mixture from the inflowing warm water. A glass (22.5 mm inner diameter) and an aluminum (20.0 mm inner diameter) tube were equipped with two thermocouples as indicated in Figure 6.4. The center thermocouple had an exposed junction to yield a fast response to changes in temperature. This thermocouple was placed at approximately 1/3 the length of the tube below the tube's mouth.

(The second thermocouple was placed on the outside wall at the same height as the center thermocouple to record changes at that point. This thermocouple was extremely thin, with a foil sensor for the fastest possible response time (Omega Engineering Inc. #C01-E). Both thermocouples were made of

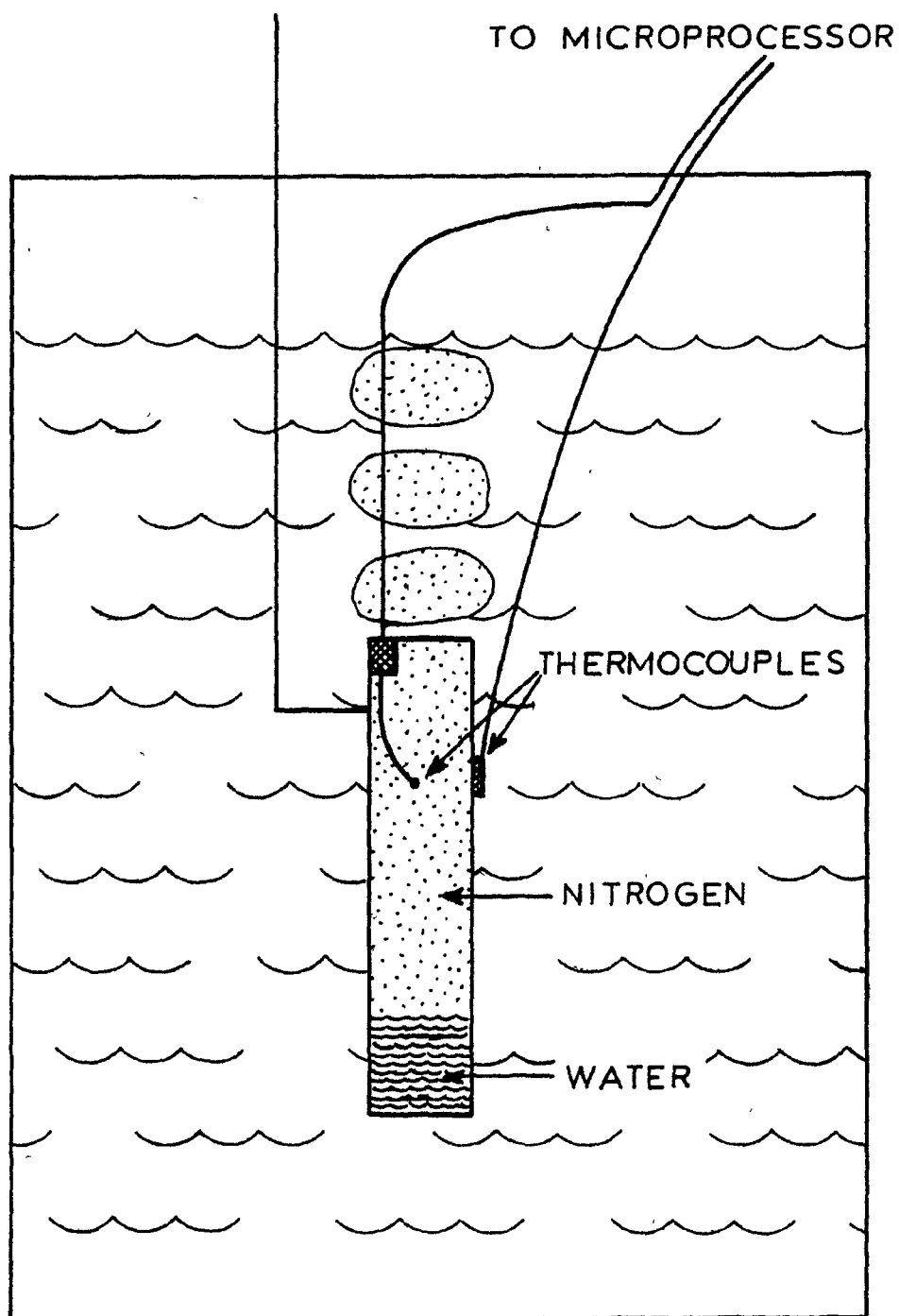


Figure 6.4 Details of an Instrumented Nitrogen Containing Tube.

chromel-constantan (type E) to supply the highest possible voltage output for the cryogenic temperatures investigated. The analog signals generated by the two thermocouples were logged and processed using a data acquisition system based on a Motorola 6809 microprocessor.

The results of two typical tests are shown in Figures 6.5 and 6.6. The curves for the balance of this test work are given in Appendix B. The point in time when the tube was immersed was signified by a large change in the outside wall temperature. Initially both thermocouples are at 78 K as the tube was filled with liquid nitrogen. When the tube was immersed and the outside wall contacted the warmer water the temperature at this point rapidly rose. The temperature of the nitrogen liquid and/or gas remained at 78 K until the level of the incoming water contacted and passed the thermocouple. At this point the temperature of the inner thermocouple rapidly rose to approximately 273 K.

This behaviour confirmed two important points. During the boiling reaction the liquid nitrogen only changes state, and did not subsequently heat up. This was probably due to poor heat transfer through the gas phase. The infiltrating water had no effect on the gas temperature and only physically displaces the nitrogen.

The outside thermocouple did not actually measure the wall temperature due to the formation of an ice film on the wall. For both graphs, this temperature rapidly increased

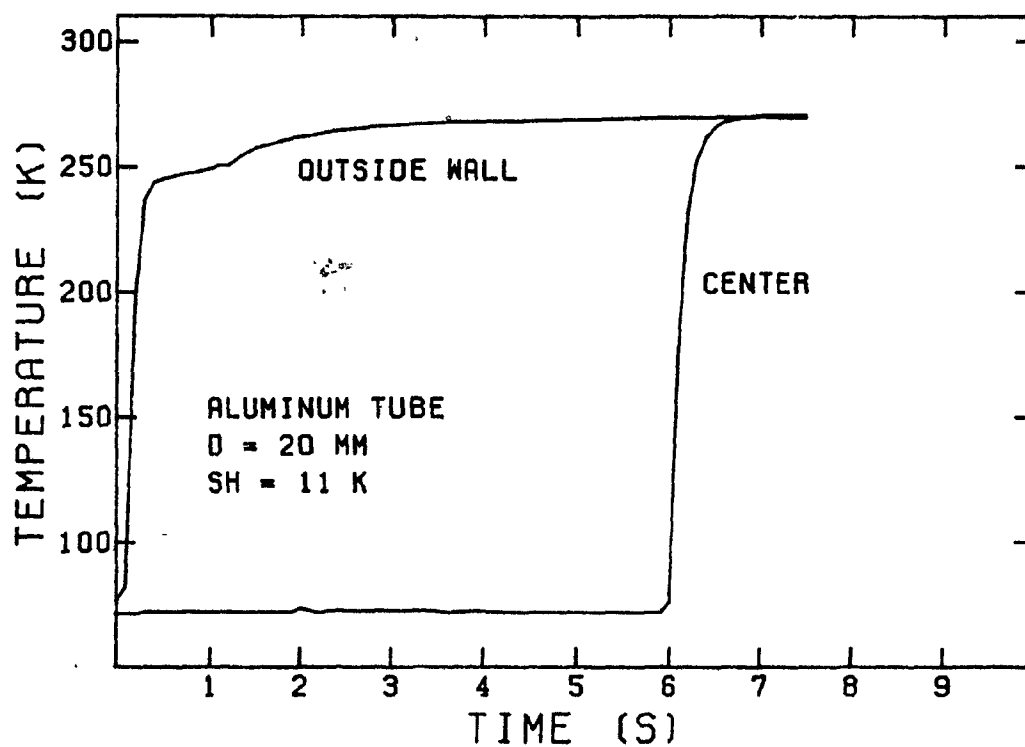


Figure 6.5 Temperature Profiles during Vaporization for an Aluminum Tube.

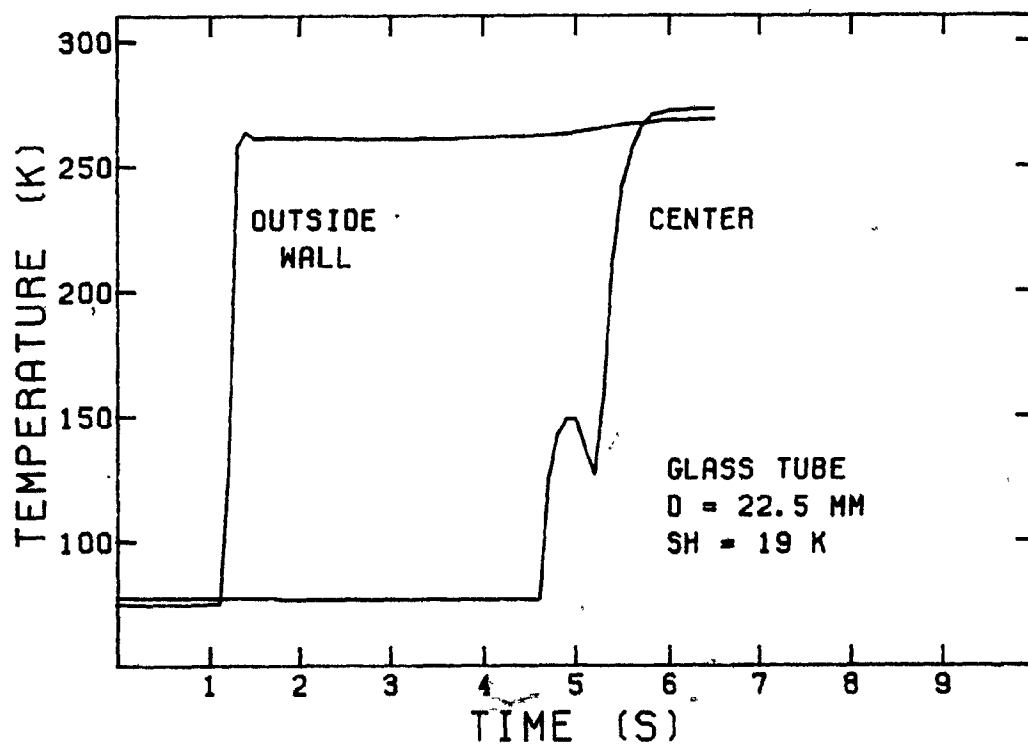


Figure 6.6 Temperature Profiles during Vaporization for a Glass Tube.

to between 250-260 K and then slowly increased to the melting point of the ice (273 K). As would be expected, the temperature of the ice phase on the aluminum tube did not increase towards 273 K as rapidly as in the glass case, owing to the superior thermal conduction properties of aluminum. Thus, since heat is more rapidly transferred through aluminum, a heavier ice shell forms and the temperature within this film takes longer to be affected by the convective heat transfer through water.

As the water forces the nitrogen out of the tube there is a great deal of turbulence at their interface. The deflection shown in Figure 6.6 for the center thermocouple confirmed this. In this case the thermocouple was first immersed in the water then back into the cold nitrogen gas before finally being completely immersed in the water.

Summarizing, the infiltrating water may only contribute a small amount to the heat balance for the vaporization of the liquid nitrogen. However, the inflowing water does physically displace the nitrogen vapour so an understanding of the criterion limiting inflow will be beneficial if this stage of the total mechanism is to be controlled. Once the liquid nitrogen vaporizes, it becomes difficult to transfer heat through the vapour phase and consequently, this phase remains at its boiling point until it leaves the tube.

6.3.2 Criteria Limiting Displacement

Throughout the presentation of the results the smallest tube (5.0 mm inner diameter) has often been the exception to the trends established for the larger nozzles. It has been visually confirmed that there is no water infiltration for the smaller tubes. The ramifications of this fact have been evident in other tests as well. As the tube diameter is decreased the proportion of gas initially ejected increases. For the smallest tubes there is a rapid initial ejection of nitrogen gas followed by a long slow bubbling period due to the expanding nitrogen. The tubes remain full of gas at the end of the test and only upon vigorous shaking can this gas be removed.

Table 6.2 summarizes the orifice and bubble Reynolds number as a function of tube diameter. The Eötvös number describing the ratio of the rising bubble's gravitation to surface tension forces is also included. The flow issuing from the smaller tubes typified by Re_0 is much lower indicating the increasing dominance of surface tension forces at the orifice. The restricted flow through the smallest nozzles leads to smaller bubbles reflected by the drop in value of the Eötvös number. For these tubes, the decrease in flow is so large that bubble formation is no longer described by the constant frequency region but rather by the constant volume region. Since the value of the Eötvös number falls below the critical value of 40, the bubbles formed from these tubes fall in the wobbling not the spherical cap regime.

TABLE 6.2

Flow Characterization for Several Nozzle Diameters

Nozzle Diameter (mm)	Orifice Reynolds Number	Bubble Reynolds Number	Bubble Eötvös Number
30.0	15,500	3,700	627
20.0	12,000	2,700	273
10.0	3,100	1,300	65
5.5	480	1,550	15

This dramatic change in flow can be understood when the properties of the two fluids are taken into account using Taylor's instability theory.⁸³ As outlined in Chapter 3, near the critical values given by the Taylor instability calculation the effects of surface tension can balance and exceed the buoyancy or gravitational forms.

If a bubble growing at the nozzle opening is considered as a perturbation between the gas and liquid phases then the implications of the instability calculations can be considered. Since for the water/nitrogen system, the critical wavelength (λ_c) equals 17.3 mm, bubbles growing at nozzles of diameter greater than 17.3 mm will be unable to block the inflowing water. In these cases, the surface tension forces are not strong enough to retard the gravitational forces of the water on the bubble surface. Consequently, water easily flows into the tube and displaces the contents. The high values for the orifice Reynolds number given in Table 6.2 for the 20 and 30 mm tube substantiate this fact.

As the diameter is decreased to a region between the critical wavelength describing fully developed countercurrent flow and half the critical wavelength, the water inflow becomes restricted. At the critical wavelength, a fully developed wave exists between the two unstable fluids. Consequently, the surface tension forces of the gas begin to effect the rate of water inflow while at values greater than λ_c , the rate of water inflow controls the speed of gas phase displacement.

As the nozzle diameter is decreased to the region between λ_c and $\lambda_c/2$, the surface tension associated with the bubbles forming at the orifice begins to restrict infiltration of water. The rate of displacement is then dictated by the release of stable gas bubbles. Again this is reflected by the decrease in the orifice Reynolds number shown in Table 6.2.

Upon further decreases in diameter of the tubes below $\lambda_c/2 = 8.7$ mm, the surface tension forces dominate at the orifice. Unlike the larger tubes, when a bubble forms at the nozzle, the surface tension forces exceed the buoyancy force due to the density difference between the gas and liquid phases. According to Taylor instability theory there should be absolutely no flow from the 5 mm nozzles. This is in fact true at the end of the experiment when a gas column remains in the tube, but during the experiment fluctuations in the system cause the bubbles to lift off. Fluctuations can include currents in the water, wetting properties of the tube material and the expansion of the gas. For aqueous systems, Davidson and Amick⁸⁷ reported "...stable stationary bubbles could not be found at an orifice having a diameter of 7.9 mm but stable bubbles formed at an orifice of 6.4 mm." Thus the critical wavelength predicted by Taylor instability must only be taken as a guideline and not a precise transition point indicating stability. In fact, stability is rarely achieved at the critical values due to random fluctuations in the system. Consequently, the critical dimension of the experimental

apparatus, in this case the tubes, must be smaller by one third to one half $\lambda_c/2$ to observe the effects of stability. This is why the decreased flow rate and residual gas volume were only observed for the 5 mm diameter tubes.

Gas flow is not completely restricted due to the large expansion forces associated with first boiling liquid nitrogen and then warming of the cold nitrogen gas. When the surface tension forces equal and exceed the expansion forces, flow from the nozzle is eliminated. The flow from tubes of a diameter less than $\lambda_c/2$ only include the first two stages of the general boiling mechanism. As the tubes are immersed, a large volume of gas is ejected into the surrounding mechanism because of the initial gas expansion. Bubbles continue to form at the nozzle until the temperature of the gas phase approaches the ambient temperature. At this point, the expansion of the gas decreases and the surface tension forces at the nozzle terminates the outflow of gas. The residual gas in the tube remains there indefinitely if the tube walls stay intact.

6.3.3 Ethyl Ether and Water System

To confirm the restricted flows predicted by Taylor instability, a second system was investigated. Ethyl ether was chosen to simulate the density of liquid nitrogen so the displacement between liquid nitrogen and water could be examined. The properties of ethyl ether are summarized below:

Property

Density = 707.9 kg/m³

Interfacial tension

ethyl ether to water = 0.0107 N/m

Each of the glass tubes was filled with ethyl ether and plunged into water. The time for the ethyl ether to buoy out of the tubes was measured. Since ethyl ether is non-gas evolving it would be inappropriate to compare the flow rates of this system to the volatile case. Instead the total time for the ethyl ether to buoy out of the tubes was compared to the total time for gas evolution for liquid nitrogen. These results are shown in Table 6.3.

For the ethyl ether/water system the critical wavelength is calculated from equation (3.40) and equals 12.1 mm. For the intermediate diameter between λ_c and $\lambda_c/2 = 6.1$ mm the total time for the water to displace the ethyl ether is slightly longer indicating restricted flow. The total times measured for the smallest tubes confirm the near total restriction of flow. Ethyl ether does flow from the 5 mm tube since this diameter is close enough to $\lambda_c/2$ to be susceptible to small fluctuations in the system. In any event the flow is still dramatically reduced as tube diameter is decreased to less than $\lambda_c/2$.

These tests indicate the importance that the physical forces of gravity and surface tension have on the rate of

TABLE 6.3

Comparison of the Displacement of Ethyl Ether to the Vaporization
of Nitrogen for Several Tubes

Tube Diameter (mm)	Buoy Out Time for Ethyl Ether(s)	Vaporization Time for Nitrogen(s)
30.0	5.8	7.4
20.0	5.4	6.1
10.0	6.1	6.1
5.5	>360	∞

nitrogen evolution. It is these forces which must be dealt with to understand the role of displacement in the magnesium/hot metal system.

6.4 INITIAL EJECTION - STAGE ONE

The immersion of each tube is characterized by a large initial ejection of nitrogen. The nature of this ejection is complex and remains as one of the most puzzling aspects of the present work. As a tube is immersed in water there are several possible ways large gas volumes can be generated.

As the liquid nitrogen at the opening of the tube contacts the warmer water, it rapidly boils creating a large gas volume. As a liquid, nitrogen has the ability to generate considerable quantities of gas. From the ideal gas law:

$$PV_g = nRT \quad (6.11)$$

where P = absolute pressure exerted on the gas phase

V_g = volume of the gas phase

n = number of moles of gas in the gas phase

R = universal gas constant

T = temperature of the gas phase

but

$$n = \frac{V_L \rho_L}{M} \quad (6.12)$$

where V_L = volume of the boiling species in the liquid state

ρ_L = density of the liquid

M = molecular weight of species considered

Substituting the above into (6.11) and solving:

$$V_g = \frac{V_L \rho_L RT}{M P} \quad (6.13)$$

Assuming atmospheric pressure and solving the above for liquid nitrogen:

$$\rho_L = 808.1 \text{ kg/m}^3$$

$$R = 8314.1 \text{ Pa-m}^3/\text{kg mole K}$$

$$T = 77.5 \text{ K}$$

$$M = 28.01 \text{ kg/kg mole}$$

$$P = 1.013 \times 10^5 \text{ Pa}$$

and

$$V_g = 183.51 V_L \quad (6.14)$$

The temperature shown above was selected since previous experiments indicated that the nitrogen leaves the tube as a gas but at its boiling point. As the tube is immersed into the water 1-2 ml of liquid nitrogen directly contacts the water. Based on equation (6.14), this contact would rapidly generate 184-367 ml of nitrogen gas.

Once the tube is completely immersed the conditions for heat transfer to the nitrogen are excellent. The liquid nitrogen at the outside wall of the tube will rapidly boil and leave the tube. Since gas is generated from the entire periphery of the tube, the rising, expanding gas bubbles carry some of the remaining liquid out of the tube. As this two phase

(mixture contacts the water it rapidly expands due to the large convective heat transfer in water. This process continues at a decreased rate as drops of liquid nitrogen contact the sides of the tube. As the proportion of gas in the tube increases the turbulence breaks down and the steady state boiling stage begins.

Via a combination of the above steps a large quantity of the total gas produced is rapidly ejected into the surrounding fluid as the tube is immersed into that fluid. It was difficult to distinguish the exact stages and steps which describe the initial blast of nitrogen. Only the magnitude of the blast could be measured by balancing the total gas volume which evolves during steady state boiling to the total quantity of nitrogen produced. The total volume of gas which must be produced can be calculated by entering the volume of liquid nitrogen immersed contained in the tube into equation (6.14). For steady state boiling the quantity of gas produced can be deduced by multiplying the flow rate for each test by the length of the test. Although steady state boiling does not last for the entire test it is responsible for up to 90% total time of each experiment. The difference between these two values equals the amount of gas lost during the initial ejection step. Represented as a percentage of the total volume, the proportion ejected for each of the investigated variables (superheat, angle, diameter, etc.) are shown in Figures 6.7 - 6.10. The results for the different shell materials used throughout the experiments are listed in Table 6.4.

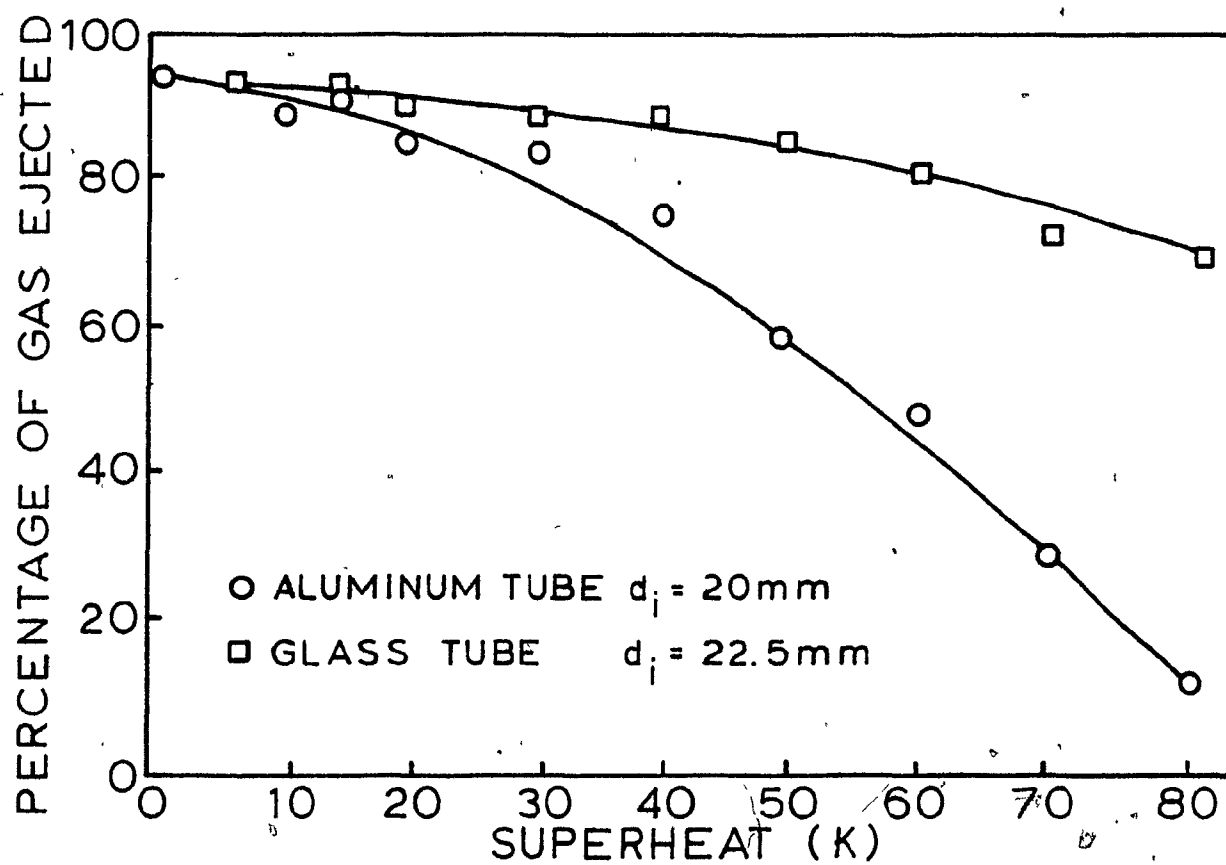


Figure 6.7 Initial Ejection of Nitrogen Gas with Increasing Bath Superheat.

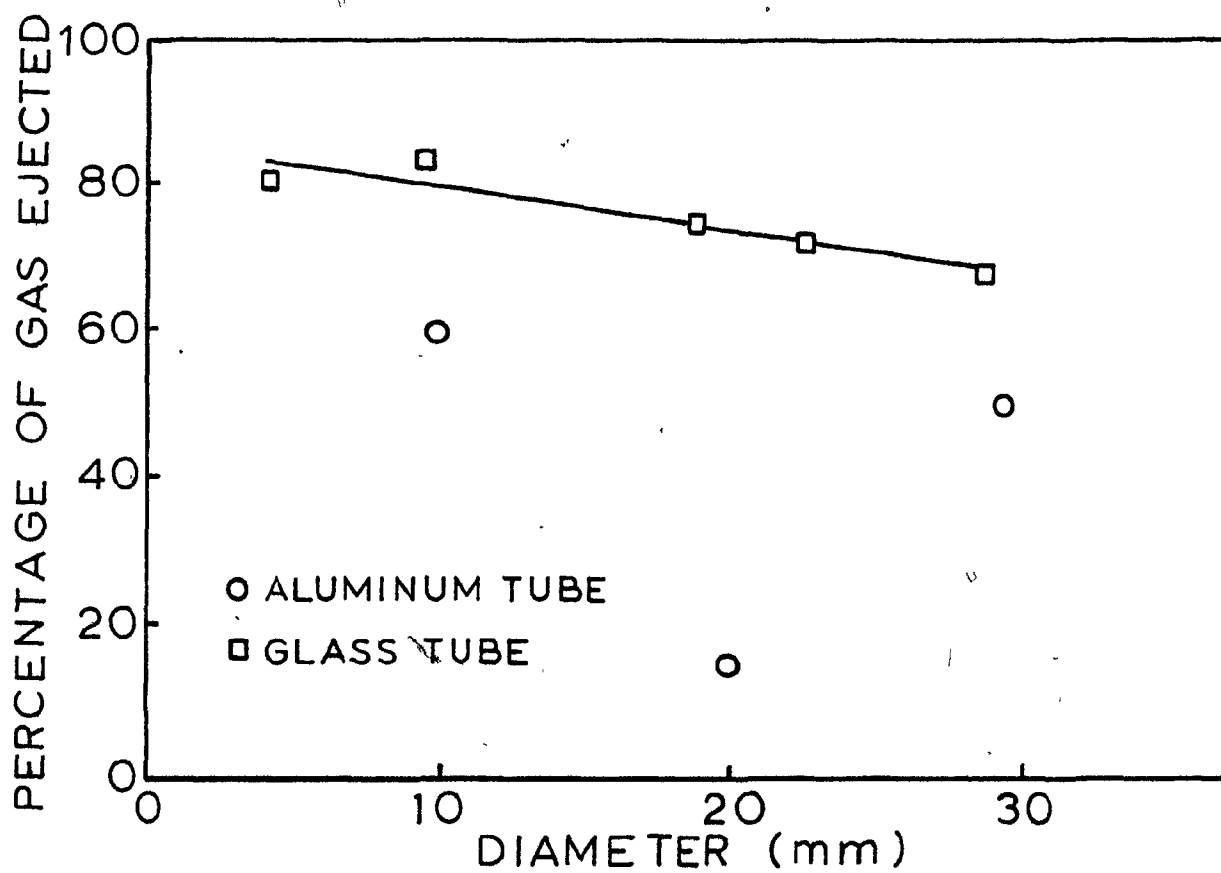


Figure 6.8 Initial Ejection of Nitrogen Gas with Increasing Tube Diameter (SH = 80 K).

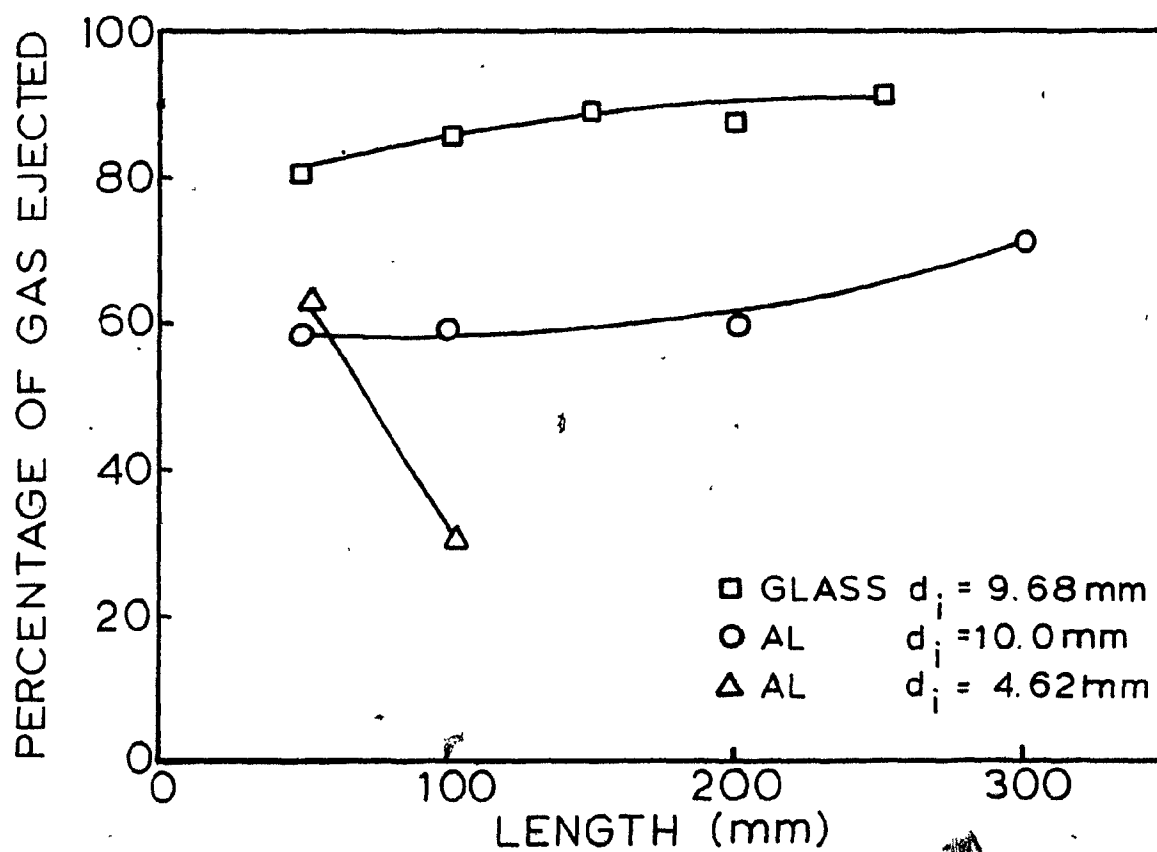


Figure 6.9 Initial Ejection of Nitrogen Gas with Increasing Tube Length (SH = 80 K).

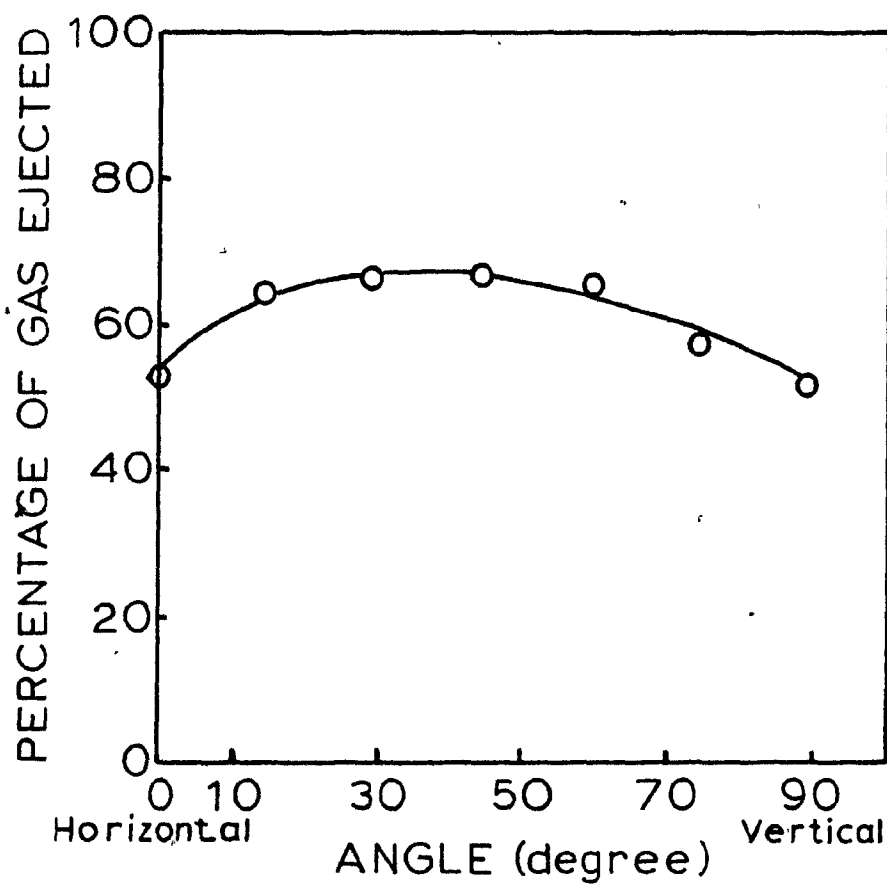


Figure 6.10 Initial Ejection of Nitrogen Gas as a Function of Tube Orientation (SH = 80 K).

TABLE 6.4

Initial Gas Ejection for the Shell Material Tested

Material of Construction	Total Gas Vol.(l)	Steady State Gas Vol.(l)	% Ejection
Aluminum	11.31	9.70	14.2
Pyrex	10.13	2.79	72.5
Graphite	8.67	2.12	75.6

Unfortunately, the resulting curves are somewhat contradictory particularly for the aluminum tubes. Figure 6.7 shows the ejection trend as a function of the bath temperature. For both tubes there is a drop in the amount ejected with increasing temperature.

As temperature increases the expanding gas must block off the ejection of liquid nitrogen. The effects are more pronounced for the aluminum tube due to the greater ease for thermal conduction during the first instants of immersion. When the amount ejected is compared with the tube diameter, discrepancies arise. The curves for the pyrex and aluminum tubes are shown in Figure 6.8. The amount of gas ejected from the pyrex tubes drops with increasing diameter. This would be expected due to the increase in the volume to surface area ratio for larger tubes. Unfortunately, in the case of the aluminum tubes there is no correlation between the data points. The reasons for this are uncertain and this discrepancy can only be eliminated with more experimentation.

As the length of the tubes is increased there is a slight increase in the quantity of gas ejected. For the longer tubes the possibility of carrying out large quantities of liquid exists since the initial bubbles rise through more liquid nitrogen. The smaller aluminum tube (10 mm inner diameter) ejects much more nitrogen (approximately 65% N_2) than its larger counterparts (20 mm inner diameter) shown above. The results for the smallest aluminum tubes are also shown although there is insufficient data to make any conclusions.

The higher amount of gas ejected by the 10.0 mm diameter aluminum tube is further confirmed by the tube orientation results shown in Figure 6.10. Again the average amount of gas lost due to the initial ejection of gaseous nitrogen is approximately 60%. Why tubes both larger and smaller than 20.0 mm inner diameter eject much more than this particular size is not understood by the author. Only further investigation into all of the aluminum tubes can eliminate this discrepancy.

The curves cited above neither support nor confirm the theories of ejection which were presented earlier. These curves only serve to show the relative amounts of gas which are evolved due to the initial ejection step. For the bulk of the tests more than half the gas was ejected in this fashion. Although difficult to study, this is an area where further work is required.

6.5 SUMMARY

The results of the experimental program were discussed in detail and a three stage mechanism describing the entire phenomenon was identified. The steps of initial ejection, steady state boiling and gas phase displacement were all described and the criteria limiting their effectiveness were highlighted. The first stage, initial ejection, proved to be the most difficult to explain due to its short duration. However, its importance in quickly injecting more than 50% of the gas phase into the surrounding fluid must be remembered.

The steady state bubbling step was characterized by bubbles being formed and released at constant intervals. The gas flow for this stage was well understood and can be described mathematically using the equations from the constant frequency region.

The displacement stage was also well understood and through balancing the buoyancy and surface tension forces of bubbles forming at the orifice, the rate of displacement of the gas phase could be decreased and even eliminated. A critical tube diameter for countercurrent flow was determined based on the physical properties of the surrounding fluid. By eliminating this stage of the mechanism the overall time required for the boiling phenomenon is greatly decreased. Unfortunately, a residual volume of gas is left trapped in the containing shell.

A second important point concerning displacement is the effects of the physical forces. In the final stage the rate of displacement and hence the total reaction time is completely based on the forces of gravity and surface tension. For very large openings the inflowing water essentially pushes the gas phase out of the tube. As the diameter decreases to less than the critical value predicted by the theory of Taylor instability, the displacement is limited by the gas leaving the tube. In these cases the gas can effectively block off the incoming liquid through surface tension forces. Once the diameter is decreased to less than $\lambda_c/2$, the flow at the nozzle

C is entirely limited by the surface tension forces. The gas is only injected into the surrounding fluid due to its expansion since the inflow of water is eliminated.

In summary, the flow issuing from a tube can be described by the three stage mechanism presented in this chapter. Each stage is unique and has its importance in characterizing the speed and nature of the boiling for every immersion experiment.

CHAPTER 7

INDUSTRIAL IMPLICATIONS AND CONCLUSIONS

7.1 INTRODUCTION

The objective of this final chapter is to extrapolate the results of the physical model to those of industrial systems involving volatile additions to liquid iron. In so doing three possible bullet designs are presented and the most promising recommended. Before describing each bullet, some general comments derived from the model will be applied to the formation of magnesium vapour.

7.2 MAGNESIUM BULLETS: GENERAL

One of the most important facts derived from the low temperature results is that magnesium liquid should not cause explosions provided the vapour is supplied an opening through which to escape. This observation was made for liquid nitrogen, which is considerably more volatile at room temperature than magnesium at 1523 K. Since modified bullets break open when the addition is in the liquid state there is no containment of the vapour phase by any frozen shell of iron. Consequently, modified bullets offer an 'explosion proof' technique for the addition of magnesium to hot metal. This ensures that no catastrophic events would be attributed to the magnesium vapour. It has partly been this fear of explosions which has to date limited the development of magnesium bullets.

When designing a magnesium bullet it is evident that the lengthy steady state boiling stage must be eliminated as far as possible. The boiling times of 6 to 16 seconds recorded in the low temperature physical model would be far too long for the subsurface injection of magnesium vapour. The total available immersion time would be quite short for magnesium bullets, due to their limited penetration in hot metal and the short amount of time they take to buoy to the surface.

To shorten the steady state boiling step, the other two stages, particularly the displacement stage, should be closely examined to see how changes in these stages affect the reaction time.

The critical diameter for the countercurrent flow characteristic of the displacement step can be evaluated for the hot metal/magnesium system by Taylor instability theory.⁸³

From Chapter 3:

$$\lambda_c = 2\pi \left(\frac{\sigma}{\Delta\rho g} \right)^{\frac{1}{3}} \quad (7.1)$$

where

λ_c = critical wavelength describing the balance between the surface tension and gravity forces

$\sigma, \Delta\rho$ = interfacial tension and density difference between the two fluids, respectively

g = acceleration due to gravity

For the hot metal/magnesium vapour system:

$$\sigma = 1.87 \text{ N/m}^{88}$$

$$\Delta\rho = \rho_{\text{iron}} = 7070 \text{ kg/m}^3$$

$$g = 9.81 \text{ m/s}^2$$

Consequently,

$$\lambda_c = 32.6 \text{ mm}$$

The important value for restrictive flow is λ_c given above while flow can be eliminated for bullet diameters less than $\lambda_c/2 = 16.3 \text{ mm}$.

The value for interfacial tension listed above assumes that the level of dissolved magnesium in the iron is low because of the desulphurization reactions. For higher levels of dissolved magnesium, the interfacial tension between the iron and magnesium vapour would rise. This change in surface tension has been given by Selçuk and Kirkwood⁸⁹ and is shown in Figure 7.1. If higher levels of dissolved magnesium are attained in the melt then the surface tension and hence λ_c would rise. The critical wavelength would have to be recalculated using a revised value for surface or interfacial tension. For magnesium desulphurization of iron this factor was neglected.

For the model, the physical forces were predominant in determining the rate at which the gaseous phase is displaced. In liquid metals, these forces should be much larger, particularly that of surface tension and hence the flow in this

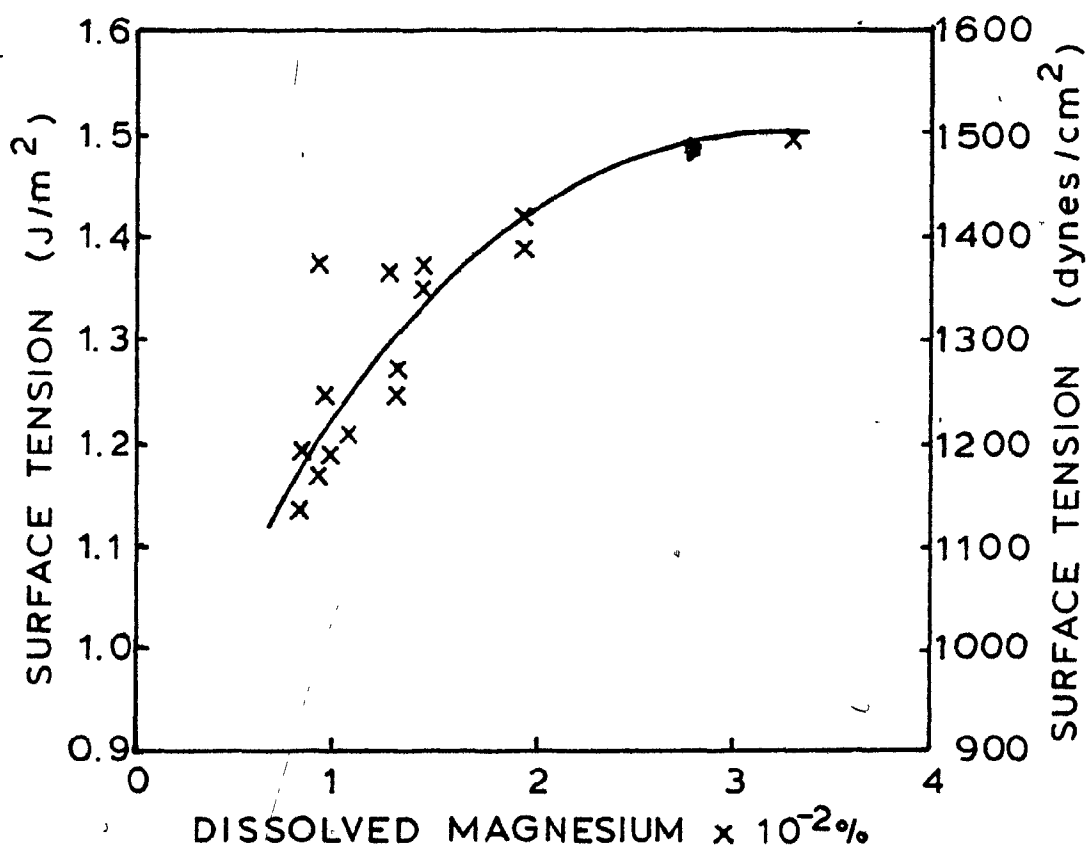


Figure 7.1 Change in the Interfacial Tension of Iron with Increasing Concentration of Dissolved Magnesium.⁸⁹

stage should be more sensitive to their values. This is not to say that the predictions given by the Taylor instability calculations do not apply, rather where gravitational forces dominate the rate of gravity driven flow should increase.

For instance, when the tube diameter exceeds λ_c and the inflowing liquid pushes the vapour phase out of the tube, the rates for this reaction should be greater in iron than water for a given diameter since it is much more difficult for the gas phase to support the much heavier iron.

The author expects that the other two stages, initial ejection and steady state boiling, would be similar to those observed in the physical model. Based on these general facts three potential bullet designs were formulated and each will be presented in the next few sections. These three designs are shown schematically in Figure 7.2.

7.2.1 Bullet Design - Type I

The first bullet was designed to eliminate the third stage of the boiling mechanism (i.e. final displacement) and thus limit the magnesium losses by shortening the steady state boiling step. The bullet would break open at the center to form two half shells full of magnesium liquid. To assure stability at the orifice, the bullet diameter should be approximately one third less than $\lambda_c/2 = 16.3$ mm. Consequently, 10 mm will be chosen. To assure good penetration of the steel, the design will be based on a length of 200 mm.



TYPE I



TYPE II



TYPE III

Figure 7.2 Proposed Bullet Designs. The Black Strips Denote the Location where the Thermal Resistance has been Placed on the Bullet's Surface (Scale 1:2).

Using the hydrodynamic analysis given in Chapter 2 the resident times which these bullets should have beneath the melt can be estimated. Assuming that the bullet was shot to the bottom of a hot metal transfer ladle and consequently had 2.5 m of hot metal to rise through, buoying up times can be evaluated. Using the technique developed by Tanoue et al.,⁸ an optimistic value for the terminal velocity can be calculated from:

$$U_B = \left(\frac{b}{\eta}\right)^{\frac{1}{2}} \quad (7.2)$$

where U_B = the terminal rise velocity

$$b = (\rho_f - \rho_s) / \rho_s g$$

$$\eta = \frac{\rho_f C_D A_B}{2 \rho_s V_B}$$

ρ_f, ρ_s = density of iron and magnesium respectively

V_B = volume of the bullet

A_S = cross sectional area perpendicular to the flow

C_D = drag coefficient

Extrapolating from Figure 2.4, $\eta \approx 260 \text{ m}^{-1}$ for $L/D = 20$. Since $b = 29.91$ for the magnesium-iron system the terminal rise velocity equals 0.34 m/s. Based on a maximum available immersion depth of 2.5 m and that buoying up takes 90% of the immersion time, the type I bullet should remain below the iron surface for 8.2 s.

Since the last stage of the boiling mechanism would have been eliminated, the bulk of the magnesium should be released by the initial ejection of liquid and gas as the magnesium begins to boil. For the low temperature model this took 1-2 s. Since heat is transferred four times faster for the model, at elevated temperatures this stage would be longer, consuming 4-8 s.

Taking Mucciardi's⁹ best results for modified bullets, the magnesium liquid would be initially released after 2 s of exposure to the melt. When these two times are combined the total required time to inject the magnesium would range from 6-10 s. Since the immersion time is 8.2 s the magnesium should be released below the melt surface. Unfortunately, the total immersion time would probably be less than 8.2 s. As discussed in Chapter 3, the immersion times estimated by Tanoue et al.⁸ tend to be somewhat high. Consequently, the magnesium would probably be released at or near the melt surface resulting in poor chemical efficiencies for desulphurization.

7.2.2 Bullet Design - Type II

The second bullet was designed to exploit the larger gravitational forces which exist in hot metal. To do this the bullet diameter should be larger than the previously calculated critical wavelength of 32.6 mm. Under these circumstances the displacement stage would be accelerated by the

flow of the heavier iron. The steady state boiling step would be shortened through the earlier initiation of a faster displacement. The type II bullets should be 35 mm in diameter and 400 mm in length yielding the minimum $L/D = 11.5$ for good penetration of the hot metal. The thermal resistance should be located such that the bullet breaks in one location producing two half shells.

Following the analysis given for the type I bullets, the larger type II bullets should buoy up at 0.59 m/s. Based on the maximum immersion depth of 2.5 m the total immersion time would be 4.7 s. Without doing an involved analysis it can be safely said that these bullets would suffer large inefficiencies. The melting of the magnesium and the initial injection of gas should be the same as the type I bullets taking 6-10 s. The type II bullets would have surfaced before starting the long steady state boiling and displacement steps.

As is evident for the first two designs it is difficult, if not impossible, to get these two types of bullets to release their contents substantially below the melt surface. The light magnesium bullets rise too fast to enable the magnesium vapour to be injected into the melt following the three stage boiling process developed from the low temperature model. As will be demonstrated, the third bullet uses an intermediate design to eliminate these problems.

7.2.3 Bullet Design - Type III

The key to this final design is to break the bullets at two rather than one location. This would produce two open ended cone shaped shells and a central tube open at both ends. All three sections would contain liquid magnesium once the bullet broke open.

The most important aspect of this design would be the open ended tube. With no restriction at the bottom of the tube, the iron should quickly enter the lower opening of the tube and force the boiling magnesium out. Since there is a large driving force in terms of density differences, this step should occur very rapidly. Unfortunately, the author has no quantitative results to substantiate this mechanism and it is only based on visual observations. However, it is estimated that the displacement would be very rapid and well within the allowed 4-6 s for an intermediate sized bullet (e.g. 20 mm in diameter). This would expose a large quantity of liquid magnesium and newly formed magnesium vapour to the hot metal. As the magnesium liquid contacts the iron problems may arise if large gas bubbles or a gas column is formed. Large quantities of gas would be difficult to dissolve and may lead to splashing of the hot metal.

This type of quick release was observed for the test work done using the gallium tube (see Section 5.3.4). In this case a large quantity of liquid nitrogen was rapidly exposed to the water. The result was a very large gas column which in turn

produced a substantial amount of splashing as it broke the surface. By using smaller bullets this effect would be minimized but not eliminated. It is considered that a bullet 20 mm in diameter by 250 mm in length would achieve the best results. This length to diameter ratio would be large enough to easily permit deep penetration into the melt while the addition volume would be small enough to limit the size of the gas bubbles produced upon vaporization.

For the type III bullet, the thermal breaks would have to be placed on the exterior surface so as to maximize the length of the central tube. Up to half the magnesium remaining in the two cone like end sections of the bullet would probably not be dispersed in the melt and would remain as inefficiencies in the process. However, by proper placement of the thermal resistances, 90% of the magnesium should be quickly dispersed into the melt from the central section.

Summarizing, this third design would appear to have the most potential. However, more work is needed to understand the cocurrent flow patterns which would be established for the central tubular section of the type III bullets. If the volume of the bullet can be balanced with a geometry which supplies sufficient penetration an excellent dispersion technique would seem to be possible.

7.3 CONCLUSIONS

A physical model has been developed to simulate the addition of solid magnesium into hot metal. The conclusions applicable to this model are outlined below.

1) If the gas produced from the liquid nitrogen is given an opening through which to escape, the gaseous phase will not produce any explosions.

2) A three stage mechanism has been postulated to describe the boiling of liquid nitrogen from an open ended tube. The three steps include the initial ejection, the steady state boiling and the displacement stages.

3) More than half of the gas phase enters the water during the initial ejection stage. The driving force for initial ejection is the large initial heat flux supplied to the liquid nitrogen via convective heat transfer from the warm water before an ice shell forms.

4) The steady state vaporization of liquid nitrogen from a tube shaped container behaves like a submerged orifice. Although the gas flow falls in the turbulent flow region, the solutions for the constant frequency regime still apply. For the experimental program, the gas flow is described by:

$$V_b = 4.7 Q^{1.1} g^{-0.6}$$

where

V_b = bubble volume

Q = gas flow rate

g = acceleration due to gravity

5) During the boiling process the liquid nitrogen simply changes phase. Consequently, the gas phase leaves the tube at a temperature equalling the boiling point. Once the bubble contacts the water it expands rapidly due to the warming of the gas by the rapid heat transfer in the water. This expansion is the reason why the equation given above disagrees with the previous results.

6) A critical nozzle diameter limiting the countercurrent flow between the water and gas phase was observed experimentally and confirmed by the theory of Taylor instability. Below the critical diameter surface tension forces dominate at the nozzle and the gravity driven flow characteristic of the displacement stage is restricted or entirely eliminated. If the diameter is selected to eliminate the countercurrent flow, the boiling phenomenon becomes limited to the first two steps, particularly the initial ejection stage.

From the results obtained for the physical model, several predictions can be advanced for the magnesium - hot metal system.

1) Based on the results of the physical model, a magnesium addition will not cause explosions if the magnesium vapour is provided an opening through which to escape.

2) For a modified bullet which is designed to break open in one location, the total immersion time is shorter than the time required for the initial release and boiling of magnesium addition. Consequently, it is impossible to obtain the desired subsurface release of the addition.

3) Upon changing the design to open the bullets at two locations the rapid gravity driven displacement of the central tubular section (opened at both ends) insures the quick release of the volatile contents. For this situation the bullet diameter should be large enough to permit acceptable penetration into the iron bath while limiting the total bullet volume such that a relatively small quantity of gas is released by each bullet. It is felt that a bullet 20 mm in diameter by 250 mm in length would achieve the best results for hot metal desulphurization.

APPENDIX AExperimental Results

In this section the results shown graphically in Chapter 5 will be presented in tabular form. Additional details on the total reaction time and the calculated flow rates will also be presented. The data is listed variable by variable. For example Table A1 includes the results for the bath superheat tests for the aluminum tube while Table A.4 will list the results for the diameter test. In each table the measured and calculated parameters will be distinguished.

TABLE A1

Bath Superheat Experiment: Aluminum Tube

Tube: Aluminum 20.0 mm inner diameter

MEASURED				CALCULATED	
Superheat (K)	Bubble Diameter (mm)	Frequency (Hz)	Total Time (s)	Equivalent Bubble Diameter (mm)	Flowrate (ml/s)
0	31.4	8.62	6.22	27.7	104
5.5	33.5	8.17	6.00	29.6	123
10.0	36.9	8.70	7.45	32.6	140
13.5	35.2	8.90	6.08	31.1	154
20.0	40.9	7.07	8.24	36.1	183
30.0	39.8	9.76	7.17	35.2	233
40.0	53.0	7.53	8.96	46.8	291
50.0	46.7	8.91	12.58	41.3	356
60.5	55.2	8.97	12.88	48.8	436
70.5	51.4	7.06	15.18	45.5	516
79.0	64.5	5.97	16.75	57.0	586

TABLE A2

Bath Superheat Experiment: Glass Tube

Tube: Glass 22.5 mm inner diameter

MEASURED				CALCULATED	
Superheat (K)	Bubble Diameter (mm)	Frequency (Hz)	Total Time (s)	Equivalent Bubble Diameter (mm)	Flowrate (ml/s)
0	38.2	7.13	5.52	33.6	149
5.5	41.1	7.55	5.36	36.1	167
13.5	37.8	8.91	5.33	33.2	194
20.0	45.2	8.13	5.20	39.7	219
30.0	43.4	8.72	5.33	38.2	261
40.0	46.6	6.54	4.85	41.0	306
50.0	51.5	8.70	4.98	45.3	356
61.0	54.0	6.81	5.56	47.5	416
69.0	55.8	6.94	7.45	49.1	463
80.0	61.7	6.86	7.23	54.3	532

TABLE A3

Shell Thermal Conductivity Experiment

Bath Superheat: 80 K

MEASURED					CALCULATED	
Shell No.	Thermal Conductivity (W/mk)	Bubble Diameter (mm)	Frequency (Hz)	Total Time (s)	Equivalent Bubble Diameter (mm)	Flowrate (ml/s)
1	192.5	64.5	5.97	16.75	57.0	579
2	1.09	51.1	7.81	6.09	48.2	458
3	157.5	43.5	8.14	6.03	43.5	351

Shell No. 1: Aluminum tube, 20.0 mm inner diameter

Shell No. 2: Glass tube, 18.9 mm inner diameter

Shell No. 3: Graphite tube, 17.6 mm inner diameter

TABLE A4

Shell Geometry Experiment: Diameter

Bath Superheat: 80 K

MEASURED				CALCULATED	
Aluminum Tube: Length = 200 mm					
Diameter (mm)	Bubble Diameter (mm)	Frequency (Hz)	Total Time (s)	Equivalent Bubble Diameter (mm)	Flowrate (ml/s)
4.6	11.3	5.72	-	10.6	3.57
10.0	28.5	7.08	17.08	26.5	69.0
20.0	64.5	5.97	16.75	57.0	579
29.3	83.8	5.42	13.12	69.9	970
Glass Tube: Length = 200 mm					
4.6	12.6	12.50	0.94	11.7	9.22
9.7	22.0	9.19	6.14	22.3	79.9
18.9	51.1	7.81	6.09	48.2	444
22.5*	61.7	6.86	7.23	54.3	560
28.6	76.9	6.60	7.36	68.9	1068

*length = 194 mm

TABLE A5

Shell Geometry Experiment: Length

Bath Superheat: 80 K

MEASURED				CALCULATED	
Length (mm)	Bubble Diameter (mm)	Frequency (Hz)	Total Time (s)	Equivalent Bubble Diameter (mm)	Flowrate (ml/s)
Glass Tubes: Inner Diameter = 9.68 mm					
50.0	22.6	9.14	2.38	23.1	58.9
100.0	20.3	10.22	4.11	20.7	47.8
150.0	20.7	8.66	5.42	21.1	49.9
200.0	22.0	9.19	6.14	22.4	54.0
250.0	19.4	9.58	7.08	19.8	39.0
Aluminum Tubes: Inner Diameter = 10.2 mm					
50.0	21.7	8.73	8.39	20.2	37.7
100.0	23.2	8.14	14.08	21.6	42.8
200.0*	28.5	7.08	17.08	26.5	69.1
300.0	21.5	9.36	31.95	20.0	39.4
Aluminum Tubes: Inner Diameter = 4.62 mm					
26.0	8.71	15.37	N/A	N/A	4.42
52.0	8.02	12.57	21.27	7.09	2.82
101.0	12.50	10.69	23.66	12.44	9.08
200.0	11.30	5.72	N/A	N/A	3.59

*Inner Diameter = 10.0 mm

TABLE A6

Shell Geometry Experiment: Angle

Bath Superheat: 80 K Aluminum Tubes: Inner Diameter = 10.0 mm, Length = 200.0 mm

MEASURED				CALCULATED	
Approximate Angle*	Bubble Diameter (mm)	Frequency (Hz)	Total Time (s)	Equivalent Bubble Diameter (mm)	Flowrate (ml/s)
90	28.5	7.08	17.08	26.5	82.4
75	28.5	9.28	15.19	26.5	82.4
60	28.4	9.27	12.49	26.4	81.6
45	30.7	8.61	9.37	28.5	103.0
30	33.5	8.10	7.33	31.1	133.7
15	34.0	7.90	7.40	31.6	140.3
0	23.7	8.69	28.99	22.0	47.2

* 90° corresponds to the tube in the vertical position with the open end facing up

0° corresponds to the horizontal position of the tube.

APPENDIX B

Temperature Profiles During Nitrogen Gas Evolution

The temperature profiles from the immersion of instrumented nitrogen containers are included in this appendix. The tests were performed under similar conditions using a 20.0 x 200mm aluminum tube and a 22.5 x 194mm glass tube. The temperatures of the outside wall and the contents are displayed for each test. Slight inconsistencies in temperature from experiment to experiment are due to inaccurate measurements of the cold junction temperature. The rapid increase in the outer wall temperature signifies the moment that the tube is immersed into the bath while the increase in the center temperature denotes the displacement of the gaseous nitrogen.

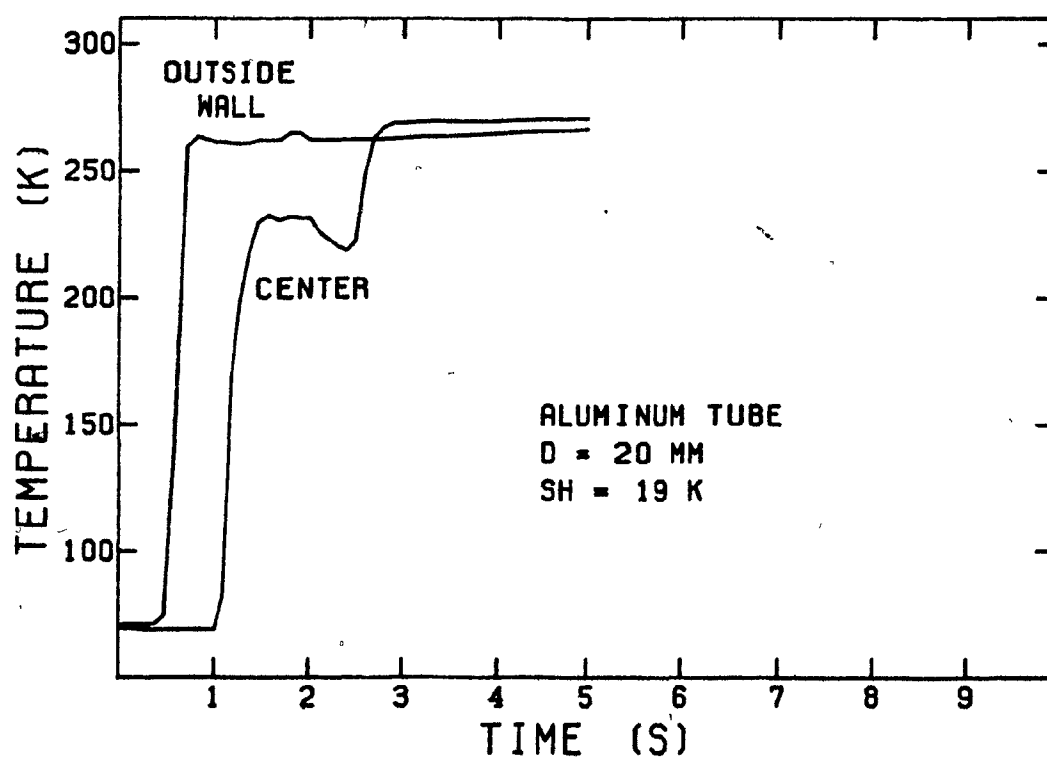


Figure B.1 Temperature Profiles during Nitrogen Vaporization from an Aluminum Tube (SH=19K).

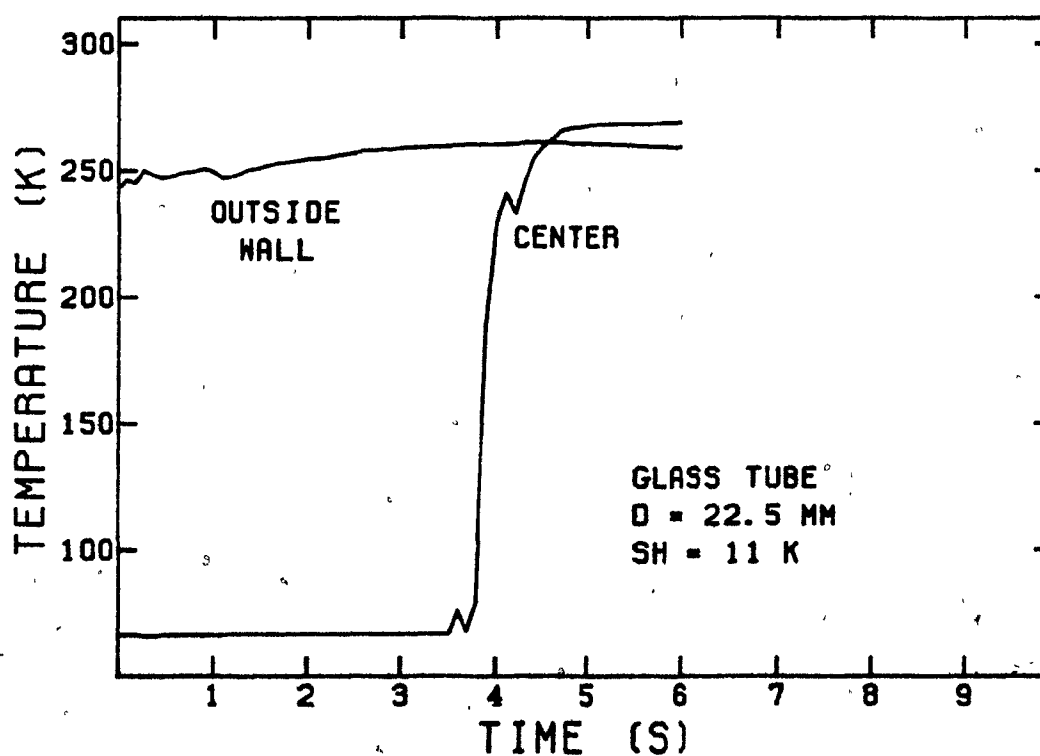


Figure B.2 Temperature Profiles during Nitrogen Vaporization from a Glass Tube (SH=11K).

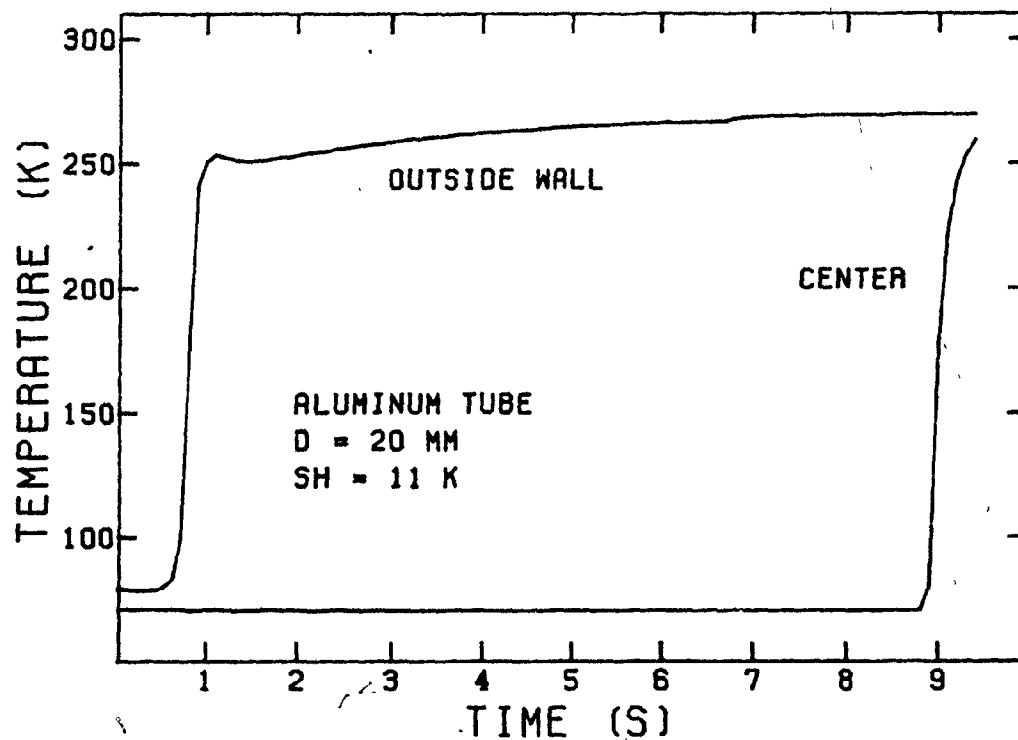


Figure B.3 Temperature Profiles during Nitrogen Vaporization from an Aluminum Tube (SH=11K).

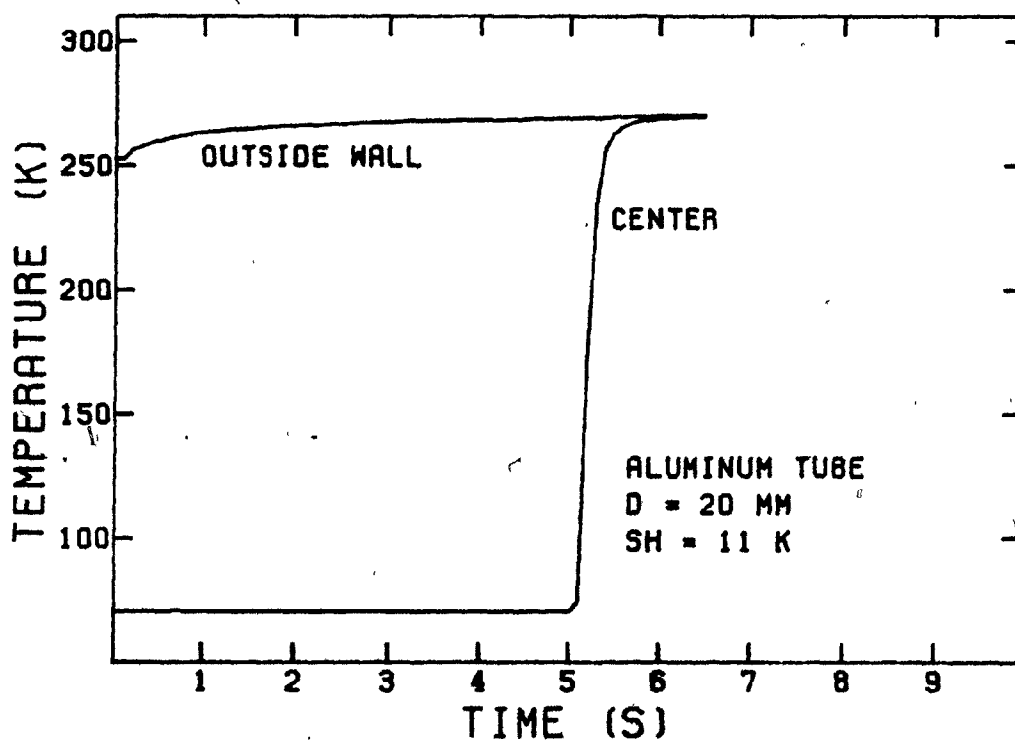


Figure B.4 Temperature Profiles during Nitrogen Vaporization from an Aluminum Tube (SH=11K).

REFERENCES

1. Guthrie, R.I.L., "A Perspective of Research and Development in North American Steelmaking" Can. Met. Quart., 1979, vol. 18, pp. 361-377
2. McGannon, H.E., ed., The Making, Shaping and Treating of Steel, United States Steel Corp., Pittsburgh, 1971, pp. 537-538
3. Orton, J.P., "The Importance of Low Sulphur on Processing and Properties of Steel", Proceedings of the Symposium on The External Desulphurization of Hot Metal, ed. W.K. Lu, McMaster University, Hamilton, 1975, pp. 1-1 to 1-19
4. Potocic, R.F. and Leewis, K.G., "Desulphurizing: Sulphur Control Plus More Production", Proceedings of the Symposium on the External Desulphurization of Hot Metal, ed. W.K. Lu, McMaster University, Hamilton, 1975, pp. 2-1 to 2-23
5. Hultgren, R., Desai, P.D., Hawkins, D.T., Gleiser, M., Kelly, K.K. and Wagmann, D.D., Selected Values of the Thermodynamic Properties of the Elements ASM, Metals Park, Ohio, 1973
6. Irons, G.A., "Desulphurization Kinetics of Molten Iron by Magnesium Vapour", Ph.D. Thesis, McGill University, Montreal 1978
7. Speer, M.C. and Parlee, N.A.D., "Dissolution and Desulphurization Reactions of Magnesium Vapour in Liquid Iron Alloys", Cast Metals Research Journal, American Foundryman's Society, Vol. 8, No. 3, 1972, pp. 122-128
8. Tanoue, T., Umerda, Y., Ichikawa, H. and Aoki, T., "Development of New Method of Aluminum Addition - Aluminum Bullet Shooting Method", The Sumitomo Search, No. 9, May 1973, pp. 74-87
9. Mucciardi, F.A., "A Study of Light Alloy Addition Techniques in Steelmaking", Ph.D. Thesis, McGill University, Montreal, 1980
10. Nakanishi, K., Ejima, A., Suzuki, T. and Sudo, F., Testu - to - Hagane, Vol. 64, No. 9, 1978, pp. 1323-32
11. Irons, G. A. and Guthrie, R.I.L., Can. Met. Quart., 1976, Vol. 15, No. 4, pp. 325-32.

12. Irons, G.A. and Guthrie, R.I.L., "The Kinetics of Molten Iron Desulphurization Using Magnesium Vapour", Transactions of the AIME, In Press, 1981
13. Elliott, J.F., Gleiser, M. and Ramakrishna, V., Thermochemistry for Steelmaking, Vol. 2, Reading, Mass.: Addison - Wesley, 1963
14. Tsuchiya, N., Ooi, H., Ejima, A. and Sanbongi, K., "Limit of Desulphurization in Blast Furnace and External Desulphurization by Sintered CaO-CaF_2 Pellets", Proceedings of the Symposium on the External Desulphurization of Hot Metal, ed. W.K. Lu, McMaster University, Hamilton, 1975, pp. 9-1 to 9-16
15. Puckoff, U. and Kister, H., "Desulphurization of Hot Metal at Hoesch - Estel", Proceedings of the Symposium on the External Desulphurization of Hot Metal, ed. W.K. Lu, McMaster University Hamilton, 1975, pp. 8-1 to 8-22
16. Silva, Y.I., Mundim, M. and Campos, U.F., "Experimental Studies on the Desulphurization of Pig Iron with Calcium Carbide Injection", Proceedings of the Thrid International Iron and Steel Congress, Chicago, Ill., April 1978, pp. 136-139
17. Forester, E., Klapdar, H., Richter, H. and Rommerswinbel, H., "Deoxidation and Desulphurization by Blowing of Calcium Compounds into Molten Steel and its Effects on the Mechanical Properties of Heavy Plates", Stahl U. Eisen, Vol. 94, No. 11, 1974, pp. 474-485
18. Gammal, T. and Krober, M., "Metallurgical Aspects of the Treatment of Steel with Magnesium and Calcium", Steelmaking Proceedings of AIME, Vol. 61, Chicago, 1978, pp. 546-554
19. Ototani, T. and Kataura, Y., "Deoxidation of Liquid Steel with Calcium Complex Alloys", Transactions of the ISIJ, Vol. 12, 1972, pp. 334-341
20. Pircher, H. and Klapdar, W., "Controlling Inclusions in Steel by Injecting Calcium into the Ladle", International Symposium on High Strength Low Alloy Steel, Washington, D.C. (1977)
21. Young, J.D., Leedale, P.R. and Timpano, F., "CAB Treatment of Carbon Steels at Stelco", Proceedings of Symposium on the Ladle Treatment of Carbon Steels, McMaster University, Ontario, May 1979
22. Sims, C.E., Saller, H.A. and Boulgar, F.W., "Relative Deoxidizing Powers of Some Deoxidizers for Steel", Transactions of the AIME, Vol. 185, pp. 814-825

23. Hieber, A.F. and Watmough, T., "An In Ladle Treatment Process for Producing Ductile Iron with Elemental Magnesium", Transactions of the A.F.S., Vol. 46, 1980, pp. 289-300
24. Polovchenko, I.G. Loginov, U.I., Duchenko, Y.S. and Solomatin, S.M., "Desulphurization of Pig Iron with Magnesium, Outside the Blast Furnace", Henry Brucher Translation #6288, 1964
25. Sussman, M.U., Elementary General Thermodynamics, Addison-Wesley, Reading, Mass., 1972, pp. 242-243
26. de Barbadillo, J.J., "Reactivity of Magnesium and Calcium in Liquid Steel", Sulphide Inclusions in Steel, Proceedings of an International Symposium, ASM, 1974
27. Geminder, G. and Hayden, R.P. "Design and Operation of Kaiser's Hot Metal Desulphurization Facility", Iron and Steelmaker, June 1979, pp. 29-34
28. Haastert, H.P., Meichsner, W., Rellermeyer, H. and Peters, K.H., "Operational Aspects of the Injection Process for Desulphurization of Hot Metal" Proceedings of the Symposium on The External Desulphurization of Hot Metal, ed. W.K. Lu, McMaster University, Hamilton, 1975, pp. 6-1 to 6-24
29. Palmer, M.A. and Becker, J.S., "Desulphurization in the Transfer Ladle", Proceedings of the Symposium on The External Desulphurization of Hot Metal, ed. W.K. Lu, McMaster University, Hamilton, 1975, pp. 16-1 to 16-24
30. Beyne, E., "Development of the Desulphurization of Iron at the Sidmar Steelworks", British Industrial and Scientific Translation, 17091, September, 1978
31. Engh, T.A., Kristensen, B. and Venås, K., "Desulphurization of Hot Metal By Injection of Magnesium Granules", Proceedings of The Light Metals Committee from the 109th Annual Meeting of The AIME, Metallurgical Society of AIME, Las Vegas, 1980, pp. 1011-1029
32. Pehlke, R.D., "Physical Chemistry of External Desulphurization of Molten Iron and Steel", Proceedings of the National Open Hearth and Basic Oxygen Steel Conference, Vol. 61, Chicago, Ill., April 1978, pp. 511-521
33. Voronova, N.A., Pliskanovskii, S.T. and Shevchenko, A.F., "Desulphurization of Pig Iron by Injecting Magnesium into Hot Metal Ladles", Steel in the U.S.S.R., Vol. 4, 1974, pp. 261-265
34. Smillie, A.M. and Huber, R.A., "Operating Experience at Youngstown Steel with Injected Salt Coated Magnesium Granules for External Desulphurization of Hot Metal", Iron and Steelmaker, June 1979, pp. 20-28

35. Koros, P.J. and Petrushka, R.G., "Materials for Hot Metal Injection", Proceeding of the Symposium on The External Desulphurization of Hot Metal, ed. W.K. Lu, McMaster University, Hamilton, 1975, pp. 7-1 to 7-25
36. Koros, P.J. Petrushka, R.G. and Kerlin, R.G., "The Lime - Mag Process for the Desulphurization of Hot Metal", Iron and Steelmaker, June 1977, pp. 34-40
37. Irons, G.A. and Guthrie, R.I.L., "The Kinetics of Magnesium Vapour Dissolution Kinetics into Pig Iron", Proceedings of The 33rd Annual Meeting of the International Magnesium Association, Montreal, 1976, pp. 63-72
38. Wood, J.K., Schoeberle, G.E. and Pugh, R.W., "The External Desulphurization of Hot Metal - A Pneumatic Injection Technique" Proceedings of the Symposium on The External Desulphurization of Hot Metal, ed. W.K. Lu, McMaster University, Hamilton, 1975, pp. 11-1 to 11-14
39. Sugita, H., "Mag - Coke Desulphurization of Hot Metal in the Ladle", Proceedings of the Symposium on The External Desulphurization of Hot Metal, ed. W.K. Lu, McMaster University, Hamilton, 1975, pp. 4-1 to 4-15
40. Shestopalov, I.I., Glovatskii, A.B. and Krasautseu, I.N., "Introduction of an Effective Method of Desulphurizing Pig Iron with Magnesium Metal" Henry Brutcher Translation #7817, 1969
41. Shestopalov, I.I., Glovatskii, A.B., Gomonov, A.A. Galaev, I.P., Grinberg, Yu.I. Ustimenko, I.Ya., Panev, U.A., Torba, V.G. and Yashchenko, N.V., "Desulphurization of Pig Iron with Magnesium Metal in Ladles", Henry Brutcher Translation #7884, 1970
42. Jarysta, H., "Simple and Economic Use of Pure Magnesium in the Production of Spheroidal Graphite (Ductile) Iron", Proceedings of the 33rd Annual Meeting of the International Magnesium Association, Montreal, 1976
44. Ashton, M.C., Buhr, R.K., Magny, J.G. and Davis, K.G., "Use of Magnesium Wire Injection for the Desulphurization of Pig Iron, Ironmaking and Steelmaking, Vol. 4, No. 2, 1975, pp. 111-114
43. Ashton, M.C., Buhr, R.K., Magny, J.G. and Davis, K.G., "The Use of Magnesium Wire Injection for the Production of Nodular Iron", Transaction of AFS, Vol. 83, 1975, pp. 51-54
45. Hardy, C. and Scott, D.M., "Treatment of Metals", 1933, U.S. Patent 1,915,824

46. Aoki, T., "Bullet Shooting: An Improved Method of Al and Ca Addition", Iron and Steel International, October 1978, pp. 307-317
47. Szekely, J. Fluid Flow Phenomena in Metals Processing Academic Press, New York, 1979, pp. 305-352
48. Hanein, H., "Hydrodynamics of Solid Additions to Liquid Steel", M. Eng. Thesis, McGill University, Montreal, 1975
49. Guthrie, R.I.L., Clift, R., and Hanein, H., "Contacting Problems Associated with Aluminum and Ferro-Alloy Additions in Steel-making Hydrodynamic Aspects", Transactions of AIME, Vol. 6B, 1975, pp. 321-329
50. Guthrie, R.I.L., Gourtsoyannis, L. and Hanein, H., "An Experimental and Mathematical Evaluation of Shooting Methods for Projecting Buoyant Alloy Additions into Liquid Steel Baths", Can. Met., Quart., Vol. 15, No. 2, 1976, pp. 145-153
51. Guthrie, R.I.L., "Addition Kinetics in Steelmaking", Proceedings of the Electric Furnace Conference, Chicago, Ill., December 1977
52. Mucciardi, F.A., "Heat Flow to Cylinders Submerged in Liquid Metal Baths", M. Eng. Thesis, McGill University, Montreal, 1977
53. Guthrie, R.I.L. and Mucciardi, F.A., "A Method of Melt Dispersing a Floatable Solid Additive in Molten Metal and a Melt Dispersible, Floatable, Solid Additive Therefore", Canadian Patent Application No. 325,818;; U.S. Patent Application No. 132,972; Japanese Patent Application No. 44514/80; U.K. Patent Application No. 8011102; French Patent Application No. 8007612; German Patent Application No. P30 13 213.9; Italian Application No. 67520-A/80
54. Guthrie, R.I.L., Private Communication, McGill University, 1980
55. Holman, J.P., Heat Transfer, 4th ed., McGraw-Hill, New York, 1976
56. Weast, R.C., ed., Handbook of Chemistry and Physics, 57th ed., CRC Press, Cleveland, 1976
57. Moser, R., Giessereiforschung in English, 1969, Vol. 21, No.3 pp. 130-39
58. Scheil, V.E. and Lukas, H.L., Giesserei techn. - wiss. Beihefte, 1965 Vol. 17, No. 2, pp. 61-64

59. Trojan, P.K. and Flinn, R.A., Transactions of ASM, 1961, Vol. 54, pp. 549-66
60. Kumar, R. and Kuloor, N.R., "The Formation of Bubbles and Drops", Advances in Chemical Engineering, ed. Drew, T.B., Cokelet, G.R., Hoopes Jr. J.W. and Vermeulen, T., Vol. 8, Academic Press, New York, 1970, pp. 255-386
61. Valantin, F.H.H., Absorption in Gas - Liquid Dispersions, E. and F.N. Spon., London, 1967, pp. 5-27
62. Clift, R., Grace, J.R. and Weber, M.E., Bubbles, Drops and Particles, Academic Press, New York 1978, pp. 16-29, pp. 321-348
63. Szekely, J. and Themelis, N.J., Rate Phenomena in Process Metallurgy, Wiley and Sons, New York, 1971, pp. 684-709
64. Wraith, A.E., ed., Gas Injection into Liquid Metals, Proceedings of a One Day Symposium, University of Newcastle Upon Tyne, U.K., 1979
65. Davidson, J.F., and Schüller, B.O.G., "Bubble Formation at an Orifice in a Viscous Liquid", Trans. Instn. Engrs. Vol. 38, 1960, pp. 144-154
66. Davidson, J.F. and Schuler, B.O.G., "Bubble Formation at an Orifice in an Inviscid Liquid", Trans. Instn. Chem. Engrs. Vol. 38, 1960, pp. 335-342
67. Davidson, J.F. and Harrison, D., Fluidized Particles, Cambridge University Press, London 1963, pp. 50-56
68. Wraith, A.E. and Chalkley, M.E., "Tuyere Injection for Metal Refining", Advances in Extractive Metallurgy, ed. Royal Institute of Mining and Metallurgy, 1977, pp. 27-33
69. Van Krevelen, D.W. and Hofstijzer, P.J., Chem. Eng. Progr., 46, 29-35, 1950
70. Rennie, J. and Evans, F., "The Formation of Froths and Foams Above Sieve Plates", Brit. Chem. Eng. Vol. 7, 1962, pp. 498-502
71. Leibson, I., Hocomb, E.G., Cacosso, A.G. and Jacmic, J.J., "Rate of Flow and Mechanics of Bubble Formation From Single Submerged Orifices", A.I.Ch.E. Journal, Vol. 2, No. 3, September 1956, pp. 296-306

72. Wraith, A.E., "Two Stage Bubble Growth at a Submerged Plate Orifice", Chem. Eng. Science, Vol. 26, 1971, pp. 1659-1671
73. Datta, R.L., Napier, D.H. and Newitt, D.M., Trans. Inst. Chem. Engrs. Vol. 28, 1950, p. 14
74. Quigley, G.J., Johnson, A.I. and Harris, B.L., Chem. Eng. Progr. Symp. Ser. Vol. S1, 1955, p. 31
75. Coppock, P.D. and Meiklejohn, G.T., Trans. Inst. Chem. Engrs. Vol. 29, 1951, p. 75
76. Benzing, R.L. and Myers, J.E., Ind. Eng. Chem. Vol. 47, 1955, p. 2087
77. Siemes, W., and Kaufmann, J.F., Chem. Eng. Sci. Vol. 5, 1956, p. 127
78. Sano, M. and Mori, K., Trans. Jpn. Inst. Met., Vol. 17, 1976, pp. 344-352
79. Irons, G.A. and Guthrie, R.I.L., "Bubble Formation at Nozzles in Pig Iron", Trans. of AIME, Vol. 9B, March 1978, pp. 101-110
80. Sahai, Y. and Guthrie, R.I.L., "The Formation and Role of Bubbles in Steelmaking Operations", International Symposium on Modern Developments in Steelmaking, Jamshedpur, India, February 1981, pp. 1.5.1-1.5.24
81. Engh, T.A., Tveit, H., Bertheussen, H., Strømsnes, P., Venås, K. and Svantas, T.M., "Model Studies of Clogging in Tuyeres and Lances", Scan. Journal of Metall., Vol. 5, 1976, pp. 21-26
82. Wallis, G.B., One Dimensional Two Phase Flow, McGraw - Hill, New York, 1969, pp. 243-281
83. Taylor, G.I., "The Instability of Liquid Surfaces When Accelerated in a Direction Perpendicular to their Planes", Proc. Roy. Soc. (London), Vol. A201, 1950, pp. 192-196
84. Zuber, N. "Hydrodynamic Aspects of Boiling Heat Transfer", A.E.C.U. 4439 Rept., U.S. Atomic Energy Commission, 1959, pp. 118-136
85. Perry, R.H. and Chilton, C.H., eds. Chemical Engineers' Handbook, 5th ed., McGraw - Hill, New York, 1973
86. Irons, G.A. and Guthrie, R.I.L., "Bubble Behaviour in Molten Metals", Can. Met. Quart., In Press, 1980

87. Davidson, L. and Amick, E., "Formation of Gas Bubbles at Horizontal Orifices", A.I.Ch.E. Journal, Vol. 2, 1956, p. 336
88. Whalen, T.J., Kaufman, S.M. and Humenik Jr., M. "Surface Tensions and Surface Absorptions in Liquid Iron - Carbon Ternary Solutions", Structure and Properties of Liquid Metals, Transactions of the ASM, Vol. 55, 1962, pp. 778-785
89. Selçuk, E. and Kirkwood, D.H., "Surface Energies of Liquid Cast Irons Containing Magnesium and Cerium", Journal of the Iron and Steel Institute, February 1973, pp. 134-140